UC Berkeley
UC Berkeley Electronic Theses and Dissertations

Title
Observation of the electroweak production of two W bosons with the same electric charge in association with two jets in pp collisions at sqrt{s}=13 TeV with the ATLAS detector

Permalink
https://escholarship.org/uc/item/6t60494q

Author
Duffield, Emily

Publication Date
2019

Peer reviewed|Thesis/dissertation

Observation of the electroweak production of two W bosons with the same electric charge in association with two jets in pp collisions at $\sqrt{s} = 13$ TeV with the ATLAS detector

by

Emily Duffield

A dissertation submitted in partial satisfaction of the

requirements for the degree of

Doctor of Philosophy

in

Physics

in the

Graduate Division

of the

University of California, Berkeley

Committee in charge:

Professor Marjorie Shapiro, Chair
Professor Robert Jacobsen
Professor Karl Van Bibber

Summer 2019

Observation of the electroweak production of two W bosons with the same electric charge in association with two jets in pp collisions at $\sqrt{s} = 13$ TeV with the ATLAS detector

Abstract

Observation of the electroweak production of two W bosons with the same electric charge in association with two jets in pp collisions at $\sqrt{s} = 13$ TeV with the ATLAS detector

by

Emily Duffield

Doctor of Philosophy in Physics

University of California, Berkeley

Professor Marjorie Shapiro, Chair

This dissertation presents the observation of $W^{\pm}W^{\pm}$ electroweak production in proton-proton collisions with a center-of-mass energy of 13 TeV at the Large Hadron Collider using the ATLAS detector. The W bosons are required to decay leptonically, giving a signature of two leptons (electrons or muons) with the same electric charge, two jets with a large invariant mass and rapidity separation, and missing transverse energy. The $W^{\pm}W^{\pm}$ electroweak fiducial cross section is measured using 36.1 fb^{-1} of data recorded in 2015 and 2016. A total of 122 candidate events are observed with a fitted background of 69 ± 7 events, corresponding to an observed signal significance of 6.5 standard deviations. The measured fiducial cross section is $\sigma_{\mathrm{fid}} = 2.89 \, ^{+0.51}_{-0.48}(\mathrm{stat}) \, ^{+0.29}_{-0.28}(\mathrm{syst})$ fb and is in agreement with Standard Model predictions.

To My Mom

For a million different reasons, this never would have happened without you.

Contents

List of Figures

List of Tables

Acknowledgments

This dissertation represents the culmination of almost an entire decade of my life, first as an undergraduate student and then as a graduate student. There have been so many important people over the years who have guided me and supported me throughout this journey. For them, I am forever thankful.

While it would be impossible to list everyone by name, I would like to give special thanks to a few truly remarkable groups and individuals.

To Marjorie Shapiro, my advisor at UC-Berkeley, thank you for always being in my corner. Your constant advice, support, and encouragement helped me throughout my entire UC-Berkeley experience, and especially during those times when difficult situations arose.

To Simone Pagan Griso, I have always considered you my unofficial second advisor. Thank you for always taking the time to answer my questions and for being a constant source of guidance during my graduate career.

To Karolos Potamianos, thank you for all of your help throughout my time at CERN. During what could have been a very isolating and overwhelming transition, you never failed to help in whatever way you could, whether it be by answering questions about the pixel detector or by just chatting about life.

To the LBNL ATLAS group as a whole, I feel so lucky to have worked and learned alongside such a talented group of people. Thank you all for providing such a warm, welcoming, and collaborative environment.

To my UC-Berkeley graduate classmates, I do not think a better class of students has ever existed at Berkeley. The friendships we forged, the laughter we shared, and the support you provided will never be forgotten.

To the University of Minnesota, thank you for providing me with an extraordinary undergraduate experience. Not only did you thoroughly prepare me for graduate school, but you also provided an amazing community that will always feel like a second family. Special thanks to Kate, my undergraduate honors advisor, for providing the advice and support that made this journey possible.

To my husband, thank you for your constant and unwavering love and support throughout this entire journey. I will be forever thankful for everything you have done for me, from waiting patiently during our years apart, to not complaining when I turned our living room into my private office while writing this dissertation.

Finally, to my mom and dad, I could write an entire dissertation listing all the reasons why I am so thankful to be your daughter. Thank you for always believing in me, and for doing everything in your power to help me along the way, from driving me and all my belongings across the country six years ago, to reading this entire dissertation. I would not be where I am today without you.

Chapter 1

Introduction

Since its formulation in the 1960-70s, the Standard Model of particle physics has been very successful at describing the fundamental particles and their interactions. One of the fundamental building blocks of the Standard Model is the unified description of the electromagnetic and weak forces into the electroweak theory [1, 2, 3]. This theory, based on local gauge symmetries, requires the existence of the massless photon and massive W and Z bosons (electroweak gauge bosons) to mediate interactions between fundamental particles. These bosons acquire their mass via electroweak symmetry breaking (EWSB). With the discovery of a Higgs boson in 2012 [4, 5], the exact nature of this symmetry breaking has been the focus of a great deal of study.

A promising avenue for examining the symmetry breaking is provided by the electroweak theory prediction of self-interactions between electroweak gauge bosons. These self-interactions are referred to as *electroweak gauge boson scattering* or *vector boson scattering* (VBS). These interactions include the 2→2 scattering of gauge bosons via quartic gauge boson vertices and triple gauge boson vertices mediated by an electroweak gauge boson or a Higgs boson. VBS is intrinsically tied to EWSB in two ways: (1) EWSB introduces the longitudinally polarized modes of the massive electroweak gauge bosons which are being scattered, and (2) without a Higgs boson, the scattering of longitudinally polarized bosons violates unitarity at center-of-mass energies around 1 TeV [6, 7, 8]. As a result, VBS is a key process for not only probing EWSB, but also providing indirect measurements of properties of the Higgs boson.

In addition to probing EWSB, studying VBS also provides insight into the gauge structure of the boson self-interactions. Prior to the first data taking period of the Large Hadron Collider (LHC), only triple gauge couplings (TGCs) [9, 10, 11] had been constrained using collider data, while no unambiguous demonstrations of quartic gauge couplings (QGCs) had been observed. Observation of VBS at the LHC would provide information on QGCs of massive electroweak gauge bosons, since the cross section contains contributions from both triple and quartic gauge boson vertices.

At the LHC, VBS occurs as shown in Figure 1.1, where the final state is two gauge

bosons produced in association with two jets resulting from the quarks[1]. In addition to this diagram, there are several other diagrams (examples of which are shown in Figure 1.2) that produce the same final state. The complete set of diagrams producing the same final state as VBS can be separated into two gauge-invariant classes: *electroweak production* and *strong production*. Electroweak production involves only electroweak interactions at leading order and includes VBS and other electroweak diagrams, such as Figure 1.2(left). Strong production involves diagrams which contain both electroweak and strong interactions, as shown in Figure 1.2(right). While electroweak production and strong production can be separated in a gauge-invariant way, VBS cannot be separated from other completely electroweak diagrams producing two gauge bosons and two jets (e.g. Figure 1.2(left)) in a gauge-invariant manner. As a result, instead of directly measuring VBS, the process measured is the electroweak production of two gauge bosons with two jets.
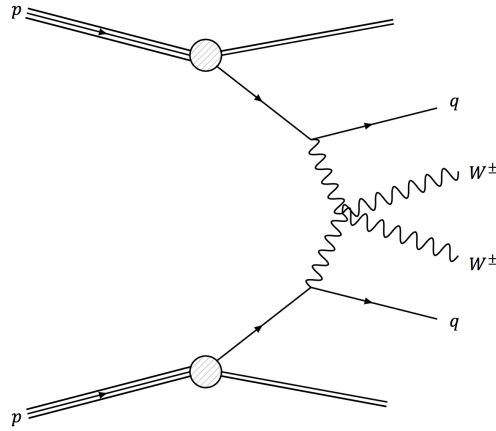
Figure 1.1: Example diagram of VBS at the LHC with a final state consisting of two W bosons with the same electric charge and two outgoing quarks.

The observation of a VBS process with the ATLAS detector via the electroweak production of two W bosons with the same electric charge in association with two jets is described in detail in this dissertation [12]. This observation was performed using 36.1 fb^{-1} of proton-proton (pp) collision data with a center-of-mass energy of 13 TeV collected from the LHC using the ATLAS detector in 2015 and 2016. Previous evidence of $W^{\pm}W^{\pm}jj$ electroweak production was seen by the ATLAS and CMS collaboration in 20.3 fb^{-1} of 8 TeV data [13, 14], with ATLAS seeing an excess of 3.6 σ in data over background-only expectation, and CMS seeing an excess of 2.0 σ over backgrounds. A recent publication from CMS reported an observation of $W^{\pm}W^{\pm}jj$ production in 35.9 fb^{-1} of 13 TeV pp collision data, with a significance of 5.5 σ [15].

---

[1]Colored particles, such as quarks, cannot exist in isolation. Therefore, a single quark from a proton-proton collision will give rise to several hadrons which will hit the detector. The collection of these hadrons is called a jet.
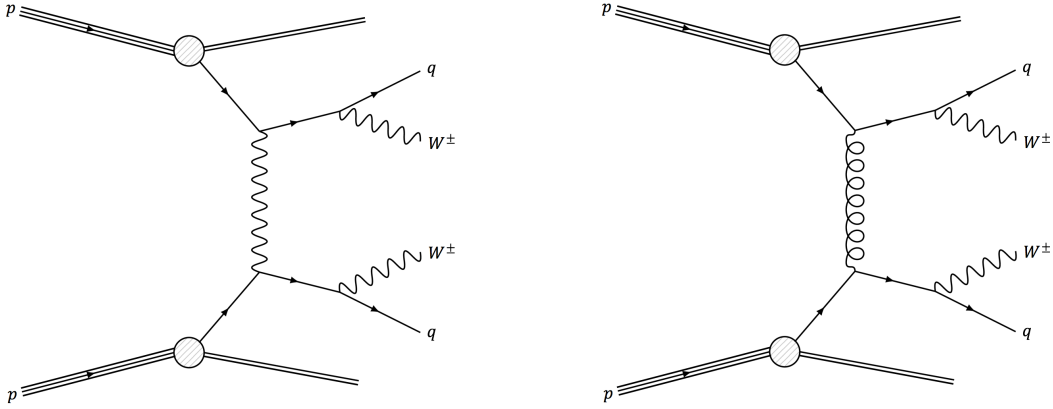
Figure 1.2: Examples of non-VBS diagrams that contribute to electroweak production (left) and strong production (right) at the LHC with a final state consisting of two W bosons with the same electric charge and two outgoing quarks.

This dissertation is structured as follows: Chapter 2 reviews the Standard Model and EWSB. Chapter 3 gives an overview of the ATLAS detector and the LHC. Chapter 4 describes the overall strategy of the analysis detailed in this dissertation. Chapter 5 outlines the simulation samples used to conduct the analysis and how the samples are produced. Chapter 6 explains the procedures used to reconstruct physics objects from detector data. Chapter 7 describes the analysis selection requirements applied to data and simulated samples. Chapter 8 explains how background contributions from various physics processes are estimated. Chapter 9 details the theoretical prediction of $W^\pm W^\pm jj$ electroweak production in this analysis. Chapter 10 discusses the theoretical uncertainties associated with physics processes in this analysis. Chapter 11 describes the standard ATLAS analysis uncertainties. Chapter 12 details the method used to observe $W^\pm W^\pm jj$ electroweak production. Chapter 13 presents the results of the analysis. Chapter 14 summarizes the conclusions.

Chapter 2

Theory

This chapter describes the theory and motivation for this analysis. A brief overview of the Standard Model is presented, with more detail given to the description of EWSB and VBS. Production of the final state studied in this analysis, $W^{\pm}W^{\pm}jj$, at the LHC is also discussed.

2.1 Standard Model Overview

The Standard Model describes the fundamental constituents of matter and their interactions with striking accuracy, and it has remained largely unchanged since the mid-1970s. The Standard Model has been found to be theoretically self-consistent, and most Standard Model predictions have been verified. These verified predictions include the existence of the W and Z bosons [16, 17], the top quark [18, 19], the charm quark [20, 21, 22], the bottom quark [23], and a Higgs boson [4, 5]. A thorough description of the Standard Model and its theoretical framework can be found in Refs. [24, 25, 26].

The Standard Model describes two types of particles (fermions and bosons) using a mathematical framework provided by Quantum Field Theory (QFT) [24]. This framework is based on symmetries which map conserved quantities to the invariance of the Lagrangian under a certain transformation (Noether's theorem). Fermions are fundamental Dirac quantum fields, while gauge bosons are fundamental fields with spin-1. The interaction term between the fermions and gauge bosons is fully determined under the postulate of local gauge invariance, as discussed below (see Section 2.1.2). The Standard Model is described by a local $SU(3)_C \times SU(2)_L \times U(1)_Y$ gauge symmetry, where $SU(3)_C$ is the symmetry group for the strong interaction, and $SU(2)_L \times U(1)_Y$ is the symmetry group for the unified electroweak interaction.

2.1.1 Particles of the Standard Model

The fundamental particles of the Standard Model are summarized in Table 2.2. The Standard Model consists of 12 flavors of fermions (each with its own antiparticle), 5 gauge bosons (the

W^+, W^-, Z, photon, and gluon), and one scalar boson (the Higgs).

Fermions are spin-$\frac{1}{2}$ point-like particles which form matter. They are organized into three generations as outlined in Table 2.1. Each generation consists of two quarks which interact via the electroweak and strong forces, and two leptons (a charged lepton and a neutrino) which only interact via the electroweak force. For the two quarks of each generation, there is an *up-type* quark which has a charge $Q = +\frac{2}{3}$, and a *down-type* quark with charge $Q = -\frac{1}{3}$. The three generations differ only in the masses of the particles, with the first generation being the lightest.

Generation	1	2	3
Leptons	e	μ	τ
	ν_e	ν_μ	ν_τ
Quarks	u	c	t
	d	s	b

Table 2.1: Standard Model generations of quarks and leptons.

Bosons are fundamental particles with integer spin. The gauge bosons have spin-1, and the scalar boson has spin-0. All observed bosons are gauge bosons except the Higgs boson, which is a scalar boson. As stated previously, the forces of the Standard Model are mediated by the gauge bosons:

- The **electromagnetic force** is mediated by the photon (γ) and is responsible for interactions such as the radiation of photons from excited atoms.

- The **strong nuclear force** is mediated by gluons (g) and is responsible for binding the quarks in protons and neutrons. The strong nuclear force is also responsible for the interactions between quarks and hadrons.

- The **weak nuclear force** is mediated by the $W^\pm$ and Z bosons and is responsible for processes such as nuclear β-decay (nuclear reactions).

At low energy, the electromagnetic and weak forces appear distinct. Above the unification energy, around 100 GeV, the electromagnetic and weak forces are unified into a single interaction known as the *electroweak interaction.*

In an ordinary QFT, gauge bosons are theorized to be massless. While this is true for the photon and the gluons in the Standard Model, this is not the case for the $W^\pm$ and Z bosons. In fact, the $W^\pm$ and Z bosons have a mass roughly 100 times the mass of the proton. In the Standard Model, the masses of the $W^\pm$ and Z bosons are explained by the spontaneous breaking of the electroweak gauge symmetry resulting from the presence of a spin-0 field (Higgs field). This field interacts with the electroweak gauge bosons to provide their masses while preserving the local gauge invariance. The process of EWSB is discussed in further detail in Section 2.1.4.

	Particle	Spin	Electric Charge	Mass
Leptons	electron (e)	$\frac{1}{2}$	-1	0.511 MeV
	muon (μ)			105.6 MeV
	tau (τ)			1777 MeV
	electron neutrino (ν_e)	$\frac{1}{2}$	0	<2 eV
	muon neutrino (ν_μ)			<0.19 MeV
	tau neutrino (ν_τ)			<18.2 MeV
Quarks	up (u)	$\frac{1}{2}$	$+\frac{2}{3}$	1.9-2.7 MeV
	charm (c)			1.27 ± 0.02 GeV
	top (t)			172.9 ± 0.4 GeV
	down (d)	$\frac{1}{2}$	$-\frac{1}{3}$	4.5-5.2 MeV
	strange (s)			88-104 MeV
	bottom (b)			$4.18^{+0.03}_{-0.02}$ GeV
Bosons	photon (γ)	1	0	0
	gluon (g)		0	0
	Z		0	91.2 GeV
	$W^\pm$		± 1	80.4 GeV
	Higgs (H)	0	0	125.18 GeV

Table 2.2: Properties of fundamental Standard Model particles [26].

2.1.2 Lagrangian Density of the Standard Model

The fundamental particles and their interactions can be expressed mathematically as quantum fields. The dynamics of these fields can be expressed by Lagrangian densities. The classical Standard Model Lagrangian density can be written as [24]:

$$\mathcal{L}_{SM} = \mathcal{L}_{gauge} + \mathcal{L}_{fermion} + \mathcal{L}_{Higgs} + \mathcal{L}_{Yukawa} \tag{2.1}$$

where:

$$\mathcal{L}_{gauge} = -\frac{1}{4}G^a_{\mu\nu}G^{a\mu\nu} - \frac{1}{4}W^a_{\mu\nu}W^{a\mu\nu} - \frac{1}{4}B_{\mu\nu}B^{\mu\nu} \tag{2.2}$$

$$\mathcal{L}_{fermion} = \sum_{Q_L} i\overline{Q_L}\gamma^\mu D_\mu Q_L + \sum_{q^u_R} i\overline{q^u_R}\gamma^\mu D_\mu q^u_R + \sum_{q^d_R} i\overline{q^d_R}\gamma^\mu D_\mu q^d_R$$
$$+ \sum_{L_L} i\overline{L_L}\gamma^\mu D_\mu L_L + \sum_{l_R} i\overline{l_R}\gamma^\mu D_\mu l_R \tag{2.3}$$

$$\mathcal{L}_{Higgs} = \left(D_\mu \Phi\right)^\dagger \left(D_\mu \Phi\right) + \mu^2 \Phi^\dagger \Phi - \lambda \left(\Phi^\dagger \Phi\right) \tag{2.4}$$

$$\mathcal{L}_{Yukawa} = -\sum_{L_L, l_R} y_{L_L, l_R} \overline{L_L} \phi l_R - \sum_{Q, q} y_{Qq} \overline{Q_L} \phi q_R^d - \sum_{Q, q} y_{Qq} \overline{Q_L} \tilde{\phi} q_R^u + h.c. \tag{2.5}$$

This representation of $\mathcal{L}_{SM}$ ignores the ghost and gauge-fixing terms necessary to quantize the Lagrangian. Einstein summation convention is used, with γ^μ denoting the Dirac matrices ($\gamma^\mu = \left\{\gamma^0, \gamma^1, \gamma^2, \gamma^3\right\}$), and the adjoint spinor $\overline{\psi} = \psi^\dagger \gamma^0$.

Bosonic Fields

The fields B_μ, W_μ^a, and G_μ^a, detailed in Table 2.3, denote the different gauge boson fields. The self-interactions of the gauge boson fields are described in Equation 2.2, where the fields are expressed as field strength tensors:

$$A_{\mu\nu}^a = \partial_\mu A_\nu^a - \partial_\nu A_\mu^a + g f^{abc} A_\mu^b A_\nu^c, \tag{2.6}$$

where $A_\mu^a \in \left\{B_\mu, W_\mu^a, G_\mu^a\right\}$, g is the gauge coupling $g \in \left\{g_Y, g_w, g_s\right\}$, and f^{abc} is the fundamental structure constants[1] of the gauge group.

Field	Associated Charge	Group	Coupling
B_μ	weak hypercharge, Y_W	$U(1)_Y$	g_Y
W_μ^a $(a = 1, 2, 3)$	weak isospin, T_3	$SU(2)_L$	g_w
G_μ^a $(a = 1, ..., 8)$	color	$SU(3)_C$	g_s

Table 2.3: Summary of spin-1 Bosonic fields in the Standard Model and their properties [26].

The interactions of the gauge boson fields with the fermion fields are included in Equation 2.3 in the covariant derivative D_μ. The covariant derivative is defined as:

$$D_\mu = \partial_\mu + i g_Y Y_W B_\mu + i g_w T_a W_\mu^a + i g_s \Lambda_a G_\mu^a, \tag{2.7}$$

where Y_W (the weak hypercharge), T_a (the weak isospin), and Λ_a (the strong isospin) are the generators of the gauge symmetry groups (see Table 2.3). The weak isospin is defined as $T_a = \frac{1}{2}\sigma_a$ $(a = 1, 2, 3)$, where σ_a represents the Pauli matrices [26]. The strong isospin can be written as $\Lambda_a = \frac{1}{2}\lambda_a$ $(a = 1, ..., 8)$ where λ_a are the Gell-Mann matrices [26].

There is only one fundamental scalar boson field in the theory, the Higgs field (H), which is a component of the $SU(2)_L$ doublet field Φ (see Equation 2.4). The Higgs field is discussed in more detail in Section 2.1.4.

---

[1] f^{abc} is defined by the relation $\left[T^a, T^b\right] = i f^{abc} T^c$, where T^i are the symmetry group generators. For SU(2), $T^i = \sigma^i$ (the Pauli matrices) and for SU(3), $T^i = \frac{\lambda^i}{2}$ (the Gell-Mann matrices).

Fermionic Fields

Left-handed (LH) fermion fields are defined as an $SU(2)_L$ doublet, while right-handed (RH) fermion fields are defined as a singlet. In Equations 2.3-2.5, LH and RH leptons are denoted by L_L and l_R, respectively. Similarly, LH and RH quarks are written as Q_L and q_R, respectively. The characteristics of these fields are summarized in Table 2.4. The RH neutrino field has been ignored here.

Due to parity violation, the LH and RH fields transform differently under the group symmetry:

$$\psi_{L/R} = \frac{1}{2}\left(1 \mp \gamma^5\right)\psi, \tag{2.8}$$

where ψ denotes the four-component Dirac fermion field, and γ^5 is defined as $\gamma^5 = i\gamma^0\gamma^1\gamma^2\gamma^3$.

For fermions, the weak hypercharge and weak isospin can be related to the electric charge Q, with:

$$Q = \frac{Y_W}{2} + T_3. \tag{2.9}$$

For LH quarks, the correct basis to use to describe the mass eigenstates is different from the correct basis to use for EW decays. Transforming between these bases is done using the CKM mass-mixing matrix [26].

Symbol	Fermions	Particles			Q	Y_W	T_3
L_L	LH leptons	$\begin{pmatrix}\nu_{e,L}\\e_L\end{pmatrix}$	$\begin{pmatrix}\nu_{\mu,L}\\\mu_L\end{pmatrix}$	$\begin{pmatrix}\nu_{\tau,L}\\\tau_L\end{pmatrix}$	0 -1	-1 -1	$1/2$ $-1/2$
l_R	RH leptons	e_R	μ_R	τ_R	-1	-2	0
Q_L	LH quarks	$\begin{pmatrix}u_L\\d_L\end{pmatrix}$	$\begin{pmatrix}c_L\\s_L\end{pmatrix}$	$\begin{pmatrix}t_L\\b_L\end{pmatrix}$	$2/3$ $-1/3$	$1/3$ $1/3$	$1/2$ $-1/2$
q_R^u	RH up-type quark	u_R	c_R	t_R	$2/3$	$4/3$	0
q_R^d	RH down-type quark	d_R	s_R	b_R	$-1/3$	$-2/3$	0

Table 2.4: Summary of Fermionic fields in the Standard Model and their properties [26]. Y_W denotes the weak hypercharge, Q represents the electric charge, and T_3 is the weak isospin.

2.1.3 Electroweak Gauge Theory

Electroweak gauge theory is built upon the theoretical framework of the local gauge symmetry $U(1)_Y \times SU(2)_L$. This theory requires the presence of gauge bosons in the covariant derivative (see Equation 2.6). With the addition of the gauge bosons, the interactions between the gauge boson fields and the fermions can be deduced from Equation 2.3, where the

gauge bosons couple with all fermions. This introduces a problem though, since the photon does not couple to neutrinos. Thus, the gauge fields do not describe the observed gauge bosons.

To obtain photon fields without any coupling to neutrinos, the gauge boson fields B_μ and W_μ^a are required to mix in the following way:

$$\begin{pmatrix} A_\mu \\ Z_\mu \end{pmatrix} = \begin{pmatrix} \cos\theta_w & \sin\theta_w \\ -\sin\theta_w & \cos\theta_w \end{pmatrix} \begin{pmatrix} B_\mu \\ W_\mu^3 \end{pmatrix} \tag{2.10}$$

$$W_\mu^\pm = \frac{1}{\sqrt{2}}\left(W_\mu^1 \mp iW_\mu^2\right), \tag{2.11}$$

where A_μ is the photon field, Z_μ is the Z boson field, and the W bosons are described by $W_\mu^\pm$. Equation 2.10 introduces θ_w which is the electroweak mixing angle. θ_w is chosen such that A_μ: (1) decouples from the neutrinos, and (2) couples to both LH and RH electrons in the same way. In addition, since B_μ couples equally to LH and RH fields while W_μ^3 only couples to LH fermions, the Z boson does not couple to LH and RH fermions equally. Since the W boson fields originate purely from $SU(2)_L$ gauge fields (see Equation 2.11), the W bosons do not couple to RH fermions.

2.1.4   Electroweak Symmetry Breaking

The interactions of gauge bosons with themselves and with fermions are described by $\mathcal{L}_{gauge}$ and $\mathcal{L}_{fermion}$ (see Equations 2.2, 2.3). Adding mass terms for the gauge bosons to either of these Lagrangians is forbidden due to gauge invariance. It has been known for over 30 years, however, that the W and Z bosons have mass [16, 17]. In the 1960s, three physicists (Brout, Englert, and Higgs) proposed a mechanism to introduce mass terms while preserving global symmetry. This mechanism is known as the Brout-Englert-Higgs Mechanism [27, 28] and is often referred to simply as the Higgs Mechanism. With this mechanism, the gauge symmetry is *spontaneously broken* and is thus called *electroweak symmetry breaking (EWSB)*.

In this mechanism, a complex scalar $SU(2)_L$ doublet field Φ with a weak hypercharge of $Y_W = 1$ is introduced:

$$\Phi = \begin{pmatrix} \phi^+ \\ \phi^0 \end{pmatrix} = \frac{1}{\sqrt{2}}\begin{pmatrix} \phi_1^+ + i\phi_2^+ \\ \phi_1^0 + i\phi_2^0 \end{pmatrix}, \tag{2.12}$$

where $\phi_{1,2}^{0,+}$ are real, giving the field four degrees of freedom. By convention, ϕ_1^0 is assigned to be the charge-neutral, non-zero vacuum expectation value (VEV), v.

The Higgs Lagrangian (see Equation 2.4) can be re-written in a form with a kinetic term and a potential term:

$$\mathcal{L}_{Higgs} = \left(D_\mu\Phi\right)^\dagger\left(D_\mu\Phi\right) - V(\Phi), \tag{2.13}$$

where

$$V(\Phi) = -\mu^2 \Phi^\dagger \Phi + \lambda \left(\Phi^\dagger \Phi \right). \tag{2.14}$$

In Equation 2.14, there are two free scale parameters: the mass parameter μ, and the quartic coupling parameter λ. These parameters are defined such that $\lambda > 0$ and $\mu > 0$. This Higgs potential is invariant under $SU(2)_L \times U(1)_Y$. The minimum of the Higgs potential (with $\lambda, \mu > 0$) is not at $\Phi = 0$, but at a finite value. To make things easier, the unitary gauge is used such that $\phi_1^+ = 0$, $\phi_2^+ = 0$, and $\phi_2^0 = 0$. In this gauge, the minimum of the Higgs potential is then:

$$\Phi_{min} = \frac{1}{\sqrt{2}} \begin{pmatrix} 0 \\ v \end{pmatrix}, \tag{2.15}$$

where

$$v = \sqrt{\frac{\mu^2}{\lambda}}. \tag{2.16}$$

By choosing this minimum to be the vacuum state ($\langle \Phi \rangle = \Phi_{min}$), the $SU(2)_L \times U(1)_Y$ symmetry of the physical vacuum is spontaneously broken. As a result, the only remaining symmetry is the $U(1)_{EM}$ symmetry, given by:

$$\Phi \rightarrow \exp i\theta_a (\frac{Y_W}{2} + T_3)\Phi, \tag{2.17}$$

where $Q = \frac{Y_W}{2} + T_3$. Therefore, the symmetry breaking can be described as:

$$SU(2)_L \times U(1)_Y \longrightarrow U(1)_{EM}. \tag{2.18}$$

The Higgs field can be expanded around the vacuum (see Equation 2.15) with:

$$\Phi_H = \frac{1}{\sqrt{2}} \begin{pmatrix} 0 \\ v + H \end{pmatrix}, \tag{2.19}$$

where H is a scalar field representing the physical Higgs boson. The other three degrees of freedom, which as stated earlier were set to zero in the unitarity gauge, correspond to massless Goldstone bosons.

Expanding the potential with respect to Φ_H results in:

$$V(H) = -\frac{1}{4}\mu^2 v^2 + \mu^2 H^2 + \lambda v H^3 + \frac{1}{4}\lambda H^4, \tag{2.20}$$

which gives a Higgs mass, m_H, of

$$m_H = \sqrt{2\mu^2} = \sqrt{2\lambda}v. \tag{2.21}$$

Mass terms for the electroweak gauge bosons are found by expanding the Higgs kinetic term, $\left(D_\mu\Phi\right)^\dagger\left(D_\mu\Phi\right)$, and finding the terms of form $\frac{1}{2}m_V^2 V^\mu V_\mu$. The resulting mass terms are:

$$M_{W^\pm} = \frac{v g_w}{2}, \tag{2.22}$$

$$M_Z = \frac{v}{2}\sqrt{g_w^2 + g_Y^2}, \tag{2.23}$$

$$M_\gamma = 0. \tag{2.24}$$

Expanding the kinetic term of the Higgs Lagrangian also leads to the interaction terms between the gauge bosons and the Higgs boson (see Section 2.2.2).

Mass terms for the fermions are introduced through Yukawa coupling terms between the fermion fields and the Higgs fields in the Yukawa Lagrangian (see Equation 2.5). The Yukawa couplings, $y_f \in \left\{y_{L_L l_R}, y_{Qq^u}, y_{Qq^d}\right\}$, are free parameters constrained by measurements of the fermion masses. Expanding Equation 2.5 with Φ_H (Equation 2.19) leads to the mass terms for the fermions and the interactions between fermions and the Higgs boson. The masses of fermions are proportional to Yukawa couplings and the VEV, v:

$$m_f = \frac{1}{\sqrt{2}} v y_f. \tag{2.25}$$

2.1.5 Limitations of the Standard Model

Despite the overarching success of the Standard Model, there are still a number of limitations within the theory. These limitations include both theoretical issues with the structure of the Standard Model and experimentally observed phenomena not explained by the Standard Model. A summary of a few of these issues is listed below.

- Only 5% of the energy in the Universe is described by the Standard Model. Of the remaining 95%, astrophysical observations suggest 27% is dark matter and 68% is dark energy [29]. Neither dark matter nor dark energy are explained by the Standard Model [30].

- According to the Standard Model, neutrinos are massless particles. However, experimental observations of neutrino oscillations [31] have shown neutrinos do have mass.

- Gravity, one of the four fundamental forces, is not included in the Standard Model. Therefore, the Standard Model is only accurate up to the Planck scale, $\mathcal{O}(10^{19}$ GeV$)$, where gravity becomes the dominant force.

- After the Big Bang, matter and anti-matter should have been produced in roughly equal amounts. The observable Universe, however, is composed of mostly matter and photons, with very little anti-matter. The Standard Model does not contain any mechanism to sufficiently explain the observed level of matter-antimatter asymmetry [32].

- A significant theoretical problem, referred to as the *hierarchy problem*, exists in the Standard Model due to the discrepancy between the electroweak scale, $\mathcal{O}(10^2 \text{ GeV})$, and the Planck scale, $\mathcal{O}(10^{19} \text{ GeV})$ [33]. The hierarchy problem results in the need for unnatural fine-tuned cancellations of loop contributions.

2.2 Vector Boson Scattering

Vector Boson Scattering (VBS) refers to the self-interactions of spin-1 bosons which contain three- and four-particle vertices. VBS is predicted by the gauge structure of the Standard Model (see Section 2.1.4). Below, the Leading Order (LO) Feynman representations of VBS are introduced, the Feynman rules of the interaction vertices are defined, and the importance of the Higgs boson in VBS is discussed.

2.2.1 Leading Order Diagrams

Leading Order VBS processes involve several Feynman diagrams connecting two initial state gauge bosons and two final state gauge bosons. The various diagrams are usually discussed in terms of channels defined by the Mandelstam variables which describe the kinematics of two particles scattering into two particles. The variables describe the energy, momentum, and angles of the particles in a manner that is Lorentz invariant. The Mandelstam variables are defined:

$$
\begin{aligned}
s &= (p_i + k_i)^2 = (p_f + k_f)^2 \\
t &= (p_f - p_i)^2 = (k_f - k_i)^2 \\
u &= (k_f - p_i)^2 = (p_f - k_i)^2
\end{aligned}
\tag{2.26}
$$

where p_i and k_i are the momenta of the initial state particles, and p_f, k_f are the momenta of the final state particles.

The letters s, t, and u are also used as the description of scattering events (and Feynman diagrams) where the interaction exchanges an intermediate particle with a squared four-momentum equal to s, t, or u. They are described as interactions taking place via the s-channel (space channel), t-channel (time channel), or u-channel, respectively.

The possible channels of VBS are the s-, t-, and u-channel vector boson exchange, the four particle vertex, and the s-, t-, and u-channel exchange of a Higgs boson. Figure 2.1 shows the Feynman diagrams for VBS diagrams with a vector boson exchange in the s-, t-, and u-channels. The remaining VBS diagrams are shown in Figure 2.2.

(a) s-channel

(b) t-channel
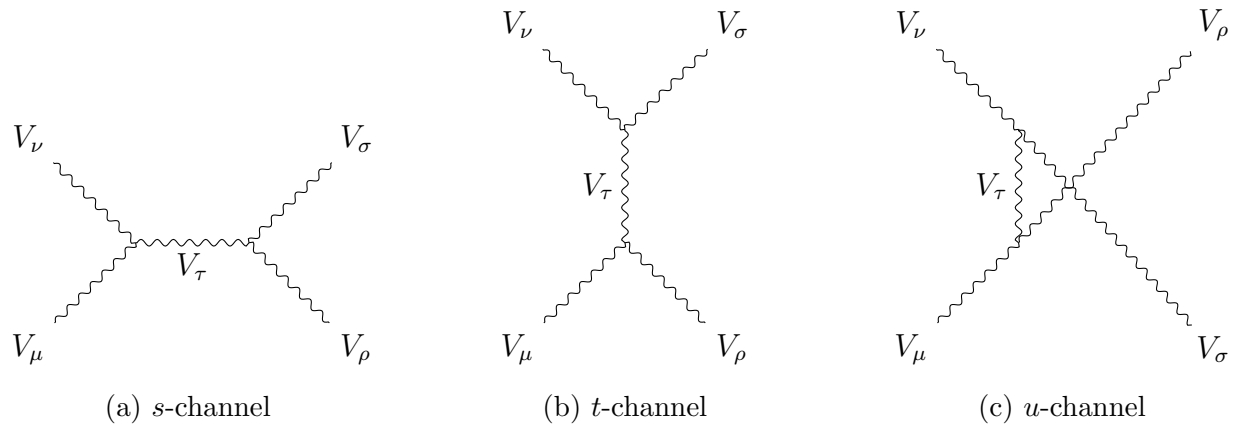
(c) u-channel

Figure 2.1: Feynman diagrams showing VBS via different channels.

(a) s-channel, Higgs exchange

(b) t-channel, Higgs exchange

(c) u-channel, Higgs exchange
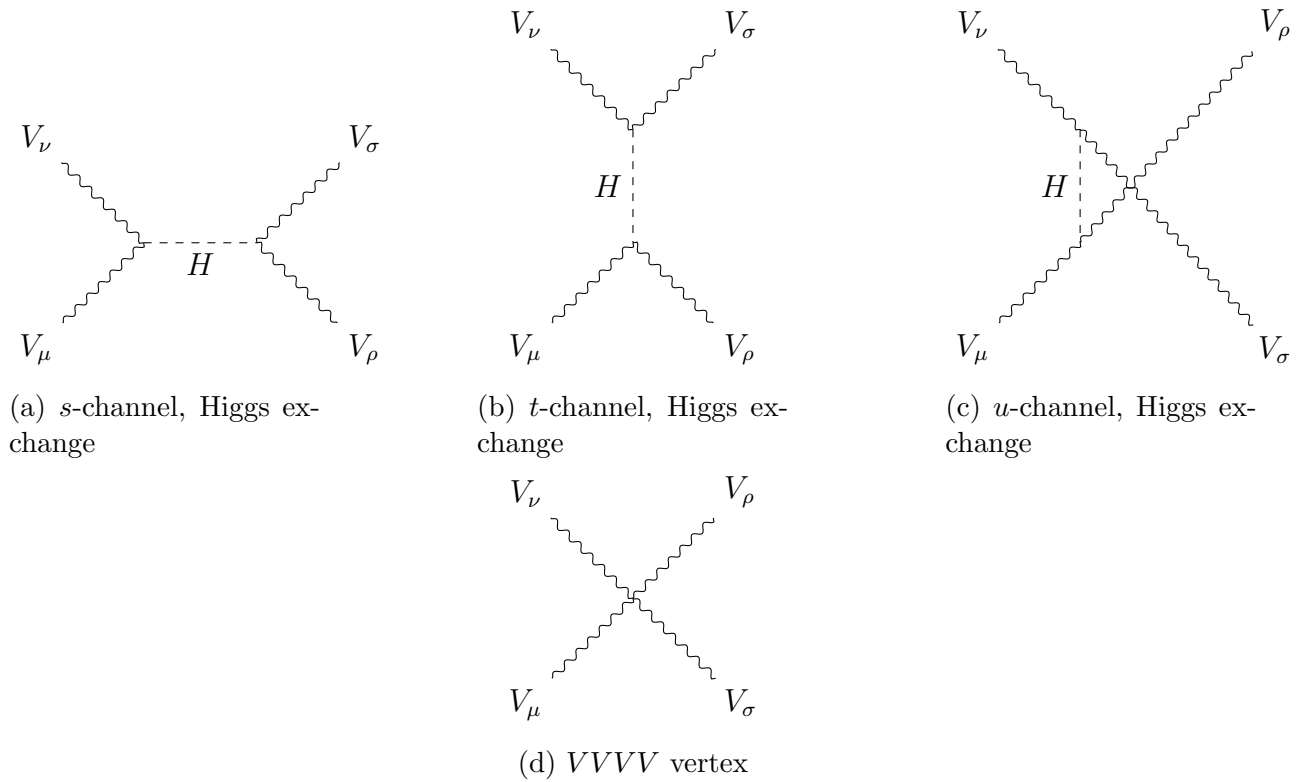
(d) $VVVV$ vertex

Figure 2.2: Feynman diagrams showing VBS diagrams via Higgs exchange and $VVVV$ vertex.

While Figures 2.1 and 2.2 show all LO VBS diagrams with two initial and two final vector (gauge) bosons, not all channels are possible for all boson combinations. For example, the s-channel diagrams are forbidden for $W^\pm W^\pm \to W^\pm W^\pm$ due to charge conservation. In order to discuss the details of these different diagrams, the theory of the gauge boson self-interactions must be discussed.

2.2.2 Feynman Rules

The Feynman rules describing the gauge boson self-interactions that are present in VBS processes are shown below. The Feynman rules for the remaining vertices not shown below can be found in Ref. [34]. All four-momenta are considered to be incoming. For the following vertices, the coupling constant g refers to g_w, the $SU(2)_L$ gauge coupling constant. The metric tensor, $g_{\mu\nu}$, is a 4×4 matrix diagonalized with the signature $\{+1, -1, -1, -1\}$.

Triple Electroweak Gauge Boson Vertices:

The Standard Model only allows charged triple gauge boson coupling vertices of the form W^+W^-V, where $V \in \left\{Z^0, \gamma\right\}$.
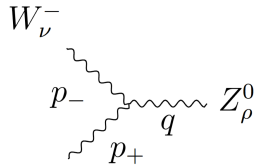
$$= ig\cos\theta_w \left[g_{\mu\nu}(p_- - p_+)_\rho + g_{\mu\rho}(p_+ - q)_\nu + g_{\rho\nu}(q - p_-)_\mu \right] \quad (2.27)$$
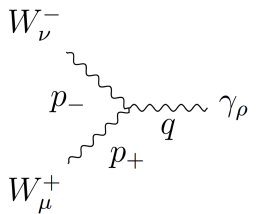
$$= ie \left[g_{\mu\nu}(p_- - p_+)_\rho + g_{\mu\rho}(p_+ - q)_\nu + g_{\rho\nu}(q - p_-)_\mu \right] \quad (2.28)$$

Quartic Electroweak Gauge Boson Vertices:

Shown below are the charged quartic electroweak gauge boson coupling vertices W^+W^-VV' where $VV' \in \left\{ Z^0Z^0, Z^0\gamma, \gamma\gamma, W^+W^- \right\}$. These vertices are independent of the boson momenta and depend on the combination of metric tensors, $g_{\mu\nu}$.

W_ν^- Z_ρ^0

W_μ^+ Z_σ^0

$$= ig^2 \cos^2 \theta_w \left[g_{\nu\sigma}g_{\mu\rho} + g_{\nu\rho}g_{\mu\sigma} - 2g_{\mu\nu}g_{\rho\sigma} \right] \qquad (2.29)$$

W_ν^- γ_ρ

W_μ^+ γ_σ

$$= ie^2 \left[g_{\nu\sigma}g_{\mu\rho} + g_{\nu\rho}g_{\mu\sigma} - 2g_{\mu\nu}g_{\rho\sigma} \right] \qquad (2.30)$$

W_ν^- Z_ρ^0

W_μ^+ γ_σ

$$= ieg \cos \theta_w \left[g_{\nu\sigma}g_{\mu\rho} + g_{\nu\rho}g_{\mu\sigma} - 2g_{\mu\nu}g_{\rho\sigma} \right] \qquad (2.31)$$

W_ν^- W_ρ^-

W_μ^+ W_σ^+
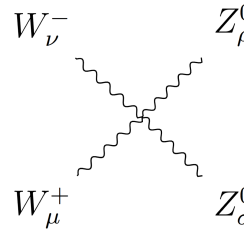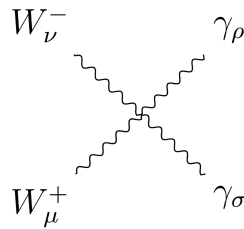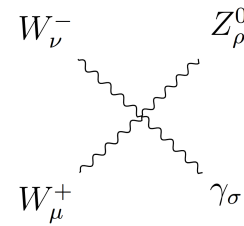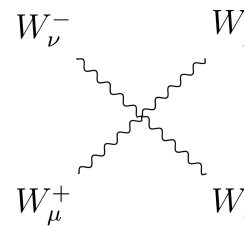
$$= ig^2 \left[2g_{\nu\rho}g_{\mu\sigma} - g_{\mu\nu}g_{\sigma\rho} - g_{\nu\sigma}g_{\mu\rho} \right] \qquad (2.32)$$

Higgs & Gauge Boson Vertices:

In the Standard Model, the Higgs boson can couple to gauge bosons with the vertex VVH, where $VV \in \left\{ Z^0 Z^0, W^+ W^- \right\}$. In the following equations, v (the VEV) can be written in terms of the W boson mass using $v = \frac{2M_W}{g}$, or the mass of the Z boson by using $v = \frac{2M_Z \cos \theta_w}{g}$.

$$W_\nu^-$$
$$\cdots H \qquad = \frac{1}{2} i v g^2 g_{\mu\nu} \tag{2.33}$$
$$W_\mu^+$$

$$Z_\nu^0$$
$$\cdots H \qquad = \frac{i v g^2}{2 \cos^2 \theta_w} g_{\mu\nu} \tag{2.34}$$
$$Z_\mu^0$$

2.2.3 Importance of the Higgs Boson in VBS

The Higgs boson plays a very important role in VBS. Figure 2.3 shows the three LO $W^\pm W^\pm$ scattering diagrams not involving the Higgs. If these were the only contributions to $W^\pm W^\pm$ scattering (where the bosons are longitudinally polarized), problems would arise at high energies, specifically regarding the scattering cross section.
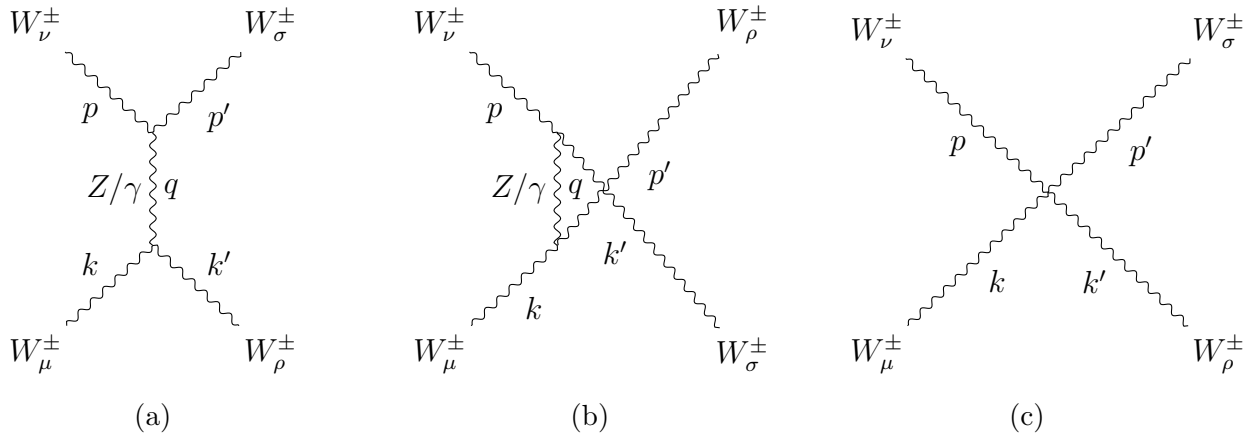
Figure 2.3: Leading Order $W^\pm W^\pm$ scattering with triple gauge boson couplings in the t-channel (a), and u-channel (b), and the quartic gauge coupling (c).

For a 2→ 2 scattering process where all particles have the same mass, m, the center-of-mass cross section can be written as:

$$\sigma = \frac{1}{32\pi^2 s} \int d\Omega \sqrt{1 - \frac{4m^2}{s}} |\mathcal{M}|^2, \tag{2.35}$$

where s is the center-of-mass energy and $\mathcal{M}$ is the scattering amplitude.

Using the Feynman rules from Section 2.2.2, the scattering amplitudes for the three diagrams in Figure 2.3 can be written as:

- t-channel TGC diagram:

$$
\begin{aligned}
i\mathcal{M}_{TGC,t} = i\epsilon_\nu(p)\epsilon_\sigma^*(p')&\Big[g^{\nu\sigma}(p-p')^\tau - g^{\nu\tau}(q+p)^\sigma + g^{\tau\sigma}(q+p')^\nu\Big] \\
&\times \Big(\frac{g^2 \cos^2 \theta_w}{q^2 - M_Z^2} + \frac{g^2 \sin^2 \theta_W}{q^2}\Big)g_{\lambda\tau} \\
&\times \Big[g^{\mu\rho}(k-k')^\lambda - g^{\mu\lambda}(q+k)^\rho + g^{\lambda\rho}(q+k')^\mu\Big]\epsilon_\mu(k)\epsilon_\rho^*(k')
\end{aligned}
\tag{2.36}
$$

- u-channel TGC diagram:

$$
\begin{aligned}
i\mathcal{M}_{TGC,u} = i\epsilon_\nu(p)\epsilon_\sigma^*(k')&\Big[g^{\nu\tau}(p-k')^\tau - g^{\nu\tau}(q+p)^\sigma + g^{\tau\mu}(q+k')^\nu\Big] \\
&\times \Big(\frac{g^2 \cos^2 \theta_w}{q^2 - M_Z^2} + \frac{g^2 \sin^2 \theta_W}{q^2}\Big)g_{\lambda\tau} \\
&\times \Big[g^{\mu\rho}(k-p')^\lambda - g^{\mu\lambda}(q+k)^\rho + g^{\lambda\rho}(q+p')^\mu\Big]\epsilon_\mu(k)\epsilon_\rho^*(p')
\end{aligned}
\tag{2.37}
$$

- QGC diagram:

$$i\mathcal{M}_{QGC} = ig^2\epsilon_\nu(p)\epsilon_\sigma^*(p')\epsilon_\mu(k)\epsilon_\rho^*(k')\Big(2g^{\nu\sigma}g^{\mu\rho} - g^{\mu\nu}g^{\sigma\rho} - g^{\nu\rho}g^{\sigma\mu}\Big) \tag{2.38}$$

In these equations, $\epsilon_\mu(p)$ represents the longitudinal polarization vector for the boson V^μ with momentum p. For a boson with 4-momentum $k^\mu = \{E_k, 0, 0, k\}$, the polarization vector would take the form $\epsilon_\mu = \{\frac{k}{m}, 0, 0, \frac{E_k}{m}\}$. In the limit that the momentum of the boson is much larger than the mass, the polarization vector becomes proportional to the momentum:

$$\epsilon_\mu = \frac{k^\mu}{m} + \mathcal{O}(\frac{m}{E_k}). \tag{2.39}$$

If this high momentum limit for the polarization vectors is substituted into the scattering amplitude equations above, after writing the equation in terms of the Mandelstam variables and removing all terms that do not increase with energy, the resulting amplitude grows as:

$$\mathcal{M}_{gauge} = \mathcal{M}_{TGC,t} + \mathcal{M}_{TGC,u} + \mathcal{M}_{QGC} \approx \frac{s}{m_w^2} + \mathcal{O}(1), \tag{2.40}$$

where $\mathcal{O}(1)$ is all terms that do not increase with energy.

Substituting Equation 2.40 in for the scattering amplitude in Equation 2.35 reveals that the cross section would be proportional to $\frac{s}{m_W^4}$. This indefinite increase of the cross section as energy increases will eventually violate unitarity, meaning that the predicted probability for VBS in pp collisions would eventually be larger than one. For VBS, the energy at which unitarity would be violated is $s \sim 1 - 2$ TeV [8, 7, 6].

In addition to the VBS processes shown in Figure 2.3, VBS can also occur with the exchange of a Higgs boson. The Feynman diagrams of LO $W^\pm W^\pm$ scattering processes which exchange a Higgs boson can be seen in Figure 2.4.

(a)   (b)

Figure 2.4: Leading Order $W^\pm W^\pm$ scattering with a Higgs exchange in the t-channel (a) and u-channel (b).

The scattering amplitude of the processes in Figure 2.4 are as follows:

- t-channel Higgs exchange:

$$i\mathcal{M}_{t,Higgs} = -ig^2 m_W^2 \frac{1}{q^2 - m_h^2}\left[\epsilon_\nu(p)\epsilon_\sigma^*(p')g^{\nu\sigma}g^{\mu\rho}\epsilon_\mu(k)\epsilon_\rho^*(k')\right] \tag{2.41}$$

- u-channel Higgs exchange:

$$i\mathcal{M}_{u,Higgs} = -ig^2 m_W^2 \frac{1}{q^2 - m_h^2}\left[\epsilon_\nu(p)\epsilon_\sigma^*(k')g^{\nu\sigma}g^{\mu\rho}\epsilon_\mu(k)\epsilon_\rho^*(p')\right] \tag{2.42}$$

Simplifying these scattering amplitudes in terms of the Mandelstam variables (as was done to the LO VBS $W^\pm W^\pm$ scattering processes mediated by a gauge boson), the resulting amplitude is:

$$\mathcal{M}_{Higgs} = \mathcal{M}_{t,Higgs} + \mathcal{M}_{u,Higgs} \approx -\frac{s}{m_w^2} + \mathcal{O}(1), \tag{2.43}$$

where once again $\mathcal{O}(1)$ are all the terms which do not increase with energy.

The resulting scattering amplitude has the same $\frac{s}{m_W^2}$ dependence as the gauge-only VBS scattering amplitude, but with the opposite sign. As a result, the combined amplitude, $\mathcal{M}_{gauge} + \mathcal{M}_{Higgs}$, asymptotes to a constant as s increases, which leads to a VBS cross section that decreases with energy, preserving unitarity.

2.3 Theoretical Description of pp Collisions

In high-energy scattering, the proton cannot be modeled as simply two non-interacting *up* quarks and a *down* quark existing freely in a bag; the internal structure of the proton must be considered [26]. In reality, the three previously mentioned quarks, the *valence* quarks, exist in a sea of virtual quark-antiquark pairs which arise from the gluons holding the quarks together. All of these partons contribute to the internal structure of the proton. The interactions between the quarks and gluons are described by *quantum chromodynamics (QCD)*.

Quantum Chromodynamics

Quantum Chromodynamics (QCD) is a non-abelian gauge theory that describes the interactions between quarks and gluons via the strong force. Quarks and gluons carry the conserved quantum number, color, which is analogous to electric charge. To account for the three quark colors (red, blue, and green), QCD is governed by the SU(3) symmetry group.

QFT assumes that particles are essentially free and propagating without any interaction. As a result, QFT considers all interactions as perturbations on a free theory. This perturbative approximation is largely correct as long as the coupling constants for each force are much less than one[2]. For the strong coupling constant $\alpha_S \equiv \frac{g_s^2}{4\pi}$, this assumption is not always valid.

For the strong force, the coupling "constant" α_S changes with the energy scale (Q) of the interaction due to the participation of virtual particles. As Q increases, α_S decreases. This *running* of α_S results in two key QCD characteristics:

- **Confinement:** At low energies (where α_S is stronger), quarks and gluons cannot be observed as free, isolated particles. Instead, quarks are always confined into color-neutral bound states (hadrons).

- **Asymptotic Freedom:** In the high energy limit (where α_S is weak), the strength of the strong force becomes small, and quarks and gluons behave as *nearly free* particles.

---

[2]If the coupling constants for each force are much less than one, that is analogous to saying a single interaction is more likely to occur than multiple interactions.

When α_S is known at some energy scale μ_R (the *renormalization scale*), the dependence of α_S on Q can be calculated using perturbation theory. The coupling constant α_S is related to the renormalization scale μ_R by the renormalization group equation (RGE):

$$\mu_R^2 \frac{d\alpha_S}{d\mu_R^2} = \beta(\alpha_S) = -\alpha_S^2 \Big(b_0 + b_1 \alpha_S + b_2 \alpha_S^2 + \dots \Big), \tag{2.44}$$

where the coefficients b_n give a correction to the β-function based on diagrams with n loops [26]. To first order in α_S, the dependence on Q is given by [35]:

$$\begin{aligned}
\alpha_S(Q^2) &= \frac{\alpha_S(\mu_R^2)}{1 + b_0 \alpha_S(\mu_R^2) \log \frac{Q^2}{\mu_R^2}} \\
&= \frac{1}{b_0 \ln \frac{Q^2}{\Lambda_{QCD}^2}},
\end{aligned} \tag{2.45}$$

where Λ_{QCD} is the scale at which the coupling diverges. The perturbation theory is only valid for scales $Q \gg \Lambda_{QCD}$, which corresponds to $\alpha_S(Q^2) \ll 1$. Experimental measurements indicate $\Lambda_{QCD} \approx 200$ GeV [26]. In other words, QCD interactions can be separated into two regimes: perturbative QCD for interactions at energies above Λ_{QCD}, and non-perturbative QCD for interactions at energies below Λ_{QCD}. Figure 2.5 shows the running of α_S as a function of Q, comparing theoretical predictions with measurements from various experimental sources.
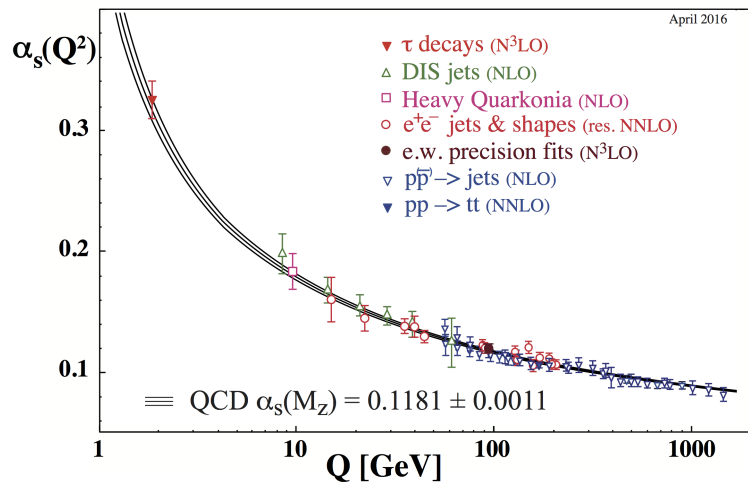
Figure 2.5: Summary of measurements of α_S as a function of the respective energy scale Q [26]. The degree of QCD perturbation theory used in the extraction of α_S is indicated in brackets.

Parton Distribution Functions

The composite nature of the colliding protons is described by the *parton model* [36, 37, 38]. The parton model was first developed in the context of deep inelastic scattering experiments, and then generalized to describe hadron-hadron collisions. In this model, protons are described as collections of point-like particles (partons) which are bound together by their interactions.

QCD calculations for *pp* collisions rely on QCD *factorization*, where the hard perturbative processes (e.g., the hard scattering between partons within the colliding protons) can be factorized from the soft non-perturbative processes (e.g., the description of how the remaining partons behave within the colliding protons). This factorization is possible due to the time scale of the perturbative and non-perturbative processes.

In the center-of-mass reference frame for the *pp* collision, the incoming protons are highly boosted. As a result, due to Lorentz contraction, the time scale of the *pp* collision is very short. The internal interactions between each proton's partons, however, are time-dilated and do not influence the hard scattering. In other words, while the internal parton interactions can affect the outcome of the *pp* collision, the interactions do not interfere quantum mechanically with the hard scatter. Therefore, the effects of the internal parton interactions can be factorized as probabilities instead of amplitudes.

In the short duration of the collision, the two partons participating in the hard scatter can each be assigned a definite fraction x of the total momentum of their respective proton. These fractions are determined by universal *parton distribution functions (PDFs)* which characterize the partons. The PDFs, $f_{a/A}(x_a, \mu_F^2)$, describe the probability that a parton a within hadron A carries a fraction x_a of the hadron momentum. The *factorization scale*, μ_F, represents at what level of detail the hadron is being probed. Usually, μ_F is chosen to be near the scale of the hard scattering interaction, $\mu_F \sim Q$ [37].

PDFs cannot be calculated from first principles because they exist in the realm of non-perturbative QCD. As a result, the PDFs are determined from fits to existing data. Specifically, the dependence on x must be determined from data, while the dependence on μ_F can be derived from the DGLAP equations [39, 40, 41]. This work is done by a number of PDF fitting collaborations including: CT10 [42], MMHT [43], and NNPDF [44].

The latest proton PDFs determined by the NNPDF collaboration are shown in Figure 2.6. At high x, most of the proton momentum is carried by the proton valence quarks (*uud*), while at low x the gluons and sea quarks are more prominent. Figure 2.6(left) and Figure 2.6(right) show the PDFs probed at different scales. When compared, these two plots highlight that when the proton is probed at a higher energy, the sea quarks and the gluons carry a larger fraction of the proton momentum.
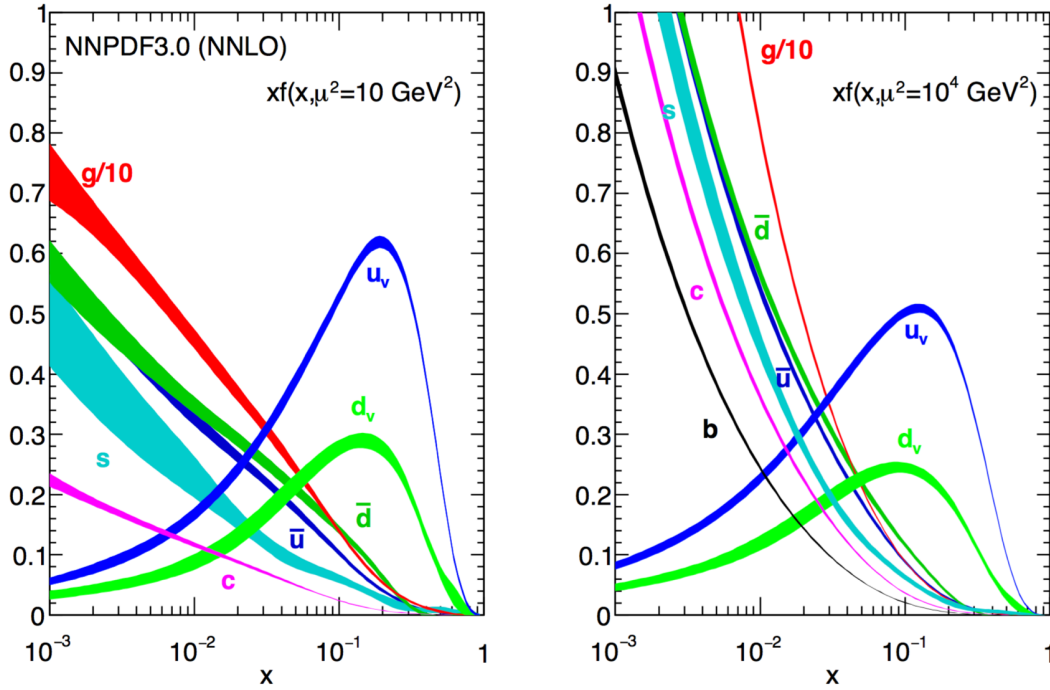
Figure 2.6: Proton parton distribution functions (PDFs) at $Q^2 = 10$ GeV^2 (left) and $Q^2 = 10^4$ GeV^2 (right) according to the NNPDF collaboration [26].

pp Collision Cross Section

Figure 2.7 illustrates a pp collision where only partons a and b participate in the interaction. The cross section for one such process is calculated by summing over the relevant partons ($a \in A, b \in B$) and integrating over the PDFs:

$$\sigma_{AB}(pp \to X) = \sum_{a \in A, b \in B} \int \mathrm{d}x_a \mathrm{d}x_b f_{a/A}(x_a, \mu_F^2) f_{b/B}(x_b, \mu_F^2) \times \hat{\sigma}_{ab \to X}(\mu_R), \qquad (2.46)$$

where a and b represent partons within proton A and proton B with momentum fractions x_a and x_b, respectively, and $\hat{\sigma}_{ab \to X}(\mu_R)$ is the hard scattering cross section for those partons. It is important to note that this calculation requires the choice of two unphysical scales: μ_F and μ_R (used to compute $\hat{\sigma}_{ab \to X}(\mu_R)$). In principle, the results should be independent of the choice of μ_F and μ_R, however, the calculation of $\hat{\sigma}_{ab \to X}(\mu_R)$ can introduce some dependency.

The parton hard scattering cross section ($\hat{\sigma}_{ab \to X}(\mu_R)$) is calculated using perturbative QCD and a power series expansion of α_S:

$$\hat{\sigma}_{ab \to X}(\mu_R) = \hat{\sigma}_0 + \alpha_S(\mu_R^2)\hat{\sigma}_1 + \alpha_S^2(\mu_R^2)\hat{\sigma}_2 + \mathcal{O}(\alpha_S^3), \qquad (2.47)$$
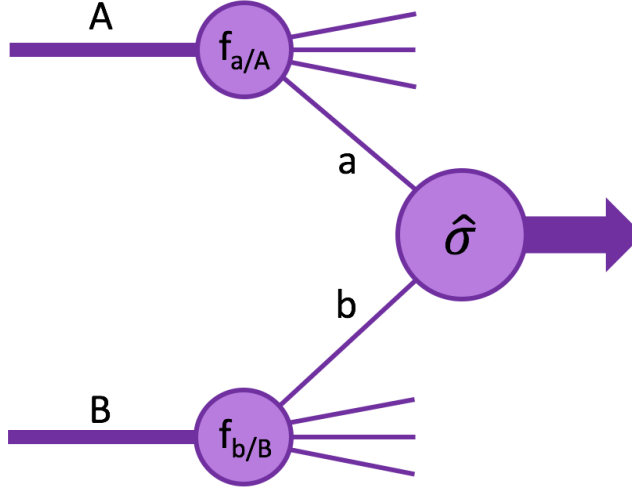
Figure 2.7: Structure of a generic hard scattering process involving two incoming protons, A and B, with PDFs $f_{a/A}$ and $f_{b/B}$, respectively. Replicated from [45].

where $\hat{\sigma}_0$ represents the cross section calculated at Leading Order[3] (LO), and each subsequent $\hat{\sigma}$ adds higher-order corrections, i.e., $\hat{\sigma}_1$ adds Next-to-Leading Order corrections (NLO) and $\hat{\sigma}_2$ adds Next-to-Next-to-Leading Order corrections (NNLO). Each higher-order correction is applied with an additional factor of $\alpha_S(\mu_R^2)$. Therefore, the μ_R-scale choice can impact the $\sigma_{AB}(pp \rightarrow X)$ cross section depending upon the α_S order of the $\hat{\sigma}_{ab \rightarrow X}(\mu_R)$ calculation.

Figure 2.8 shows the production cross section $(pp \rightarrow X, Y, Z)$ of significant SM processes measured with the ATLAS detector as a function of the center-of-mass energy $(\sqrt{s})$. The $pp \rightarrow WW$ cross section quoted in Figure 2.8 is a measure of the inclusive WW cross section. The cross section for $W^{\pm}W^{\pm}$ electroweak production at the LHC will be several orders of magnitude smaller.

---

[3]Leading Order calculations take into account only the matrix element computation. Radiative corrections, such as for the emission of real or virtual partons, are taken into account with higher-order calculations.
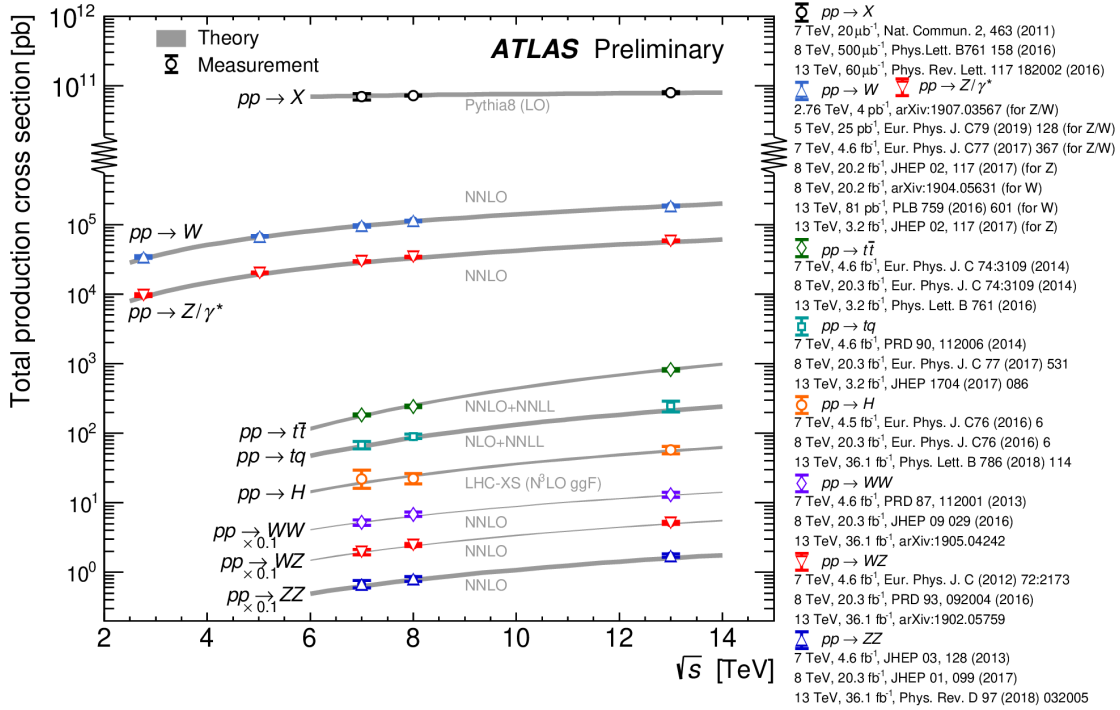
Figure 2.8: Summary of total production cross section measurements by ATLAS as a function of the center-of-mass energy $\sqrt{s}$ from 7 to 13 TeV for a few select processes [46]. The diboson measurements are scaled by a factor of 0.1 to remove overlaps in the figure.

2.4   VBS at the LHC

At the LHC, VBS is studied via the interaction of two gauge bosons, each radiated off initial state quarks from the colliding proton beams (see Figure 1.1). The VBS final state consists of two gauge bosons and two quarks which hadronize, producing jets. This final state is denoted as $VVjj$ where $V \in \{W^{\pm}, Z\}$. Processes which produce this final state ($VVjj$) can be separated into two gauge-invariant classes: electroweak production and strong production.

$\boldsymbol{VVjj}$ **electroweak production:**   This category, denoted as $VVjj{-}$EW, includes Feynman diagrams of order[4] $\mathcal{O}(\alpha_{EW}^6)$ at LO. Figure 2.9 shows a few representative $VVjj{-}$EW diagrams. The diagrams considered to be the VBS diagrams are: the quartic and triple gauge boson self-interaction diagrams (Figure 2.9(a)-(c)) and the diagrams that exchange a Higgs boson (Figure 2.9(d),(e)). The remaining diagrams (Figure 2.9(f)-(i)) are representative of the non-VBS electroweak production diagrams which cannot be separated from the VBS diagrams in a gauge-invariant manner. These non-VBS electroweak production diagrams include

---
[4]This α_{EW} order includes the V decay vertices.

non-resonant diagrams (Figure 2.9(f)), triboson production diagrams[5] (Figure 2.9(g)), and diagrams where multiple gauge bosons radiate from the incoming quarks (Figure 2.9(h),(i)).
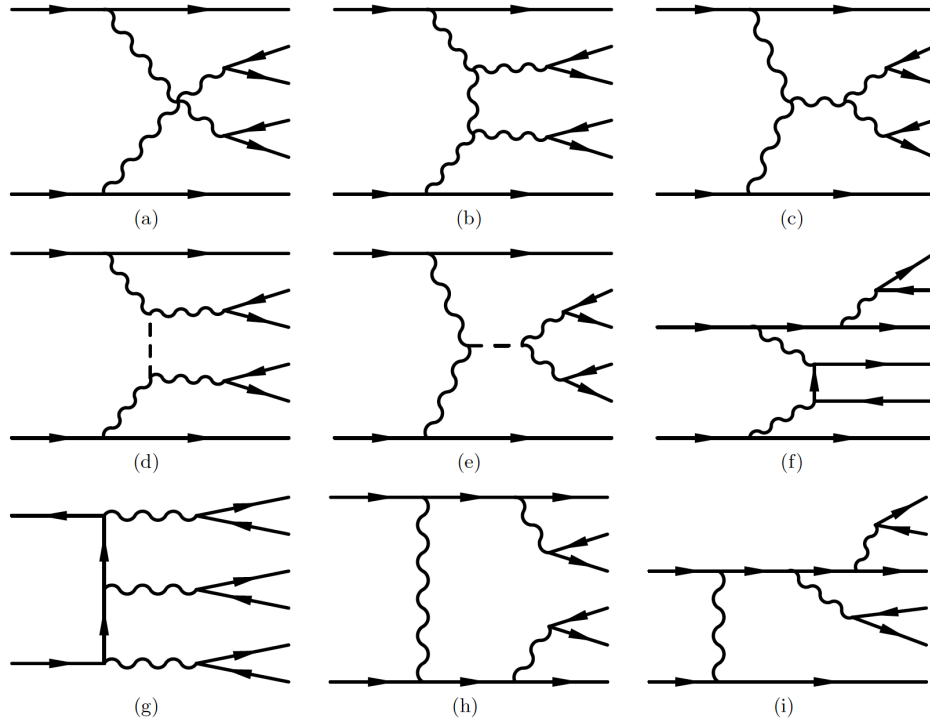
Figure 2.9: Representative Feynman diagrams for $VVjj-$EW production [47]. Solid lines denote fermions, dashed lines represent a Higgs boson, and the wavy lines illustrate $W^\pm/Z$ bosons. Depending upon the final VV state, some of the diagrams shown may not contribute. Diagrams (a)-(e) constitute VBS diagrams. Diagrams (f)-(i) illustrate additional $VVjj-$EW diagrams which cannot be separated from the VBS diagrams in a gauge-invariant way.

$VVjj$ strong production: At LO the Feynman diagrams classified as strong production, or $VVjj-$QCD, are of the order $\mathcal{O}(\alpha_{EW}^4\alpha_s^2)$. Examples of these diagrams are shown in Figure 2.10. For $VVjj-$EW, only diagrams with two quarks in the initial state contribute, while for $VVjj-$QCD, diagrams with a quark-gluon initial state and gluon-gluon initial state also contribute. Due to these added initial state contributions and the abundance of gluons in the colliding protons (see Figure 2.6), the various $VVjj$ cross sections are, for the most part, dominated by strong production. In addition, while $VVjj-$QCD is sensitive to TGC of electroweak gauge bosons (see Figure 2.10(e)), the gauge bosons are not radiated from the initial quarks and, therefore, are not directly sensitive to EWSB.

---

[5]For the triboson production diagrams, one of the bosons must decay hadronically for the diagram to be considered a non-VBS electroweak production diagram.
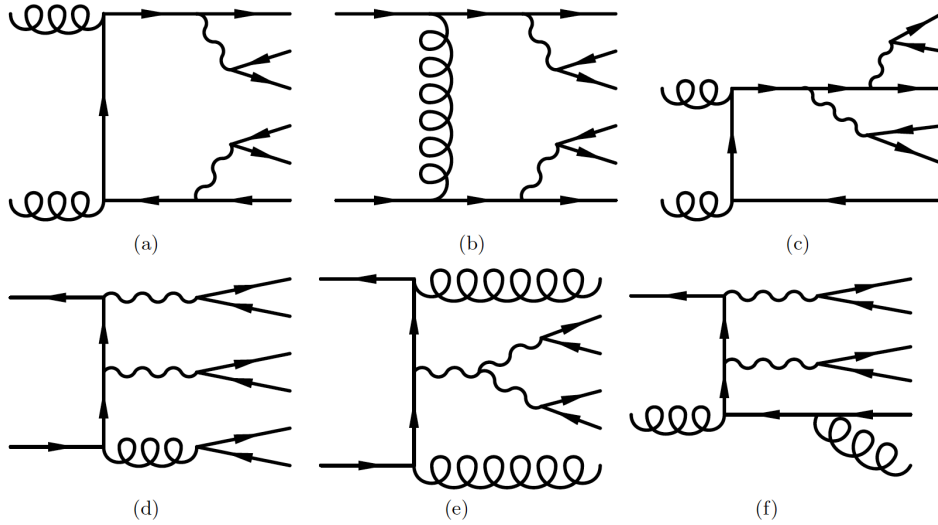
Figure 2.10: Representative Feynman diagrams for $VVjj-$QCD production [47]. Solid lines denote fermions, curly lines represent gluons, and the wavy lines illustrate $W^{\pm}/Z$ bosons. Depending upon the final VV state, some of the diagrams shown may not contribute.

For both $VVjj-$EW and $VVjj-$QCD, the gauge bosons can decay hadronically ($V \to$ hadrons) or leptonically $\left(W(Z) \to l\nu(l^+l^-/\nu\nu)\right)$. The branching fractions for each decay mode are listed in Table 2.5. While the majority of $VVjj$ events at the LHC decay hadronically, leptonic decays produce a cleaner signature to detect. Therefore, only leptonically decaying $VVjj$ events are considered from this point forward. Specifically, only leptonic decays to electrons or muons are considered since leptonic decays to taus are identified with a lower efficiency and produce a higher background compared to the other leptonic decay channels.

Decay Mode	Branching Fraction (%)
$W \to l\nu$	10.86 ± 0.09
$W \to$ hadrons	67.41 ± 0.27
$Z \to l^+l^-$	3.3658 ± 0.0023
$Z \to$ invisible	20.000 ± 0.055
$Z \to$ hadrons	69.911 ± 0.056

Table 2.5: Branching fractions for different W, Z boson decay modes [26]. In this table: $V \to$ hadrons includes decays to quarks and gluons, $Z \to$ invisible includes decays to particles which cannot be detected such as neutrinos, and l represents each lepton (e, μ, τ) and not a sum over them.

In order to probe VBS, $VVjj-$EW production must be observed over $VVjj-$QCD production (which is largely dominant). For some $VVjj$ production, such as $W^{\pm}W^{\pm}jj$ for example, this occurs somewhat naturally. For $W^{\pm}W^{\pm}jj$, the magnitude of the $W^{\pm}W^{\pm}jj-$QCD production is significantly reduced compared to the other $VVjj-$QCD channels due to charge conservation. As a result of the charge conservation required to produce two W bosons with the same electric charge, $W^{\pm}W^{\pm}jj$ strong production cannot occur via any diagrams with a gluon-gluon initial state or a gluon-quark initial state, thus greatly reducing the $W^{\pm}W^{\pm}jj-$QCD cross section.

In addition, the nature of the $VVjj-$EW and $VVjj-$QCD interactions provides a mechanism for suppressing $VVjj-$QCD production. In $VVjj-$EW production, the initial gauge bosons are radiated off the incoming quarks (see Figure 1.1). Since the gauge bosons are simply radiated, the trajectory of the incoming quarks (after the gauge boson radiation) is altered only slightly. As a result, two hadronic jets are produced at a small angles relative to the colliding proton beams.

Alternatively, in $VVjj-$QCD production the color connection between the incoming quarks (see Figure 2.10(b)) pulls the quarks closer together. As a result, the quarks scatter at large angles with respect to the colliding proton beams. In addition, because the $VVjj-$EW scattering diagrams do not directly involve colored particle interactions, the amount of gluon radiation, and therefore the amount of hadronic activity, is smaller than for $VVjj-$QCD production. With these topological differences, a phase space can be designed preferentially for $VVjj-$EW production (see Chapter 4).

Table 2.6 shows $VVjj-$EW and $VVjj-$QCD cross sections for leptonically (e or μ) decaying $W^{\pm}$ and Z bosons in one such phase space[6] designed to select $VVjj-$EW production and suppress $VVjj-$QCD production. From Table 2.6, it is clear the best channel for observing electroweak production over strong production is $W^{\pm}W^{\pm}jj$.

---

[6]This phase space differs only slightly from the fiducial region described in Section 9.1.1.

final state	sensitive to $VV \rightarrow$	σ_{EW} [fb]	σ_{QCD} [fb]
$l^+l^-l'^+l'^-jj$	ZZ	0.098	0.100
$l^+l^-l'^{\pm}\nu'jj$	$W^{\pm}Z$	2.34	4.38
$l^+l'^-\nu\nu'jj$	W^+W^-, ZZ	12.3	21.8
$l^{\pm}l'^{\pm}\nu\nu'jj$	$W^{\pm}W^{\pm}$	3.97	0.346
$l^{\pm}\nu\nu'\nu'jj$	$W^{\pm}Z$	7.64	15.5
$\nu\nu\nu'\nu'jj$	ZZ	1.68	1.38

Table 2.6: Predicted LO cross sections for $VVjj$ electroweak and strong production at $\sqrt{s} = 13$ TeV organized by final state ($l^{\pm} \in \{e^{\pm}, \mu^{\pm}\}$) [47]. Cross sections are calculated using SHERPA-generated simulated data in a typical VBS phase space designed to enrich electroweak production and suppress strong production.

Chapter 3

ATLAS Detector and the LHC

3.1 Large Hadron Collider

The Large Hadron Collider [48] is a circular accelerator located 100 meters underground on the border of France and Switzerland near Geneva, Switzerland. It reuses the tunnel and injection chain of the Large Electron-Positron (LEP) collider [49]. The accelerator has a circumference of 26.7 km and is designed to collide beams of protons with a center-of-mass energy of 14 TeV. The focused and accelerated beams of protons collide at four collision points along the ring. Each of these collision points houses a major physics detector: the A Large Ion Collider Experiment (ALICE) [50], the ATLAS experiment [51], the Compact Muon Solenoid (CMS) [52], and the Large Hadron Collider beauty (LHCb) experiment [53].

ALICE studies the properties of quark-gluon plasma using lead ion collisions. ATLAS and CMS are both general purpose particle detectors designed to search for physics beyond the Standard Model and to measure the Standard Model predictions that have not yet been observed. LHCb is designed to study the interactions of b-hadrons.

Figure 3.1 shows the location of each experiment around the LHC ring from an aerial viewpoint. The location of the LHC along the border of France and Switzerland is also illustrated.
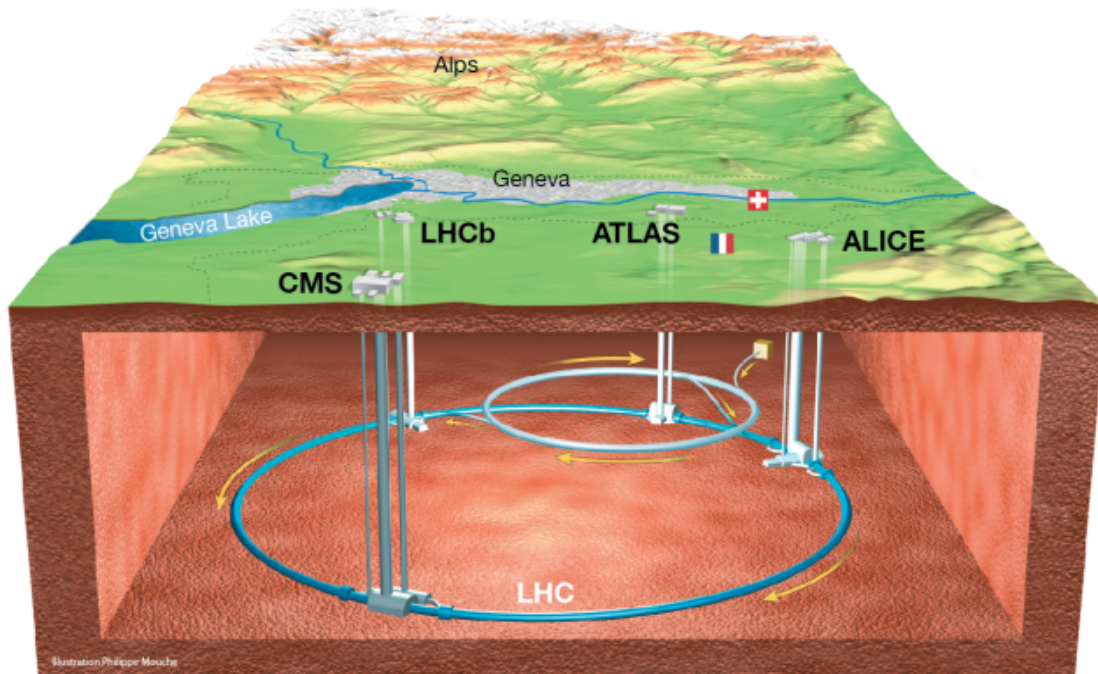
Figure 3.1: The locations of the four main LHC experiments: ALICE, ATLAS, CMS, and LHCb [54]. The LHC tunnel is 26.7 km in circumference and is situated 100 meters underground on the border of France and Switzerland near the city of Geneva, Switzerland.

The first data-taking period of the LHC (Run-1) began in 2010 and concluded at the end of 2012. Following a two-year shutdown for upgrades, the second data-taking period (Run-2) began in 2015 and finished in 2018. After another shutdown, Run-3 is slated to begin in 2021 and run through 2023. At the conclusion of Run-3, the LHC will enter a new regime: the High-Luminosity LHC [55]. Table 3.1 provides a broad summary of the LHC data-taking schedule, past and future. The analysis presented in this dissertation is conducted using Run-2 data collected in 2015 and 2016. Hereinafter, only the performance of the LHC and the ATLAS detector during 2015 and 2016 is presented.

Run-1	Run-2	Run-3	HL-LHC
$2012-2012$	$2015-2018$	$2021-2023$	$2024-$
$\sqrt{s} = 7, 8$ TeV	$\sqrt{s} = 13$ TeV	$\sqrt{s} = 14$ TeV	$\sqrt{s} = 14$ TeV
4.5 fb^{-1}, 20.3 fb^{-1}	139 fb^{-1}	expect 300 fb^{-1}	expect 3000 fb^{-1}

Table 3.1: Timescale, center-of-mass energy, and recorded/expected integrated luminosity for the different LHC data taking periods.

3.1.1 Accelerator Complex

To achieve two beams of protons that can collide with a center-of-mass energy of 13 TeV, a sequence of machines known as an *accelerator complex* is required [56]. A diagram of the accelerator complex used to deliver proton beams to the LHC is shown in Figure 3.2. The process begins with a bottle of hydrogen gas. An electric field is used to strip the electrons from the hydrogen atoms, thus isolating protons. Next, Linac2, the first accelerator in the sequence, accelerates the protons to an energy of 50 MeV before injecting them into the Proton Synchrotron Booster (PSB). In the PSB the protons are accelerated to an energy of 1.4 GeV. The protons then progress through the Proton Synchrotron (PS) and the Super Proton Synchrotron (SPS) where the protons are accelerated to an energy of 25 GeV and 450 GeV, respectively. Following this, the protons are transferred into two beam pipes which feed into the LHC while moving in opposite directions. Once the protons are circulating through the LHC in the two beam pipes, it takes 20 minutes to accelerate each beam of protons to a final energy of 6.5 TeV. The same two beams will circulate for several hours inside the LHC.

The beam pipes, also referred to as the *beamline*, are kept at ultrahigh vacuum. Inside the beam pipes, the proton beams are directed using very strong superconducting electromagnets; 1,232 dipole magnets are used to keep the protons moving in a circular pattern around the ring, and 392 quadrupole magnets are used to focus the proton beams before the collision points. The superconducting magnets have an operating temperature of 1.9 K, which is maintained by a distribution system of almost 100 tonnes of liquid helium.
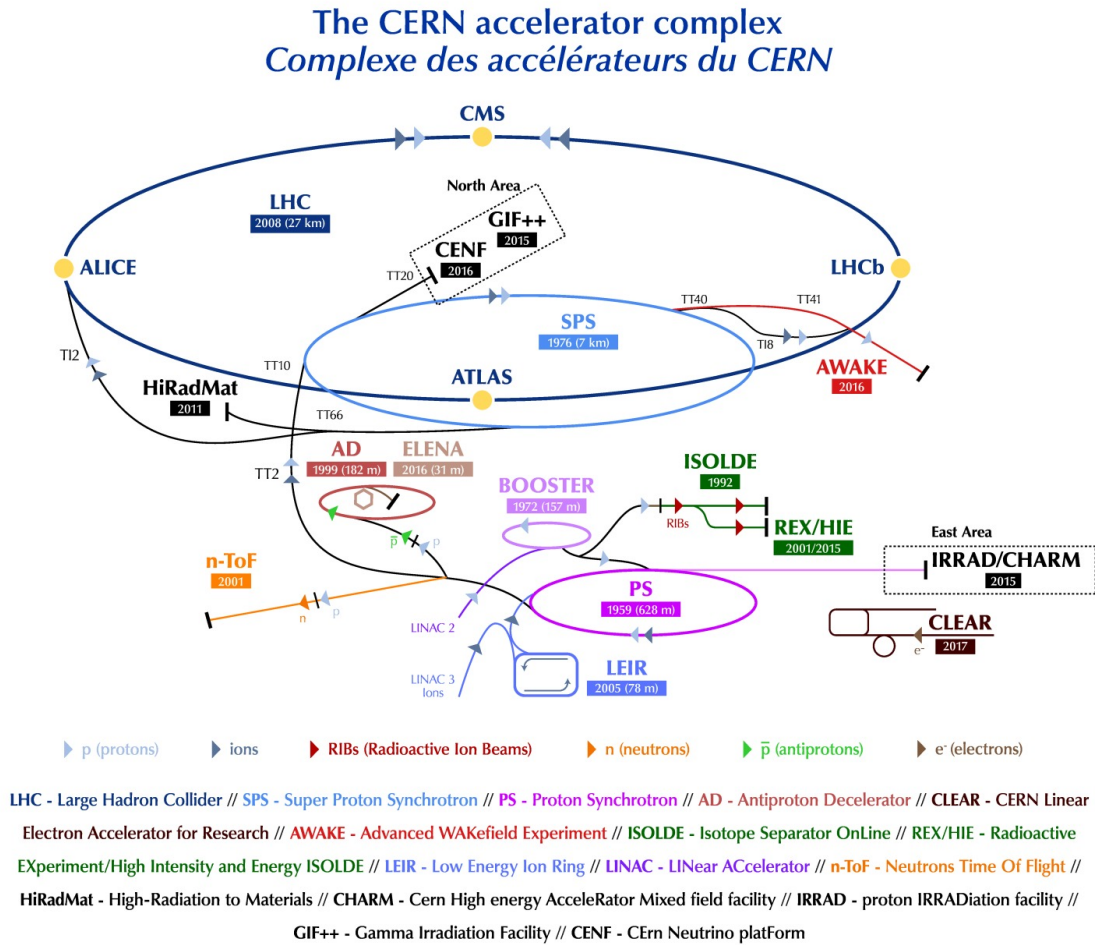
Figure 3.2: CERN accelerator complex [57].

3.1.2 Run-2 Performance

At the LHC, the proton beams are not continuous due to the Radio Frequency (RF) cavities [58] used to accelerate the particles. Instead, the beams are segmented into tight groups of protons called *bunches*. Each proton beam in the LHC contains 2,808 bunches, with each bunch containing roughly 1.1×10^{11} protons [59]. A bunch crossing occurred every 25 ns during operations in 2015 and 2016.

Given these parameters, the potential number of collisions per second, i.e., *instantaneous luminosity* ($\mathcal{L}$), can be written as [26]:

$$\mathcal{L} = f \frac{n_1 n_2}{4\pi \sigma_x \sigma_y}, \tag{3.1}$$

where f=11.245 kHz is the collision frequency of the LHC beams, n_1 and n_2 are the number

of protons in each beam, and σ_x and σ_y are the Root Mean Square (RMS) beam widths in the horizontal and vertical directions. The maximum instantaneous luminosity reached in 2015 and 2016 was 5×10^{33} cm^{-2}s^{-1} and 13×10^{33} cm^{-2}s^{-1}, respectively [59].

For physics analyses, the interesting quantity is not instantaneous luminosity, but the total integrated luminosity: $L = \int \mathcal{L} dt$. Knowing the total luminosity allows for the number of measured events for any process to be converted into a cross section by dividing the number of events by the total luminosity, i.e. $\sigma = \frac{N}{L}$. The total integrated luminosity delivered by the LHC in 2015+2016 is 42.7 fb^{-1}; however, only 39.5 fb^{-1} was recorded by the ATLAS detector[1]. Figure 3.3 shows the integrated luminosity for 2015 and 2016 as a function of time.
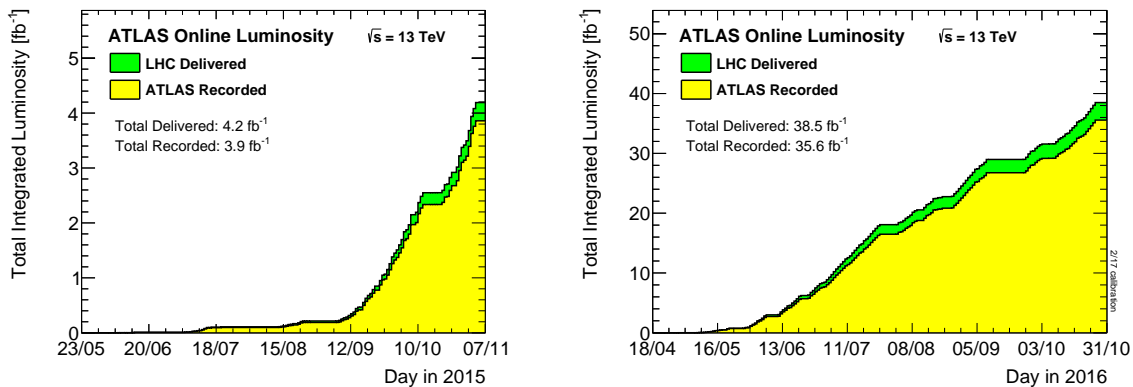
Figure 3.3: Total integrated luminosity versus time delivered by the LHC (green) and recorded by ATLAS (yellow) in 2015 (left) and 2016 (right) [60].

The instantaneous luminosity is important, however, for determining the average number of *pp* collisions that occur per bunch crossing. The number of *pp* collisions that occur per bunch crossing is commonly referred to as *pile-up*. Higher pile-up results in more activity in the detector. With more activity in the detector, the performance of the event reconstruction algorithms can worsen due to the increased complexity involved in processing the high level of activity. Figure 3.4 shows the mean number of interactions per bunch crossing for 2015 and 2016. Pile-up is modeled in simulated data using the instantaneous luminosity distribution.

---

[1]Some collision data is not recorded by the ATLAS detector at the beginning and end of a fill due to detector turn on/off conditions.
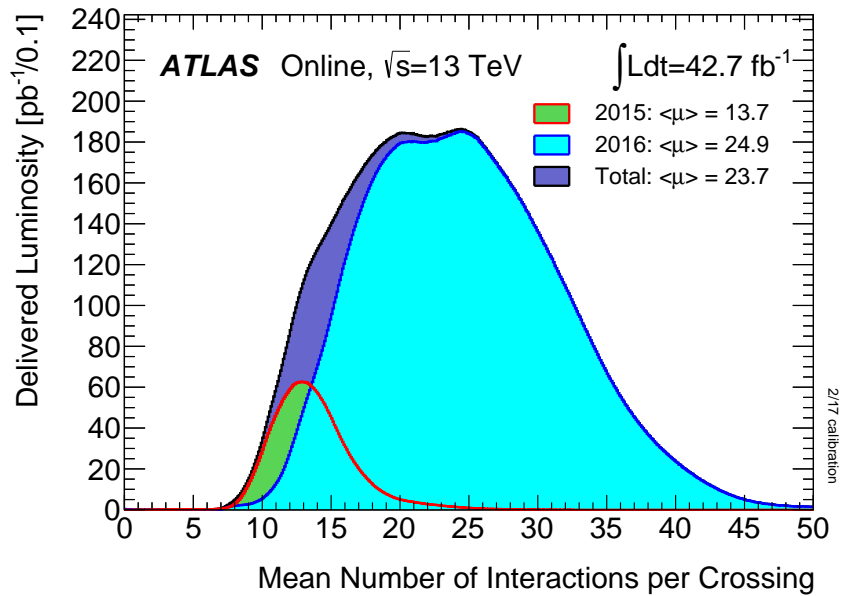
Figure 3.4: The luminosity-weighted distribution of the mean number of interactions per bunch crossing from 2015 and 2016 pp runs at the LHC [60]. The number of interactions per bunch crossing depends upon the instantaneous luminosity, which is measured in roughly 60 second intervals. As a result, the mean number of interactions per bunch crossing can change as a function of time.

3.2   ATLAS Detector

The ATLAS detector, shown in Figure 3.5, is a general purpose particle detector. It consists of a cylindrical barrel with endcap disks on both ends. The detector is comprised of three sub-detector systems: the inner detector (ID), the calorimeter, and the muon system. These sub-detectors are arranged as concentric cylinders around the interaction point[2] (IP) with increasing radii. Closest to the IP is the ID which is used to track the trajectories of charged particles and measure their momenta. Beyond the ID lies the calorimeters which are used to measure the energy of charged and neutral particles. Furthest from the IP is the muon spectrometer (MS) which measures the momentum and trajectory of muons. Details of each sub-detector are provided in Sections 3.2.2 - 3.2.4.

ATLAS also utilizes a system of magnets to aid with the measurement of charged particle trajectories. A solenoid that generates a 2 Tesla magnetic field sits between the ID and the calorimeters. As charged particles move through the ID, the solenoid bends their trajectories. Using the Lorentz force equation [61], the momentum of the charge particles can then be determined. In addition to the solenoid, a large toroidal magnet within the outermost part of

---

[2]The interaction point refers to the point where the proton beams collide inside the ATLAS detector.

the detector produces a $0.2-3.5$ Tesla magnetic field depending upon position. This toroidal magnetic field curves charged particles as they move through the MS.
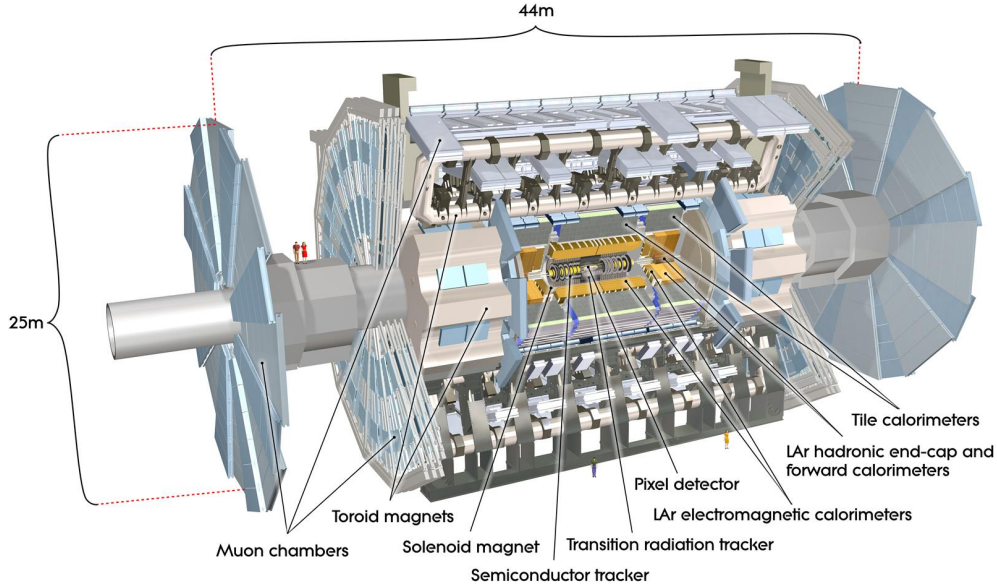
Figure 3.5: Computer generated illustration of the ATLAS detector [62].

3.2.1 Coordinate System

ATLAS employs a right-handed coordinate system, with the origin located at the nominal IP (located at the center of the detector). A schematic of the coordinate system is shown in Figure 3.6. When viewed from above, the z-axis points along the beamline in the counterclockwise direction, the x-axis points towards the center of the LHC ring, and the y-axis points upward. The x-y plane is referred to as the *transverse plane* because it is perpendicular to the beamline. In this plane, cylindrical coordinates r and ϕ are used, where r is the transverse distance from the beamline and ϕ is defined as the azimuthal angle around the beamline. The polar angle, θ, is measured from the positive z-axis. However, instead of using θ, it is more common to use the pseudorapidity which is defined as:

$$\eta = -ln(tan(\frac{\theta}{2})). \tag{3.2}$$

In the limit of a massless particle, pseudorapidity is invariant with respect to Lorentz boosts along the beamline. For cases with massive particles, the most common descriptor is rapidity, which is defined as:

$$y = \frac{1}{2}ln(\frac{E + p_z}{E - p_z}). \tag{3.3}$$

Rapidity is also independent of boosts along the beamline. Differences in solid angle, ΔR, can be measured using the differences in azimuthal angle and pseudorapidity:

$$\Delta R = \sqrt{\Delta\phi^2 + \Delta\eta^2}. \tag{3.4}$$
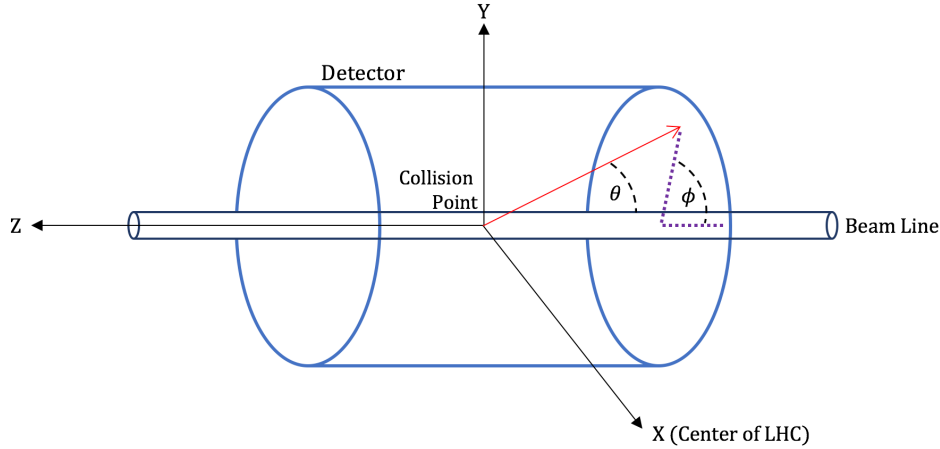
Figure 3.6: Illustration of the ATLAS coordinate system. Replicated from [63].

3.2.2 Inner Detector

The ID consists of three sub-systems that function together as a tracking system which measures the trajectory and momentum of charged particles. The innermost part of the ID is the pixel detector, followed by the semi-conductor tracker (SCT), and finally the transition radiation tracker (TRT). Both the pixel detector and the SCT utilize silicon sensors, while the TRT uses drift tubes interwoven with transition radiation material. Figure 3.7 shows a cut-away view of the ID barrel. More details about each sub-system are provided in Sections 3.2.2.1 - 3.2.2.3.

3.2.2.1 Pixel Detector

The pixel detector is the detector system located closest to the beamline; it is designed to provide a high level of granularity despite the high levels of radiation from the collisions. The pixel detector originally consisted of: (1) three cylindrical barrel layers of silicon pixel modules (L0, L1, and L2) located at radii of 50.5 mm, 88.5 mm, and 122.5 mm from the beamline, and (2) three endcap disks on each side of the barrel located at distances 495 mm, 580 mm, and 650 mm from the center of the detector. A fourth barrel layer, called the Insertable B-Layer (IBL), was added to the pixel detector in 2014 (after Run-1) due to the potential of significant radiation damage to the inner layers of the pixel detector at the
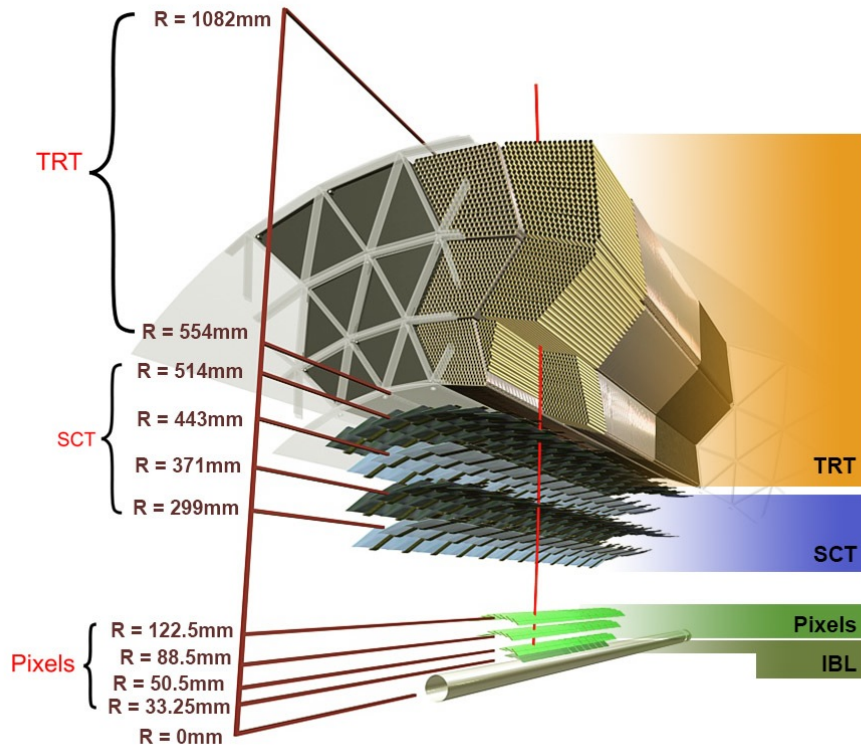
Figure 3.7: Sketch of ATLAS Inner Detector showing all its components [64].

higher operating energy of Run-2. The IBL is located at a radius of 33.25 mm from the beamline. All together, these four layers provide coverage up to $|\eta| < 2.5$.

Original Pixel Detector

The original pixel detector consists of 1,744 identical pixel modules, each measuring 19×63 mm^2 and containing 47,232 pixels. The majority of the pixels (90%) measure 50×400 μm^2, and the remaining 10% measure 50×600 μm^2. On each module, the pixels are bump-bonded to 16 front-end readout chips such that each chip is responsible for reading out 2,880 pixels[3]. The modules are then arranged into 112 *staves* in the barrel layers and 24 *sectors* in the endcaps.

The staves are long structures, each constructed with 13 modules, that are arranged parallel to the beam direction. To provide full azimuthal coverage, the staves are overlapped slightly and tilted 20° with respect to the radial direction. Each endcap sector contains six modules. The sectors are arranged as petals and then wheels, with the detecting elements perpendicular to the beam pipe. The wheels are arranged to provide some overlap which

---

[3]Due to spatial limitations on the module, 1,152 pairs of pixels are ganged to a common readout which gives a total of 46,080 readout channels per module for 47,232 pixels.

prevents loss of coverage due to edge effects. These structures (staves and sectors) also house the power, clock, and command/data connections to and from each module.

Each pixel is a 256 μm thick p-n junction of n-type bulk containing both p+ and n+ impurities. The combination of p+ and n+ impurities is crucial because it allows the pixels to continue operating even in the event high radiation causes the n-bulk to invert to a p-bulk. In either of these configurations (n-bulk or p-bulk), when a charged particle passes through the bulk, the particle ionizes thousands of electron-hole pairs. Since the array of pixels on each module are kept under a reverse bias, the electrons and holes drift in opposite directions, producing a current that is measured by readout electronics. If the number of ionized electrons exceeds a threshold value, the pixel registers this as a *hit*. When multiple neighboring pixels register hits, this is called a *cluster*. The particle hit resolution for the barrel (endcap) is approximately 115 μm in the *z (R)* direction and 10 μm in the $R-\phi$ direction.

Insertable B-Layer (IBL)

The IBL was installed in the ATLAS detector during the long shutdown between Run-1 and Run-2. The IBL was commissioned to maintain robust and high-precision tracking in the high-radiation and higher-energy environment expected in Run-2 [65]. To accommodate the IBL, the original beam pipe was replaced with a smaller beam pipe, leaving just enough room to insert the IBL between the new beam pipe and L0 of the original pixel detector. The increase in expected radiation and the proximity of the IBL to the IP (only 3.3 cm away) required upgraded electronics for the IBL. As a result, a new readout chip (FE-I4) was developed. The FE-I4 chips are less susceptible to radiation damage and have a higher active area compared to the front-end chips in the original pixel detector[4].

In addition to a new readout chip, updates were also made to the silicon pixel sensors. For the first time in an experiment of this scale, 3D pixel sensors were introduced and used alongside the planar-style pixels used in the original pixel detector. It has been known for many years that 3D pixel sensors are quite suitable for environments with high doses of radiation due to the shorter electrode distance compared to planar pixels [66].

In the 3D pixels a double-sided process is used, where n+ columns and p+ columns are embedded vertically on opposite sides of a p-type bulk. In this arrangement, the n+ and p+ columns act as the electrodes providing the voltage and ground, respectively. The 3D pixels measure $50 \times 250 \times 230$ μm^3 and are used in addition to planar n-in-n silicon pixels. The IBL planar pixels use the same silicon pixel technology as the pixels used in the original pixel detector. However, the IBL planar pixel size was reduced to $50 \times 250 \times 200$ μm^3 to improve tracking resolution and cluster identification in the higher track density of Run-2.

The IBL is comprised of 14 staves overlapped with a 14° offset to provide full coverage. For the IBL, each stave consists of 12 double-chip planar modules and 4 single-chip 3D modules. A double-chip planar module houses two front-end readout chips with 26,880 planar pixels embedded in each chip. A single-chip 3D module consists of a single front-

---

[4]The active area for the updated readout chips (FE-I4) is approximately 90%, while the active area for the readout chips in the original pixel detector (FE-I3) is only 70%.

end readout chip with 26,880 3D pixels embedded in the chip. In total, the IBL adds an additional 244 modules and 10.5 million pixels to the pixel detector, where the particle hit resolution in the z direction is 72 μm and 10 μm in the transverse plane.

3.2.2.2 Semi-Conductor Tracker

The SCT surrounds the pixel detector and covers an area of 62 m^2, compared to the 2.3 m^2 covered by the pixel detector. Because of the increased coverage area, the SCT uses single-sided p-in-n silicon strips instead of pixels. The strips allow for a larger coverage area without dramatically increasing the number of required readout channels and while significantly reducing the cost.

Each silicon strip sensor has a thickness of 285 μm, an area of 6.4 $\times$ 6.3 cm^2, a *pitch*[5] of 80 μm, and contains 768 readout strips. An SCT barrel module consists of four sensors, with two pairs of sensors each bonded to form two 12.8 cm long strips. The two strips are arranged on top of one another with a small angle (40 mrad) between them to allow for position measurements in the ϕ and z directions. The SCT endcap modules are trapezoidal in shape and consist of sensors with radially arranged readout strips. While all the barrel modules are identical, two different module layouts are utilized in the endcaps: two-sensor and four-sensor. The two-sensor endcap modules contain only two sensors glued back-to-back, while the four-sensor endcap modules have four sensors, with a pair of sensors on each side. As in the barrel, the sensors on each side of the module (both two-sensor and four-sensor) are arranged at a 40 mrad stereo angle.

The SCT has 2,112 barrel modules arranged in four barrel layers, and 1,976 endcap modules in two endcaps, where each endcap has nine disks. Each endcap disk consists of three rings of modules, where the inner ring is comprised of two-sensor modules and the middle and outer rings have four-sensor modules. The spatial resolution for SCT barrel (endcap) modules is 17 μm in the transverse plane and 580 μm in the z (R) direction.

3.2.2.3 Transition Radiation Tracker

The outermost sub-detector of the ID is the TRT. It consists of straw drift tubes which are 4 mm in diameter and filled with a Xenon gas mixture that is 70% Xe, 27% CO_2, and 3% O_2. This gas becomes ionized when charged particles pass through it. In the center of each tube is a 31 μm diameter anode tungsten gold-plated wire held at ground potential. The electric field between the ground wire and the tube walls (which are held at roughly -1500 V) causes any ionization in the tube to cascade until the charge reaches the wire, which is connected to the readout electronics.

In the barrel, there are 73 layers of 144 cm-long tubes that are interleaved with transition radiation fibers which run parallel to the beam pipe. In each endcap there are 160 layers of 37-cm long tubes interleaved with transition radiation foils which spread out radially from the beam pipe like the spokes of a wheel. In total, there are approximately 351,000 readout

---

[5]The pitch is the distance between the center of two neighboring readout strips.

channels in the TRT. As a particle passes through the TRT barrel (endcap), it typically creates about 36 (22) hits. The intrinsic resolution of the TRT is 130 μm in the $R - \phi$ direction with coverage up to $|\eta| < 2.0$.

The transition radiation fibers interleaved with the drift tubes provide a method to distinguish between tracks left by electrons and tracks left by pions. Transition radiation is produced when a charged particle crosses a boundary between two mediums with different dielectric constants and is proportional to the Lorentz factor γ of the particle. Thus, for an electron and a pion with the same momentum, the electron is more likely than the pion to produce transition radiation since the electron has a smaller rest-mass. When the photons from the transition radiation ionize the gas in the straw tubes, the resulting cascade is much higher than the signal produced from tracking a minimum-ionizing particle. As a result, the TRT straws can distinguish the two types of signals with a *high threshold* for transition radiation hits and a *low threshold* for tracking hits. The ratio of high threshold hits to low threshold hits is then used to discriminate between electrons and pions.

3.2.3   Calorimeters

The calorimeter system is located outside the ID and solenoid magnet. The system is composed of separate electromagnetic and hadronic calorimeters that have both barrel and endcap components. An additional forward calorimeter provides high η measurements. Together these components provide a full coverage in ϕ and $|\eta| < 4.9$. In this coverage area, the calorimeters stop and measure the energy of electrons, photons, and jets. The calorimeters are sampling calorimeters, meaning that only part of the energy shower is observed. Showers are initiated with an absorbing material which is interleaved with active material for detecting the showers. Figure 3.8 shows the layout of the calorimeters.

3.2.3.1   Electromagnetic Calorimeter

The EM calorimeter uses liquid argon (LAr) as an active medium with kapton electrodes alternated with lead absorbers. The EM calorimeter has both barrel and endcap components. The barrel component covers $|\eta| < 1.5$ and the endcap component covers $1.4 < |\eta| < 3.2$. There is also an LAr presampler layer which covers $|\eta| < 1.8$ and provides a measurement of the energy lost to showers starting before the calorimeter.

The barrel consists of three layers with decreasing segmentation to capture the energy and direction of photons and electrons. The first layer has a thickness of 4.3 X_0 with a cell width ($\Delta\eta \times \Delta\phi$) of 0.003 × 0.1. The second layer comprises the bulk of the EM calorimeter with a thickness of 16 X_0 and a cell width of 0.025 × 0.025. The third layer, designed to capture any leftover energy, has a thickness of 2 X_0 and a coarser cell width of 0.05 × 0.025. All the layers are bent like accordions, which allows for a gapless ϕ measurement. A diagram of a barrel module is shown in Figure 3.9. The endcap component consists of two layers with an accordion shape oriented to prevent gaps in η.
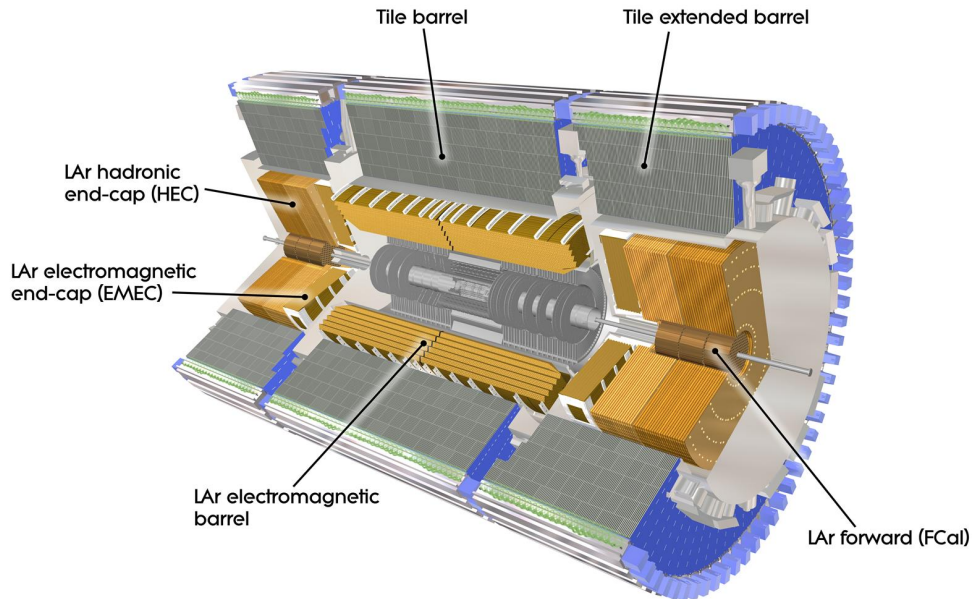
Figure 3.8: Cut-away view of the ATLAS calorimeter system [67].
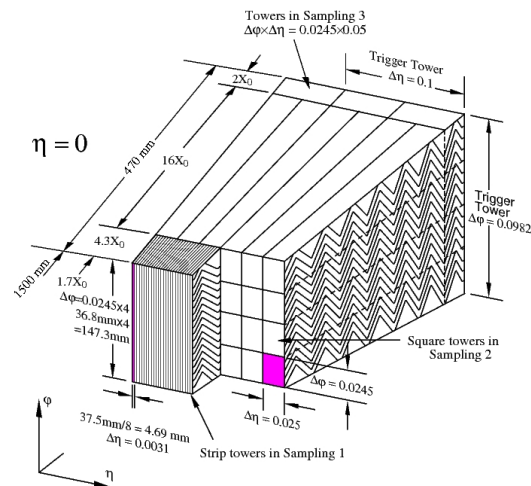
Figure 3.9: Schematic of the cells in a barrel module of the EM calorimeter [51].

3.2.3.2 Hadronic Calorimeter

The hadronic calorimeter is divided into three components: the tile calorimeter, the Hadronic Endcap Calorimeter (HEC), and the forward calorimeter (FCal). The tile calorimeter sits outside the LAr EM calorimeter and covers $|\eta| < 1.7$. Figure 3.10 shows a schematic of a hadronic tile module. The module uses layers of steel absorbers with scintillating tiles as

the active material, and is read out by photomultiplier tubes. The HEC provides hadronic calorimetry for $1.5 < \eta < 3.2$ using LAr active material and copper plate absorbers. The FCal closes the gap between the HEC and beam pipe, covering $3.1 < |\eta| < 4.9$, and is split into three layers. All three layers use LAr as the active material. The first layer uses copper plates as the absorber, while the second and third layer use tungsten rods that run between two copper end plates.
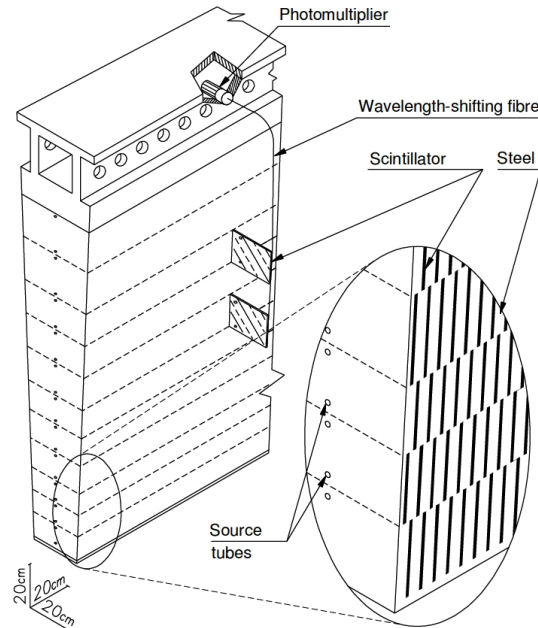
Figure 3.10: Schematic of the structure of the tile calorimeter [51].

3.2.4 Muon Spectrometer

The MS lies beyond the calorimeters and is the outermost sub-detector. Because the calorimeters were designed to stop electrons, photons, and hadrons, the MS is primarily responsible for measuring muons which do not lose much energy as they pass through the calorimeters. The MS consists of a toroidal magnet system, two particle tracking systems, and two types of trigger chambers, as shown in Figure 3.11.

Three toroid magnets are used to produce the magnetic field necessary to bend the trajectory of muons for momentum and trajectory measurements: one toroid for the barrel and one for each endcap. Each toroid consists of eight coils arranged symmetrically around the beam. The barrel toroid is designed to produce a magnetic field between 0.2-2.5 T, while each endcap toroid can produce a 0.2-3.5 T magnetic field.

The two types of tracking systems utilized in the MS are the Monitored Drift Tubes (MDTs) and the Cathode Strip Chambers (CSCs). The MDTs are comprised of 3-8 layers of drift tubes and are responsible for the majority of the precision tracking in the MS. The

drift tubes are pressurized, 30 mm in diameter, and filled with 93% Ar gas and 7% CO_2 gas. They provide coverage out to $|\eta| < 2.7$ in the outer barrel and $|\eta| < 2.0$ in the inner barrel, with a resolution of 35 μm per chamber. For the forward regions of the inner barrel $(2.0 < |\eta| < 2.7)$ where high muon rates are expected, MDTs are not suitable because the MDT counting rate is limited to 150 Hz/cm^2. This region is instead instrumented with CSCs which provide momentum measurements at a higher rate with better resolution. The CSC chambers are arranged in two endcap wheels with 16 chambers per wheel. Each chamber has 4 CSC planes, where each plane consists of two cathode strip planes sandwiching the anode wires. The chamber is filled with a gas mixture comprised of 80% Ar and 20% CO_2. The arrangement of the CSCs results in a resolution of 40 μm in the bending direction, 5 mm in the transverse direction, and a timing resolution of 7 ns.

Muons are triggered in the MS by the Resistive Plate Chambers (RPC) in the barrel and Thin Gap Chambers (TGC) in the endcaps. Together these chambers provide muon triggering capabilities for $|\eta| < 2.4$. Different technologies are used in the barrel and endcaps for two reasons: (1) a different rate of muons is expected in both regions, and (2) a different level of precision is required in both regions. The barrel trigger system has 3 RPC layers, with the inner two layers sandwiching the middle MDT layer. These inner two layers allow triggering on low p_T muons, while the third RPC layer, which is located outside the outermost MDT layer, allows for the triggering of high p_T muons. The endcap trigger system is composed of 4 TGC layers which are similarly arranged at various distances to allow for triggering across the full range of momenta interest.
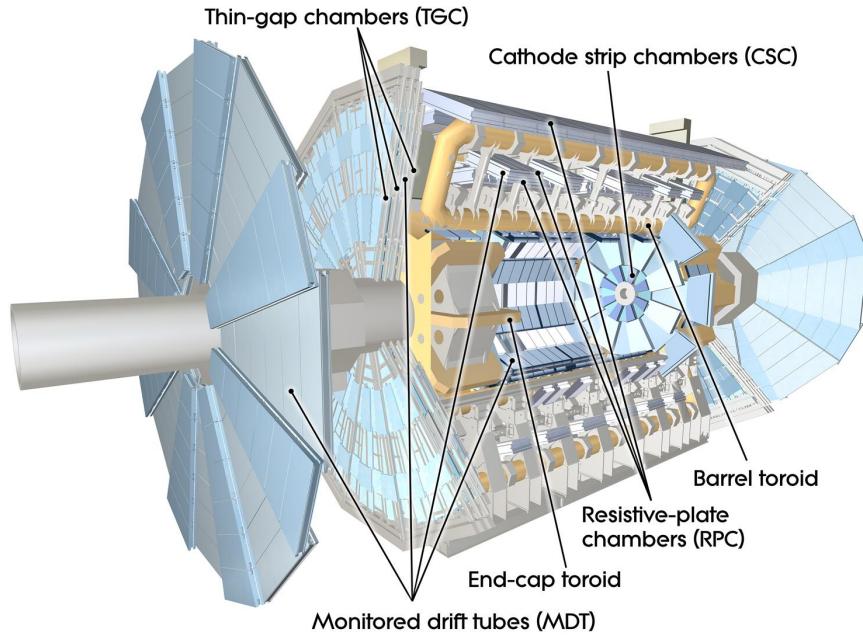
Figure 3.11: Diagram of ATLAS Muon System (MS) [51].

3.2.5 Trigger System

In 2015 & 2016, there were roughly one billion interactions occurring every second in the ATLAS detector[6]. However, only a fraction of these events can be recorded due to the limitations of the electronics/detectors to process the events and the limited storage capabilities around the globe. The act of quickly determining which events may be interesting to study further is referred to as *triggering*.

The ATLAS trigger system reduces the event rate from 20 MHz to 1 kHz in two stages [68]. The first stage is the Level 1 (L1) hardware triggers, which make a decision regarding whether or not to keep each event within 2.5 μs of the event occurring. The L1 triggers use data from the calorimeters and muon system to reduce the event rate from 20 MHz to 100 kHz. In order to make a decision in less than 2.5 μs, the granularity of the calorimeter is reduced and only information from the RPC and TGC in the muon system is considered. The combined L1 trigger rate is shown in Figure 3.12 with the contribution of the different trigger types (single lepton, multilepton, jet, etc.). The total L1 trigger output is less than the sum of the different categories due to the removal of overlap of events that pass more than one type of trigger.
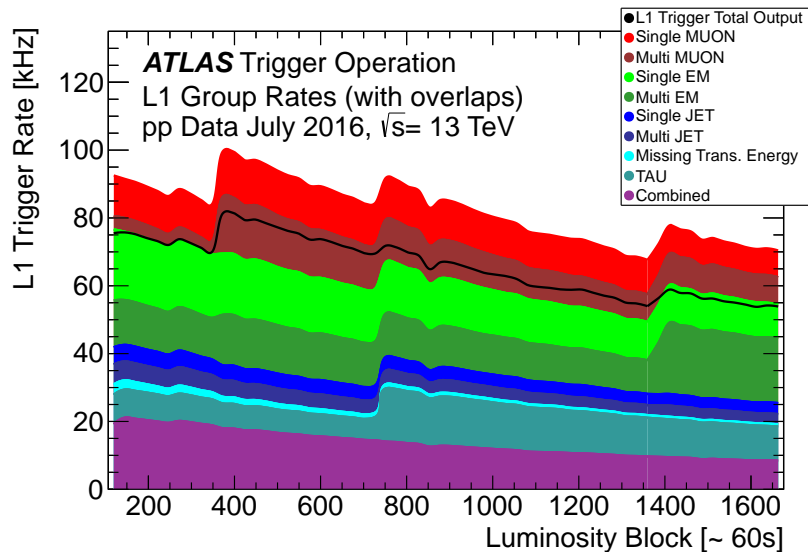
Figure 3.12: The L1 trigger rate broken down into different trigger types as a function of luminosity block for data collected in July 2016 [69]. One luminosity block is approximately 60 seconds. The total L1 trigger output is lower than the sum of the different categories due to the removal of overlaps between events that pass more than one type of trigger.

---

[6]From Figure 3.4, there were roughly 24 interactions per bunch crossing in the ATLAS detector. With bunch crossing occurring every 25 ns, that is 40 million bunch crossings a second, which leads to the estimate of roughly one billion interactions every second.

Once an event has passed an L1 trigger, all the information stored by the various sub-detectors for this event is read out and stored on the detectors' readout boards. These events are then further processed by the High Level Triggers (HLT) using a software algorithm to determine whether or not to record the event permanently. Unlike the L1 triggers, the HLT have access to finer-granularity calorimeter data, precision measurements from the MS, and tracking information from the ID. With this additional information, the HLT can implement additional triggers which target more specific physics events, such as identifying jets which are the result of *b*-hadron decays. The HLT also receives Region-of-Interest (RoI) information from the L1 triggers. With this information, the HLT can focus on reconstructing events in regions indicated by the L1 trigger to be of interest, thus reducing the speed of the algorithm. All together, the HLT reduces the event rate from 100 kHz to 1 kHz. Figure 3.13 shows the HLT trigger rate for a subset of data collected in July 2016, broken up into trigger type and the combined rate. The total HLT rate is lower than the combined sum of the different subsets due to the removal of the overlap between events that pass more than one trigger type.
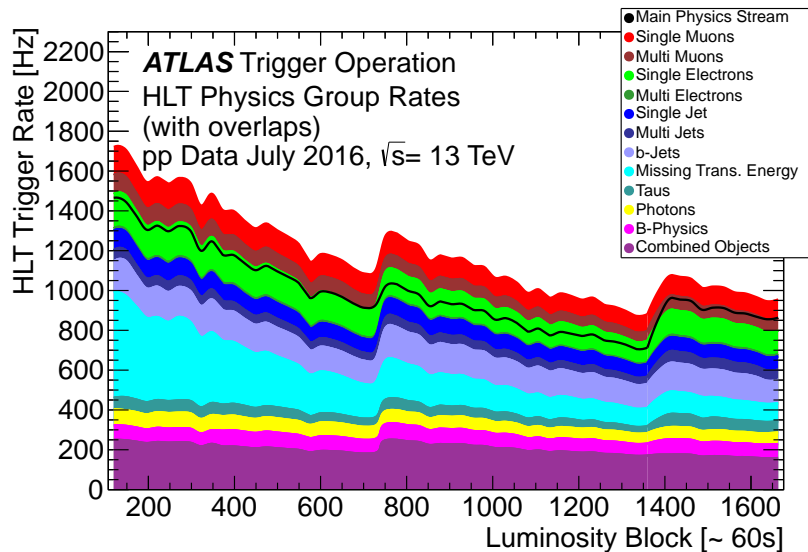
Figure 3.13: The HLT trigger rate broken down into different trigger types as a function of luminosity block for data collected in July 2016 [69]. One luminosity block is approximately 60 seconds. The total HLT trigger output is lower than the sum of the different categories due to the removal of overlaps between events that pass more than one type of trigger.

After the events pass the HLT selection, they are transferred to a storage site near the ATLAS detector before being exported to a specialized computer storage center for offline reconstruction (see Chapter 6).

3.2.6 Electron Triggers

Electron candidates are formed initially using information collected by the calorimeters. For energy deposited within a given region of the calorimeter, the L1 trigger denotes this as an electron/photon candidate if the energy deposit passes a set η-dependent transverse energy threshold. Additionally, the L1 triggers can also impose hadronic isolation requirements. When events passing the L1 triggers are processed by the HLT, more detailed information collected from the calorimeter, such as shower shapes and energy ratios, is used to reconstruct electron/photon candidates as clusters of energy in the EM calorimeter. Electron and photon candidates are distinguished using tracking information from other sub-detectors. If a track can be matched with an energy cluster (while satisfying a set of requirements), it is identified as an electron.

3.2.7 Muon Triggers

Muon candidates are identified at L1 by a sequence of hits in two or three layers in either the RPCs or TGCs of the MS that point towards the interaction region. The HLT algorithm then takes muon candidates passing the L1 trigger and, using information from the MDT chambers, constructs a track. Once the muon candidate is constructed in the MS, it is combined with a track found in the ID (where the p_T is the weighted average of the MS and ID tracks).

Chapter 4

Analysis Strategy

The focus of this dissertation is the observation of the electroweak production of two same-sign W bosons in association with two jets. Figure 4.1 depicts the Feynman diagram for the process of interest. $W^{\pm}W^{\pm}jj-$EW production includes additional diagrams (see Figure 2.9) which cannot be separated from the diagrams in Figure 4.1 in a gauge-invariant manner (see Section 2.4). The W bosons are reconstructed from their leptonic decay products. The W boson leptonic decay channels provide a cleaner signature in the detector and allow for easier identification of the W boson charge. Therefore, the observed final state is two same-sign leptons, two neutrinos, and two jets. Since neutrinos do not interact with the detector, the presence of neutrinos is represented by missing transverse energy (E_T^{miss}) in the event.
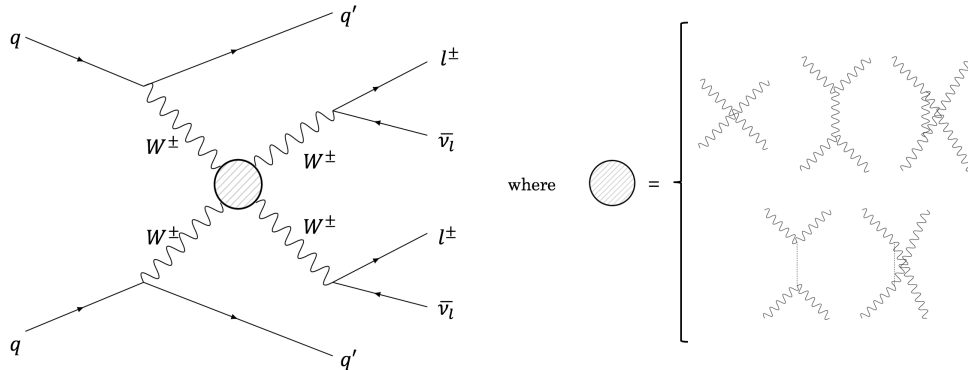
Figure 4.1: Example Feynman diagram of the $W^{\pm}W^{\pm}jj$ electroweak scattering final state, where both W bosons decay into a lepton and a neutrino.

W bosons decay to electrons, muons, and taus approximately 11% of the time (each) (see Table 2.5). Tau leptons, however, are not stable particles and, thus, are only indirectly observable through their decay products. As a result, $W \to \tau\nu$ decays are properly identified with a lower efficiency compared to the other leptonic W decay channels. For this reason, events with tau leptons in the final state are not considered in this analysis. For the remainder of this dissertation, references to leptons refer to only electrons and muons unless stated

otherwise. This analysis is conducted in six channels defined by the final state leptons. The channels are divided by lepton flavor and charge: e^+e^+, e^-e^-, $\mu^+\mu^+$, $\mu^-\mu^-$, $e^+\mu^+$, and $e^-\mu^-$.

Every ATLAS event contains numerous objects[1] resulting from, not only the primary interaction, but also secondary interactions and pile-up events. In a $W^\pm W^\pm jj$ event, the objects resulting from the $W^\pm W^\pm jj$ production should carry a larger fraction of the event momentum than secondary objects. Hence, to determine which objects are significant, the objects in the event are ordered (within their type) by their transverse momentum (p_T). The two objects with the largest and second largest p_T are referred to as the leading object and the subleading object, respectively, e.g., the leading and subleading leptons in the event are the two leptons with the highest p_T.

With this, it is important to note that the $e^+\mu^+$and $e^-\mu^-$ channels contain events where the electron is the leading lepton and the muon is the subleading lepton ($e\mu$) as well as events where the muon was the leading lepton and the electron was the subleading lepton (μe).

$W^\pm W^\pm jj$ production is ideal for studying VBS because the $W^\pm W^\pm jj$ electroweak production (which contains the VBS diagrams) can be enhanced over the $W^\pm W^\pm jj$ strong production (see Table 2.6). Due to the interaction of the initial quarks (see Section 2.4), the final state jets (resulting from the initial state quarks hadronizing) possess different kinematics in $W^\pm W^\pm jj$−EW and $W^\pm W^\pm jj$−QCD. The jets resulting from the quarks which radiated the W bosons are referred to as the *tagging jets*. $W^\pm W^\pm jj$−EW tagging jets tend to have a higher invariant mass (m_{jj}) and a larger rapidity separation (Δy_{jj}) than $W^\pm W^\pm jj$−QCD tagging jets. The m_{jj} and Δy_{jj} distributions for $W^\pm W^\pm jj$−EW and $W^\pm W^\pm jj$−QCD are shown in Figure 4.2. Applying selections on these kinematic quantities allows for $W^\pm W^\pm jj$−QCD production to be suppressed quite efficiently.
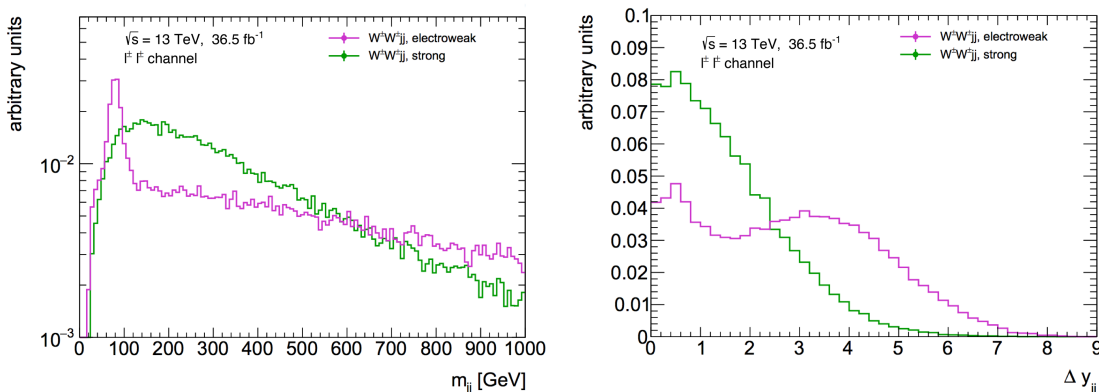
Figure 4.2: MC simulated invariant mass (left) and rapidity separation (right) of tagging jets associated with $W^\pm W^\pm jj$−EW and $W^\pm W^\pm jj$−QCD events.

Given this, the final state corresponding to $W^\pm W^\pm jj$−EW is: two same-sign leptons,

---

[1]*Object* refers to the products of the pp collision, including leptons, jets, etc.

two forward[2] jets with a large invariant mass, and missing energy due to the two neutrinos. This final state topology is a signature of $W^\pm W^\pm jj$ events and is depicted in Figure 4.3. Based on this topology, a signal region is constructed to isolate $W^\pm W^\pm jj-$EW events (see Section 7.5.1). This signal region is largely defined by selecting events with two same-sign leptons, a high m_{jj}, and a large Δy_{jj}.
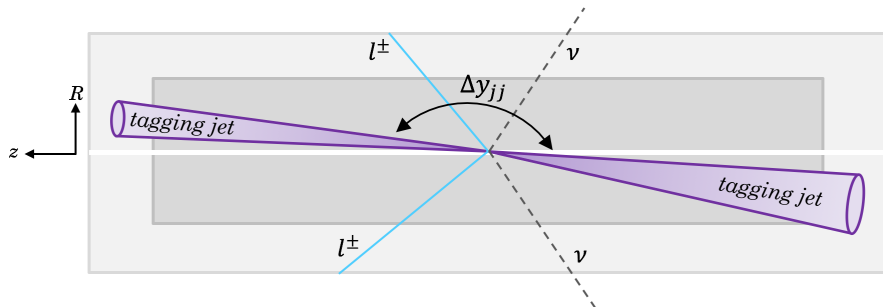
Figure 4.3: Example of $W^\pm W^\pm jj$ event topology in $z - R$ plane of the ATLAS detector. Two same-sign leptons (l) and neutrinos (ν) from the W boson decays are depicted, as well as the two jets resulting from the quarks which radiated the initial W bosons.

While the event topology shown in Figure 4.3 is a signature of $W^\pm W^\pm jj-$EW events, there are a number of other Standard Model processes which can mimic this final state, e.g., $W^\pm W^\pm jj-$QCD. All together, these processes can be grouped into three categories:

- **Prompt:** This category consists of Standard Model processes that produce events directly mimicking the $W^\pm W^\pm jj-$EW event signature with two *prompt* same-sign leptons. A prompt lepton is a lepton that is a direct product of the decay of interest. In this analysis, prompt leptons are leptons resulting from massive gauge boson decays.

- **e/γ Conversions:** This background consists of Standard Model processes that produce a final state with two opposite-sign leptons that are incorrectly identified as same-sign leptons.

- **Non-Prompt:** This background consists of Standard Model processes where one (or more) of the final state leptons are *non-prompt*. A non-prompt lepton is a lepton which is not the direct product of the decay of interest, but is instead the result of a misidentified jet or secondary decay. For example, a lepton produced during a b-hadron decay in the detector that is subsequently identified as a final state lepton is a non-prompt lepton.

---

[2]*Forward* refers to the angle of the jet with respect to the beam pipe. A forward jet creates a small angle with respect to the beam pipe, i.e., a large η.

In order to successfully observe $W^{\pm}W^{\pm}jj-$EW events, these backgrounds must be modeled accurately and reduced as much as possible. In the following sections, each background is discussed in greater detail and the method for modeling each background is described.

4.1 Prompt Background

The prompt background consists of Standard Model processes that produce a final state with (at least) two prompt same-sign leptons. In this analysis, $W^{\pm}W^{\pm}jj-$QCD production is categorized as a prompt background. Additional sources of prompt background are:

$WZjj$ production: If the W and Z bosons decay leptonically, the final state can be: $W^{\pm}Zjj \rightarrow l^{\pm}\nu l^+l^-jj$. If one of the leptons from the Z decay is not reconstructed or properly identified[3], then the event appears to have two same-sign prompt leptons produced in association with two jets. $WZjj$ production is the largest source of prompt background in this analysis.

$ZZjj$ production: If both Z bosons decay leptonically, the final state can be: $ZZjj \rightarrow l^+l^-l^+l^-jj$. If two leptons are not reconstructed or properly identified, the final state can appear as two same-sign leptons with two jets. This background has a smaller impact since it requires two leptons be missed in order to contribute in the signal region.

$t\bar{t} + V$ processes: $t\bar{t} + V$ can result in a final state, for example: $t\bar{t} + Z \rightarrow l^{\pm}\nu l^+l^-jjj_bj_b$, where j_b is a jet resulting from the b-quark produced in the t-quark decays. Jets resulting from b-quarks are often referred to as *b-jets*. In the example final state listed above, if a lepton is not reconstructed or properly identified, the final state can mimic the VBS $W^{\pm}W^{\pm}jj-$EW final state. Similarly, the $W^{\pm}W^{\pm}jj-$EW final state can also be mimicked by $t\bar{t} + W$ processes.

VVV processes: VVV involving W and Z bosons (WWW, WWZ, WZZ, and ZZZ) produce final states that have between two and six leptons. If the correct number of leptons are incorrectly identified or not reconstructed, the resulting event can mimic the $W^{\pm}W^{\pm}jj-$EW event topology, although the contribution from this prompt background is much smaller.

---

[3]A lepton can be misidentified or not reconstructed if, for example, the lepton travels outside the acceptance area of the detector.

4.1.1 Summary

The contributions of these prompt processes are estimated using Monte Carlo (MC) generated data samples (see Chapter 5). In order to reduce prompt background contributions, the following additional event selection requirements are implemented in the signal region:

- The event cannot have any jets which have been identified as b-jets. This selection reduces the $t\bar{t} + V$ background contribution.

- Events with three leptons are required to pass additional requirements (see Section 7.5). If the event fails to meet these selections, the event is removed from consideration. This requirement reduces the $WZjj$ background contribution in the signal region.

For the $WZjj$ background, a scale factor is utilized to scale the $WZjj$ background contribution in the signal region (see Section 8.1.2). The accuracy of the prompt background modeling is examined in validation regions (see Section 8.1).

4.2 e/γ Conversions

The e/γ conversion background groups together: (1) Standard Model processes that produce opposite-sign leptons which are reconstructed as same-sign leptons (charge misID), and (2) Standard Model processes where one lepton in the same-sign lepton pair is the product of an on-shell photon. For both of these groups, the background is largely the result of photon conversions, where a photon converts into an e^+e^- pair. Further details regarding these two e/γ conversion backgrounds are given below in Sections 4.2.1 - 4.2.2.

4.2.1 Charge MisID Background

The charge misID background results mainly from Drell-Yan[4] events ($q\bar{q} \rightarrow Z/\gamma^* \rightarrow e^+e^-$) and fully leptonic $t\bar{t}$ decays ($t\bar{t} \rightarrow W^+bW^-b \rightarrow l^+\nu l'^-\nu bb$). The final state for these processes involves two opposite-sign leptons. If the charge of one of these leptons is misidentified, the final state can appear to be the $W^\pm W^\pm jj$−EW final state. The charge of a lepton can be misidentified in one of two main ways:

- The lepton charge is incorrectly reconstructed as it moves through the detector.

- If the lepton is an electron, it may radiate a photon as it moves through the detector. If this photon converts into an e^+e^- pair, it is possible for the final reconstructed electron to be one of the photon-converted electrons instead of the prompt electron. If the reconstructed electron has the opposite charge of the prompt electron, the event can appear to contain two same-sign leptons.

---

[4]The Drell-Yan process occurs at the LHC when a quark of one proton and an anti-quark of another proton annihilate and produce a virtual Z/γ that then decays into an opposite-sign pair of leptons.

Since MC simulation has proven to be inefficient at modeling charge misID in the ATLAS detector, this background is estimated using a data-driven method. Using this method, the charge misID background is estimated by selecting opposite-sign data events and weighting them with the probability that one of the leptons is reconstructed with the wrong charge (see Section 8.2.2). Studies have shown that (in this analysis) charge misID does not impact muons. As a result, only events which contain at least one electron (excludes $\mu\mu$ channels) are weighted with the probability for charge misID.

4.2.2 $V\gamma jj$ Processes

$V\gamma jj$ processes ($V \in \{W^{\pm}, Z\}$) are the second contribution to the e/γ conversion background. If the W/Z decays leptonically and the γ converts into an e^+e^- pair, the resulting final states can be, for example: $W^{\pm}\gamma jj \to l^{\pm}\nu e^+e^- jj$. Here, the jets produced in association with the $V\gamma$ can be the result of: (1) the quarks that radiated the V/γ bosons, or (2) gluons that radiated off the quarks. If the photon converts into an e^+e^- pair and one of the resulting electrons is not properly identified or reconstructed, the result can be a same-sign lepton pair final state with two jets.

This background is estimated using MC simulated samples. The accuracy of the $V\gamma jj$ background modeling in MC is established in a validation region defined to isolate $Z\gamma jj$ events. In this region there is some disagreement between the data and MC. The level of disagreement is measured and used as a scale factor that is applied to the $V\gamma jj$ background in the signal region (see Section 8.2.3).

4.2.3 Summary

The e/γ conversion background consists of the charge misID background and $V\gamma jj$ production background. The charge misID background is estimated using a data-driven method. The $V\gamma jj$ background is estimated using MC simulation and is scaled by a normalization scale factor in the signal region. To reduce the contribution of the e/γ conversion background in the signal region, the final state dilepton mass in the e^+e^+ and e^-e^- channels is required to be away from the peak of the Z boson mass. This selection reduces the contribution of processes involving Z decays.

4.3 Non-Prompt Background

The non-prompt background consists of Standard Model processes where one (or more) of the leptons are non-prompt. The main contributions to the non-prompt background come from:

- Semi-leptonic $t\bar{t}$ processes, e.g., $t\bar{t} \to WbWb \to l\nu q\bar{q}bb$

- Leptonic W+jets processes, e.g., $W \to l\nu + $ jets

Additional smaller contributions come from:

- single top processes, e.g., $Wt \to l\nu Wb \to l\nu q\bar{q}b$

- QCD multijet processes, e.g., $q\bar{q} \to q\bar{q}gg$

In all of these processes, a single lepton (at most) is prompt, and one (or more) of the produced jets can be: (1) incorrectly reconstructed as a lepton, or (2) produce a non-prompt lepton in the event (such as the semi-leptonic decay of a produced b-hadron in a jet).

The probability of a jet to be reconstructed as a lepton is not well modeled in MC simulation, therefore this background is estimated with a data-driven method. The method used is very similar to the concept of the method used to determine the charge misID background. A scale factor (the fake factor) is determined; this scale factor is a measure of how likely an event is to be due to non-prompt backgrounds. The non-prompt background contribution is determined by weighting data events using this fake factor (see Section 8.3).

In order to reduce the non-prompt background contribution in the signal region, additional requirements are placed on the events in the signal region:

- Leptons are required to be isolated (see Chapter 6), thereby reducing the probability the lepton is actually a jet.

- Events with jets identified as b-jets are vetoed. This selection reduces the $t\bar{t}$ contribution.

- The amount of E_T^{miss} in the event must meet the minimum expected for two neutrinos. Since many of the non-prompt background processes produce one prompt neutrino, this selection reduces the non-prompt background contribution in the signal region.

4.4 Background Summary

The relative contribution of the prompt background, the e/γ conversion background, and the non-prompt background in the signal region is represented in Figure 4.4 for all six lepton channels individually. There is no e/γ conversion background contribution in the $\mu\mu$ channels. The largest source of background in the $e\mu$ and $\mu\mu$ channels is the prompt background, while the largest source of background in the ee channels is the non-prompt background.

A number of the background processes in this analysis involve W bosons ($WZjj$, W+jets, $W^\pm W^\pm jj$−QCD, etc.). Due to the higher number of up quarks in the colliding protons, W^+ bosons are more frequently produced than W^- bosons [70]. The impact of this can be seen in Figure 4.4 when comparing the background composition for lepton channels with the same flavor but different charge (e.g., e^+e^+ and e^-e^-).
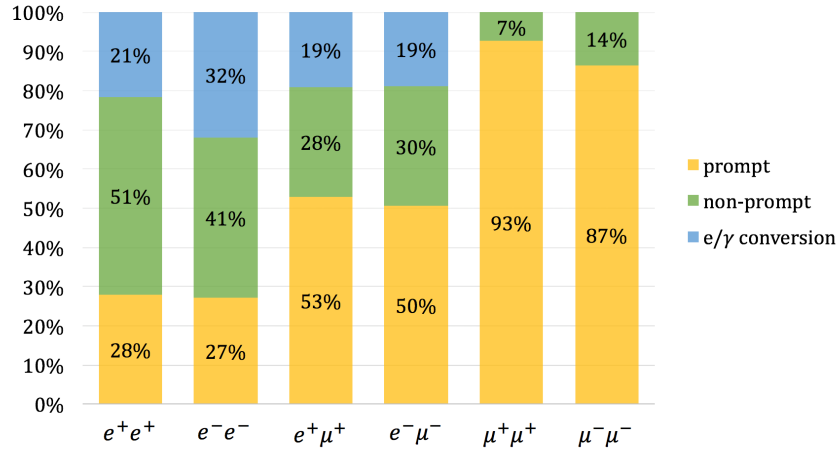
Figure 4.4: Relative contribution of prompt, non-prompt, and e/γ conversion backgrounds to the expected background in the signal region for all six analysis channels.

4.5 $W^{\pm}W^{\pm}jj-$ EW Observation Method

Observing the Standard Model $W^{\pm}W^{\pm}jj$ electroweak production requires the number of observed events passing analysis selections to be compared to the theoretical prediction of the Standard Model. The observed events are compared to the Standard Model theoretical prediction in bins of their m_{jj} distributions. The m_{jj} distributions of the observed data events, the estimated background contributions (with relevant uncertainties), and the theoretical Standard Model $W^{\pm}W^{\pm}jj$ signal are input into a profile likelihood fit (see Chapter 12). For each m_{jj} bin, this fit compares the number of observed events to the number of expected events, where the number of expected events is the sum of the background and $W^{\pm}W^{\pm}jj-$EW signal. The result of this fit is compared to a fit performed with a background-only hypothesis to determine the likelihood the observed events represent $W^{\pm}W^{\pm}jj$ electroweak production. If the background-only hypothesis is rejected by more than 5 standard deviations (5 σ), the process is said to be observed.

The remainder of this dissertation details the observation of $W^{\pm}W^{\pm}jj$ electroweak production using data collected by the ATLAS detector with $\sqrt{s} = 13$ TeV. Chapter 5 discusses the MC simulated samples used for: (1) estimating the Standard Model $W^{\pm}W^{\pm}jj$ electroweak signal and the prompt background, and (2) assisting with the estimation of the non-prompt and e/γ conversion backgrounds. The analysis selections defining the signal region and validation regions used to test background modeling are outlined in Chapter 7. In Chapters 8 and 9, the methods used for estimating the background and signal processes are discussed in detail. The sources of uncertainty for this analysis are introduced in Chapters 8, 10, and 11. Finally, the fit method is described in Chapter 12, and the results are presented in Chapter 13.

Chapter 5

Event Simulation

This chapter discusses hadron collision event simulation. First, the methodology used by event generators to simulate particle collisions at the LHC is introduced. Then, different event generators providing $W^\pm W^\pm jj$ predictions are discussed. Finally, the specific simulated samples used in this analysis to estimate the signal and background contributions are described.

5.1   Monte Carlo Event Generator Methodology

In MC event generators, hadron collision events are produced individually with a step-by-step process, where random numbers obtained from quantum mechanical probability distributions are utilized at various stages [26]. The steps to generate a collision event are illustrated in Figure 5.1 and summarized below.

1. The event generation begins with two initial **incoming protons**. In Figure 5.1, the incoming protons are each shown as three parallel, green lines near the middle of the illustration. These protons are treated as a bag of partons described by PDFs (see Section 2.3).

2. A parton from each proton collide to provide the **hard scattering** process of interest, e.g., $u\bar{d} \to W^+$, $gg \to g$, *etc.* If unstable particles (such as a W/Z boson, a top quark, or a gluon) are produced in the initial hard event, their decay is treated as part of the hard process in order to properly transfer particle properties (such as spin correlations). In Figure 5.1, the hard scattering component is shown in red. The large red circle represents the initial hard scatter, and the smaller red circles depict subsequent unstable-particle decays. The hard scattering is calculated using matrix elements derived with Feynman rules at a fixed order in perturbation theory.

3. The partons can emit QCD radiation referred to collectively as the **parton shower**. This radiation can be emitted by partons before the collision (Initial State Radiation
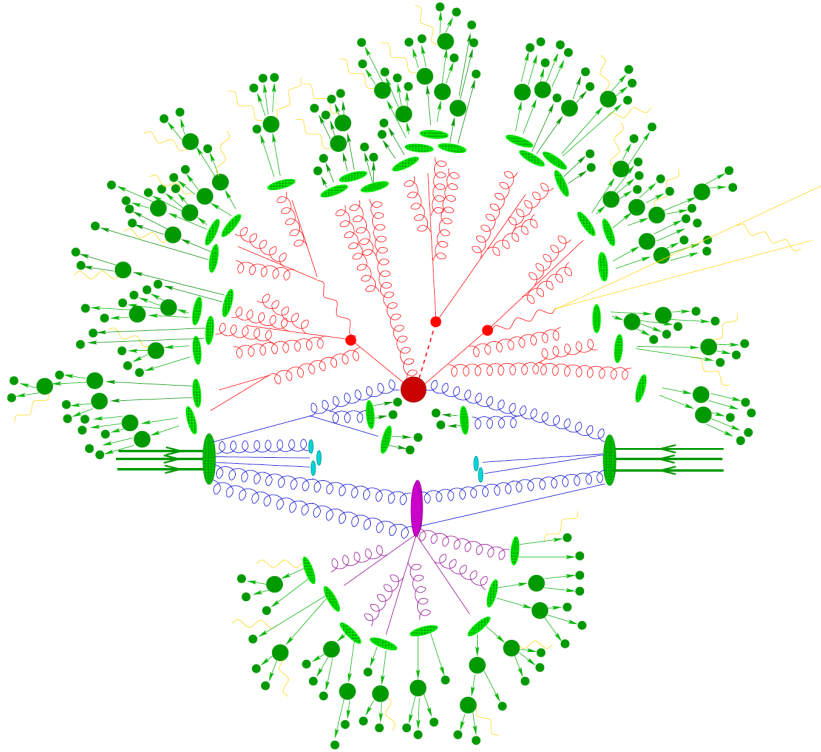
Figure 5.1: Visualization of the simulation of a *pp* collision event [71]. The incoming protons are shown as parallel, green lines and ellipses near the center of the illustration. The hard scatter is shown in red, the parton shower is shown in blue, and the hadronization and hadron decays are shown in bright and dark green, respectively. The purple dot and lines represent a secondary interaction, and QED radiation is shown in yellow.

[ISR]) or after the collision (Final State Radiation [FSR]). The algorithms applied to progress the parton showers are designed such that the cross section of the event's hard process is not impacted by the parton shower [72].

4. Showering algorithms are based on a number of small-angle and low-energy approximations and thus do not accurately describe hard, wide-angle emissions, such as jets. As a result, the parton shower description of hard collision events is commonly improved upon by either [26]: **Matrix Element and Parton Shower matching** (ME+PS) or the **matching of NLO calculations and the Parton Shower** (NLO+PS). The ME+PS method allows for LO matrix elements to be used for hard, large-angle emissions. The NLO+PS method increases the accuracy of the basic process generation from LO to NLO and includes the radiation of an additional parton with LO accuracy.

5. Given the number of partons in each proton, additional parton pairs may collide within a single *pp* collision. This process is referred to as **multi-parton interactions (MPI)** and is illustrated in Figure 5.1 as the purple oval and purple lines. The MPI may also

have ISR or FSR resulting from the parton shower. These underlying events can impact the reconstruction of the primary hard scatter during analysis.

6. After the parton shower, the resulting partons are grouped into color-neutral composite states to form hadrons through **hadronization**. There is no calculation for this process from first principles, thus this hadronization is modeled based on the general properties of QCD. There are two main hadronization models currently utilized: the *string* model and the *cluster* model. In the *string* model, the color confinement force between two quarks (of color and anti-color) is modeled as a string. This string is then stretched until it breaks, creating a new quark pair. This process is repeated until the string energy is low enough that, when broken, it produces hadrons. In the *cluster* model, quark pairs are grouped into colorless clusters. These clusters then decay into either other colorless clusters or hadrons. The process is repeated until all the clusters have decayed into hadrons.

7. The majority of the primary hadrons resulting from the hadronization are unstable and will decay at different timescales. For ATLAS, if the decay length of the particle is less than 10 mm, the event generator will **decay the unstable particle**. In addition to hadrons, the event generator will also decay τ leptons which have a decay length of 87 μm.

8. During the hadron/τ decays, **electromagnetic (QED) radiation** can occur which can be modeled similarly to the parton shower using electric charge instead of color charge. Another common method of modeling the radiation utilizes the YFS formalism [73] which allows any LO process to be corrected to any order (within the reach of QED effects). The QED radiation is illustrated in Figure 5.1 with yellow lines.

At this point, the event generator has completed its job and has fully simulated the pp collision event through to the final state particles. Events which are simulated to only this point are referred to as being *generator-level* (or truth-level). Generator-level events can be used to determine theoretical calculations, e.g., theoretical cross section predictions. In order to compare the generated events with ATLAS collision data, however, the response of the detector as particles pass through it must be simulated in the following additional steps:

9. Final state particles are processed through a **detector simulation** of ATLAS built using GEANT4 [74, 75, 76]. This process results in simulated energy deposits and coordinates, which are stored in a file as "hits".

10. The simulated hits are put through a **digitization** process which converts the hits to digital signals that are identical to the signals read out from the detector during data-taking. At this point, additional interactions[1] per bunch crossing (pile-up) and the cavern background are simulated [78, 79].

---

[1]The additional interactions are selected as minimum bias events, meaning inelastic collision events are selected to produce as little bias as possible [77].

At this stage, the event simulation process is complete, and the events are referred to as being *detector-level*. From this point forward, collision data and simulation can be processed in the same manner. Before analysis, the collision data and simulation must go through reconstruction which turns the digital signals into tracks and physics objects[2] (see Chapter 6).

Not all event generators are designed to single-handedly simulate all of the steps to produce a generator-level sample. General purpose generators (such as SHERPA [71], HER-WIG [80, 81, 82], and PYTHIA [83]) can simulate the entire process from matrix element to parton shower, hadronization, and additional decays/radiation. Some generators, however, such as MADGRAPH [84, 85], POWHEG [86], WHIZARD [87], and VBFNLO [88, 89], only generate a fixed order calculation for the hard scattering process and must be interfaced with other generators (such as PYTHIA or HERWIG) for the parton shower. In addition, *after-burner* programs exist which can be used to redecay specific particles with more accuracy, such as: PHOTOS++ [90] for QED radiative corrections, MADSPIN [91] for decays of heavy resonances, and EVTGEN [92] for heavy flavor hadron decays.

The predictions of event generators can be *tuned* by adjusting parameters of the parton shower and hadronization to match the results observed in experimental data [72]. Every generator has a number of relatively free parameters that can be tuned. The majority of these parameters tune the model for the non-perturbative hadronization, while a smaller number of parameters tune the model for the perturbative hard process. For a given generator, the number of tuning parameters can be large (more than 30 parameters for some generators), however the majority of the physics modeling is determined by a select few: (1) the value of α_S, (2) the parameters related to the non-perturbative hadron fragmentation distributions, and (3) the parameters related to modeling the underlying event. While all of these parameters have a physical motivation, the value of the parameters are only known (usually) through rough-scale approximations, and they must be matched to experimental data for the generator to perform well. Most of the hadronization parameters are tuned using LEP data. The hard process parameters are often tuned using Tevatron and LHC data.

5.2 $W^\pm W^\pm jj$ Event Generator Comparison

Several MC generators are available which can simulate the $W^\pm W^\pm jj$ process at LO and NLO. Recently, the $W^\pm W^\pm$ scattering predictions of these generators were compared in two publications: Ref. [93] and Ref. [94]. The results of these comparisons are summarized below.

---

[2]Detector-level samples that have gone through reconstruction are often referred to as *reco-level* samples.

5.2.1 Generators

Hard scattering cross sections for electroweak $pp \to \mu^+\nu_\mu e^+\nu_e jj$ production at $\sqrt{s} = 13$ TeV are calculated using five[3] MC generators in Ref. [93] and three MC generators in Ref. [94]. Briefly, these generators are:

- MADGRAPH5_aMC@NLO (MG5_aMC): An automatic meta-code[4] which simulates any scattering process at LO or NLO, including NLO QCD corrections using the MC@NLO method [95]. Parton showers are produced by interfacing with an external generator. Utilized in Ref. [93] and Ref. [94].

- POWHEG-BOX: A computer framework for interfacing NLO QCD calculations with parton showers using the POWHEG method [96]. For this generator, the matrix elements are either: (1) provided as input by the user, or (2) selected from previously-implemented processes that are stored in the framework library. For this comparison between Ref. [93] and Ref. [94], the matrix element is provided by a previously-implemented process based on VBFNLO calculations [97]. The parton shower is performed by an external generator. Utilized in Ref. [93] and Ref. [94].

- VBFNLO: A specialized generator designed specifically for processes with electroweak bosons. This generator provides matrix elements at NLO accuracy in perturbative QCD. It must be interfaced with another generator for the parton shower. Utilized in Ref. [93].

- PHANTOM: A dedicated tree-level generator for six-parton final states at order $\mathcal{O}(\alpha_{EW}^6)$ and $\mathcal{O}(\alpha_S^2\alpha_{EW}^4)$ (including interference) for pp, $p\bar{p}$, and e^+e^- colliders [98]. This generator must be interfaced with another generator for the parton shower. Utilized in Ref. [93].

- WHIZARD: A multi-purpose generator which generates LO matrix elements automatically using O'MEGA [99]. It is capable of simulating the parton shower, but the parton shower may also be simulated using an external generator. Utilized in Ref. [93].

- SHERPA: A C++ based multi-purpose generator which simulates all steps required to produce generator-level samples (i.e., matrix element, parton shower, hadronization, underlying event, etc.). SHERPA VBS samples suffer from a non-optimal setting of the color flow setup for the parton shower on top of VBS-like scattering processes, leading to an excess of central emissions from the parton shower [100]. Utilized in Ref. [94].

Generators which require an external parton shower generator are interfaced with either PYTHIA or HERWIG (or both for comparison). Both PYTHIA and HERWIG are multi-purpose

---

[3]Only predictions from samples matched to parton showers are included in this number. More cross sections are calculated in Ref. [93] without any parton showering.

[4]Meta-code is code that generates code.

event generators capable of generating matrix elements in addition to producing/matching the parton shower and hadronization. The most significant difference between PYTHIA and HERWIG regards the hadronization, where PYTHIA employs the string method and HERWIG uses the cluster method.

5.2.2   Generator Configurations

Beyond the combination of matrix element generator and parton shower generator, there are a few different configurations compared in Ref. [93] and Ref. [94], including: LO diagram contributions, parton shower settings, μ_R/μ_F-scale settings, and implementing an intermediate simulated W boson before the final state. The details of these configuration settings are discussed below.

5.2.2.1   Leading Order Contributions

One of the main distinguishing features between different $W^{\pm}W^{\pm}jj$ event generators is what LO diagrams are considered in the calculation. Figure 5.2 illustrates different types of LO Feynman diagrams which can be included in the simulation, including: *VBS* diagrams (top left), which includes all vertices in Figure 4.1 and is sensitive to QGC; *s-channel decay chain* diagrams (top right), which includes diagrams where the initial quark and anti-quark legs annihilate; *triboson* diagrams (bottom left), which includes diagrams where the final state jets are produced by a virtual boson; and *non-VBS t-channel* diagrams (bottom right), which includes diagrams with no direct boson-boson interactions.

These different contributions are categorized according to their quark lines:

- **t-channel:** Diagrams where the initial and final quarks are connected by a continuous fermion line. This includes relevant VBS and non-VBS t-channel diagrams.

- **u-channel:** Diagrams with crossed fermion lines with respect to the t-channel.

- **s-channel:** Diagrams where the initial quarks are connected by a continuous fermion line (combination of s-channel decay chains and triboson contributions).

When calculating the theoretical predictions for $W^{\pm}W^{\pm}jj$, some event generators utilize an approximation known as the *VBS approximation*[5] [101]. This approximation consists of considering all t- and u-channel diagrams while discarding the s-channel diagrams and neglecting any interference between the different channels. In Ref. [93] and Ref. [94], for the generated samples summarized here, samples with matrix elements generated by POWHEG-BOX and VBFNLO implement this approximation. The performance of this approximation compared to the full calculation is examined in Ref. [93].

---

[5]This approximation is also known as the t-/u- approximation or the VBF approximation.
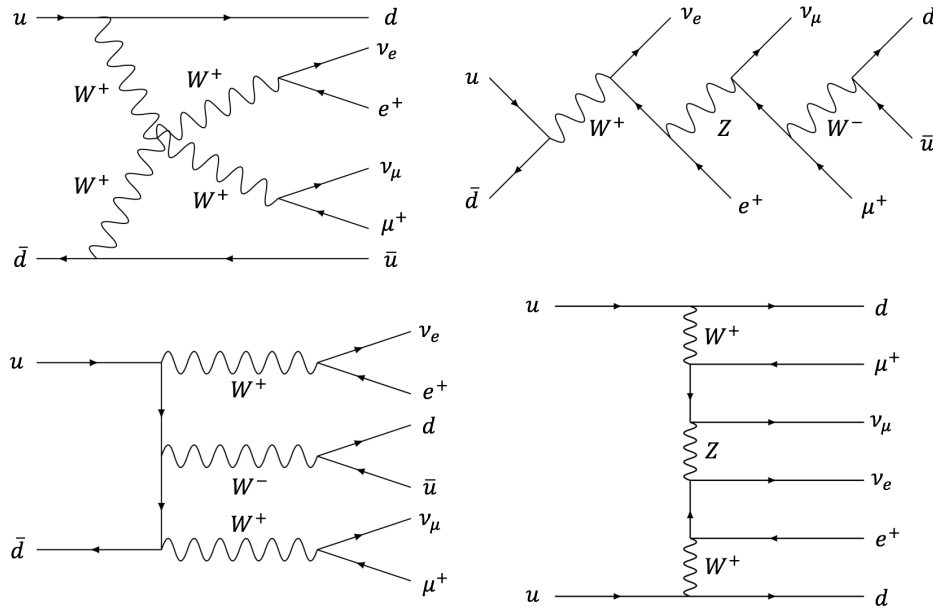
Figure 5.2: Example of LO diagrams that contribute to $pp \rightarrow \mu^+\nu_\mu e^+\nu_e jj$ at order $\mathcal{O}(\alpha^6)$. These contributions are classified as VBS (top left), s-channel decay chain (top right), triboson (bottom left), and t-channel (bottom right). The combined contribution of the s-channel decay chain and the triboson contributions are referred to as the s-channel contribution.

5.2.2.2 Parton Shower Settings

PYTHIA and HERWIG are both utilized as parton shower generators in Ref. [93] and Ref. [94].

The default HERWIG parton shower is an *angular-ordered* parton shower. An alternative parton shower, a *dipole-type* parton shower, is available for HERWIG. Both the default and the dipole-type HERWIG parton showers are studied in Ref. [93] and Ref. [94]. Samples generated using the HERWIG dipole-type parton shower are labeled with "Dipole Shower".

In addition, two different recoil schemes[6] are studied in Ref. [93] and Ref. [94] for PYTHIA. Using the default global recoil scheme, the recoil of an ISR is taken by the entire final state. In the *dipole* recoil scheme, however, only one final state parton takes the recoil of an ISR [102]. Samples that were generated using the dipole recoil scheme are labeled with "Dipole Recoil".

Finally, recall from Section 5.1 that the parameters of the parton shower and hadronization in event generators are tuned to better match experimental data. The resulting optimized set of parameters is referred to as an *MC tune*. These tunes are produced independently for each generator. For some generators, such as PYTHIA, multiple tunes exist which have been optimized for different processes or using different collections of experimental data. The tunes used in Ref. [93] and Ref. [94] are:

---

[6]The recoil scheme determines at what scale energy-momentum preservation is enforced.

- PYTHIA 8 Monash Tune [103]: General purpose tune optimized in 2013 using data from a wide array of colliders including LEP, Tevatron, and the LHC. This tune includes an updated analysis of the constraints on fragmentation in *ee* collisions.

- PYTHIA 8 A14 Tune [104]: General purpose high p_T tune produced by ATLAS in 2014 using high p_T events[7] sensitive to ATLAS jet and underlying event observables. This tune builds off of the Monash tune settings.

- PYTHIA 8 AZNLO Tune [105]: ATLAS tune optimized in 2013 for the description of the Z boson p_T spectrum, specifically at low p_T.

- HERWIG 7 H7.1 Default Tune [106]: General purpose tune produced by HERWIG. The parton shower cutoffs and hadronization were optimized in 2018.

- SHERPA Default Tune [107]: General purpose tune produced by SHERPA. This tune was produced without utilizing Tevatron data.

For both SHERPA and HERWIG, the default tune is used (when applicable) in both Ref. [93] and Ref [94]. For PYTHIA, Ref. [93] uses the Monash tune for all generated samples. Ref. [94] uses the A14 tune for samples where the matrix element was generated with MG5_aMC and the AZNLO tune for samples generated with POWHEG-BOX.

5.2.2.3   Factorization/Renormalization Scale

Two unphysical scales need to be defined in the generator: the μ_F-scale and the μ_R-scale (see Section 2.3). The choice of these scales is highly dependent upon the process being studied. Generally, the scales should be chosen such that the scales are close to the energy scale of the event. The scales can be set to fixed values or be a *dynamic scale*, where the scale is chosen for each event based on the kinematic properties of said event. All together, three different scales are implemented in Ref. [93] and Ref [94].

All the samples generated/studied in Ref. [93] and half of the samples generated/studied in Ref. [94] use the dynamic scale:

$$\mu_R = \mu_F = \sqrt{p_T^{j1} p_T^{j2}}, \tag{5.1}$$

where p_T^{j1} and p_T^{j2} are the values of the transverse momentum for the leading and subleading jet, respectively. Samples in Ref. [94] are also generated with the dynamic scale $\mu_F = \mu_R = m_{VV}$ (diboson invariant mass) and the fixed scale $\mu_F = \mu_R = m_W$ (W boson mass).

---

[7]Events recorded at $\sqrt{s} = 7$ TeV.

5.2.2.4   Intermediate W Generation

In order to simplify the calculation, several of the MG5_aMC matrix element calculations are simulated in two steps (both in Ref. [93] and Ref. [94]). These two steps are:

1. $pp \to W^+W^+jj$ using MG5_aMC

2. $W^+W^+jj \to \mu^+\nu_\mu e^+\nu_e jj$ using MADSPIN

MADSPIN uses an LO calculation of the partial and total W decay widths while MG5_aMC (and the other generators) uses an NLO calculation. To account for the difference between the LO and NLO widths, the "two-step" predictions (generated using MADSPIN) are rescaled by a constant factor. Predictions corrected in this manner are labeled with Γ_{resc}.

5.2.2.5   Summary

With all the configurations described above, Ref. [93] and Ref. [94] compared the $W^\pm W^\pm jj$ production cross sections predicted using various event generator configurations for electroweak $pp \to \mu^+\nu_\mu e^+\nu_e jj$ production at $\sqrt{s} = 13$ TeV. The samples and their configurations are summarized in Table 5.1. Samples which were generated at LO and NLO accuracy in perturbative QCD are indicated with two checkmarks in Table 5.1. For ease of comparison, if Ref. [93] and Ref. [94] both studied a sample generated with the same matrix element and parton shower generators, the same "Sample Name" (i.e., MG5_aMC+Py8) is listed for both samples. The μ-scale is dynamic unless stated otherwise.

Sample Name	Contributions	μ-scale	Shower	Tune	LO	NLO	Ref.
MG5_aMC+Py8	s,t,u	$\sqrt{p_T^{j1}p_T^{j2}}$	Pythia 8.235	A14	✓		[94]
MG5_aMC+Py8,Γ_{resc}	s,t,u	$\sqrt{p_T^{j1}p_T^{j2}}$	Pythia 8.235	A14		✓	[94]
MG5_aMC+Py8,Γ_{resc}	s,t,u	$\sqrt{p_T^{j1}p_T^{j2}}$	Pythia 8.223	Monash	✓	✓	[93]
MG5_aMC+Py8-dipole recoil	s,t,u	$\sqrt{p_T^{j1}p_T^{j2}}$	Pythia 8.235	A14, Dipole Recoil	✓		[94]
MG5_aMC+H7	s,t,u	$\sqrt{p_T^{j1}p_T^{j2}}$	Herwig 7.1.3	H7.1-Default	✓		[94]
MG5_aMC+H7,Γ_{resc}	s,t,u	$\sqrt{p_T^{j1}p_T^{j2}}$	Herwig 7.1.3	H7.1-Default		✓	[94]
MG5_aMC+H7,Γ_{resc}	s,t,u	$\sqrt{p_T^{j1}p_T^{j2}}$	Herwig 7.1.2	H7.1-Default	✓	✓	[93]
MG5_aMC+H7-dipole shower	s,t,u	$\sqrt{p_T^{j1}p_T^{j2}}$	Herwig 7.1.3	H7.1-Default, Dipole Shower	✓		[94]
PowhegBox+Py8	t,u	m_W (fixed)	Pythia 8.212	AZNLO		✓	[94]
PowhegBox+Py8	t,u	$\sqrt{p_T^{j1}p_T^{j2}}$	Pythia 8.230	Monash		✓	[93]
PowhegBox+Py8-dipole recoil	t,u	m_W (fixed)	Pythia 8.212	AZNLO, Dipole Recoil		✓	[94]
PowhegBox+H7	t,u	m_W (fixed)	Herwig 7.1.3	H7.1-Default		✓	[94]
PowhegBox+H7-dipole shower	t,u	m_W (fixed)	Herwig 7.1.3	H7.1-Default, Dipole Shower		✓	[94]
VBFNLO+H7	t,u	$\sqrt{p_T^{j1}p_T^{j2}}$	Herwig 7.1.2	H7.1-Default	✓	✓	[93]
VBFNLO+H7-dipole shower	t,u	$\sqrt{p_T^{j1}p_T^{j2}}$	Herwig 7.1.2	H7.1-Default, Dipole Shower	✓	✓	[93]
Phantom+Py8	s,t,u	$\sqrt{p_T^{j1}p_T^{j2}}$	Pythia 8.223	Monash	✓		[93]
Phantom+H7	s,t,u	$\sqrt{p_T^{j1}p_T^{j2}}$	Herwig 7.1.2	H7.1-Default	✓		[93]
Whizard+Py8	s,t,u	$\sqrt{p_T^{j1}p_T^{j2}}$	Pythia 8.223	Monash	✓		[93]
Sherpa	s,t,u	m_{VV}	Sherpa 2.2.2	Default	✓		[94]

Table 5.1: Summary of $W^{\pm}W^{\pm}jj$ samples generated in Ref. [93] and Ref. [94] to study the consistency of the predicted $W^{\pm}W^{\pm}jj$ cross sections. The *Sample Name* corresponds with the short-hand name used in Figure 5.3. Two entries with the same "Sample Name" refer to a matrix element/parton shower generator combination studied in both references. Samples which are generated at LO and NLO accuracy in perturbative QCD are indicated with two checkmarks. The μ-scale is dynamic unless stated otherwise.

5.2.3 Predicted Cross Sections

For each of the samples listed in Table 5.1, the cross section for electroweak $pp \rightarrow \mu^+\nu_\mu e^+\nu_e jj$ production is predicted in a fiducial region where electroweak production dominates. This fiducial region (*Ref-fiducial region*) is fully defined in Ref. [93] and differs slightly from the analysis fiducial region used in the rest of this dissertation (see Section 9.1.1). The Ref-fiducial region has slightly more relaxed lepton p_T and jet p_T selections and a tighter Δy_{jj} selection, compared to the analysis fiducial region.

Figure 5.3 shows the predicted cross sections in the Ref-fiducial region as reported in Ref. [93] and Ref. [94]. Predictions from Ref. [93] are illustrated with open markers, while predictions from Ref. [94] are shown with filled markers. The predictions calculated using matrix elements generated to LO accuracy are shown as blue squares, while predictions

calculated using NLO matrix elements are represented by red triangles.
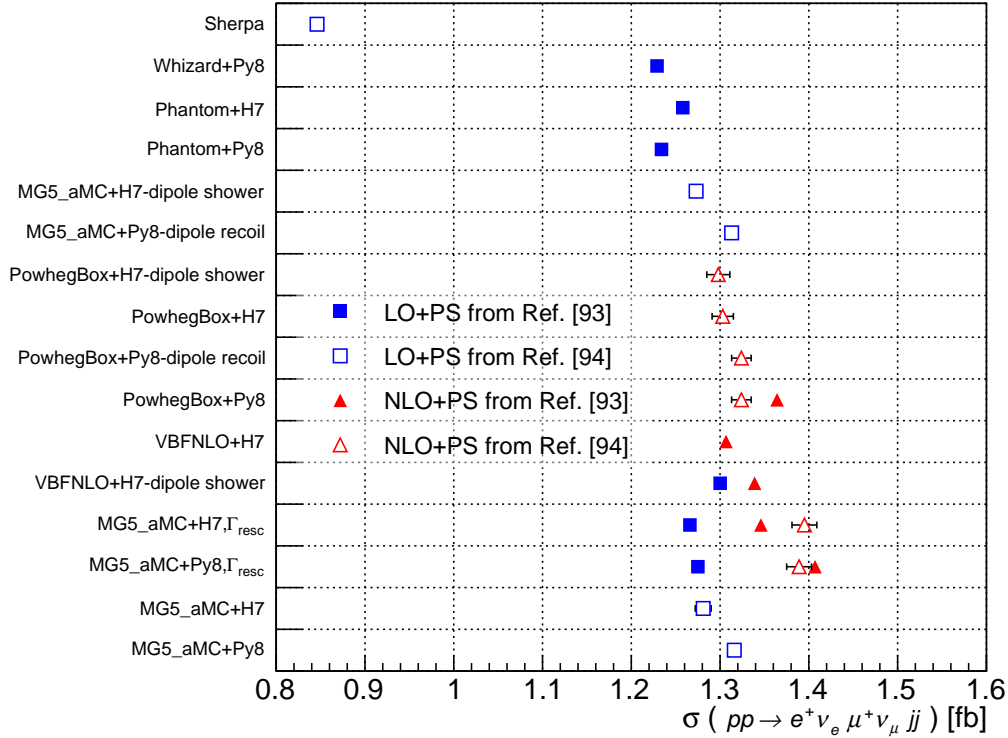
Figure 5.3: $W^\pm W^\pm jj$ production cross sections measured using various event generator configurations for $pp \to e^+\nu_e\mu^+\nu_\mu jj$ calculated from Ref [93] and Ref [94]. LO calculations are shown as blue filled squares (Ref. [93]) and blue open squares (Ref. [94]). NLO calculations are represented by red filled triangles (Ref. [93]) and red open triangles (Ref. [94]). Statistical uncertainties are shown, although for many values the uncertainty is smaller than the size of the marker.

From Figure 5.3 several observations can be made:

- **Impact of Parton Shower Model:** Changing the parton shower model for a given hard scattering calculation (e.g., difference between PYTHIA and HERWIG for POWHEG-BOX) results in, at most, a 5% shift in the predicted cross section.

- **Impact of Dipole Recoil:** Shifting the recoil scheme from a global scheme to a dipole scheme only shifts the predicted cross section by 0.2%[8].

---

[8]This shift is calculated by comparing the MG5_aMC+Py8 cross section to the MG5_aMC+Py8-dipole recoil predicted cross section, where both samples were generated with LO matrix elements, from Ref. [94].

- **Agreement Between References:** For the specific generator configurations studied by both Ref. [93] and Ref. [94] (such as PowhegBox+Py8), the predicted cross sections reported by both references agree within 3%.

- **NLO ME+PS Cross Section Agreement:** The cross sections predicted by both references with NLO accuracy in the matrix element agree within 10%.

- **LO ME+PS Cross Section Agreement:** The cross sections predicted by both references with LO accuracy in the matrix element agree within 7%, with the exception of the Sherpa[9] prediction which differs from the other LO+PS calculations by roughly 35%.

- **Impact of** SHERPA **Color Flow:** The large difference between the Sherpa cross section and all other cross section calculations highlights the impact of the suboptimal color flow setting in SHERPA. The Sherpa sample includes one additional jet in the matrix element, which leads to the significantly reduced cross section due to the large suppression from unnaturally large Sudakov factors [108].

All together, with the exception of the Sherpa sample, all predicted cross sections (both at LO and NLO) agree within 13%. Considering only NLO calculations, the level of agreement becomes 10%, while for LO calculations (not including the Sherpa prediction) the agreement is within 7%. For comparison, the theoretical uncertainty on the predicted cross section measured in this analysis is roughly 15% (see Section 9.1.4). Thus, the differences observed between the various generator cross section calculations is smaller than the current level of theoretical uncertainty in this analysis.

While a number of the generator-level samples were available for the analysis detailed in this dissertation, the only samples initially simulated at detector-level were the Powheg-Box+Py8 and Sherpa samples. The process of producing a detector-level sample is lengthy and requires a significant amount of computing resources. As a result, no additional detector-level $W^{\pm}W^{\pm}jj$ samples were simulated beyond the two previously mentioned, even after the inadequacies of the available samples were revealed. The complete details of the detector-level samples utilized in this analysis are described in the next section (Section 5.3).

5.3   Simulated Analysis Samples

The specific configurations of the signal and background MC samples utilized in this analysis are detailed in this section. All samples are generated using standard ATLAS configurations for each event generator (e.g., choice of tune) as determined by the ATLAS collaboration [109, 110, 111, 112]. The various configurations are summarized in Table 5.2.

---

[9]In Section 5.2, "Sherpa" refers to the specific simulated $W^{\pm}W^{\pm}jj$ sample examined in Ref. [94], and "SHERPA" refers to the event generator as a whole.

5.3.1 Signal Samples

Two signal samples are studied in this analysis, one simulated using SHERPA and one simulated with POWHEG-BOX. The nominal signal sample is the SHERPA sample, while the POWHEG-BOX sample is used for systematics, validation, and a second set of reference values[10]. These signal samples are dedicated $W^\pm W^\pm jj-$EW samples of order α^6_{EW} where two same-sign W bosons are simulated with the presence of two jets.

The SHERPA generated sample is used as the nominal $W^\pm W^\pm$ sample, as POWHEG-BOX does not model resonant triboson contributions[11] in the matrix element. Additionally, the POWHEG-BOX sample employs a fixed μ_R/μ_F-scale of $\mu_R = \mu_F = m_W$, while SHERPA uses the preferable event-by-event dynamic μ_R/μ_F-scale.

Sherpa Signal Sample

The SHERPA $W^\pm W^\pm jj-$EW sample is simulated using SHERPA 2.2.2 [71]. The order of the electroweak coupling in the process is fixed to $\mathcal{O}(\alpha_{EW}) = 6$. Matrix element diagrams are calculated for up to one additional parton at LO using COMIX [113] and then merged with the SHERPA parton shower [114] using the CKKW ME+PS@LO prescription [115]. The decay of taus are treated with the SHERPA parton shower algorithm. The NNPDF3.0 PDF is implemented at NNLO in QCD with $\alpha_S = 0.118$ [44]. The baseline choice for the μ_R-scale and μ_F-scale is defined per event as the matrix-element-level invariant mass of the WW system.

Powheg Signal Sample

The POWHEG $W^\pm W^\pm jj-$EW sample is simulated with the POWHEG-BOX v2 event generator [96] interfaced to the PYTHIA 8.230 [83] parton shower model. Samples are generated at NLO accuracy in perturbative QCD, and the NNPDF3.0 PDF set is used in the matrix element at NLO. For the modeling of non-perturbative effects, the AZNLO set of tuned parameters [116] is used with the CTEQ6L1 PDF set [117]. The EVTGEN 1.2.0 program [92] is used for the b- and c-hadron decay properties. The QED emissions from electroweak vertices and charged leptons are modeled using PHOTOS++ 3.52 [90]. For this sample, the event generator cross section is used since it is already at NLO.

5.3.2 Background Samples

A number of different MC samples are needed to estimate the background processes in this analysis. The prompt background ($W^\pm W^\pm jj-$QCD, $WZjj$, $t\bar{t}+V$, $ZZjj$, VVV) is estimated entirely from MC samples, as is the $V\gamma$ background. All MC samples utilized during background estimation are described below and are grouped by process.

---

[10]The suboptimal color flow setting was not known when the decision was made to make SHERPA the nominal sample.

[11]The resonant triboson contributions become non-negligible at NLO in QCD [93].

$W^{\pm}W^{\pm}jj -$ QCD Sample

The $W^{\pm}W^{\pm}jj-$QCD sample is simulated using SHERPA 2.2.2. The order of the electroweak coupling is set to $\mathcal{O}(\alpha_{EW}) = 4$. The order of the strong coupling is not fixed and is determined automatically by SHERPA from the matrix element depending upon the number of jets in the final state. An algorithm is applied to match the real emission to the truncated parton shower [115]. The decays of taus are treated with the SHERPA parton shower algorithm. The NNPDF3.0 PDF is implemented at NNLO in QCD with $\alpha_S = 0.118$. The baseline choice for the μ_R-scale and μ_F-scale is defined per event as the matrix-element-level invariant mass of the WW system.

VV Samples

Diboson processes, where one of the bosons decays hadronically and the other decays leptonically, are simulated using the SHERPA 2.2.1 event generator [71]. Diboson processes with four charged leptons, three charged leptons and a neutrino, or two charged leptons and two neutrinos are simulated with the SHERPA 2.2.2 event generator with matrix elements that contain all diagrams with $\mathcal{O}(\alpha_{EW}) = 4$. All VV processes are calculated for up to three additional partons at LO and one additional parton at NLO using COMIX and OPENLOOPS [118]. They are merged with the SHERPA parton shower according to the ME+PS@NLO prescription [119]. In conjunction with a dedicated parton shower tune developed by the SHERPA authors, the NNPDF3.0nnlo PDF set is used.

VVV Samples

Events with three bosons (VVV with $V \in \{W^{\pm}, Z\}$) are simulated with SHERPA 2.1.1 using the CT10NLO PDF set as well as a dedicated set of tuned parton shower parameters developed by the SHERPA authors for v2.1.1. Matrix elements are generated with NLO accuracy in perturbative QCD for all combinations except WWZ, which is generated with LO accuracy. OPENLOOPS is used to evaluate loops in the NLO matrix element. Up to two additional partons are simulated in the final state with LO accuracy.

Top Samples

$t\bar{t}+W/Z$: Events which contain a $t\bar{t}$ pair produced with a boson (W,Z) are generated at NLO using MADGRAPH5_aMC@NLO [84] and are showered by PYTHIA 8.210. The NNPDF3.0nlo PDF set is used in the matrix element, while the NNPDF2.3lo PDF and A14 tune is used in the parton shower. A dynamic μ_R- and μ_F-scale is used, which is defined as $H_{\mathrm{T}}/2$, where H_T is the scalar sum of the p_T of all outgoing partons [111].

$t+W/Z$: $t+W$ events are generated using POWHEG-BOX v1, which uses the 4-flavor scheme for the NLO matrix element calculations together with the fixed four-flavor PDF set CT10f4. Alternatively, $t + Z$ events are generated using MADGRAPH5_aMC@NLO. For both $t + W$

events and $t + Z$ events, the top-quark spin correlations are preserved. For the t-channel events, top quarks are decayed using MADSPIN [91]. The parton shower, hadronization, and underlying event for both $t + W$ and $t + Z$ are simulated using PYTHIA 6.428 [120] with the CTEQ6L1 PDF set and the corresponding Perugia 2012 set of tuned parameters [121]. The top quark mass is set to 172.5 GeV, and the h_{damp} parameter, which controls the p_T of the first additional gluon emission beyond the Born configuration, is set to this top quark mass. The EVTGEN 1.2.0 program is used for properties of b- and c-hadron decays.

$t\bar{t}$: POWHEG-BOX v2 is used to generate $t\bar{t}$ events at NLO with the NNPDF3.0nlo PDF set in the matrix element. The parton shower, hadronization, and underlying event are simulated using PYTHIA 8.210 with the NNPDF2.3lo PDF set and A14 set of tuned parameters. The top mass (m_t) is set to 172.5 GeV and the h_{damp} parameter is set to $1.5 \times m_t$. The EVTGEN 1.2.0 program is used for properties of b- and c-hadron decays. Events are also passed through a filter which preferentially selects dilepton final states.

$V\gamma$ Samples

$V\gamma$ events are simulated using SHERPA 2.2.1 with $\mathcal{O}(\alpha_{EW}) = 3$. The events are calculated at LO accuracy for up to three partons and NLO accuracy for up to one parton using the CT10NLO PDF set. All off-shell contributions are taken into account. Electroweak $V\gamma$ events with associated jets ($V\gamma jj$−EW) are simulated using the SHERPA 2.2.4 event generator with the NNPDF3.0nnlo PDF set. The $V\gamma jj$−EW events are produced with $\mathcal{O}(\alpha_{EW}) = 5$ and an LO QCD accuracy.

V+jets Samples

W+jets: Events which contain a W boson and associated jets are simulated using the SHERPA 2.2.1 event generator. Matrix elements are calculated for up to four partons at LO and two partons at NLO using COMIX and OPENLOOPS. Events are merged with the SHERPA parton shower according to the ME+PS@NLO prescription. The NNPDF3.0nnlo PDF set is used in conjunction with dedicated parton shower tuning developed by the SHERPA authors. Events are normalized with NNLO cross sections.

Z+jets: Events which contain a Z boson and associated jets are generated using MAD-GRAPH5_aMC@NLO at LO in QCD for up to four additional partons and interfaced to PYTHIA 8.186 for the parton shower and underlying event modeling. The b- and c-hadron decays are corrected by EVTGEN v1.2.0. The matrix element calculation is performed with the NNPDF3.0nlo PDF set. The parton shower is modeled with the A14 PYTHIA tune and the NNPDF2.3lo PDF set.

Summary of all MC Samples

A summary of all the MC simulated samples used is presented in Table 5.2.

Process	Generator	Parton Shower	Tune	PDF Set
$W^{\pm}W^{\pm}jj-$EW	SHERPA 2.2.2	SHERPA 2.2.2	SHERPA default	NNPDF3.0
$W^{\pm}W^{\pm}jj-$EW	POWHEG-BOX v2	PYTHIA 8.230	AZNLO	NNPDF3.0
$W^{\pm}W^{\pm}jj-$QCD	SHERPA 2.2.2	SHERPA 2.2.2	SHERPA default	NNPDF3.0
$VV \to q\bar{q}ll$	SHERPA 2.2.1	SHERPA 2.2.1	SHERPA default	NNPDF3.0nnlo
$VV \to llll$	SHERPA 2.2.2	SHERPA 2.2.2	SHERPA default	NNPDF3.0nnlo
$VV \to lll\nu$	SHERPA 2.2.2	SHERPA 2.2.2	SHERPA default	NNPDF3.0nnlo
$VV \to ll\nu\nu$	SHERPA 2.2.2	SHERPA 2.2.2	SHERPA default	NNPDF3.0nnlo
$VVV, V = \{W^{\pm}, Z\}$	SHERPA 2.1.1	SHERPA 2.1.1	SHERPA default	CT10NLO
$t\bar{t}V$	MADGRAPH5_aMC@NLO	PYTHIA 8.210	A14	NNPDF2.3lo
$t + W$	POWHEG-BOX v1	PYTHIA 6.428	Perugia 2012	CTEQ6L1
$t + Z$	MADGRAPH5_aMC@NLO	PYTHIA 6.428	Perugia 2012	CTEQ6L1
$t\bar{t}$	POWHEG-BOX v2	PYTHIA 8.210	A14	NNPDF2.3lo
$V\gamma$	SHERPA 2.2.1	SHERPA 2.2.1	SHERPA default	CT10NLO
$V\gamma -$EW	SHERPA 2.2.4	SHERPA 2.2.4	SHERPA default	NNPDF3.0nnlo
$W+$jets	SHERPA 2.2.1	SHERPA 2.2.1	SHERPA default	NNPDF3.0nnlo
$Z+$jets	MADGRAPH5_aMC@NLO	PYTHIA 8.186	A14	NNPDF2.3lo

Table 5.2: Summary of the MC simulated samples utilized to estimate signal and background processes.

Chapter 6

Object Reconstruction

All ATLAS analyses depend upon the reconstruction of the digital signals read out from the detector into physics objects (tracks, electrons, jets, etc.). The techniques used to classify the physics objects pertinent to this analysis are described in this chapter.

First, the reconstruction of tracks and primary vertices[1] are discussed. Following this, details are provided regarding the reconstruction, identification, and isolation of muons, electrons, jets and missing transverse energy.

6.1   Track Reconstruction

The momentum and trajectory of each charged particle moving through the detector is described as a *track*. Tracks are reconstructed from measured space points (hits) in the pixel detector, the SCT, and the TRT. Hit points are grouped together to make seeds, and these seeds are then turned into tracks using the ATLAS tracking algorithms [122, 123].

The primary tracking algorithm is the inside-out method, which assumes that the tracks originate from the IP. Using this method, track seeds are constructed from three hits in the pixel detector layers and the SCT layers starting with seeds with only SCT hits, then seeds with only pixel detector hits, and finally seeds with hits in both the SCT and the pixel detector. Starting in Run-2, an additional requirement was added to the seed-building algorithm requiring one additional hit from a different detector layer to align with the seed. Once the track seeds have been determined, a combinatorial Kalman filter [124] is used to build track candidates from these seeds. These track candidates are built by incorporating hits from the unused pixel detector layers and SCT layers which align with the seed's preliminary trajectory.

Since the filter creates all realistic combinations of hits, a number of track candidates can exist with overlapping hits. As a result, track candidates are assigned a *track score* based on how precisely the hits align with the track candidate and whether or not the track has any

---

[1]Tracks and primary vertices are used to seed higher-level object reconstruction.

holes[2]. Using these track scores, an ambiguity solver filters out the poor track candidates. Once the collection of track candidates has been refined, each track candidate is extended into the TRT where a similar process is repeated with the new TRT hits. The result of the inside-out tracking algorithm is a final track collection where each track consists of a collection of hits identified as belonging to a single track pointing to the IP.

Once this algorithm is complete, a second tracking algorithm is executed with the remaining unused hits. This algorithm follows an outside-in method, where track candidates are constructed beginning with TRT hits and moving inward. This algorithm is designed to construct any secondary particles which do not originate from the IP. Figure 6.1 shows an example of tracks seeded using the inside-out method, and TRT track segments seeded using the outside-in method.
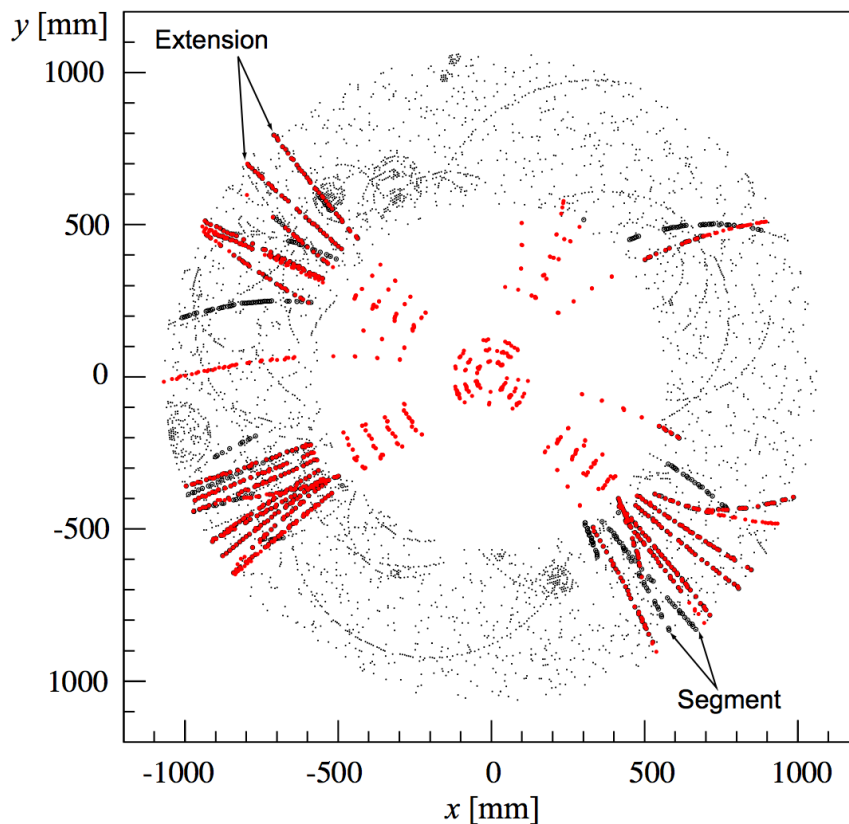
Figure 6.1: Transverse view of a $t\bar{t}$ event in the barrel region of the ID [122]. TRT hits are shown as small black dots. Inside-out seeded tracks that have been extended into the TRT are shown in red (extension). Outside-in track seeds are shown as the black circles (segment).

Reconstructed tracks are categorized into two track collections, *Loose* and *Tight Primary*,

---

[2]A track contains a hole if an intermediate layer is missing a hit when adjacent layers have hits recorded.

depending upon the track p_T, the track η, and the number of hits in the different sub-detectors. The track reconstruction efficiency for Loose and Tight Primary tracks is shown in Figure 6.2 as a function of p_T and η. The track reconstruction efficiency for Tight Primary tracks is between 80-90% at low η and high p_T, and drops off slightly at low p_T and high η. All tracks in this analysis are required to be Tight Primary tracks.
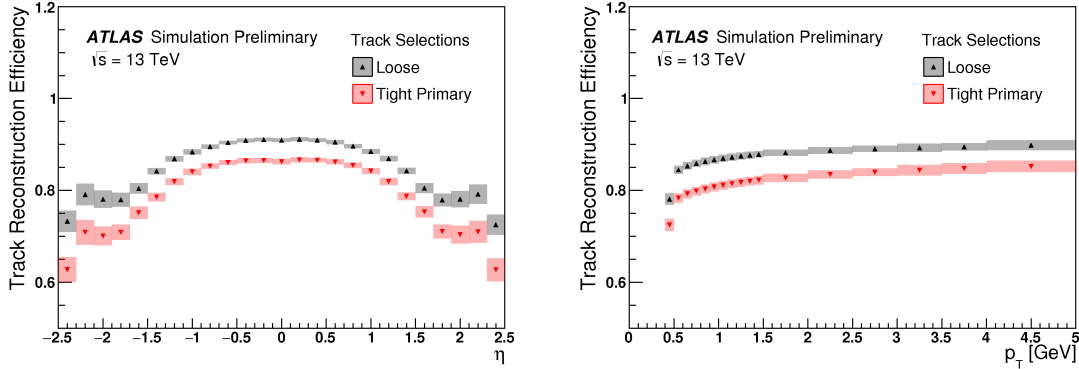
Figure 6.2: Track reconstruction efficiency for simulated Loose and Tight Primary tracks as a function of η (left) and p_T (right) [125].

All reconstructed tracks are described by five parameters, four of which are shown in Figure 6.3. These parameters are determined for each track when the track is fit, and they are measured at the point of closest approach to the beamline. The five parameters are:

- d_0: the transverse impact parameter[3]

- z_0: the longitudinal impact parameter[4]

- ϕ_0: the azimuthal angle of the trajectory

- $\cos\theta$: the cosine of the angle the track forms with the beam

- q/p_T: the charge of the track divided by the momentum in the transverse plane

Many of these track parameters are utilized when reconstructing/identifying the leptons and jets associated with these tracks.

---

[3]The distance of closest approach of the track to the primary vertex in the plane transverse to the beam.
[4]The z coordinate of the point of closest approach of the track to the primary vertex.
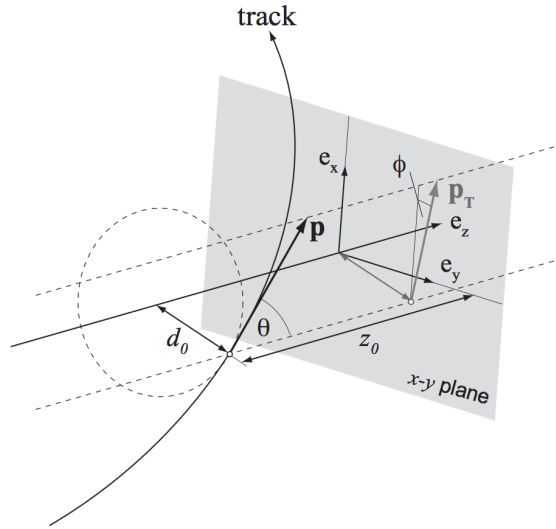
Figure 6.3: Depiction of four of the five track parameters used to describe each reconstructed track [126]. Shown here is the transverse impact parameter (d_0), the longitudinal impact parameter (z_0), the azimuthal angle of trajectory in the transverse plane (ϕ_0), and the trajectory angle measured with respect to the z axis (θ).

6.2 Primary Vertex Reconstruction

Since there are a high number of tracks that are reconstructed in a single event, a primary vertex (PV) reconstruction algorithm is used to determine which tracks originate from the same pp collision [127]. The primary vertices are reconstructed using an iterative fitting procedure. First, a set of tracks that satisfy a selection criteria is defined, and from these tracks a seed position for the first vertex is selected. These tracks and the seed position are then used to estimate the best vertex position with a χ^2 minimization algorithm. After the vertex position is determined, tracks that are incompatible with this vertex are removed and used to seed a new vertex. This process continues until all tracks are associated with a vertex.

Since there are several pp collisions that occur within each bunch crossing, it is likely that some tracks will be associated with vertices from pile-up events (secondary vertices) instead of the hard collision PV. In the combined 2015+2016 dataset, the average number of interactions per crossing ($< \mu >$) is 23.7 (see Figure 3.4), so reconstructing the PV is essential for determining which particles come from pile-up.

The PV is defined as the vertex with the highest track p_T^2. If a track isn't associated with the PV, it is typically considered pile-up. Figure 6.4 shows the number of tracks as a function of $< \mu >$ for 2016, demonstrating the importance of determining the PV.
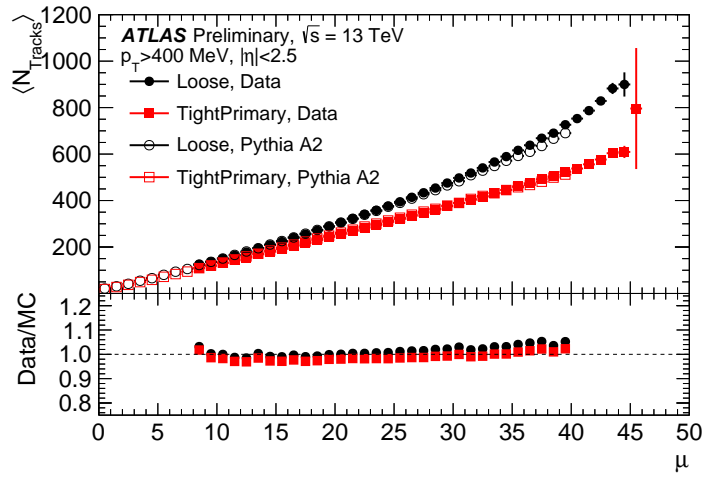
Figure 6.4: Number of tracks as a function of the average number of interactions per crossing for 2016 data [128]. Filled points are the 2016 data and open points are MC simulation.

6.3   Muons

Reconstruction and Identification

Muon reconstruction is performed independently in the ID and the MS [122, 129]. The information from the individual sub-detectors is then combined to form the reconstructed muon collections most commonly used in analyses. There are four *types* of reconstructed muons, which vary based on which sub-detectors are included in the reconstruction:

- **Combined (CB) Muon:** A muon reconstructed by combining track segments reconstructed independently in both the ID and MS while taking into account the energy loss from crossing the calorimeters. CB muons are reconstructed using primarily an outside-in method, starting with the MS track segments and extrapolating to ID track segments using a χ^2 method.

- **Segment-tagged (ST) Muon:** A muon reconstructed with tracks in the ID that cross only one layer of the MS, due to either having low p_T or because they fall in regions of reduced acceptance in the MS.

- **Calorimeter-tagged (CT) Muon:** A muon reconstructed with tracks in the ID that are matched to an energy deposit in the calorimeter that is compatible with a minimum-ionizing particle. CT muons have the lowest purity of the different muons, but they do recover detector acceptance in areas of the MS with limited geometric coverage.

- **Extrapolated (ME) Muon:** A muon reconstructed based only on MS track segments and a relaxed requirement regarding where the muon originates from with respect to the IP. ME muons are mainly used to extend the acceptance for muon reconstruction into the forward region, which is not covered by the ID ($2.5 < |\eta| < 2.7$).

When two muon types share the same ID track segment, preference is given first to CB muons, then ST muons, and lastly CT muons. If an ME muon overlaps with another muon type in the MS, the track with the better track fit quality and larger number of hits is selected.

Muon reconstruction efficiency is determined using a tag-and-probe method with two stages. The first stage has a CB muon as the tag, and the probe is a CT muon. This efficiency is then corrected by the efficiency of the ID reconstruction where ID tracks are the tag and MS tracks are the probe. The overall reconstruction efficiency is the product of these two efficiencies. Figure 6.5 shows the muon reconstruction efficiency for *Medium* muons as a function of p_T and η. *Medium* refers to the muon identification category.

There are four generic muon identification categories which apply various hit and momentum requirements on the muons: Loose, Medium, Tight, and High p_T. The Medium identification efficiency for prompt muons from W decays with p_T between 4-20 GeV (20-100 GeV) is 95.5% (96.1%). A full description of the different muon identification types can be found in Ref. [129].

The muon reconstruction efficiency is at or above 98% for Medium muons with $|\eta| > 0.1$. In the region $|\eta| < 0.1$, the reconstruction efficiency for Medium muons drops to roughly 62%. This drop is due to reduced detector acceptance since the services for the ID and calorimeter are located in this area. By reducing the muon identification selection from Medium to Loose in this low η range, the muon reconstruction efficiency can be increased to above 95%.

The level of agreement of the measured efficiency (ϵ_{data}) compared to the efficiency in simulation (ϵ_{MC}) is expressed as the efficiency scale factors: $SF = \epsilon_{data}/\epsilon_{MC}$. These scale factors are then applied to the simulation to make sure that the muons are reconstructed with the same efficiency that they are reconstructed with in the data. The SFs are calculated in bins of p_T and η using $J/\psi \rightarrow \mu\mu$ and $Z \rightarrow \mu\mu$ events [129].
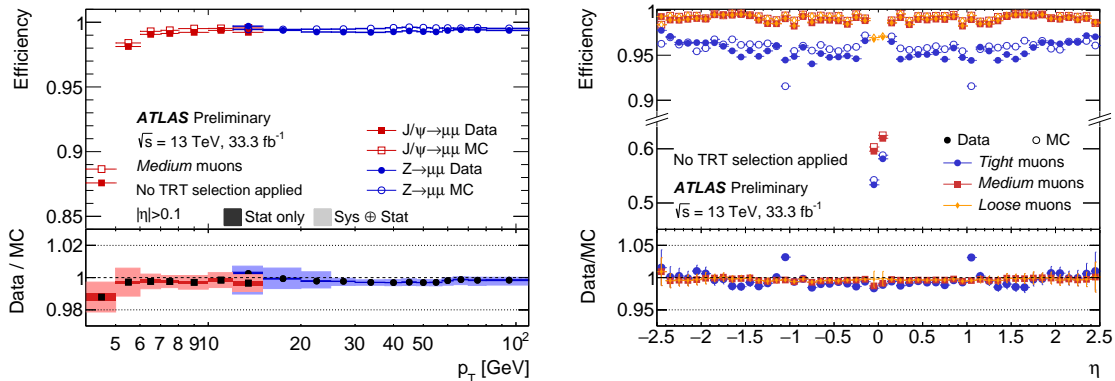
Figure 6.5: *Left:* Reconstruction efficiency for Medium muons as a function of muon p_T [130]. *Right:* Reconstruction efficiency for Medium muons as a function of η [130]. Also shown is the reconstruction efficiency for Loose muons in the region $|\eta| < 0.1$ where the efficiency for Loose muons and Medium muons differs significantly.

Isolation

In addition to reconstruction and identification, the isolation of each muon is also categorized. Isolation variables are primarily used to reject leptons which are not produced by the initial pp hard scattering. A series of isolation working points are determined by measuring and placing a requirement on (1) the amount of energy deposited near the track in the calorimeter, and (2) the sum of any p_T near the muon track from other tracks. There are four working points: *Tight* and *Loose* (which are defined to reach a specific, flat isolation efficiency), and *Gradient* and *GradientLoose* (which target varying isolation efficiencies depending upon track p_T). Figure 6.6 shows the isolation efficiency for the Gradient working point as a function of muon p_T for data and MC.

Analysis Selections

All selected muons are CB muons. The selected muons are required to pass Medium identification requirements. When an isolation requirement is applied on muons, the Gradient working point is used.
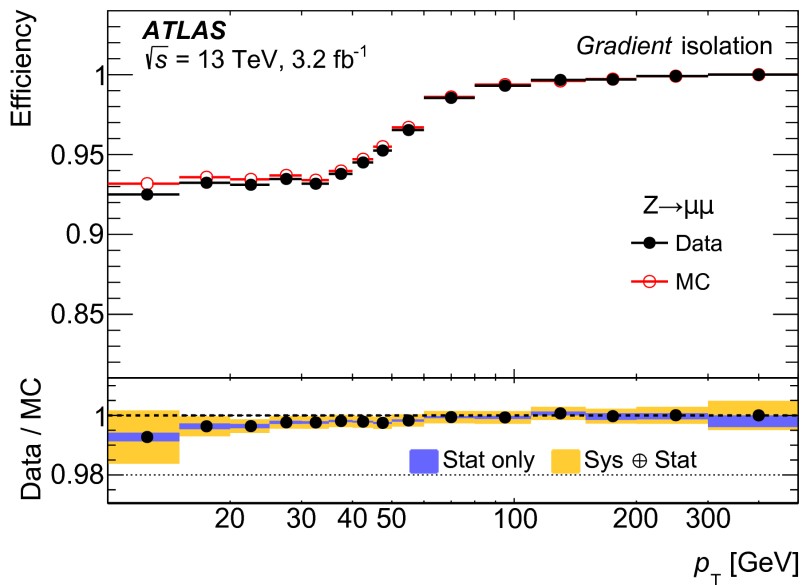
Figure 6.6: Isolation efficiency for the Gradient muon isolation working point shown as a function of the muon transverse momentum (p_T) [129]. Efficiency is measured using $Z \to \mu^+\mu^-$ events in data and MC.

6.4 Electrons

Reconstruction

Electrons are reconstructed using three main data points: clusters of energy in the EM calorimeter, ID tracks, and the matching of ID tracks to clusters in $\eta \times \phi$ space.

To determine clusters of energy in the EM calorimeter, the EM calorimeter is divided into a grid of 200×256 elements (towers) of size $\Delta\phi \times \Delta\eta = 0.025 \times 0.025$. This grid corresponds to the granularity of the second layer of the calorimeter (see Section 3.2.3.1). For each element, the energy deposited in each layer of the EM calorimeter is summed and associated with that element. The EM energy clusters are then determined by applying a sliding-window algorithm [131] to 3×5 towers in $\eta \times \phi$.

Once the EM clusters have been determined, tracks are reconstructed in the ID and extended into the calorimeter. Then, EM clusters and ID tracks are matched using requirements including $|\eta_{cluster} - \eta_{track}| < 0.05$ and $-0.10 < q \times \Delta(\phi_{cluster}, \phi_{track}) < 0.05$. A more detailed description of the ATLAS electron reconstruction method can be found in Ref. [132]. Figure 6.7 shows the electron reconstruction efficiency (relative to the reconstructed clusters) for $Z \to ee$ events as a function of the electron transverse energy, E_T. As with muon reconstruction, the electron reconstruction scale factors are determined using the tag-and-probe method using $Z \to ee$ events.

As shown in Figure 6.7, the electron reconstruction efficiency in collision data and MC

simulated events is greater than 97% for all values of transverse energy.
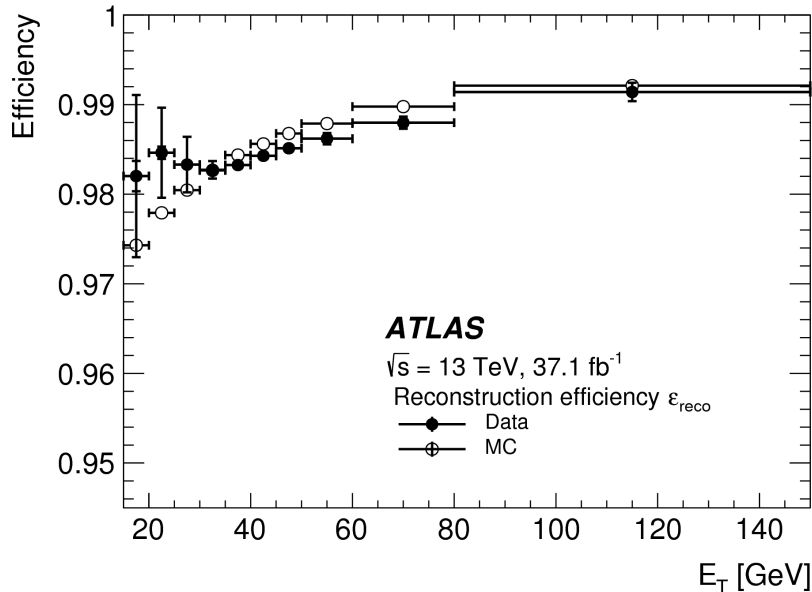
Figure 6.7: Reconstruction efficiency for electrons as a function of the electron transverse energy, E_T, for $Z \to ee$ data and MC events [132].

Identification

As was the case with muons, electron candidates are divided into four identification categories (*Very Loose, Loose, Medium, Tight*) based on quality requirements such as ID hit requirements, shower shape, and track quality. A detailed description of the four likelihood-based (LH) identification categories can be found in Ref. [132]. Figure 6.8 shows the LH electron identification efficiencies for Loose, Medium, and Tight electrons as a function of E_T (left) and η (right). Typical efficiency for the Tight selection is between 55% and 90%, while for the Medium selection the efficiency is between 75% and 95%.
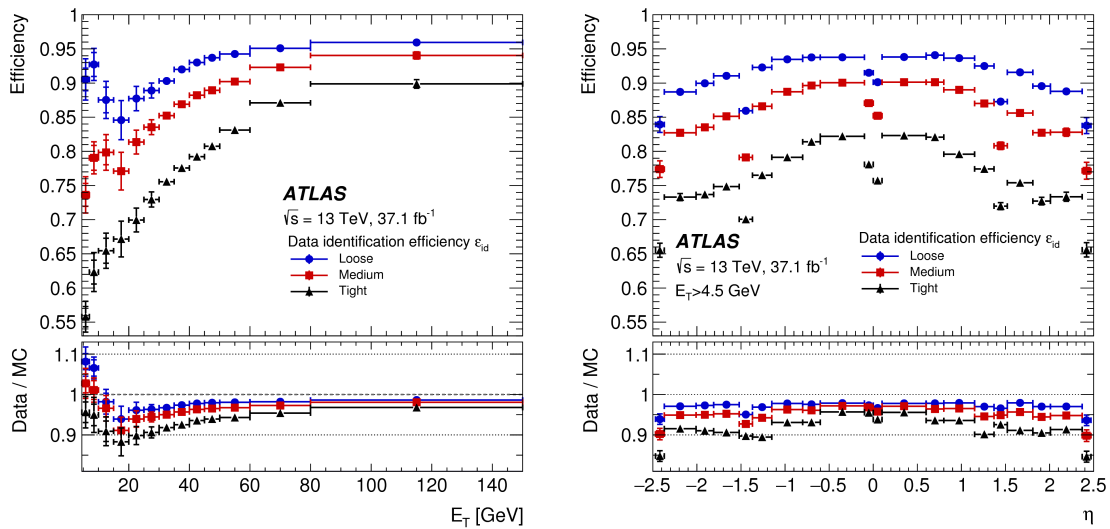
Figure 6.8: Electron LH identification efficiencies as a function of electron transverse energy, E_T, (left) and η (right) for $Z \rightarrow ee$ events measured in data and MC [132]. Efficiencies of Loose, Medium, and Tight electrons are shown.

Isolation

Electron isolation working points fall into three categories: *Loose isolation,* which targets the same fixed isolation efficiency for all p_T and η; *Gradient isolation*, which targets a fixed isolation dependent on the electron p_T but is flat in η; and *Fixed isolation*, which applies a set cut on the variables used to determine the isolation, regardless of the resulting efficiency. Within these categories, several more specific working points are defined. A complete description of the different isolation working points can be found in Ref. [132]. Figure 6.9 shows the isolation efficiency for two Loose isolation working points and two Gradient isolation working points as a function of E_T. The Gradient working point efficiency drops to 90% at low E_T, whereas the Loose working point efficiency remains above 95% at low E_T.
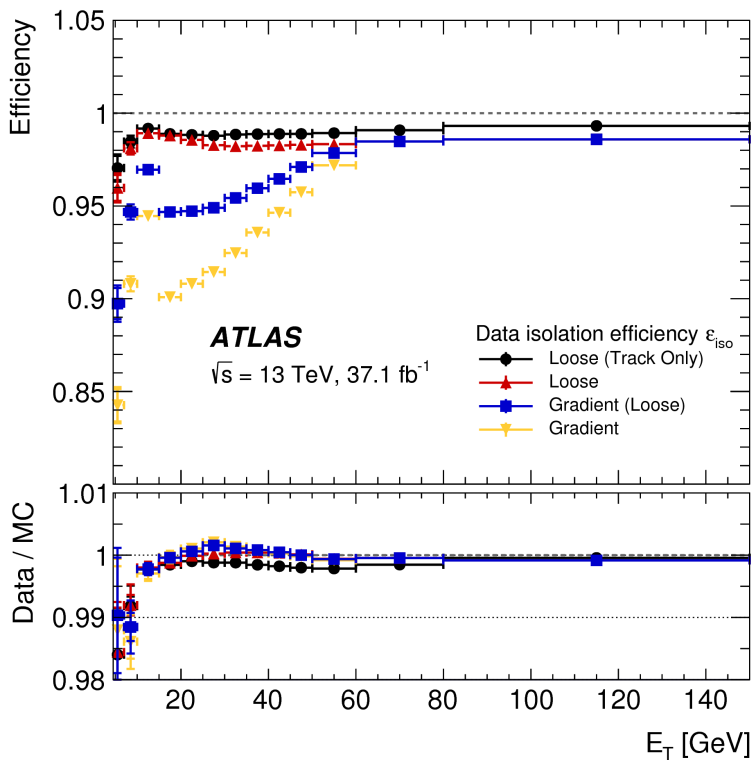
Figure 6.9: Isolation efficiency in data for two Gradient isolation working points and two Loose isolation working points shown as a function of the electron transverse energy (E_T) [132]. Lower panel shows the ratio of the efficiency measured in data compared to MC. Efficiency is measured using $Z \to ee$ events.

Analysis Selections

In this analysis, two of the four electron identification working points are utilized: Tight (for nominal signal region electrons) and Medium (for non-prompt background estimation). As was the case for muons, when isolation requirements are applied to electrons, the Gradient working point is used.

6.5   Jets

Jet reconstruction[5] begins by forming *topo-clusters* from energy deposits in the EM and hadronic calorimeters [133]. Topo-clusters are topological clusters that are formed by grouping cells with neighboring cells where the energy deposited in said cells is significantly more

---

[5]The jet reconstruction described in this section follows the standard ATLAS collaboration procedure for jets.

than the expected noise. Each cluster is seeded with a cell with a signal-to-noise ratio greater than four; neighboring cells are then added to the cluster if their signal-to-noise ratio is larger than two [134]. This is repeated until there are no such cells remaining. The center of the cluster is taken as the energy-weighted average of all the cells.

Jets are then formed by combining clusters using an anti-k_t algorithm [135] with a radius parameter of $R = 0.4$. The algorithm works by comparing the distances between clusters to the distance between a primary cluster (cluster with the highest transverse energy) and the beam. The radius parameter R is used to restrict the size of the jets. Figure 6.10 shows the mean topo-cluster multiplicity per jet as a function of jet p_T (left) and η (right). After the jets are formed, the origin of the jet is corrected such that the four-momentum of the jet points to the PV instead of the center of the detector (while keeping the jet energy constant). This correction improves jet η resolution.
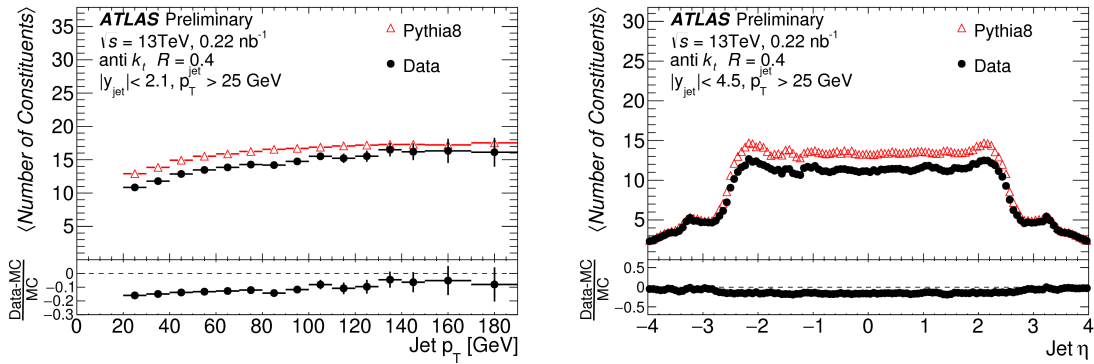
Figure 6.10: Mean topo-cluster multiplicity in a jet as a function of jet p_T (left) and jet η (right) [136].

Next the jets must be corrected to remove the contribution of pile-up to the jet p_T [133]. This is done using an area-based method where, for each event, the pile-up contribution to the jet p_T is subtracted according to its area. The pile-up contribution, ρ, is defined as the energy density in the event calculated from all positive-energy topo-clusters with $|\eta| < 2$ that are clustered using the anti-k_t algorithm with R=0.4. The area, A, of each jet is determined using ghost association. Ghost association is where simulated ghost particles of infinitesimal momentum are added to the event uniformly in solid angle before jet reconstruction. Then, A is measured by comparing the number of ghost particles associated with the jet after clustering relative to before clustering. Thus, the jet p_T is corrected by subtracting $\rho \times A$.

There is, however, a residual correction that needs to be applied due to the fact that the ρ calculation does not take into account the sensitivity to pile-up in the forward calorimeters or in the core of high-p_T jets. This residual correction, derived from simulation, is dependent upon the number of reconstructed primary vertices (N_{PV}) in the event and the instantaneous luminosity of the event.

The impact of the area-based correction and the residual correction on the dependence of jet p_T on *in-time*[6] pile-up and *out-of-time*[7] pile-up can be seen in Figure 6.11. The dependence is shown as a function of η for simulated jets with $p_T = 25$ GeV. After both corrections are applied, the dependence is approximately zero in all η bins.
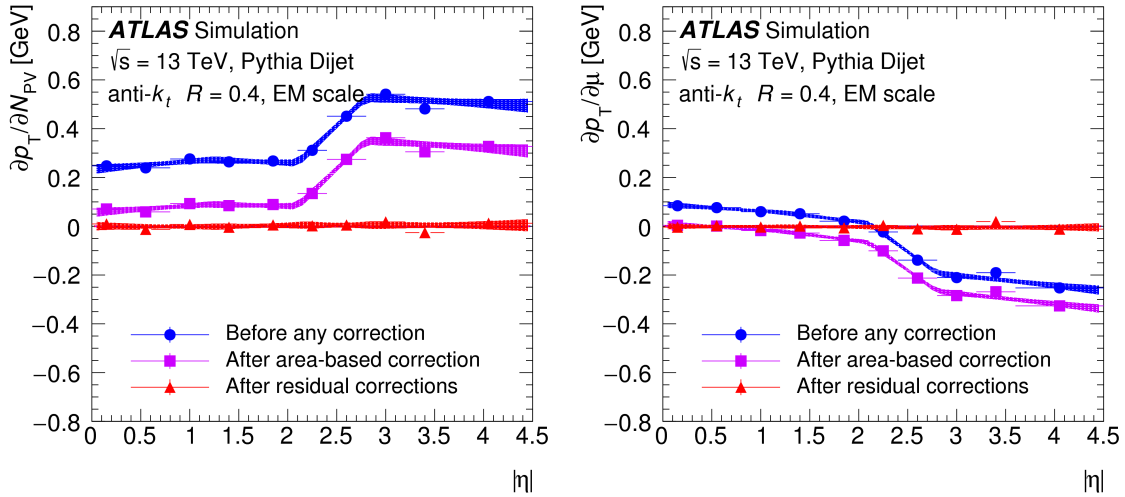
Figure 6.11: Dependence of jet p_T on in-time pile-up (left) and out-of-time pile-up (right) as a function of jet $|\eta|$ for simulated jets with $p_T = 25$ GeV before any pile-up corrections, after the area-based corrections, and after the residual correction [133].

In addition to removing the pile-up contribution, the jet energy scale (JES) is corrected using two types of calibrations: *absolute* and *in-situ*. The absolute calibration corrects the reconstructed jet momentum to the particle-level energy scale, while the *in-situ* calibration corrects for differences in jet response between data and MC.

The absolute calibration used for this analysis, referred to as EM+JES, starts with treating every cluster as an electromagnetic (EM) shower. A correction is then applied based on the measured jet energy at the EM scale. This correction is determined using MC by comparing the energy of a reconstructed jet (E^{reco}) to the energy of the corresponding *truth* jet (E^{truth}). A truth jet is a jet formed using the same clustering algorithm, except instead of using the calorimeter-measured energy deposits, the true energy of the simulated particles is used as input. Figure 6.13 shows the average energy response in the full ATLAS simulation, where the average energy response is defined as the mean of a Gaussian fit of the E^{reco}/E^{truth} distribution for jets. The absolute JES calibration factor is taken as the inverse of the average energy response [138]. The absolute calibration also applies a correction to

---

[6]*In-time pile-up* refers to additional pp collisions occurring in the same bunch-crossing as the collision of interest [137].

[7]*Out-of-time pile-up* refers to additional pp collisions occurring in the bunch-crossings just before and after the collision of interest, which can impact the signal in the collision of interest [137].

the jet η, which corrects for the difference between η^{reco} and η^{truth}. This correction is derived using the same method as the energy correction.
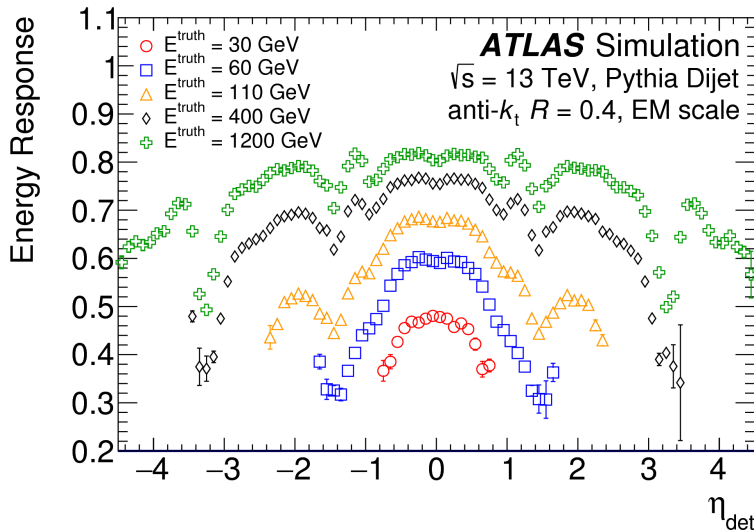
Figure 6.12: The average energy response as a function of η_{det} (the jet η pointing from the geometric center of the detector instead of the IP) for jets with different truth energies (E^{truth}) [133]. Origin and pile-up corrections have already been applied. The drops in average energy response at certain η_{det} occur at gaps/transitions in the calorimeter sub-detectors.

The *in-situ* calibration corrects for differences in jet response between data and MC. These corrections are derived using various techniques which measure jet energy indirectly in events where a jet balances against one or more different, well-measured objects:

- Jets with $|\eta| < 0.8$ and $p_T < 950$ GeV are balanced against photons or Z bosons which decayed leptonically.

- Jets with $0.8 < |\eta_{det}| < 4.5$ are balanced against well-measured jets with $|\eta_{det}| < 0.8$[8].

- Jets with $|\eta| < 1.2$ and 30 GeV $< p_T < 2$ TeV are balanced against several lower p_T jets.

A full description of these various *in-situ* calibration processes can be found in Ref. [133]. For each *in-situ* calibration, the jet response is defined in data and MC as the average ratio of jet p_T to reference-object p_T, binned in reference-object p_T. The data-to-MC ratio of jet response is used to determine the calibration factor. The data-to-MC ratios of these different corrections are combined across overlapping regions of jet p_T into a single ratio using the method described in Ref. [138]. Figure 6.13 shows the final derived data-to-MC ratio as a function of jet p_T with the original ratios from a few of the specific methods shown with

---

[8]η_{det} is the jet η calculated with respect to the center of the detector instead of the IP.

their original binning. The inverse of the combined data-to-MC ratio is taken as the *in-situ* correction that is applied to data. At low p_T (30 GeV), the combined correction is roughly 4% and decreases to 2% for jets with $p_T = 2$ TeV.
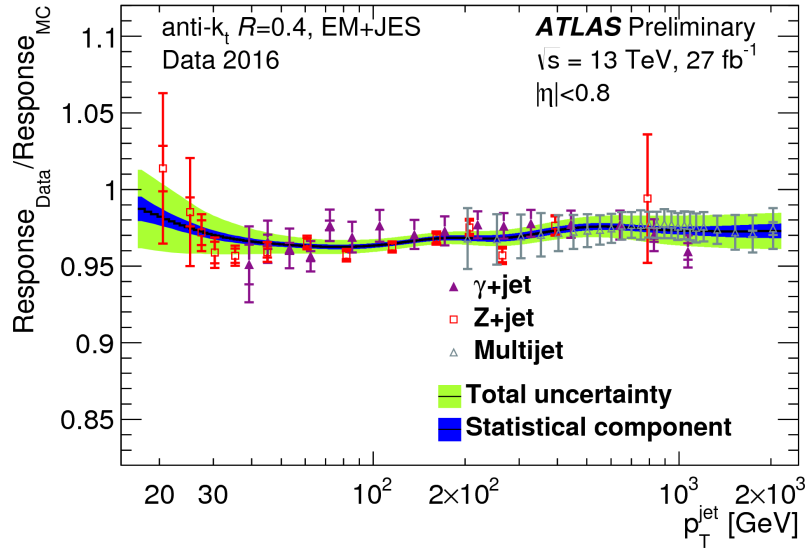
Figure 6.13: Data-to-MC ratio of the EM+JES jet response as a function of jet p_T for three different *in-situ* calibrations [139]. The final derived correction is shown as the black line. Bands for statistical (dark blue) and total (light green) uncertainty are also shown.

The methods outlined thus far in this section introduce a number of systematic uncertainties, which are collectively referred to as the JES uncertainty (see Section 11.2).

6.5.1 *b*-tagged Jets

Jets that contain a *b*-quark, referred to as *b*-jets or *b*-tagged jets, can be distinguished from jets that contain only light quarks using the long lifetime of *b*-hadrons [140, 141]. The average lifetime of a *b*-hadron is approximately 1.5 ps, which corresponds to a decay length that is long enough to distinguish the *secondary* vertex for the *b*-hadron decay from the PV [26]. This secondary vertex can be reconstructed and used to identify jets that contain a *b*-quark. ATLAS uses a combination of several algorithms to identify *b*-jets:

- **IP3D:** An impact-parameter-based algorithm that uses all the tracks associated with the jet. Tracks generated from *b*-hadron decays tend to have large impact parameters which allow their contributions to be separated from that of tracks from the PV. The algorithm uses the impact parameters' significance ($\frac{d_0}{\sigma_{d_0}}$ and $\frac{z_0}{\sigma_{z_0}}$), measured in simulation, to determine the likelihood that a track originates from a *b*-jet.

- **SV1:** A secondary vertex finding algorithm. All track pairs within the jet are tested for a two-track vertex[9]. If the two-track vertex appears to be from the decay of a long-lived particle (e.g., K_s), it is removed. A single vertex is then fit using the tracks from all remaining two-track vertices, and the track with the worst fit is removed. This is repeated until all outlier tracks are removed and the overall χ^2/DOF of the track fit to the vertex passes a quality threshold.

- **JetFitter:** This algorithm attempts to find an axis and decay position of the b-hadron. The algorithm uses a Kalman filter starting with the axis from the PV and tries to find a common line with the b- and c-vertices, which approximates the b-hadron flight path and position. This approach allows for the b-vertex to be determined even if there is only one track attached to the vertex.

The results from these three algorithms are combined into a single multivariate discriminant using a Boosted Decision Tree (BDT) with the MV2 b-tagger [140]. The BDT is trained using b-jets as signal, and c-jets and light-flavor jets as background. Since c-hadrons also have sufficiently long lifetimes to lead to reconstructible secondary vertices, the ability to reject c-jets is also important. As a result, in order to enhance the c-jet rejection, the c-jet fraction in the training is set to 7%, and the light-flavor jet background is set to 93%. The resulting b-tagger algorithm, referred to as MV2c10[10], is the b-tagging discriminant used in this analysis. Figure 6.14(left) shows the MV2c10 BDT output for the signal (b-jet) and background (c-jet, light-jet) components.

Different working points are chosen to provide a specific b-jet efficiency (measured using a $t\bar{t}$ sample) by applying a single cut on the MV2c10 BDT output value. The working points correspond to selecting b-jets with an efficiency of 60%, 70%, 77%, and 85%. Figure 6.14(right) shows the c-jet and light-flavor jet rejection rates as a function of the b-tagging efficiency of the MV2c10 algorithm. The rejection rates for light-flavor jets and c-jets are defined as the inverse of the efficiency for tagging a light-flavor jet as a b-jet, or a c-jet as a b-jet, respectively. In this analysis, jets are b-tagged with the 85% efficiency working point.

---

[9]A two-track vertex is a vertex constructed from two tracks.

[10]The naming convention for MV1 from Run-1 was such that for MV1cXX, the XX referred to the c-jet fraction used during training. In Run-1, the MV1c10 tagger had a 10% c-jet fraction. The value in Run-2 was optimized resulting in a 7% fraction, however the naming convention was not changed for simplicity.
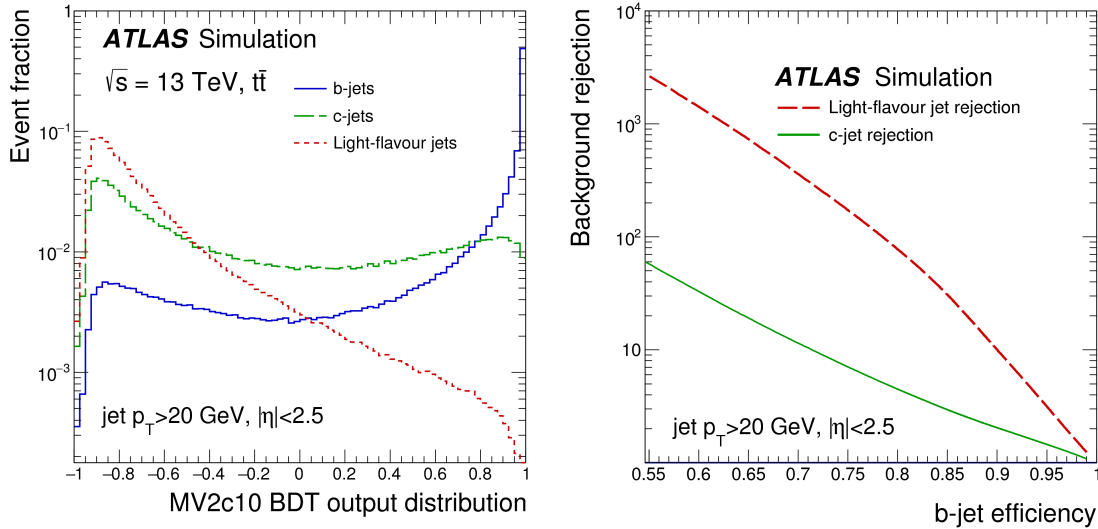
Figure 6.14: *Left:* MV2c10 BDT output for *b*-jets, *c*-jets, and light-flavor jets evaluated using $t\bar{t}$ events [140]. *Right:* *c*-jet and light-flavor jet rejection rate as a function of the *b*-tagging efficiency of the MV2c10 *b*-tagging algorithm [142]. The rejection rates for light-flavor jets and *c*-jets are defined as the inverse of the efficiency for tagging a light-flavor jet as a *b*-jet, or *c*-jet as a *b*-jet, respectively. The performance was evaluated using simulated $t\bar{t}$ events.

6.6   Missing Transverse Momentum

In the plane transverse to the beam, momentum is conserved, which means that the transverse momenta of all final state particles should effectively sum to zero. The same cannot be said for the longitudinal plane, where particles can move collinear to the beamline and not interact with the detector. If there is an imbalance in the transverse momenta, it may indicate that particles which are invisible to the detector were produced in the collision (e.g., neutrinos). Any measured imbalance in the transverse momenta is referred to as missing transverse energy (E_T^{miss}).

E_T^{miss} is constructed using two signals [143]. The first signal is from *hard events*, meaning fully reconstructed and calibrated electrons, muons, taus, photons, and jets. The second signal is from what are called *soft events*. Soft events refer to any reconstructed charged particle tracks that are associated with the hard-scatter vertex but are not associated with any of the previously mentioned hard events, or more clearly, the unused tracks.

For the E_T^{miss} calculation, muons are reconstructed from ID and MS tracks; electrons and taus are identified using combined calorimeter and tracking information. Photons and jets are primarily reconstructed from calorimeter signals at the EM scale. More details about the definition of E_T^{miss} terms can be found in Ref. [143]. Figure 6.15 shows the E_x^{miss} and E_y^{miss} resolution as a function of the sum of all the transverse energy in the event.
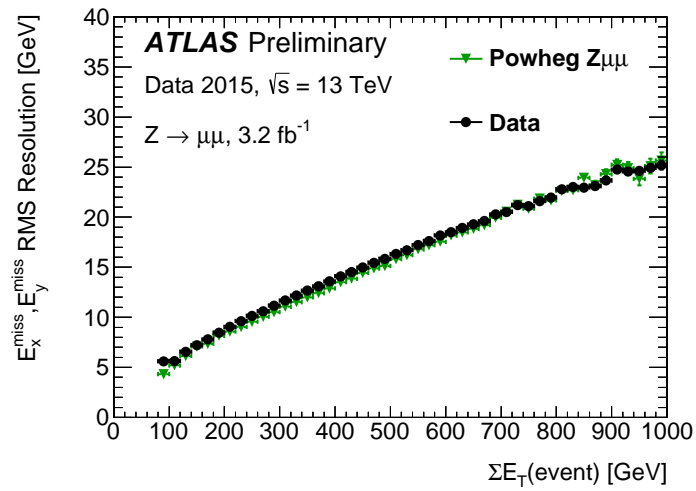
Figure 6.15: Resolution of $E_{x(y)}^{miss}$ in bins of the sum of transverse energy for $Z \to \mu\mu$ MC simulated events and $Z \to \mu\mu$ data events collected in 2015 [144].

Chapter 7

Event Selection

This analysis is performed on the 2015+2016 pp collision dataset with $\sqrt{s} = 13$ TeV measured by the ATLAS detector. Events are required to pass standard data quality requirements that ensure the detector was fully operational. Periods of data-taking which pass the standard data quality requirements are listed in a *Good Runs List (GRL)*. The GRL is used to evaluate which events are suitable for analysis. In 2015 (2016), the GRL removed 12 (7.1)% of the data recorded by the ATLAS detector. After these selections, the data set corresponds to an integrated luminosity of 36.1 fb^{-1} with an uncertainty of 2.1% [145].

This chapter describes how events from this 36.1 fb^{-1} data set are selected for analysis. First, the preselection requirements applied prior to the analysis selections are introduced. Following this, the process of removing the overlap between reconstructed objects is discussed, and the analysis triggers utilized are detailed. Next, the requirements on individual objects within the event (electrons, muons, jets) are described. Finally, the analysis selections defining the signal region and validation regions are outlined.

7.1 Preselection

Before entering into the analysis event selection chain, events are required to meet some preselection requirements. These preselections, described below, include several *event cleaning* requirements and relaxed object kinematic requirements.

Event Cleaning Requirements

A number of cleaning cuts are applied to events to select a high-quality sample of pp collision events. These requirements include:

- Remove events flagged as *bad* due to problems in the calorimeters.

- Veto incomplete events missing information from a sub-detector.

- Remove events impacted by an upset in the SCT.

- Remove events which contain *noisy* cells in the Electromagnetic Endcap Calorimeter (EMEC).

- Remove events with selected jets which are identified as *bad* due to detector problems or interference from beam background.

- At least one vertex in the event must be reconstructed from at least three tracks with $p_T > 0.5$ GeV to reduce the impact of pile-up.

Since these requirements are applied on an event-by-event basis, they are not included in the GRL. The GRL only indicates poor data quality in approximately 60-sec intervals (a lumiblock).

Relaxed Object Kinematic Requirements

In addition to the event cleaning cuts, preselection requirements are imposed on leptons and jets:

Electrons: Electrons are required to have a $p_T > 6$ GeV and $|\eta| < 2.47$. The impact parameters must satisfy $|z_0 \sin\theta| < 0.5$ mm and $\frac{d_0}{\sigma_{d_0}} < 5$. There are no isolation requirements imposed, but the electron is required to pass the LooseLH identification requirement with an additional hit in L0 of the pixel detector.

Muons: Muons are required to have a $p_T > 6$ GeV with $|\eta| < 2.7$. The impact parameters must satisfy $|z_0 \sin\theta| < 0.5$ mm and $\frac{d_0}{\sigma_{d_0}} < 10$. There is also no isolation requirement for muons, and the muon must pass the Loose identification requirements.

Jets: Jets are required to have have $|\eta| < 4.5$, with two p_T requirements within this region. Central jets with $|\eta| < 2.4$ are required to have a $p_T > 25$ GeV, while more forward jets ($2.4 < |\eta| < 4.5$) must have $p_T > 30$ GeV. During preselection, jets within the central region ($|\eta| < 2.5$) are *b*-tagged using the MV2c10 algorithm (see Section 6.5.1). Jets are defined as *b*-tagged if the MV2c10 output (see Figure 6.14) is larger than 0.1758475. This value corresponds to the 85% *b*-jet efficiency working point.

By applying these lepton/jet preselections, events with no possible significance are removed. This act reduces the size of the data set and lessens the analysis processing time.

7.2 Object Overlap Removal

After preselection, an object overlap removal procedure is applied to the data. This procedure removes potential duplications due to the same object being reconstructed by two (or more) reconstruction algorithms, i.e., an object is reconstructed as two different leptons or as a lepton and a jet. Different removal conditions are applied in each of these cases. Lepton-lepton overlaps are resolved first, followed by lepton-jet overlaps. The overlap removal procedures in these different cases are:

Lepton-Lepton Overlap Removal

electron-electron: Two electrons are defined as overlapping if they are reconstructed from objects that have an overlapping EM cluster or share an ID track. If this occurs, the electron with the higher p_T is kept while the other electron is removed from the event.

electron-muon: An electron and a muon are defined as overlapping if they share an ID track. This can occur if the muon radiates an FSR high-energy photon. If the muon is not tagged as a muon in the MS, the electron is kept. Otherwise, the muon is saved and the electron is removed.

muon-muon: No muon-muon overlap removal procedure is applied.

Lepton-Jet Overlap Removal

The identification and removal of b-tagged jets plays an important role in this analysis. As a result, a lepton-jet overlap removal procedure that gives precedence to b-tagged jets is utilized.

electron-jet: If the separation between an electron and the center of a jet meets the requirement $\Delta R_{e,j} < 0.4$, the objects are defined as overlapping. If the jet is not b-tagged and the electron is quite close to the center of the jet ($\Delta R_{e,j} < 0.2$), the jet is removed from the event and the electron is kept. However, if the jet is b-tagged, the electron is removed from the event and the jet is kept. If the electron-jet separation is between 0.2 and 0.4 ($0.2 < \Delta R_{e,j} < 0.4$), the electron is removed from the event and the jet is kept.

muon-jet: The muon-jet overlap procedure is the same as the electron-jet procedure, with one additional requirement. In addition to the procedure described above, the muon is checked to see if it is associated to the jet as a ghost particle [146]. If the jet contains a ghost-associated muon and has less than three tracks in the jet, the jet is removed.

7.3 Analysis Triggers

The final state of $W^{\pm}W^{\pm}jj-$EW production contains two leptons. Therefore, single electron and single muon triggers are used to select events with electrons and muons. In a number of ATLAS analyses, dilepton triggers[1] are utilized in conjunction with single lepton triggers to gain in trigger efficiency for low p_T leptons. Including dilepton triggers in this analysis was considered, but it was found unnecessary as the p_T of the W bosons in the $W^{\pm}W^{\pm}jj$ events was sufficiently high such that the resulting leptons met the p_T threshold of the single lepton triggers.

7.3.1 Single Electron Triggers

The logical OR of three different single electron triggers is utilized. The trigger scheme was slightly different for the 2015 data and 2016 data, so different electron triggers are used for the data collected in 2015 and the data collected in 2016. The three triggers used in 2015 are:

- **HLT_e24_lhmedium_L1EM20VH:** An electron trigger requiring electron $E_T > 24$ GeV and passing the mediumLH identification requirement. This HLT is seeded by L1 trigger L1EM20VH, which requires at L1 the electron $E_T > 20$ GeV with hadronic cone isolation requirements[2] (H) and an η requirement which varies depending upon the energy loss (V).

- **HLT_e60_lhmedium:** An electron trigger requiring electron $E_T > 60$ GeV and passing the mediumLH identification requirement. This HLT is seeded by L1 trigger L1EM22VHI, which requires at L1 the electron $E_T > 22$ GeV with hadronic cone isolation requirements (H), electromagnetic isolations (I), and an η requirement which varies depending upon the energy loss (V).

- **HLT_e120_lhloose:** An electron trigger requiring electron $E_T > 120$ GeV and passing the looseLH identification requirement. This HLT is also seeded by L1 trigger L1EM22VHI.

The efficiency of the HLT_e24_lhmedium_L1EM20VH trigger in data as a function of the electron E_T can be seen in Figure 7.1(left). In this figure the efficiency of a similar trigger in MC is also shown.

In 2016 a slightly different ATLAS trigger scheme was introduced, resulting in three different single electron triggers being applied:

---

[1]Dilepton triggers are designed to select events which contain two leptons.

[2]This requirement is a veto against energy deposited in the hadronic calorimeter behind the electron candidate's EM cluster.

- **HLT_e26_lhtight_nod0_ivarloose:** An electron trigger requiring electron $E_T > 26$ GeV and meeting the tightLH identification requirement assessed with no d_0 requirements but applying a loose variable-size p_T/E_T cone isolation. This trigger is seeded by L1 trigger EM22VHI, which requires at L1 the electron $E_T > 22$ GeV with an η requirement that varies with the energy loss (V), a hadronic cone isolation requirement (H), and an electromagnetic isolation requirement (I).

- **HLT_e60_lhmedium_nod0:** An electron trigger requiring electron $E_T > 60$ GeV and passing the mediumLH identification requirement assessed with no d_0 requirements. This trigger is also seeded by L1 trigger EM22VHI.

- **HLT_e140_lhloose_nod0:** An electron trigger requiring electron $E_T > 140$ GeV and meeting the looseLH identification requirement assessed with no d_0 requirements. This trigger is also seeded by L1 trigger EM22VHI.

The efficiency of the logical OR of these three triggers is shown in Figure 7.1(right) as a function of the electron E_T for 2016 data and MC.
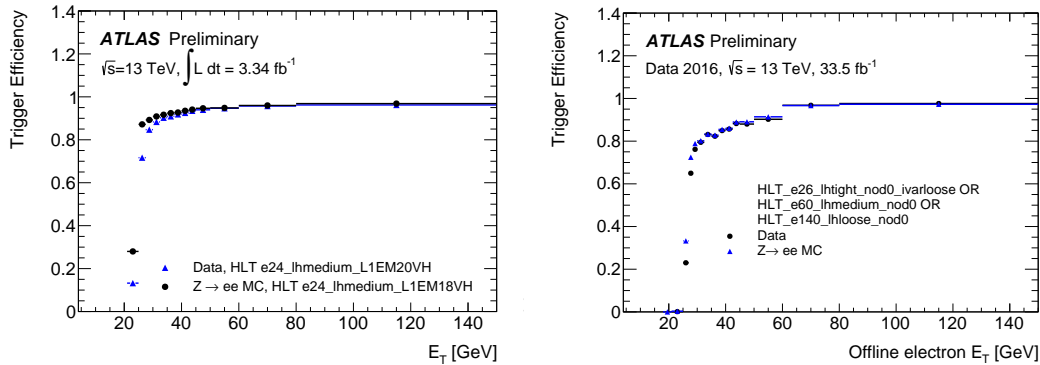
Figure 7.1: *Left:* Efficiency of the HLT_e24_lhmedium_L1EM20VH trigger as a function of the reconstructed electron candidates' transverse energy, E_T [147]. The efficiency was measured with a tag-and-probe method using $Z \to ee$ decays from data collected in 2015. Shown for comparison is the expected efficiency determined from $Z \to ee$ MC where the simulated trigger has a lower L1 energy threshold of $E_T > 18$ GeV. *Right:* Efficiency of the logical OR between the triggers HLT_e26_lhtight_nod0_ivarloose, HLT_e60_lhmedium_nod0, and HLT_e140_lhloose_nod0 as a function of the electron's reconstructed transverse energy (E_T) for 2016 data and MC [147]. The efficiencies were measured with a tag-and-probe method using $Z \to ee$ decays.

7.3.2 Single Muon Triggers

The logical OR of two single muon triggers is used to identify events with muons. As was the case for the electrons, the differences in the trigger scheme between 2015 and 2016 results in

slightly different triggers being applied to 2015 and 2016 data. The triggers utilized in 2015 are:

- **HLT_mu20_iloose_L1MU15:** A muon trigger requiring reconstructed muon $p_T >$ 20 GeV with an added loose p_T cone isolation[3]. This HLT is seeded by the L1 trigger MU15, which requires at L1 the muon $p_T > 15$ GeV.

- **HLT_mu50:** A muon trigger requiring reconstructed muon $p_T > 50$ GeV. This HLT is seeded by the L1 trigger MU20, which requires at L1 the muon $p_T > 20$ GeV.

Figure 7.2 shows, for barrel and endcap muons, the efficiency of the 2015 HLT triggers utilized in this analysis compared to the L1 trigger from which they are seeded when the triggers are applied to $Z \to \mu\mu$ data events. The lower efficiency of the L1 trigger in the barrel region compared to the endcap region is the result of reduced geometric coverage in the barrel region[4].
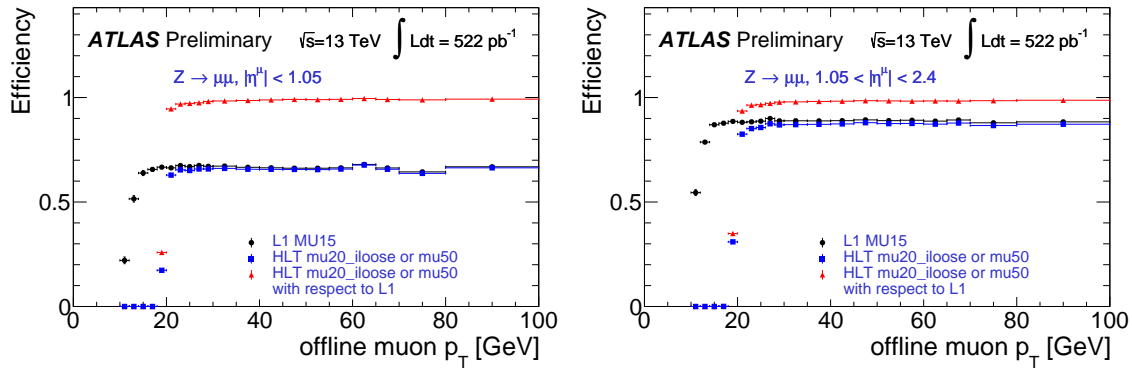
Figure 7.2: Efficiency of the L1 MU15 trigger and the efficiency (absolute and relative to L1) of the OR of triggers HLT_mu20_iloose_L1MU15 and HLT_mu50 as a function of the reconstructed muon candidates p_T in the barrel region (left) and endcap region (right) [148]. The efficiency was measured with a tag-and-probe method using $Z \to \mu\mu$ decays from data collected in 2015.

The 2016 trigger scheme for the single muon triggers results in a change of the lower p_T muon trigger, while the higher p_T trigger remains unchanged:

- **HLT_mu26_ivarmedium:** A muon trigger requiring reconstructed muon $p_T > 26$ GeV with an added medium variable p_T cone isolation[5]. This HLT is seeded by the L1 trigger MU20, which requires at L1 the muon $p_T > 20$ GeV.

---

[3]The loose p_T isolation cone requires that the ratio of the sum of p_T in a cone around the track to the track p_T be less than 0.12.

[4]The geometric coverage in the barrel region is reduced to allow for support services.

[5]The medium variable p_T isolation cone requires that the ratio of the sum of p_T in a variable cone around the track to the track p_T be less than 0.07.

- **HLT_mu50:** A muon trigger requiring reconstructed muon $p_T > 50$ GeV. This HLT is seeded by the L1 trigger MU20, which requires at L1 the muon $p_T > 20$ GeV.

Figure 7.3 shows the efficiency of the 2016 HLT triggers (and the L1 triggers from which they are seeded) as a function of the reconstructed muon p_T for $Z \to \mu\mu$ data events. The efficiency is shown for barrel muons and endcap muons separately. Once again, the lower efficiency of the L1 trigger in the barrel region compared to the endcap region is the result of reduced geometric coverage in the barrel region.
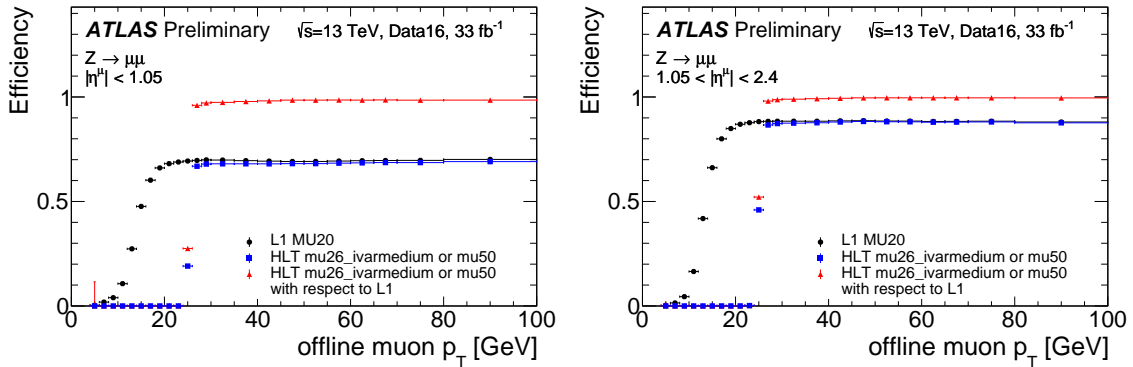
Figure 7.3: Efficiency of the L1 MU20 trigger and the efficiency (absolute and relative to L1) of the OR of triggers HLT_mu26_ivarmedium and HLT_mu50 as a function of the reconstructed muon candidates p_T in the barrel region (left) and endcap region (right) [148]. The efficiency was measured with a tag-and-probe method using $Z \to \mu\mu$ decays from data collected in 2016.

7.4 Object Selections

Objects that have passed preselection and overlap removal are further processed through several additional object selections. These object selection definitions are utilized during $W^{\pm}W^{\pm}jj$ event selection. The various object selections applied to electrons, muons, and jets are outlined below.

7.4.1 Muon

After preselection and overlap removal, three different analysis muon definitions are constructed using the muon reconstruction, identification, and isolation categories (see Section 6.3). These three definitions are: signal, loose, and veto. *Signal* muons are used when selecting events that match the signal event signature. *Loose* muons are used when estimating the non-prompt background. *Veto* muons are used when estimating backgrounds with three leptons. Table 7.1 outlines the selections applied for each muon category. For the

muons, the main discriminants between the categories (outside of lepton p_T) are the isolation requirement and the d_0 resolution.

Signal Muons	Loose Muons	Veto Muons
$p_T > 27$ GeV	$p_T > 27$ GeV	$p_T > 15$ GeV
$|\eta| < 2.5$	$|\eta| < 2.5$	$|\eta| < 2.5$
$|z_0 sin\theta| < 0.5$ mm	$|z_0 sin\theta| < 0.5$ mm	$|z_0 sin\theta| < 0.5$ mm
$d_0/\sigma_{d_0} < 3$	$d_0/\sigma_{d_0} < 10$	$d_0/\sigma_{d_0} < 3$
Medium Identification	Medium Identification	Medium Identification
Gradient Isolation	-	Gradient Isolation
	Not Signal Muon	

Table 7.1: Summary of selections defining signal, loose, and veto muons.

7.4.2 Electrons

As was the case with muons, electrons are defined as either signal, loose, or veto. The selections defining each electron category are summarized in Table 7.2. The main discriminants between the different electron definitions (beyond electron p_T) are the identification and isolation requirements.

Signal Electrons	Loose Electrons	Veto Electrons
$p_T > 27$ GeV	$p_T > 27$ GeV	$p_T > 15$ GeV
$|\eta| < 2.47$ not including $1.37 < |\eta| < 1.52$	$|\eta| < 2.47$ not including $1.37 < |\eta| < 1.52$	$|\eta| < 2.47$ not including $1.37 < |\eta| < 1.52$
$|z_0 sin\theta| < 0.5$ mm $d_0/\sigma_{d_0} < 5$ Tight Identification Gradient Isolation	$|z_0 sin\theta| < 0.5$ mm $d_0/\sigma_{d_0} < 5$ Medium Identification - Not Signal Electron	$|z_0 sin\theta| < 0.5$ mm $d_0/\sigma_{d_0} < 5$ Medium Identification Gradient Isolation

Table 7.2: Summary of selections defining signal, loose, and veto electrons.

7.4.3 Jets

During preselection, jets are required to pass loose p_T and η selections, and b-tagged jets are identified. Additional jet kinematic selections are applied during analysis event selection (see Section 7.5). After overlap removal and prior to the analysis event selections, one further jet cleaning selection is applied: a cut on the *jet vertex tagger* (JVT) fraction [149].

The JVT is a tool used to reduce the contribution from pile-up jets. Using a two-dimensional likelihood discriminant, a cut is placed on the fraction of tracks in the jet associated with the jet's PV (JVT>0.59). Figure 7.4 shows the efficiency of this selection in data and MC for $Z \rightarrow \mu\mu$ events balanced against a jet, such that the event should only contain a single jet. Figure 7.4 illustrates that as the amount of pile-up in the event increases, the number of jets in the event remains at one (as it should) when the JVT selection is applied.
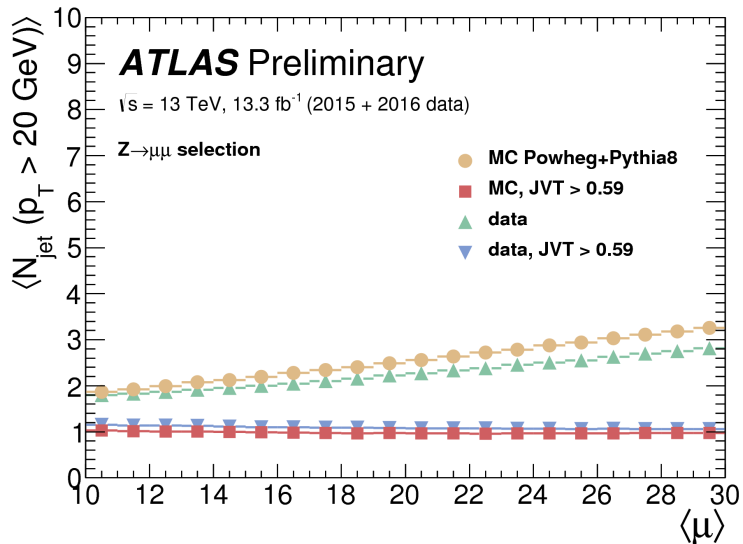
Figure 7.4: The average number of jets with $p_T > 20$ GeV in data and MC before and after a JVT > 0.59 cut [150]. Events are selected with exactly two muons with $p_T > 25$ GeV and a dimuon mass within a window around the mass of the Z boson. A $\Delta\phi(Z, jet) > 2.8$ is applied to ensure that the jet is balanced against the Z boson.

Therefore, for an event to be considered during analysis selection, jets in the event must pass the JVT > 0.59 selection.

7.5 Analysis Selections

This analysis was conducted using a number of various phase-space regions. This section outlines the definitions and motivations for the kinematic selections for the signal region and

the various validation/control regions used to estimate, validate, and reduce backgrounds.

7.5.1 Signal Region

Table 7.3 outlines the various selections which define the signal region. Unless stated otherwise, lepton selections are applied to the leading and subleading leptons in the event.

Cut Name	Description
Preselection	Cuts outlined in Section 7.1
Trigger	Leptons pass single lepton triggers
Signal Leptons	Leptons are *signal* leptons
Electron Author	Author = 1, unambiguous electrons
Dilepton Mass	$m_{ll} \geq 20$ GeV
3rd Lepton Veto	Remove events with three or more preselected leptons
Same-Sign Leptons	Leading and subleading lepton have the same electric charge
Jet Cuts	$N_{jet} \geq 2$ and leading(subleading) jet $p_T > 65(35)$ GeV
Loose m_{jj}	$m_{jj} > 200$ GeV for tagging jets
Z-Veto	$|m_{ee} - m_Z| > 15$ GeV (*ee* channels only)
Missing E_T	$E_T^{miss} \geq 30$ GeV
b-Jet Veto	$N_{b-jet} = 0$
Δy_{jj} Cut	$|\Delta y_{jj}| > 2$ between tagging jets
Tight m_{jj}	$m_{jj} > 500$ GeV for tagging jets

Table 7.3: Summary of selections used to construct signal region. Unless stated otherwise, selections applied to leptons are applied to the leading and subleading leptons. Tagging jets are defined as the leading and subleading jets.

Most of these selections serve one of two main purposes: (1) enhance $W^\pm W^\pm jj-$EW events, or (2) reduce background contributions. The cuts from Table 7.3 falling into these two categories are described below.

Enhance $W^\pm W^\pm jj -$ EW Signal Events

The signature of $W^\pm W^\pm jj-$EW events (see Chapter 4) includes two same-sign leptons, two neutrinos, and two forward jets. To enhance this signature, the following selections are applied:

Leptons: Exactly two leptons with the same electric charge are required to be present in the event. These leptons are selected as the leptons with the highest p_T in the event. Both leptons are required to have $p_T > 27$ GeV, which aligns with the threshold of the single lepton triggers. The leptons are required to be *signal* leptons (see Section 7.4).

Neutrinos: Due to the presence of two neutrinos in the $W^{\pm}W^{\pm}jj$ final state, events are expected to have missing transverse energy. As a result, a cut requiring $E_T^{miss} \geq 30$ GeV is applied to enhance $W^{\pm}W^{\pm}jj$ events. This selection also helps reduce charge misID background.

Jets: The event is required to have at least two forward jets with high p_T. The leading jet is required to have a $p_T > 65$ GeV and the subleading jet is required to have $p_T > 35$ GeV. These two jets (the tagging jets) are used to calculate the invariant mass (m_{jj}) and rapidity separation (Δy_{jj}) associated with the event. $W^{\pm}W^{\pm}jj-$EW events can be enhanced over $W^{\pm}W^{\pm}jj-$QCD events by requiring $m_{jj} > 500$ GeV and $|\Delta y_{jj}| > 2$ (see Chapter 4).

Reduce Background Events

In addition to selections to enhance the $W^{\pm}W^{\pm}jj-$EW signal, a number of cuts in Table 7.3 are designed to reduce the contributions from background processes:

- To suppress background from processes which produce more than two leptons in the final state (such as WZ and ZZ production), events which have three (or more) *veto* leptons are removed.

- In order to reduce the e/γ conversions background, a Z-veto cut requiring $|m_{ee}-m_Z| > 15$ GeV and a requirement of $|\eta^e| < 1.37$ are applied in the $e^{\pm}e^{\pm}$ channels. In addition, an $m_{ll} \geq 20$ GeV cut is required to reduce uncertainty on the modeling of low mass Drell-Yan processes.

- Background contributions from top processes are reduced by requiring the event to contain no b-tagged jets. Jets are b-tagged using the 85% efficiency working point of the MV2c10 tagger (see Section 6.5.1).

The two remaining cuts, preselection and electron author, are better classified as selections to purify the events. Preselection removes poor quality events and removes physics objects (such as very low p_T leptons and jets) which are not analytically relevant. The electron author cut provides an additional confirmation that electrons in the event cannot be reconstructed as photons.

Electrons are reconstructed from clusters of energy in the calorimeter (see Section 6.4). Photons are also reconstructed from clusters of energy in the calorimeter. The main discriminant between an object classified as an electron or photon is whether or not an ID track can be associated with the candidate. If an ID track matches the candidate, it is classified as an electron; otherwise, the object is classified as a photon.

An additional classification can be performed which further determines if the candidate is unambiguously an electron/photon or if the object could be reconstructed as either. This classification, referred to as *electron author*, uses the candidate's E/p, associated track p_T,

pixel hit count, and secondary vertex information to determine whether or not the candidate is an unambiguous electron [132]. Candidates with electron author = 1 have been classified as unambiguous electrons, while candidates with electron author = 16 could be reconstructed as either an electron or a photon. Consequently, in order to remove any ambiguity[6], the requirement electron author = 1 is applied to all signal electrons in this analysis.

Signal Region Performance

Table 7.4 details the event yield in collision data for each of the signal region selections. The selection with the largest impact on the signal region data yield is the requirement that the leading and subleading leptons in the event have the same electric charge. Once this same-sign leptons selection is applied, only 0.05% of the previous data yield in the signal region remains. Every selection after the same-sign leptons selection reduces the signal region data yield by over 15%, illustrating the importance of each signal region selection.

Cut Name	Observed Data Yield
Trigger	4.61×10^7
Signal Leptons	2.43×10^7
Electron Author	2.42×10^7
Dilepton Mass	2.42×10^7
3rd Lepton Veto	2.41×10^7
Same-Sign Leptons	12,160
Jet Cuts	2,611
$m_{jj} > 200$ GeV (Loose)	1,524
Z-Veto	1,265
Missing E_T	1,059
b-Jet Veto	391
Δy_{jj} Cut	223
$m_{jj} > 500$ GeV (Tight)	122

Table 7.4: Observed data yield for each signal region selection. Values are shown for all lepton channels combined.

---

[6]Since the electron identification requirements applied to signal electrons impose ID track requirements, most electrons are already unambiguous.

7.5.2 Validation and Control Regions

In addition to the signal region, a number of validation regions (VRs) and control regions (CRs) are utilized in this analysis. These different validation/control regions are defined below. The characteristic selections of each validation/control region are written in purple. Unless stated otherwise, each region is examined in all six lepton channels.

7.5.2.1 Validation Regions

Three validation regions are utilized in this analysis. These validation regions are constructed to evaluate the modeling of various backgrounds and include: the inclusive - charge misID validation region, the low N_{jet} validation region, and the non-prompt validation region.

Inclusive - Charge MisID Validation Region: The inclusive - charge misID validation region, defined in Table 7.5, is used to validate the charge misID background estimation. The validation region is very close to the signal region while being more inclusive and removing any requirements on the jets and E_T^{miss}. The charge misID background is isolated by reversing the Z-veto and instead requiring the dilepton mass be within the Z-mass window. This particular validation region is only used in the $e^\pm e^\pm$ channels.

<div align="center">

Inclusive - Charge MisID Validation Region

Cut Name	Description
Preselection	Cuts outlined in Section 7.1
Trigger	Leptons pass single lepton triggers
Signal Leptons	Leptons are *signal* leptons
Electron Author	Author = 1, unambiguous electrons
Dilepton Mass	$m_{ll} \geq 20$ GeV
3rd Lepton Veto	Remove events with three or more preselected leptons
Same-Sign Leptons	Leading and subleading leptons have the same electric charge
Z-Peak	$|m_{ee} - m_Z| < 15$ GeV

</div>

Table 7.5: Inclusive - Charge misID Validation Region selections. Region used in the $e^\pm e^\pm$ channels to test the charge misID background modeling.

Low N_{jet} Validation Region: The low N_{jet} validation region, defined in Table 7.6, is used to assess background modeling in the region where the signal region jet cut requirements are not met, i.e., the event has less than two jets, or the jets do not meet the signal region p_T requirements outlined in Table 7.3. For this region the number of jets in the event is counted using preselection jets. Backgrounds studied in this region include $WZjj$, non-prompt, and charge misID.

Low N_{jet} Validation Region

Cut Name	Description
Preselection	Cuts outlined in Section 7.1
Trigger	Leptons pass single lepton triggers
Signal Leptons	Leptons are *signal* leptons
Electron Author	Author $= 1$, unambiguous electrons
Dilepton Mass	$m_{ll} \geq 20$ GeV
3rd Lepton Veto	Remove events with three or more preselected leptons
Same-Sign Leptons	Leading and subleading leptons have the same electric charge
Z-Veto	$|m_{ee} - m_Z| > 15$ GeV (*ee* channels only)
Missing E_T	$E_T^{miss} \geq 30$ GeV
b-Jet Veto	$N_{b-jet} = 0$
Low Jet Cuts	$N_{jet} < 2$ **OR** leading $p_T^{jet} < 65$ GeV **OR** subleading $p_T^{jet} < 35$ GeV

Table 7.6: Low N_{jet} Validation Region selections. Modeling of $WZjj$, non-prompt, and charge misID backgrounds are examined in this region.

Non-Prompt Validation Region: The non-prompt validation region, defined in Table 7.7, is enriched with $t\bar{t}$ events by requiring there be a *b*-tagged jet in the event. A $t\bar{t}$ rich environment, where non-prompt events are more likely to occur, allows for better understanding of how well the non-prompt background estimation method models the data. There is also a contribution from the charge misidentified background that is modeled in this region.

Non-Prompt Validation Region

Cut Name	Description
Preselection	Cuts outlined in Section 7.1
Trigger	Leptons pass single lepton triggers
Signal Leptons	Leptons are *signal* leptons
Electron Author	Author $= 1$, unambiguous electrons
Dilepton Mass	$m_{ll} \geq 20$ GeV
3rd Lepton Veto	Remove events with three or more preselected leptons
Same-Sign Leptons	Leading and subleading leptons have the same electric charge
Jet Cuts	$N_{jet} \geq 2$ and leading(subleading) jet $p_T > 65(35)$ GeV
Z-Veto	$|m_{ee} - m_Z| > 15$ GeV (*ee* channels only)
Require *b*-Jet	$N_{b-jet} = 1$

Table 7.7: Non-Prompt Validation Region selections.

7.5.2.2 Control Regions

Three control regions are utilized in this analysis. Like the validation regions, the control regions are used to evaluate the modeling of background processes. The control regions are also used to constrain backgrounds before/during the fitting procedure. These regions include: the low m_{jj} control region, the WZ control region, and the $Z\gamma$ control region.

Low m_{jj} Control Region: The low m_{jj} control region, constructed using the selections detailed in Table 7.8, is the same as the signal region with the tight m_{jj} cut reversed ($m_{jj} <$ 500 GeV). Reversing the tight m_{jj} selection provides a method of evaluating the modeling of all backgrounds in a region with similar composition to the signal region. This control region consists of a single bin in m_{jj}, which is also used as input to the fit (see Chapter 12).

<div align="center">

Low m_{jj} Control Region

Cut Name	Description
Preselection	Cuts outlined in Section 7.1
Trigger	Leptons pass single lepton triggers
Signal Leptons	leptons are *signal* leptons
Electron Author	Author $= 1$, unambiguous electrons
Dilepton Mass	$m_{ll} \geq 20$ GeV
3rd Lepton Veto	Remove events with three or more preselected leptons
Same-Sign Leptons	Leading and subleading leptons have the same electric charge
Jet Cuts	$N_{jet} \geq 2$ and leading(subleading) jet $p_T > 65(35)$ GeV
Loose m_{jj}	$m_{jj} > 200$ GeV
Z-Veto	$|m_{ee} - m_Z| > 15$ GeV (*ee* channels only)
Missing E_T	$E_T^{miss} \geq 30$ GeV
b-Jet Veto	$N_{b-jet} = 0$
Δy_{jj} Cut	$|\Delta y_{jj}| > 2$ between tagging jets
Reverse Tight m_{jj} Cut	$m_{jj} < 500$ GeV

</div>

Table 7.8: Low m_{jj} Control Region selections. This control region is provided as input to the fit to help constrain background processes.

WZ Control Region: The WZ control region, detailed in Table 7.9, is the region used to determine the normalization of the WZ background during the fit (see Chapter 12). The region is designed to provide a highly pure sample of WZ events using the cuts described in Table 7.9. For this region, instead of looking at each channel individually, all channels are combined and a single *ll* channel is studied.

WZ Control Region

Cut Name	Description
Preselection	Cuts outlined in Section 7.1
Trigger	Leptons pass single lepton triggers
Signal Leptons	leading and subleading leptons are *signal* leptons
Electron Author	Author = 1, unambiguous electrons
Dilepton Mass	$m_{ll} \geq 20$ GeV for leading and subleading leptons
Jet Cuts	$N_{jet} \geq 2$ and leading(subleading) jet $p_T > 65(35)$ GeV
Loose m_{jj}	$m_{jj} > 200$ GeV
Z-Veto	$|m_{ee} - m_Z| > 15$ GeV (*ee* channels only)
Missing E_T	$E_T^{miss} \geq 30$ GeV
b-Jet Veto	$N_{b-jet} = 0$
Δy_{jj} Cut	$|\Delta y_{jj}| > 2$ between tagging jets
3rd Lepton	Require an additional 3rd *veto* lepton
Z Candidate	Require opposite-sign dilepton pair Z candidate within three leptons
Trilepton Mass	$m_{lll} > 106$ GeV

Table 7.9: WZ Control Region selections. This control region is used during the fit to determine the WZ background normalization applied in the signal region.

$Z\gamma$ Control Region: The $Z\gamma$ control region is used to determine the normalization for the $V\gamma jj$ background. In this region a scale factor is determined which is then applied to $V\gamma$ MC samples in the signal region (see Section 8.2.3). The selections defining this region are outlined in Table 7.10.

$Z\gamma$ Control Region

Cut Name	Description
Preselection	Cuts outlined in Section 7.1
Trigger	Leptons pass single lepton triggers
Leading Lepton	*Signal* muon
Subleading Lepton	*Signal* muon with p_T requirement reduced to $p_T > 20$ GeV
3rd Lepton	Require additional *veto* electron with $p_T > 27$ GeV
Electron Author	Author = 1, unambiguous electrons
Low Missing E_T	$E_T^{miss} < 30$ GeV
$Z\gamma$ Mass Window	75 GeV $< m_{\mu\mu e} < 100$ GeV

Table 7.10: $Z\gamma$ Control Region selections.

7.5.2.3 Validation/Control Region Summary

Several validation and control regions, defined above, are utilized to examine the background modeling accuracy. The non-prompt VR, inclusive-charge misID VR, $Z\gamma$ CR, and WZ CR are designed to isolate specific background processes. On the other hand, the low N_{jet} VR and low m_{jj} CR are regions orthogonal to the signal region in which the modeling of *all* background processes is assessed.

Chapter 8

Background Estimation

Accurate modeling of the expected background contributions is essential for any analysis. In Chapter 4, the various background contributions for $W^{\pm}W^{\pm}$ electroweak production were introduced. This chapter describes the methods used to estimate each of these background contributions and how each background is modeled in both the validation/control regions and the signal region.

8.1 Prompt Processes

Prompt processes that produce events with (at least) two prompt same-sign leptons passing signal region selections are estimated using MC simulation. The prompt background accounts for approximately 54% of the expected background in the signal region. The most significant of the prompt background processes, $WZjj$ and $W^{\pm}W^{\pm}jj-$QCD, are described in detail below.

8.1.1 $W^{\pm}W^{\pm}jj - \mathrm{QCD}$

As introduced in Chapter 2, $W^{\pm}W^{\pm}jj-$QCD production is treated as a background. The Δy_{jj} cut reduces the impact of $W^{\pm}W^{\pm}jj-$QCD production in the signal region. Any residual contribution is estimated using MC simulation[1]. $W^{\pm}W^{\pm}jj-$QCD accounts for approximately 17.5% of the prompt background, and is roughly 10% of the background in the signal region. In addition to the direct contribution of the QCD process, the interference between the EW and QCD $W^{\pm}W^{\pm}$ processes (which impacts the signal estimation) is also considered. The interference is accounted for with an uncertainty (see Section 10.2.2).

---

[1]See Section 5.3.2 for $W^{\pm}W^{\pm}jj-$QCD MC details.

8.1.2 $WZjj$

The $WZjj \to l^{\pm}\nu l^{\pm}l^{\mp}jj$ process, illustrated in Figure 8.1, is the main source of prompt background after all signal region selections have been applied[2]. WZ production is often mistaken as a signal event due to the loss of one of the leptons resulting from the Z decay. This lepton can be lost because: (1) the lepton is unsuccessfully identified during reconstruction, or (2) the lepton is outside the detector acceptance.
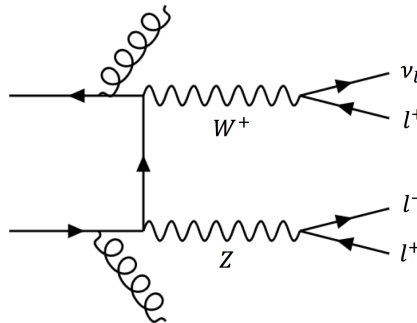
Figure 8.1: Example diagram of hadronic collision with a $WZjj$ final state.

The $WZjj$ background is estimated using MC simulated events[3] with all lepton channels combined to increase statistics. The $WZjj$ background is examined in the WZ control region (see Table 7.9). Recall from Section 7.5.2.2, the defining selections of the WZ control region are:

- A 3rd *veto* lepton is required in the event.

- An opposite-sign dilepton pair Z candidate must exist within the three leptons.

- The trilepton invariant mass (m_{lll}) is greater than 106 GeV.

Figure 8.2 shows the m_{lll} distribution in the WZ control region. As expected, the distribution is dominated by $WZjj$ events with some contamination from other prompt processes. The total event yield in the WZ control region is listed in Table 8.1.

In the fit, the WZ background is scaled by a normalization scale factor. This scale factor is determined during the simultaneous fit of the WZ control region, the low m_{jj} control region, and the signal region. During the fit, the WZ control region is considered in a single bin of m_{jj}: 200 GeV $< m_{jj} <$ 3000 GeV. The details and results of this fit are discussed in Chapters 12 and 13.

---

[2]The $WZjj$ background accounts for over 75% of the prompt background and for roughly 45% of the total background in the signal region.

[3]For details regarding the MC samples, see Section 5.3.2.
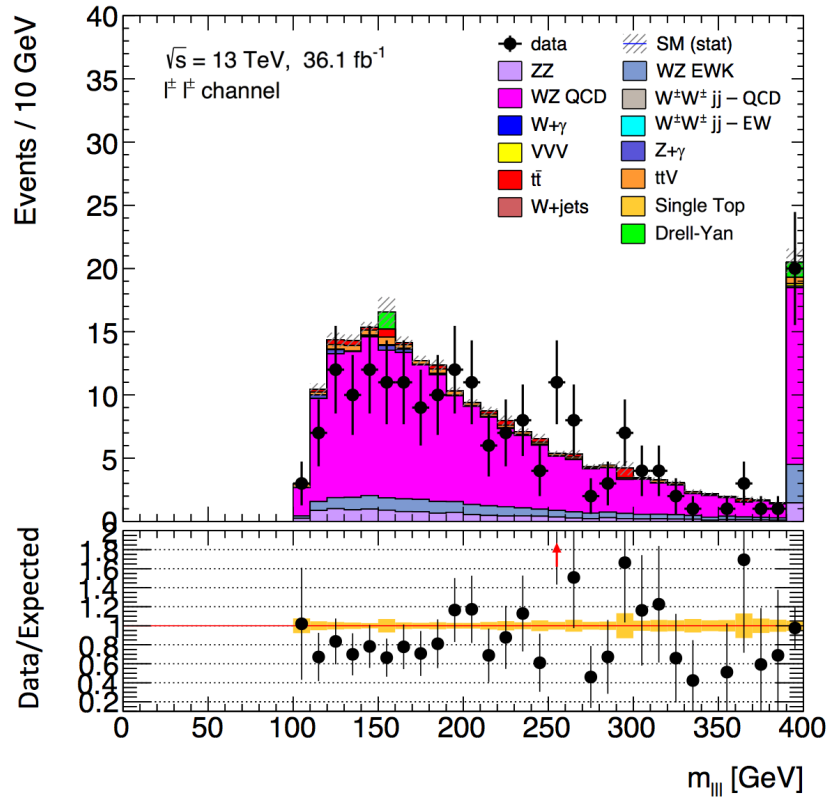
Figure 8.2: Trilepton invariant mass distribution for data and expected MC background in the WZ control region.

WZ Control Region	
WZ	197.09 ± 1.42
ZZ	14.12 ± 0.27
top	6.17 ± 0.25
$Z\gamma$	2.68 ± 0.60
VVV	1.26 ± 0.06
Total Expected	221.32 ± 1.59
Data	201

Table 8.1: Expected event yield in the WZ control region. Yields in all lepton channels are combined. Only statistical uncertainties are shown.

8.1.3 Other Prompt Processes

While the majority of the prompt background comes from $WZjj$, and less so $W^{\pm}W^{\pm}jj-$QCD, other processes can produce a prompt signal region signature. These processes include ZZ, $t\bar{t}V$, and VVV (see Section 4.1). The contributions of these processes are estimated using MC samples[4]. Together, these additional prompt processes account for roughly 3-3.5% of the background in the signal region.

8.2 e/γ Conversions

The e/γ conversions background consists of Standard Model processes that produce opposite-sign lepton final states that are incorrectly identified as same-sign lepton final states. The contributions to this background originate from two sources:

- **Charge MisID:** The charge misID background consists of Standard Model processes that produce opposite-sign leptons which are reconstructed as same-sign leptons as they travel through the detector.

- **$V\gamma$ Processes:** The $V\gamma$ background consists of Standard Model processes where one lepton in the same-sign final state is the product of an on-shell photon.

Before delving into these backgrounds, it is important to discuss a key analysis strategy relevant for both the $V\gamma$ and charge misID backgrounds: identifying $Z \to e^+e^-$ events. The following section describes how $Z \to e^+e^-$ events are identified at the LHC. Following this, the charge misID and $V\gamma$ backgrounds are discussed.

8.2.1 Identifying $Z \to e^+e^-$ Events

Previous measurements conducted at the LEP e^+e^- collider measured the Z boson mass and width to be [26, 151]:

$$m_Z = 91.1876 \pm 0.0021 \text{ GeV} \qquad\qquad \Gamma_Z = 2.4952 \pm 0.0023 \text{ GeV} \qquad (8.1)$$

In ATLAS, $Z \to e^+e^-$ events are selected by forming opposite-sign electron pairs and requiring the dielectron invariant mass (m_{ee}) to be close to the Z resonance. In a perfect world, the m_{ee} measured by the detector would be between $88 - 94$ GeV. In reality, however, the measured m_{ee} of a $Z \to e^+e^-$ dielectron system can be outside this very small window for a number of reasons, including: (1) the electrons can lose energy as they traverse the detector, (2) the electron four-momentum can be incorrectly reconstructed by the detector, (3) the true parent of the dielectron system can be an off-shell photon (γ^*) or a mixed Z/γ^* state instead of a Z boson. Therefore, the window in which m_{ee} can reside to be considered a

---

[4]For MC sample details, see Section 5.3.2.

$Z \rightarrow e^+e^-$ event (referred to as the Z mass window) is made considerably larger. The exact value of the Z mass window is chosen by each individual analysis, but the broad ATLAS Z mass window is typically $66 - 116$ GeV.

Figure 8.3 illustrates the efficacy of selecting $Z \rightarrow e^+e^-$ events by requiring an opposite-sign dielectron pair with 66 GeV $< m_{ee} <$ 116 GeV. Figure 8.3 compares the number of $Z \rightarrow e^+e^-$ events observed in data to those simulated by MC samples during a measurement of the $Z \rightarrow e^+e^-$ cross section [152]. The only event selections applied in this region require two opposite-sign electrons passing quality selections[5] with $|\eta| <$ 2.47 (excluding 1.37 $< |\eta| <$ 1.52), $p_T >$ 25 GeV, and 66 GeV $< m_{ee} <$ 116 GeV.
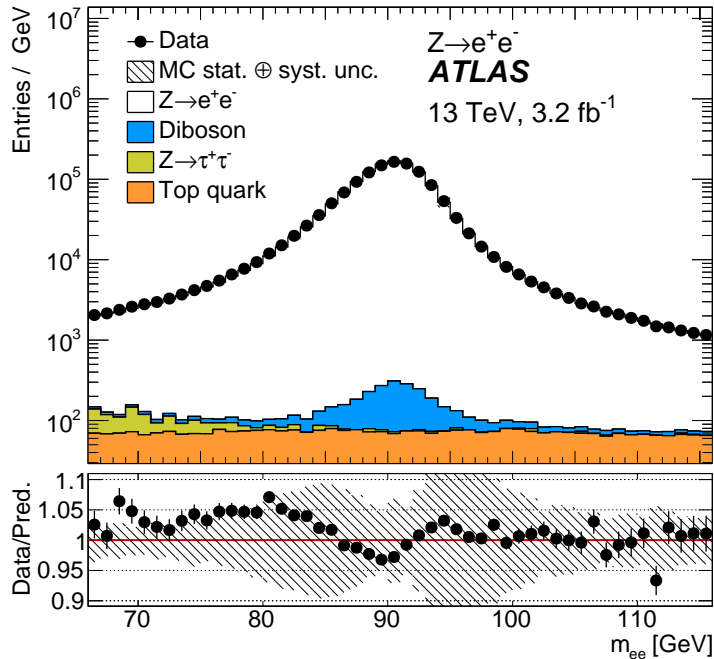
Figure 8.3: Dielectron invariant mass distribution resulting from $Z \rightarrow e^+e^-$ selections [152]. The systematic uncertainties for the signal and background distributions are combined in the shaded band, while the statistical uncertainty is shown on the data points. The luminosity uncertainties are not included.

With these minimal selections, over 99% of the observed data is attributed to $Z \rightarrow e^+e^-$ events. Hence, requiring opposite-sign electron pairs to be within a Z mass window is a very efficient way of selecting $Z \rightarrow e^+e^-$ events. In this analysis, the Z mass window used to select $Z \rightarrow e^+e^-$ events is $76 - 106$ GeV[6]. Additionally, since $Z \rightarrow ee$ events are used in

---

[5]The quality selections required include passing medium identification with $d_0/\sigma_{d_0} < 5$ and $|z_0 sin\theta| < 0.5$ mm.

[6]This window is narrower than the previously mentioned 66-116 GeV window due to the fact that this window is used to reject $Z \rightarrow e^+e^-$ events instead of selecting them.

this analysis to estimate the charge misID background, the electron pairs are not required to always form opposite-sign pairs[7].

8.2.2 Charge Misidentification

The charge misID background consists of events that contain two opposite-sign leptons where the charge of an electron is misidentified, thus leading to the event being selected as a signal event[8]. There are two main reasons for electron charge misID:

- An error occurred in the measurement of the curvature of the electron track. As particles move through the ID, they are subject to a magnetic field which causes charged particles to curve. The direction of the curvature is utilized to determine the electric charge of the particle. If the curvature is incorrectly measured, the charge of the electron can be misidentified. This effect is more important for electrons with high p_T where the electron track is more likely to be straight and is relatively uniform in η.

- The dominant mechanism for charge misID of electrons is the *trident* process, illustrated in Figure 8.4. In the trident process (bremsstrahlung), an electron radiates a photon which converts into an e^+e^- pair ($e^\pm \to e^\pm\gamma \to e^\pm e^+e^-$). Depending upon how the energy of the original electron is distributed after the photon radiation, the final reconstructed electron may be of opposite charge with respect to the initial electron. The effect strongly depends upon the amount of material traversed by the electron. The likelihood of bremsstrahlung increases by almost two orders of magnitude in the forward detector compared to the central detector.

The expected charge misID background in the signal region (and control region) is estimated from data using a data-driven method that relies on a knowledge of the charge misID probability. The background is estimated by selecting opposite-sign data that has been weighted with the probability that one of the electrons is reconstructed with the wrong charge. An additional correction for the energy loss of the reconstructed electron to the original electron (which occurs during the bremsstrahlung) is also performed.

---

[7]When estimating the charge misID background, events with charge misID will result in a same-sign dielectron pair.

[8]The rate of charge misID in muons was found to be negligible and is therefore not considered.
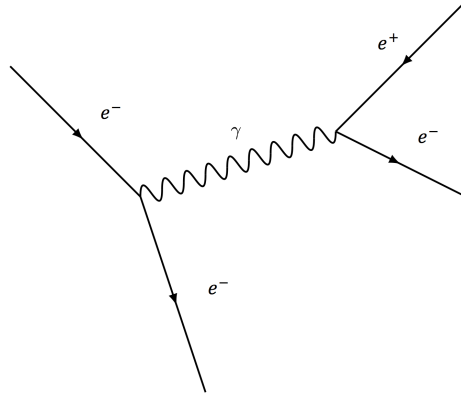
Figure 8.4: Illustration of the *trident* process where an electron radiates a photon which converts into an e^+e^- pair. If most of the energy from the original e^- ends up with the e^+, it is likely that the e^+ will be reconstructed instead of the original e^-. Since the momentum of this e^+ is similar to that of the original e^-, this is referred to as charge misID.

8.2.2.1   Charge MisID Rate Measurement

A large portion of the charge misID background events are the result of an electron radiating a photon as it moves through the detector. This interaction of the electron with the detector material is not well modeled in MC. Therefore, the MC simulation must be corrected to more accurately reflect the true charge misID rates in data.

The charge misID rates are determined using $Z \to ee$ MC events that have been corrected to data using scale factors. To determine these scale factors, the charge misID probabilities must first be measured in data and MC. The evolution from charge misID probabilities to scale factors, and finally to charge misID rates, is described immediately below.

Charge MisID Probability: The charge misID probability is determined using $Z \to ee$ events with a likelihood method. With a likelihood method, both electrons are treated as equally likely to have their charge flipped since it is not possible to know which electron actually had its charge flipped. With $Z \to ee$ events, a certain fraction of the events will be reconstructed with both electrons having the same charge due to charge misID. The expected number of same-sign events $N_{SC}^{exp}(i,j)$ is given by:

$$N_{SC}^{exp}(\epsilon_i, \epsilon_j) = n[(1 - \epsilon_i)\epsilon_j + (1 - \epsilon_j)\epsilon_i], \tag{8.2}$$

where n is the total number of events in the selected bin, and $\epsilon_{i,j}$ are the probabilities for a wrong charge reconstruction in bins i and j.

The probability of observing n_{SC} same-sign events in a single bin, when approximated

by a Poisson distribution, can be described as:

$$P(n_{SC}|\epsilon_i, \epsilon_j) = \frac{[N_{SC}^{exp}(\epsilon_i, \epsilon_j)]^{n_{SC}} e^{-N_{SC}^{exp}(\epsilon_i, \epsilon_j)}}{n_{SC}!}. \tag{8.3}$$

This probability expression is implemented in a likelihood function: $L(\epsilon_i, \epsilon_j) \equiv P(n_{SC}|\epsilon_i, \epsilon_j)$. This likelihood function is used to determine the charge misidentification rates by minimizing the sum of the negative log likelihoods per bin:

$$-\ln L = -\sum_{i,j} \ln\left[\frac{[N_{SC}^{exp}(\epsilon_i, \epsilon_j)]^{n_{SC}} e^{-N_{SC}^{exp}(\epsilon_i, \epsilon_j)}}{n_{SC}!}\right]. \tag{8.4}$$

The number of opposite-sign and same-sign $Z \to ee$ events are counted for events with two signal electrons with a reduced p_T requirement of $p_T > 20$ GeV and 75 GeV $< m_{ee} <$ 105 GeV. The measurement, outlined in Equation 8.4, is performed for both data and MC in five bins of p_T and six bins of η, resulting in charge misID probabilities for each bin.

Scale Factors: With charge misID probabilities ($\mathcal{P}$) determined for both data and $Z \to ee$ MC, scale factors are formulated to correct the measured probability in MC to data. The corrective scale factors, and the relevant systematic uncertainties, are determined by taking the ratio of the probabilities in data and MC for wrong-charge and correct-charge electrons:

$$\text{SF}_{\text{wrong}} = \frac{\mathcal{P}_{data}}{\mathcal{P}_{MC}} \qquad \text{SF}_{\text{correct}} = \frac{1 - \mathcal{P}_{data}}{1 - \mathcal{P}_{MC}}. \tag{8.5}$$

Figure 8.5 shows the calculated scale factors for electrons with wrongly-reconstructed charge (left) and correctly-reconstructed charge (right) in the two dimensional p_T and η map. These scale factors are then applied to the $Z \to ee$ MC events with the assistance of truth information[9]. Once applied, the charge misID probability in $Z \to ee$ MC events agrees with the probability in data, and the final charge misID rates, ϵ_{misID}, can be determined.

---

[9]Truth information is used to determine if the $Z \to ee$ MC event has wrongly- or correctly-reconstructed electron charges.
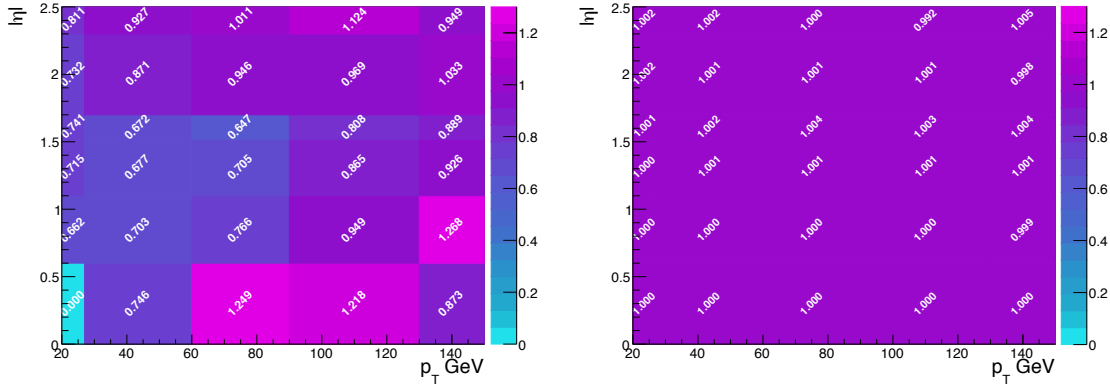
Figure 8.5: Charge misID scale factors for electrons with wrongly-reconstructed charge (left) and correctly-reconstructed charge (right) as a function of p_T and η. These scale factors are applied to $Z \to ee$ MC simulated events to correct the charge misID probability in the MC so as to match the charge misID probability in data.

Charge MisID Rates: The final charge misID rates are extracted from the corrected $Z \to ee$ MC events using truth information and the simple ratio:

$$\epsilon_{misID} = \frac{N_{\text{wrong-charge electrons}}}{N_{\text{prompt electrons}}}. \tag{8.6}$$

The final charge rates are once again measured as a function of p_T and η, but with finer binning. The final charge misID rates, as a function of electron p_T and η, can be seen in Figure 8.6.
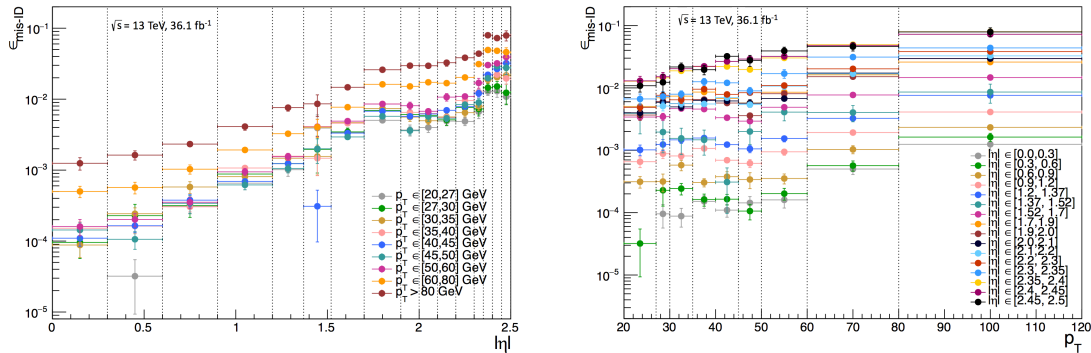
Figure 8.6: Charge misID rates as a function of electron η (left) and p_T (right) retrieved using $Z \to ee$ events after scale factors are applied.

8.2.2.2 Charge MisID Background Estimation

With charge misID rates obtained by employing the method described in the previous section (see Section 8.2.2.1), the number of same-sign events in the signal region (and control regions) due to electron charge misID can be estimated using events with opposite-sign electrons. Data events are selected using all of the signal region selections (see Table 7.3) with the exception that the leading and subleading electrons must be opposite-sign (instead of same-sign). Each event is then weighted with the probability that one of the electrons has been reconstructed with the wrong charge using:

$$w = \frac{\epsilon_1(1 - \epsilon_2) + \epsilon_2(1 - \epsilon_1)}{1 - 2(\epsilon_1 + \epsilon_2) + 2\epsilon_1\epsilon_2}, \tag{8.7}$$

where ϵ_1 and ϵ_2 are the charge misID rates for the leading and subleading electrons, respectively.

In the case of $e\mu$ events, where the electron forms an opposite-sign pair with a muon, the charge misID rate for the muon is assumed to be zero. Equation 8.7 then simplifies to:

$$w = \frac{\epsilon}{1 - \epsilon}. \tag{8.8}$$

Energy Loss Correction

Electrons with incorrectly reconstructed charge are, on average, reconstructed with a lower energy than electrons reconstructed with the correct charge. This is due to energy leakage outside of the EM cluster that reconstructs the electron. For example, wrong-charge electrons are often the result of *trident* processes where some of the initial energy and momentum is lost during the detector-material interaction.

Figure 8.7(left) compares the dilepton invariant mass of opposite-sign data events to same-sign data events in a region dominated by $Z \rightarrow ee$ events. In this region, same-sign data events are largely the result of an electron with wrongly-reconstructed charge. Therefore, the difference between the opposite-sign and same-sign m_{ll} distributions shown in Figure 8.7(left) illustrates the energy loss in electrons with wrongly-reconstructed charge. To account for this, electrons from opposite-sign data events are corrected with a residual energy scale (α) and constant term (c) derived from MC. These corrections are applied to electrons based on the probability for charge misID:

$$p_T^{\text{corrected}} = \frac{p_T^{\text{orig}}}{1 + \alpha} + dE, \tag{8.9}$$

where p_T^{orig} is the original electron energy in data, and the smearing factor, dE, is selected randomly from a Gaussian distribution centered at zero and with a width equal to the residual constant term (c)[10].

---

[10]The smearing factor accounts for the worsened energy resolution caused by the bremsstrahlung.

The residual energy scale correction term (α) and residual constant term (c) are determined by comparing the reconstructed p_T and truth p_T for wrongly-reconstructed and correctly-reconstructed electrons differentially in bins of $|\eta|$ using MC:

$$\alpha = \frac{\left(\frac{p_T^{\text{reco}}}{p_T^{\text{truth}}} - 1\right)^{\text{correct}}}{\left(\frac{p_T^{\text{reco}}}{p_T^{\text{truth}}} - 1\right)^{\text{wrong}}} \tag{8.10}$$

$$c = \langle \frac{p_T^{\text{reco}}}{p_T^{\text{truth}}} \rangle^{\text{wrong}} - \langle \frac{p_T^{\text{reco}}}{p_T^{\text{truth}}} \rangle^{\text{correct}} \tag{8.11}$$

Figure 8.7(right), like Figure 8.7(left), shows the normalized m_{ll} distributions for both same-sign and opposite-sign $Z \rightarrow ee$ events in data, but also shows the same-sign and opposite-sign MC m_{ll} distributions used to determine the energy correction factors. In addition, Figure 8.7(right) displays the estimated charge misID background with the energy correction applied (orange line). With the energy correction, the charge misID distribution agrees better with the observed same-sign data m_{ll} distribution.
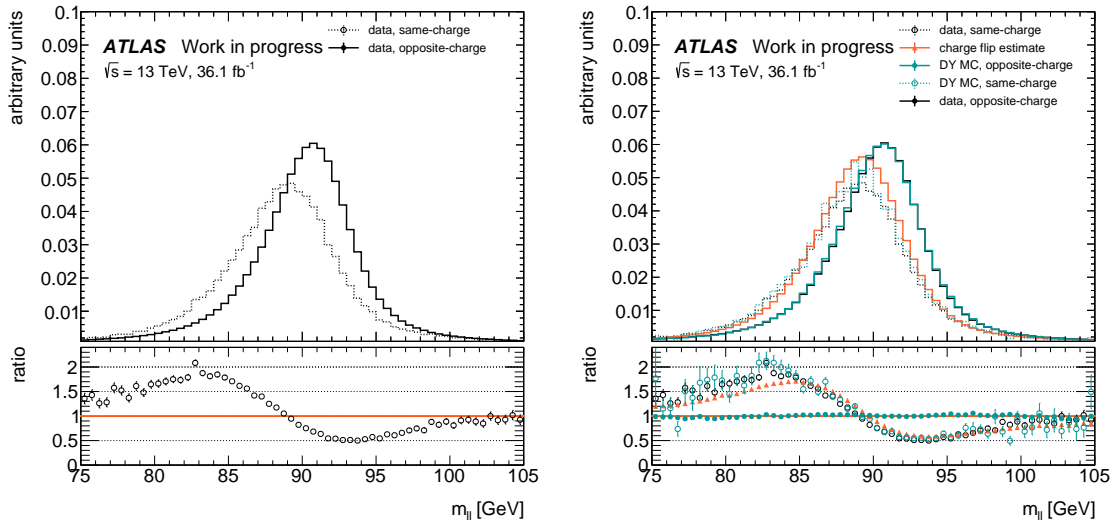
Figure 8.7: Normalized dielectron m_{ll} distributions from same-sign and opposite-sign $Z \rightarrow ee$ events. Distributions for same-sign and opposite-sign data are shown separately (left) and with the m_{ll} distributions of the $Z \rightarrow ee$ opposite-sign and same-sign MC events used to determine the energy correction (right). The estimated charge misID background with the energy correction applied is also shown (right).

Control Region Modeling

Figure 8.8 shows the m_{ll} distribution for the combined electron channel[11] in the SS Inclusive - Charge misID validation region (see Table 7.5). This region is only used in the $e^{\pm}e^{\pm}$ channels and differs from the signal region by requiring the event dilepton mass be within 15 GeV of the Z boson mass. With this selection, the region is dominated by charge misID background. The event yield in the SS Inclusive - Charge misID validation region is listed in Table 8.2. Assuming Poisson statistics in the data, the expected background and observed data almost agree within statistical uncertainties. Any remaining disagreement is accounted for with the systematic uncertainties, discussed in the next section.
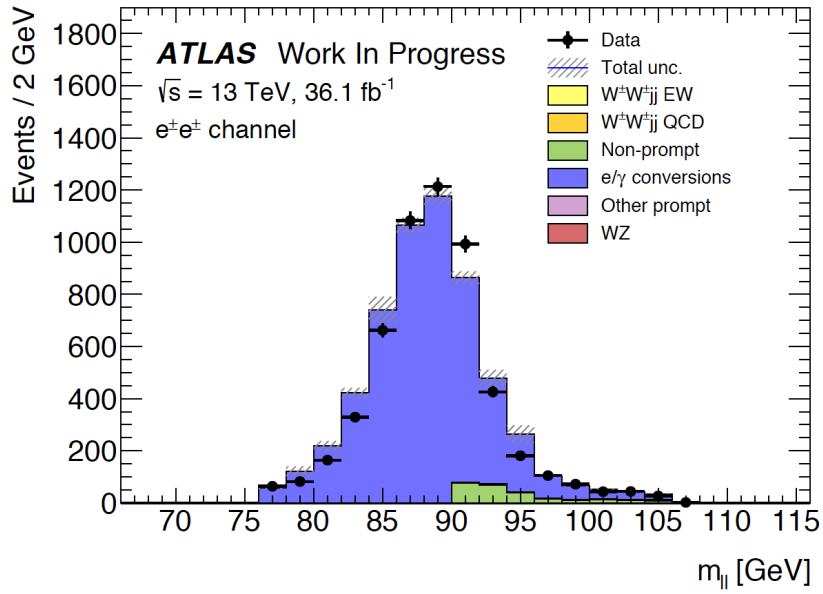
Figure 8.8: Dilepton invariant mass for $e^{\pm}e^{\pm}$ channels in the SS Inclusive - Charge misID Validation Region [153]. Only statistical uncertainties are shown.

---

[11]The combined electron channel includes e^+e^+ and e^-e^- events.

SS Inclusive - Charge MisID VR	
Combined $e^{\pm}e^{\pm}$ channel	
Charge misID	5390.51 ± 2.97
Non-prompt	193.82 ± 31.93
WZ	39.07 ± 1.36
$V\gamma$	11.12 ± 1.93
Other prompt	4.80 ± 0.20
$W^{\pm}W^{\pm}jj-$QCD	1.41 ± 0.04
$W^{\pm}W^{\pm}jj-$EW	3.82 ± 0.08
Total Expected	5645.18 ± 32.15
Data	5490

Table 8.2: Event yield for the combined $e^{\pm}e^{\pm}$ channel in the SS Inclusive - Charge MisID Validation Region. Only statistical uncertainties are shown.

8.2.2.3   Charge MisID Systematic Uncertainties

The charge misID background estimation method has two sources of systematic uncertainties: (1) the uncertainties on the charge misID scale factors, and (2) the uncertainty on the energy correction.

Scale Factors: The uncertainty due to the choice of scale factors is calculated by repeating the charge misID background estimation using alternative charge misID rates. These alternative charge misID rates are determined by two additional sets of scale factors which differ from the nominal scale factors. Figure 8.9 shows the ratio of the nominal charge misID rates compared to the up/down systematic charge misID rates. The systematic uncertainty on the scale factors translates to a variation of less than 14% in the charge misID rates.
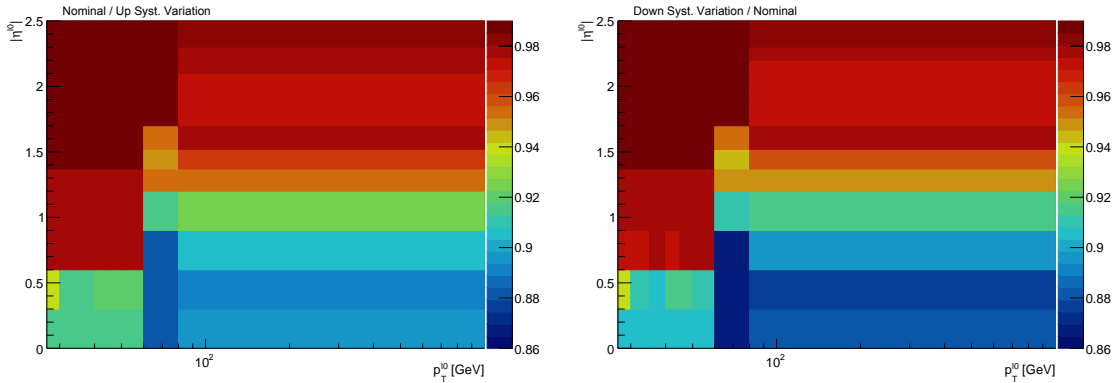
Figure 8.9: *Left:* Nominal charge misID rates divided by the charge misID rates determined using the up-systematic variation scale factors. *Right:* The charge misID rates determined using the down-systematic variation scale factors divided by the nominal charge misID rates.

Energy Correction: The systematic uncertainty due to the energy correction is determined by taking the difference between the charge misID background when using the energy correction and when not using the energy correction. Figure 8.10 shows the leading electron p_T distribution for data and expected background with the charge misID energy correction turned on (left) and turned off (right). This single systematic variation is then symmetrized to provide a positive and negative systematic uncertainty.
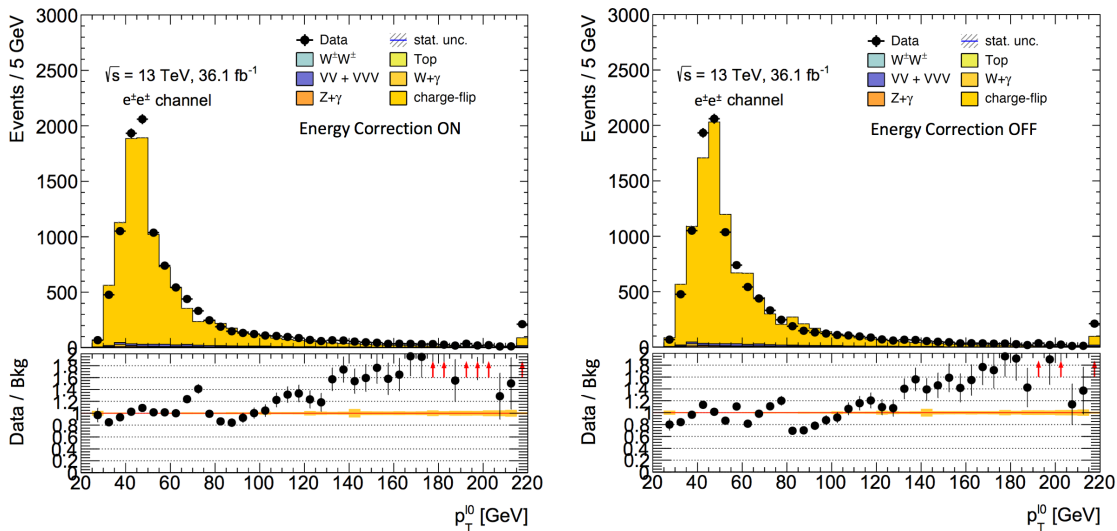
Figure 8.10: Leading electron p_T in the Inclusive SS - Charge misID validation region with the energy correction turned on (left) and turned off (right).

Impact: The relative impact on the expected event yield in the signal region for each systematic uncertainty is listed in Table 8.3 for each channel. The systematic uncertainty on the expected charge misID background is less than 10% in all channels.

<div align="center">

Impact on Charge MisID Background

	e^+e^+	e^-e^-	$e^-\mu^-$	$e^+\mu^+$
SF Up-Variation	+9.8%	+8.5%	+3.2%	+3.1%
SF Down-Variation	−7.5%	−8.5%	+0.3%	−2.0%
Energy Correction	±3.8%	±2.6%	±6.1%	±6.4%

</div>

Table 8.3: Relative impact of the systematic uncertainties on the charge misID background estimation in the signal region.

8.2.3 $V\gamma$ Production

Events with a W/Z boson and an on-shell photon, such as the process illustrated in Figure 8.11, can pass the signal region selections if: the V boson decays leptonically, the photon is reconstructed as an electron(s)[12], and only two same-sign leptons in the event are reconstructed.
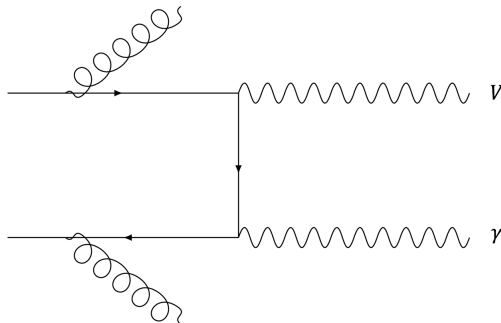
Figure 8.11: Example Feynman diagram of $V\gamma$ production.

The $V\gamma$ background contribution in this analysis is estimated using MC simulation[13]. In the signal region, the $W\gamma$ background contribution is much larger than the $Z\gamma$ background contribution. It is easier, however, to define a $Z\gamma$ control region than a $W\gamma$ control region due to the efficacy of identifying $Z \to ll$ events in data with a few simple selections (see

---

[12]The photon can be directly misidentified as an electron during reconstruction, or the photon can convert into an e^+e^- pair while passing through the detector.

[13]For details regarding the MC samples, see Section 5.3.2.

Section 8.2.1). The resulting $Z\gamma$ control region (see Table 7.10) is designed to isolate $Z\gamma \to \mu^{\pm}\mu^{\mp}e$ events with selections including:

- The leading and subleading leptons are muons (no requirement on lepton charge).

- An additional *veto* electron is in the event with $p_T > 27$ GeV[14].

- The invariant mass of the $\mu\mu e$ system is near the expected $Z\gamma$ mass.

Figure 8.12 shows the dimuon invariant mass distribution for data and expected background in the $Z\gamma$ control region. Table 8.4 displays the event yields for observed data and expected background in the $Z\gamma$ control region.
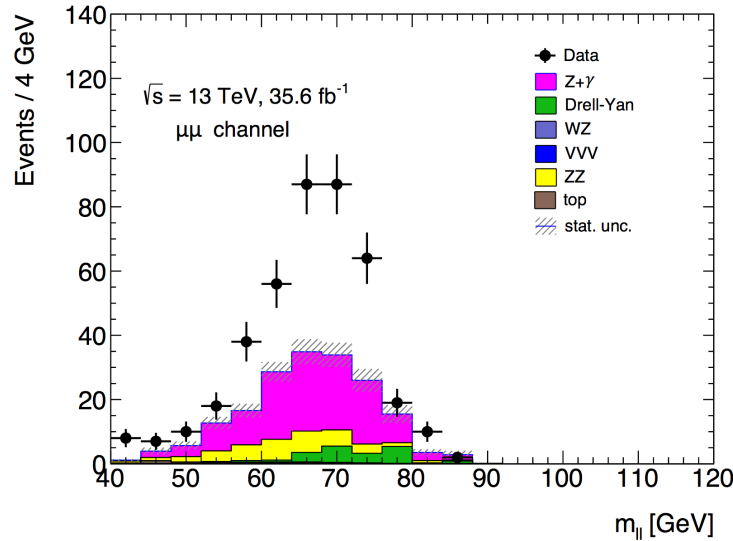
Figure 8.12: Dimuon invariant mass distribution for observed data and expected background in the $Z\gamma$ control region.

To account for the difference between the observed data and expected background, a $V\gamma$ normalization scale factor is employed. This scale factor is measured in the $Z\gamma$ control region and is used to scale the $V\gamma$ backgrounds in the signal region. The resulting normalization scale factor has a value of 1.77 and is applied to both $W\gamma$ and $Z\gamma$ backgrounds in the signal region. The full effect of the correction is assigned as a systematic uncertainty in the signal region, amounting to a 44% uncertainty.

---

[14]This selection essentially selects a signal electron with looser identification and isolation requirements.

$Z\gamma$ Control Region	
$\mu^{\pm}\mu^{\mp}e + \mu^{\mp}\mu^{\pm}e$ channel	
$Z\gamma$	24.60 ± 3.32
Drell-Yan	3.02 ± 1.54
$VV + VVV$	6.66 ± 0.32
top	1.49 ± 0.51
Total Expected	35.76 ± 3.71
Data	57

Table 8.4: Event yield in the $Z\gamma$ control region. Only statistical uncertainties are shown.

8.3   Non-Prompt Background

The non-prompt background[15] consists of Standard Model processes where one (or more) of the final state leptons is non-prompt or fake:

- **Non-Prompt Lepton:** A lepton from a secondary interaction (such as a b-hadron decay) that is incorrectly associated with the primary vertex.

- **Fake Lepton:** A highly collimated jet that is incorrectly reconstructed as a lepton (where no lepton previously existed).

The dominant sources of non-prompt background are W+jets and $t\bar{t}$ events, such as those illustrated in Figure 8.13. Both of these processes (as illustrated) produce one prompt lepton with the possibility for one of the emitted quarks to result in a non-prompt lepton.
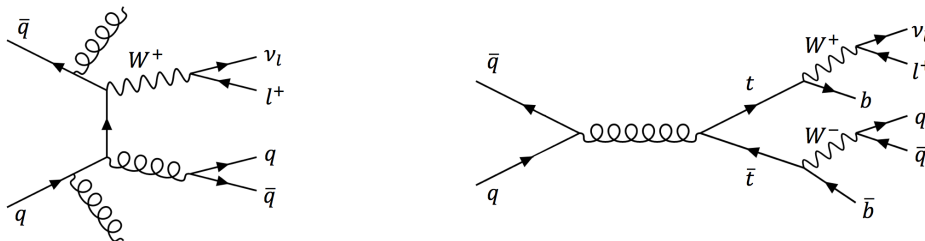
Figure 8.13: Illustration of W+jets (left) and $t\bar{t}$ (right) processes that contribute to the non-prompt background.

---

[15]This background would be more accurately named the "non-prompt and fake background", but the name is shortened to "non-prompt background" for simplicity.

The probability of a jet to be reconstructed as a lepton[16] is not well modeled in MC simulation, therefore the non-prompt background is estimated using a data-driven method. This data-driven method is very similar in concept to the method used to determine the charge misID background. In the non-prompt data-driven method, collision data is used to determine a scale factor called the *fake factor*. The fake factor is a measure of the probability an event involves a non-prompt lepton in the final state. The non-prompt background contribution is then determined by weighting collision data events with this fake factor.

In the bullet points immediately above, two different sources of non-prompt leptons are defined. Of these two sources, the first is more likely to produce a non-prompt muon while the second is more likely to produce a non-prompt electron. Given this, independent fake factors are measured for non-prompt electrons and non-prompt muons. The following sections outline how the fake factors are calculated (see Section 8.3.1), the systematic uncertainties associated with the fake factors (see Section 8.3.2), and how the non-prompt background is estimated and modeled (see Section 8.3.3).

8.3.1 Fake Factor

The fake factor measurement relies on the fact that, while a prompt lepton can be expected to pass all the *signal* lepton selections, non-prompt leptons are more likely to fail some of these selections (such as the isolation or ID requirements). As a result, the fake factor is measured using events unlikely to produce prompt leptons, where the rate at which non-prompt leptons pass the *signal* lepton selections can be examined.

The fake factor is measured using a *dijet sample*. This dijet sample has high statistics and a high purity of collision data events containing two jets with, ideally, no prompt leptons. Using this dijet sample, the fake factor is measured by comparing how often a jet is reconstructed as a *tight* lepton versus a *loose* lepton:

- **_Tight_ Lepton:** A *tight* lepton has the same selections as a *signal* lepton outlined in Tables 7.1 and 7.2 for muons and electrons, respectively, with the adjustment that the lepton p_T requirement is lowered to $p_T > 15(20)$ GeV for muons(electrons)[17].

- **_Loose_ Lepton:** *Loose* lepton selections are defined in Tables 7.1 and 7.2 for muons and electrons, respectively. *Loose* leptons have less strict isolation and ID requirements compared to *signal* leptons, and they cannot be leptons that pass the *tight* lepton selections.

To measure the fake factor, events in the dijet sample must contain both of the following: (1) a lepton (which should be a non-prompt lepton) that passes either the *tight* or *loose*

---

[16]When "a jet reconstructed as a lepton" is stated, it refers to both sources of non-prompt leptons listed in the text.

[17]Electrons and muons are selected with differing values of p_T due to an inconsistency in the dijet data sample preselections.

selections, and (2) at least one jet, known as the *tag* jet. If there is more than one jet in the event, the tag jet is taken as the leading jet in the event. This tag jet is required to pass jet quality selections and have a jet $p_T > 25(30)$ GeV for $|\eta| < 2.5$ ($2.5 < |\eta| < 4.5$). To reduce any contributions from prompt leptons, a cut limiting $m_T + E_T^{miss}$ is applied (see Section 8.3.1.2). In addition, since most non-prompt leptons in the signal region are the result of heavy-flavor[18] jets, the tag jet is required to be *b*-tagged to better recreate the signal region conditions. Finally, the lepton and tag jet are required to be balanced back-to-back with a $|\Delta\phi(l,j)| > 2.8$ cut. The complete list of selections defining this dijet region are summarized in Table 8.5.

Dijet Region Selections
One non-prompt lepton with $p_T > 15(20)$ GeV
$n_{jet} > 0$
Tag jet $p_T > 25(30)$ GeV
Tag jet is *b*-tagged
$m_T + E_T^{miss} < 50$ GeV
$|\Delta\phi(l,j)| > 2.8$
Tight or *Loose* lepton

Table 8.5: Selections defining the dijet region. These selections are applied to the dijet data sample used to determine the fake factor.

Using events which pass the selections listed in Table 8.5, the fake factor (f) is determined by taking the ratio of the number of *tight* leptons in the dijet region to the number of *loose* leptons in the dijet region:

$$f = \frac{N_{tight}}{N_{loose}}. \tag{8.12}$$

This ratio provides a measure of how often a non-prompt lepton in the dijet region is reconstructed as a *tight/signal* lepton. To account for kinematic dependencies, the fake factor is usually calculated in bins of lepton p_T (and for electrons, $|\eta|$).

Before the fake factor can be calculated, corrections must be made to Equation 8.12 to account for: (1) the impact of the kinematics of the jet which was reconstructed as a lepton (referred to as the *underlying jet*), and (2) the contamination in the dijet region from processes that produce prompt leptons (such as W+jets). The details regarding these corrections are discussed below, followed by the final fake factor measurement.

---

[18]Heavy-flavor jets are jets resulting from the hadronization of heavy quarks, such as *b*- or *c*-quarks.

8.3.1.1   Impact of Underlying Jet

In events where two jets are balanced against each other, it is expected that, on average, the two jets are produced with roughly the same p_T. In the dijet region, events containing a jet balanced against a jet reconstructed as a lepton are selected by requiring $|\Delta\phi(l,j)| > 2.8$. Since these two objects are balanced against one another, it is reasonable to expect that the lepton is reconstructed with the majority of the p_T of the underlying jet. It is clear from Figure 8.14, however, that non-prompt leptons are reconstructed with only a fraction of the underlying jet p_T. Figure 8.14 shows the lepton p_T (left) and tag jet p_T (right) in the dijet region after the $|\Delta\phi(l,j)|$ cut is applied.
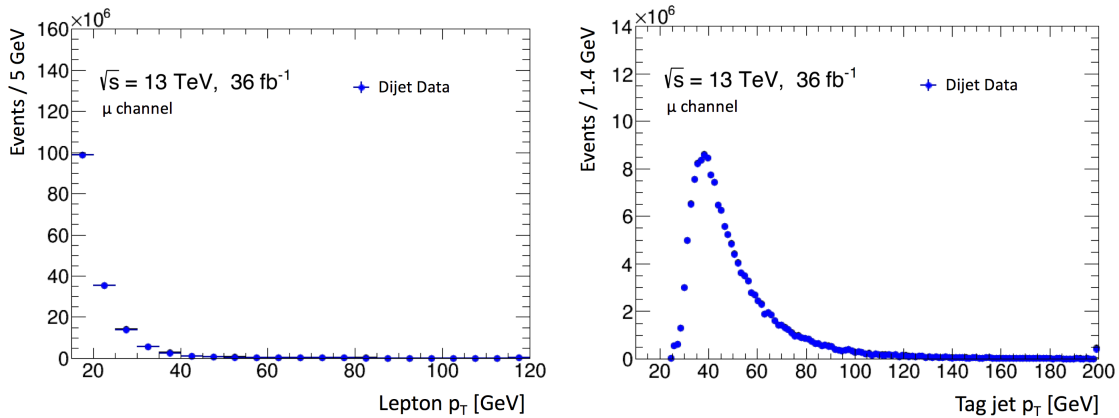
Figure 8.14: Lepton p_T (left) and tag jet p_T (right) for events producing a non-prompt muon in the dijet data region after the $|\Delta\phi(l,j)| > 2.8$ cut is applied. No selection on *tight* and *loose* muons has been applied at this point.

On average, *tight* leptons carry a larger percentage of the underlying jet p_T compared to *loose* leptons. This is due to the stricter isolation requirements applied to the *tight* leptons. The tighter isolation requirements essentially limit the amount of detector activity allowed around the lepton. Hence, leptons with multiple nearby tracks sharing the underlying jet p_T would not pass the strict isolation required for *tight* leptons.

The discrepancy between the percentage of underlying jet p_T carried by *tight* leptons and *loose* leptons in the dijet region is studied explicitly for muons using $t\bar{t}$ MC simulated events. By using MC simulated events, the non-prompt leptons can be associated with the true underlying jets. The $t\bar{t}$ MC events are required to pass all the requirements listed in Table 8.5. The p_T of the resulting *tight* and *loose* muons $[p_T(\mu)]$ are compared to the p_T of the truth-associated underlying jet $[p_T(jet)]$[19] using:

$$\Delta p_T(\mu, jet) = \frac{p_T(jet) - 2p_T(\mu)}{p_T(jet)}. \tag{8.13}$$

---

[19]In ATLAS reconstruction algorithms, the p_T of any electrons near a jet are taken into account during reconstruction; the same is not done for muons near a jet.

In Equation 8.13, $\Delta p_T(\mu, jet)$ is negative if the muon carries more than 50% of the underlying jet p_T, and positive if the muon carries less than 50%. Figure 8.15 shows the $\Delta p_T(\mu, jet)$ distributions for *tight* muons (listed as nominal in figure legend) and *loose* muons in the $t\bar{t}$ MC simulated events.
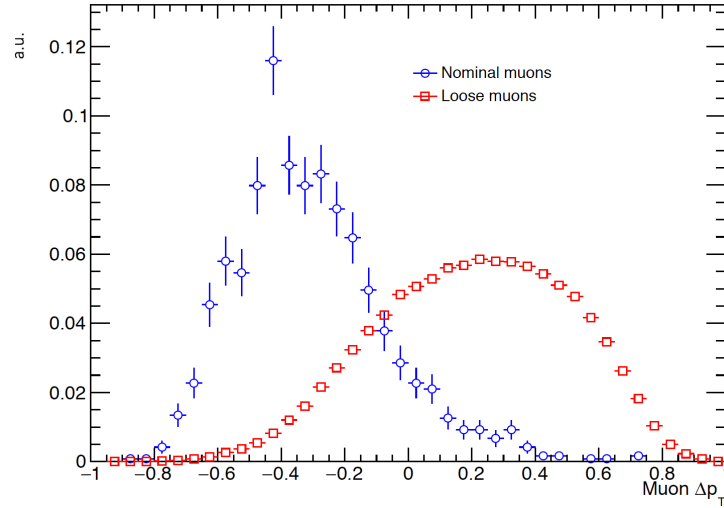
Figure 8.15: $\Delta p_T(\mu, jet)$ distribution for *tight* muons (nominal muons in legend) and *loose* muons in the dijet region for MC simulated $t\bar{t}$ events [153]. Each muon was matched to a generator-level truth jet. Both distributions are normalized to unit area.

Figure 8.15 shows that, on average, *tight* muons are reconstructed with over 50% of the underlying jet p_T, while *loose* muons, on average, are reconstructed with less than 50% of the underlying jet p_T. Thus, for a given lepton p_T bin, *loose* leptons falling within said p_T bin are likely to originate from higher p_T jets than *tight* leptons falling within the same p_T bin. Since the fake factor is measured in bins of lepton p_T, this means the kinematics of the events populating the numerator in Equation 8.12 can differ significantly from the kinematics of the events populating the denominator.

To attempt to correct for the difference between the underlying jet p_T spectra of the numerator and denominator terms in Equation 8.12, the *loose* lepton p_T is redefined as:

$$p_T^{loose} = p_T^{lep} + p_T^{cone}, \tag{8.14}$$

where the original reconstructed lepton p_T (p_T^{lep}) is added to the $\sum p_T$ of all tracks originating from the same PV with $p_T > 1$ GeV in a $\Delta R < 0.3$ cone around the lepton (p_T^{cone}). This additional activity is added to the *loose* lepton p_T in an attempt to increase the fraction of the underlying jet p_T carried by the *loose* lepton and, as a result, reduce the difference between the underlying jet p_T distribution for *tight* and *loose* leptons with similar reconstructed p_T.

The impact of this redefinition can be observed by examining the $\Delta p_T(lep, jet)$ distributions for electrons and muons using the following $\Delta p_T^*(lep, jet)$ definition[20]:

$$\Delta p_T^*(lep, jet) = \frac{p_T(jet) - p_T(lep)}{p_T(jet) + p_T(lep)}. \tag{8.15}$$

When studying muons with Equation 8.15, $p_T(jet)$ has been corrected to include the momentum of all generator-level (truth) muons within a cone $\Delta R < 0.4$:

$$p_T(jet) = p_T^{true}(jet) + \sum_{\Delta R < 0.4} p_T^{true}(\mu). \tag{8.16}$$

With these $\Delta p_T^*(lep, jet)$ and $p_T(jet)$ definitions, perfect agreement between the reconstructed lepton and underlying jet would result in a $\Delta p_T^*(lep, jet)$ value approximately equal to zero[21]. Figure 8.16 shows the $\Delta p_T^*(lep, jet)$ for *tight* leptons (listed as *nominal* in figure legend) and *loose* leptons with the original and redefined object p_T. Figure 8.16(left) shows the $\Delta p_T^*(lep, jet)$ distributions for electrons, while Figure 8.16(right) shows the distributions for muons.
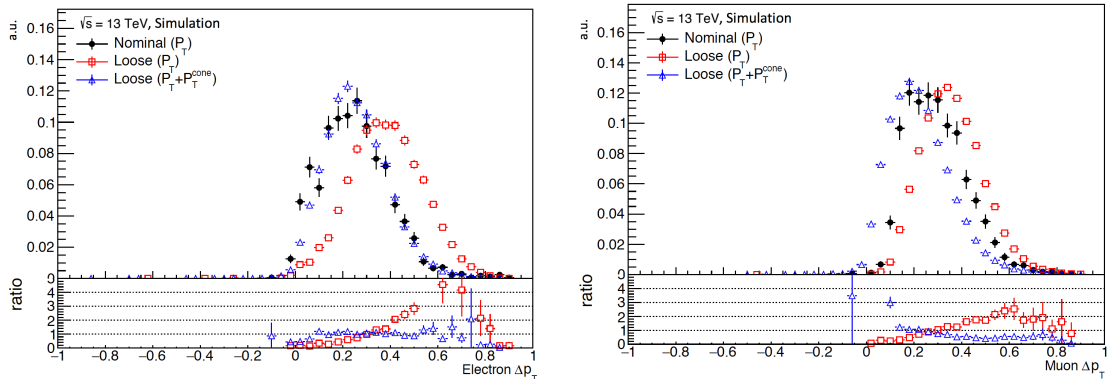
Figure 8.16: $\Delta p_T^*(lep, jet)$ distribution for *tight* leptons (listed as nominal in legend) and *loose* leptons with both $p_T^{loose} = p_T^{lep}$ and $p_T^{loose} = p_T^{lep} + p_T^{cone}$ in the dijet region for MC simulated $t\bar{t}$ events [153]. $\Delta p_T^*(lep, jet)$ distributions are shown for electrons (left) and muons (right). All distributions have been normalized to unit area.

Figure 8.16 verifies the observations from Figure 8.15 (where the jet p_T was not corrected for muons near the jet) that *tight* and *loose* leptons are reconstructed with a fraction of the underlying jet p_T. In addition, Figure 8.16 shows that by redefining the p_T of *loose* leptons to include p_T^{cone}, *tight* and *loose* leptons now reconstruct a similar fraction of the underlying jet p_T.

---

[20]The asterisk ($*$) distinguishes this $\Delta p_T(lep, jet)$ definition from the one given in Equation 8.13 which was written to more clearly demonstrate the difference between the behavior of *tight* and *loose* muons.

[21]Since any momentum carried by neutrinos cannot be detected, $\Delta p_T^*(lep, jet)$ values are expected to be shifted from zero slightly.

Throughout the remainder of this dissertation, p_T^{loose} is used as the p_T of *loose* leptons. Accordingly, the fake factor defined in Equation 8.12 is more accurately determined by taking the ratio of the number of selected events with *tight* leptons to the number of selected events with *loose* leptons in a given bin x using:

$$f_{lepton,x} = \frac{N_{tight,x(p_T)}}{N_{loose,x(p_T^{loose})}} \qquad (8.17)$$

in bins of p_T for muons, and bins of p_T and η for electrons.

8.3.1.2 Prompt Contamination

The dijet region is designed to provide a pure sample of events with a non-prompt lepton balanced against a jet. In actuality, however, the dijet region is contaminated with processes that produce prompt leptons, such as W+jets, Z+jets, $t\bar{t}$, and single top. In order to remove the prompt contamination, two steps are taken: (1) a kinematic cut is applied to reduce the prompt contamination, and (2) the remaining prompt contamination is subtracted from the data using MC simulated events.

The two largest sources of prompt events in the dijet region are W+jets and $t\bar{t}$, both of which involve $W \to l\nu$ decays. These prompt $W \to l\nu$ events are more likely to have a higher $m_T + E_T^{miss}$ due to the presence of the neutrino in the event[22]. As a result, requiring a low $m_T + E_T^{miss}$ can significantly reduce the number of W+jets and $t\bar{t}$ events in the dijet region. Hence, events in the dijet region are required to have $m_T + E_T^{miss} < 50$ GeV. Implementing the $m_T + E_T^{miss}$ cut reduces the prompt contamination by 25% in the dijet region. Figure 8.17 shows the dijet data and remaining MC estimated prompt contamination as a function of the tag jet p_T after the $m_T + E_T^{miss}$ cut is applied.

---

[22]The transverse mass, m_T, is defined as $m_T = \sqrt{2p_T E_T^{miss}(1 - \cos(\Delta\phi))}$ where $\Delta\phi$ is the azimuthal angle between the lepton and the direction of the missing momentum.
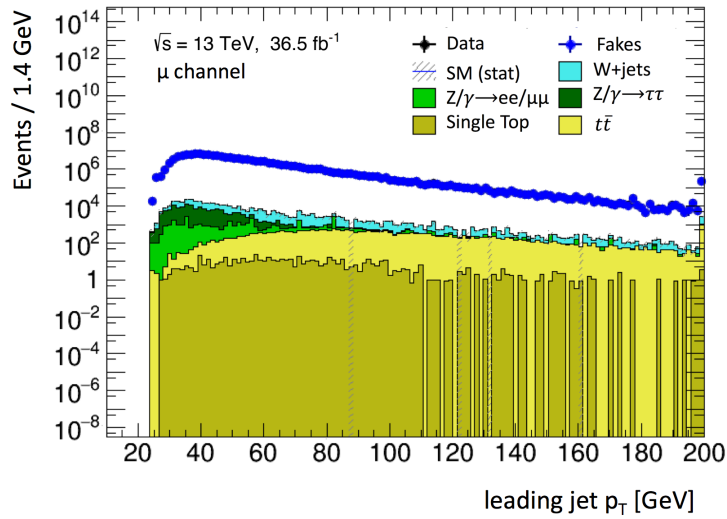
Figure 8.17: Tag jet p_T distribution in the dijet region after $m_T + E_T^{miss}$ cut is applied. Dijet data is shown with prompt contributions estimated using MC simulation. Dijet data with the prompt contribution subtracted is shown as "fakes". Plot is shown on a log scale.

After the $m_T + E_T^{miss}$ cut, the remaining prompt contamination is estimated using MC simulation and is subtracted from the dijet data. To test how well the MC simulation models the prompt contributions in the dijet region, a control region is designed to isolate the largest remaining source of prompt events: W+jets. This W+jets control region is outlined in Table 8.6.

W+jets Control Region
One lepton with $p_T > 35$ GeV
$n_{jet} > 0$
Tag jet $p_T > 25(30)$ GeV
$m_T + E_T^{miss} > 60$ GeV
Tight lepton

Table 8.6: Selections defining the W+jets control region used to assess the prompt contamination modeling accuracy.

Figure 8.18 shows the $m_T + E_T^{miss}$ distribution for *tight* muons in the W+jets control region. As expected, the region is dominated by W+jets events, with much smaller contributions from the other prompt processes. Figure 8.18 also shows the expected dijet event contribution measured with a dijet MC sample filtered for events producing a muon. The dijet data and prompt MC simulation in Figure 8.18 agree within approximately 10%. Given this level of agreement, the prompt MC simulated events in the dijet region are subtracted

from the dijet data. The residual disagreement between data and MC is assessed as a systematic uncertainty on the fake factor (see Section 8.3.2.2).
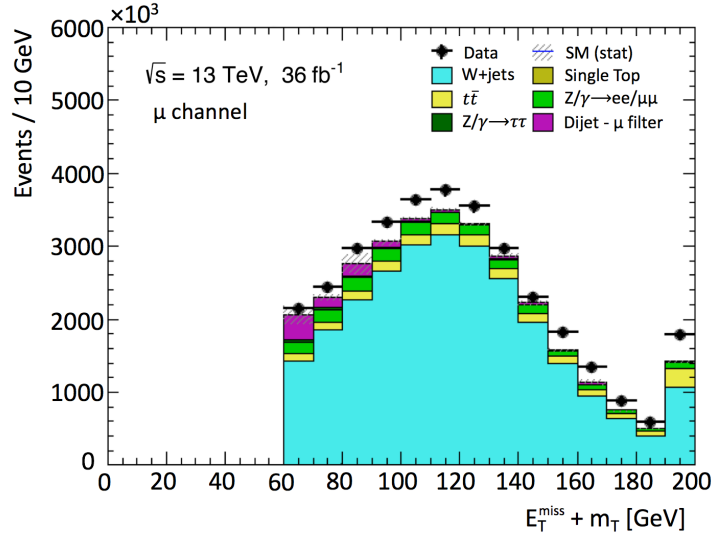
Figure 8.18: Sum of E_T^{miss} and m_T in the W+jets control region for events with a final state muon. Dijet data is shown with the prompt contribution estimated using MC samples. The expected contribution from dijet is shown with a dijet MC sample filtered for events with muons.

8.3.1.3   Final Fake Factor Measurement

Taking into account the prompt contamination subtraction, the equation for calculating the fake factor becomes:

$$f_{lepton,x} = \frac{N_{tight,x(p_T)}^{data} - N_{tight,x(p_T)}^{promptMC}}{N_{loose,x(p_T^{loose})}^{data} - N_{loose,x(p_T^{loose})}^{promptMC}}. \tag{8.18}$$

Using Equation 8.18, fake factors are calculated independently for dijet events with a non-prompt electron in the final state and dijet events with a non-prompt muon in the final state. Figure 8.19 shows the *tight* and *loose* lepton p_T distributions used to calculate the fake factors[23]. The top two plots in Figure 8.19 show the *tight* lepton p_T distributions of dijet data and MC prompt contamination with a muon in the final state (left) and an electron in the final state (right). The "fakes" distributions (which show the dijet data with the prompt MC subtracted) represent the input to the numerator of Equation 8.18 for the electron and muon fake factor, respectively. Similarly, the bottom two plots in Figure 8.19 show the *loose*

---

[23]Distributions for electrons show all η values combined. In reality, the electron fake factor is calculated in two η bins.

lepton p_T^{loose} distributions ($p_T^{loose} = p_T + p_T^{cone}$) of dijet data and prompt MC contamination with a muon in the final state (left) and an electron in the final state (right). Once again, the "fakes" distributions (which show dijet data with prompt MC subtracted) represent the input to the denominator of Equation 8.18.
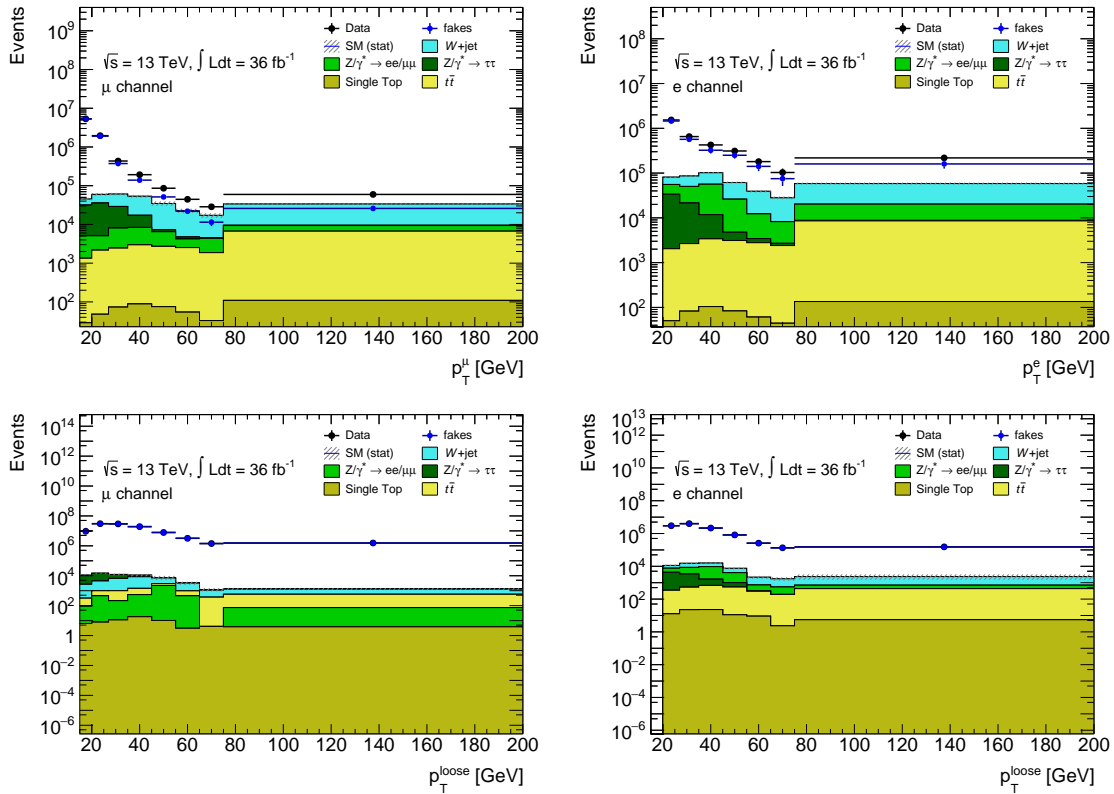
Figure 8.19: *Top: Tight* lepton p_T distributions of dijet data and MC prompt contamination in the dijet region for muon final state events (left) and electron final state events (right). *Bottom: Loose* lepton p_T^{loose} distributions ($p_T^{loose} = p_T + p_T^{cone}$) of dijet data and MC prompt contamination in the dijet region for muon final state events (left) and electron final state events (right). The "fakes" distributions represent the dijet data with the MC prompt contamination subtracted.

With Equation 8.18 and Figure 8.19, the muon fake factor is calculated in eight bins of p_T beginning with $p_T > 15$ GeV. The electron fake factor is calculated in seven bins of p_T beginning with $p_T > 20$ GeV[24] and two η bins ($|\eta| < 1.37$ and $|\eta| > 1.52$). The final fake factor measurements for electrons and muons can be seen in Figure 8.20. Several systematic

---

[24]An inconsistency in the dijet data preselections resulted in a minimum p_T of 20 GeV for electrons instead of 15 GeV. The inconsistency was not corrected in time to be propagated through the full analysis chain before the analysis publication.

uncertainties are assigned to the fake factor calculation; these uncertainties are discussed in the next section (see Section 8.3.2).
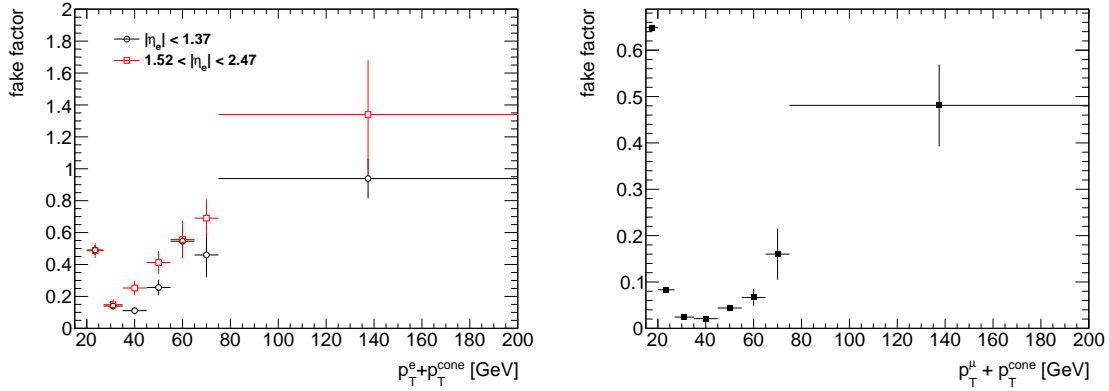
Figure 8.20: Fake factors calculated for electrons (left) and muons (right) in bins of p_T^{loose}. Error bars show statistical uncertainties only.

8.3.2   Fake Factor Systematic Uncertainties

Several systematic uncertainties are assessed on the fake factor including uncertainties for: the dijet region kinematic selections, the prompt lepton subtraction, the jet flavor composition, and the underlying jet p_T dependency. Each of these systematic uncertainties is described below.

8.3.2.1   Dijet Region Kinematic Selection Variations

To account for the impact of the dijet region selections on the fake factor, new fake factors are calculated varying the following dijet selections slightly:

- tag jet $p_T > 25(30)$ GeV for $|\eta| < 2.4 (2.4 < |\eta| < 4.5)$

- $m_T + E_T^{miss} < 50$ GeV

- $\Delta\phi(l, j) > 2.8$

The tag jet p_T threshold is increased by 5 GeV, the $m_T + E_T^{miss}$ cut is varied up and down by 5 GeV, and the $\Delta\phi(l, j)$ cut is varied by 0.1 (up and down). The difference between the fake factor determined with each individual variation and the nominal fake factor is taken as a systematic uncertainty. The systematic fake factors calculated with each kinematic systematic variation are shown in Figure 8.21 for muons and Figure 8.22 for electrons.
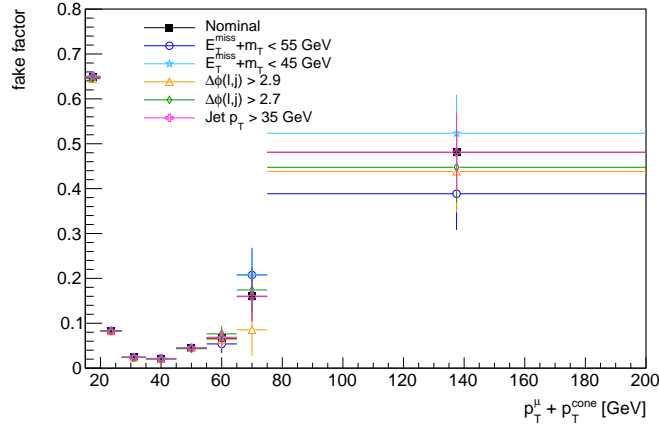
Figure 8.21: Nominal and systematic muon fake factor resulting from: increasing the jet p_T threshold by 5 GeV, varying the $m_T + E_T^{miss}$ cut up and down by 5 GeV, and varying the $\Delta\phi(l, j)$ cut by 0.1 up and down.
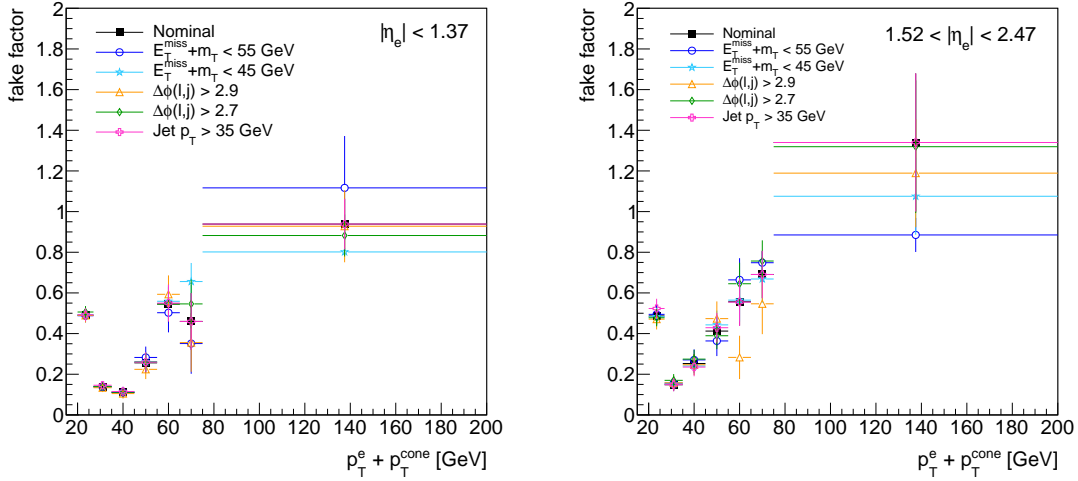
Figure 8.22: Nominal and systematic electron fake factor resulting from: increasing the jet p_T threshold by 5 GeV, varying the $m_T + E_T^{miss}$ cut up and down by 5 GeV, and varying the $\Delta\phi(l, j)$ cut by 0.1 up and down. *Left:* central electrons, $|\eta_e| < 1.37$. *Right:* forward electrons, $1.52 < |\eta_e| < 2.47$.

8.3.2.2   Prompt Lepton Subtraction

A systematic uncertainty is assessed on the fake factor to account for the 10% disagreement between the observed data and MC estimation modeling of prompt processes in the dijet region (see Section 8.3.1.2). To measure the systematic uncertainty, the subtracted MC simulated prompt contamination is increased and decreased by 10%, and the fake factors are recalculated. The systematic uncertainty is estimated by taking the difference between the varied fake factors and the nominal fake factor. The fake factors calculated with the varied prompt subtraction are shown with the nominal fake factor in Figure 8.23 for muons and Figure 8.24 for electrons.
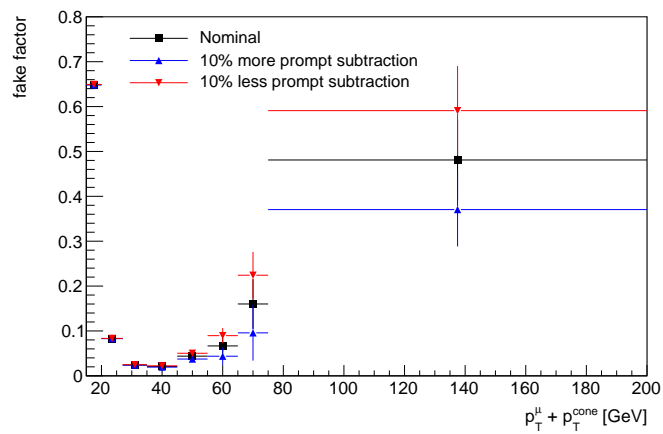
Figure 8.23: Nominal muon fake factor shown with the muon fake factors calculated with varying the prompt subtraction up and down by 10%.
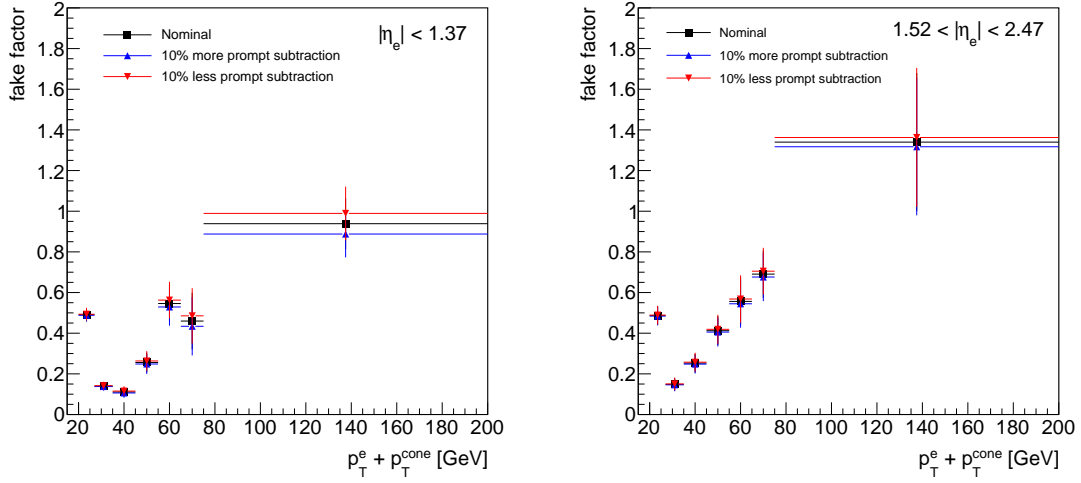
Figure 8.24: Nominal electron fake factor shown with the electron fake factors calculated with varying the prompt subtraction up and down by 10%. *Left:* central electrons, $|\eta_e| < 1.37$. *Right:* forward electrons, $1.52 < |\eta_e| < 2.47$.

8.3.2.3 Jet Flavor Composition

To account for any differences between the jet flavor composition[25] of the dijet region and the region where the fake factor is applied, the fake factor is measured with a b-tagged jet veto instead of requiring the tag jet to be b-tagged. The fake factor calculated with the b-tagged jet veto is shown with the nominal fake factor for comparison in Figure 8.25 for muons and Figure 8.26 for electrons. The resulting difference between the b-tagged jet veto fake factor and the nominal fake factor is taken as a systematic uncertainty.

This uncertainty is one of the largest sources of uncertainty on the fake factor, with shifts from the nominal fake factor averaging between $40-80\%$. The full impact of this uncertainty on the nominal fake factor in each p_T^{loose} bin is listed in Table 8.7 for the electron and muon fake factors.

---

[25]*Flavor composition* refers to whether the jets come from the fragmentation of light quarks (such as u, d) or heavy quarks (such as b, c).
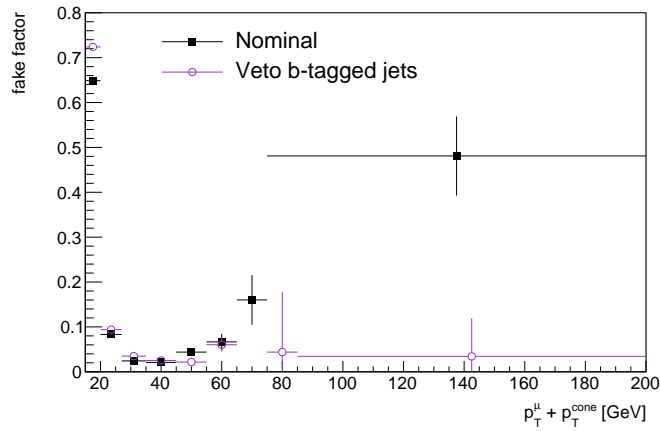
Figure 8.25: Nominal muon fake factor and systematic muon fake factor calculated with a b-tagged jet veto during dijet event selection.
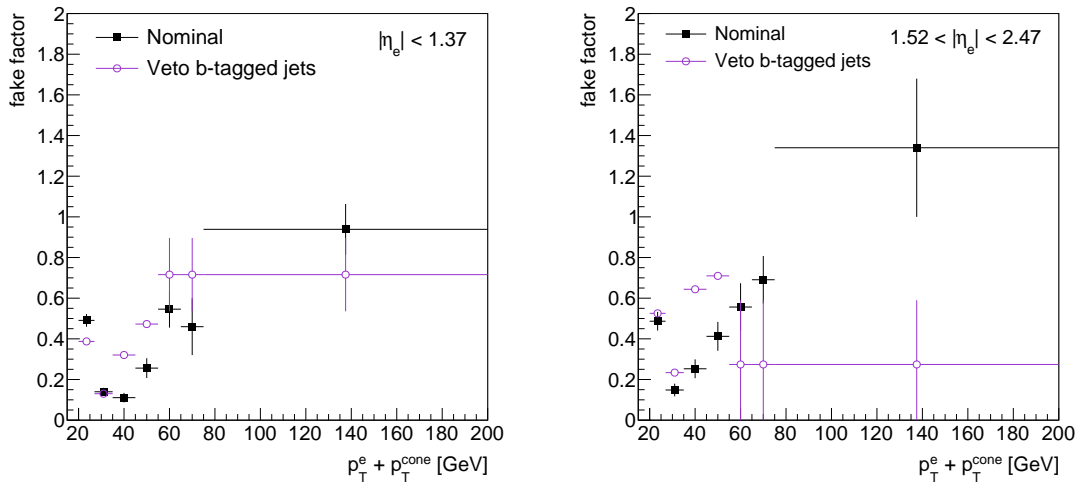
Figure 8.26: Nominal electron fake factor and systematic electron fake factor calculated with a b-tagged jet veto during dijet event selection. *Left:* central electrons, $|\eta_e| < 1.37$. *Right:* forward electrons, $1.52 < |\eta_e| < 2.47$.

Impact of Jet Flavor Systematic on Fake Factor

p_T^{loose} bin [GeV]	electron ($|\eta| < 1.37$)	electron ($|\eta| > 1.37$)	muon
15-20	-	-	11.6%
20-27	21.1%	8.0%	12.8%
27-35	6.8%	57.7%	43.9%
35-45	189.6%	154.7%	20.2%
45-55	84.7%	177.2%	50.6%
55-65	31.1%	49.8%	9.5%
65-75	55.7%	40.4%	83.8%
75-200	23.7%	70.8%	90.9%

Table 8.7: Impact of jet flavor systematic uncertainty on electron and muon fake factors in bins of *loose* lepton p_T^{loose}.

8.3.2.4   Underlying Jet p_T Dependency

The object p_T of *loose* leptons is redefined as $p_T^{loose} = p_T + p_T^{cone}$ (see Section 8.3.1.1) to improve the agreement between how *tight* leptons and *loose* leptons model the underlying jet p_T distribution. While redefining p_T^{loose} improves the agreement, both *tight* and *loose* leptons still only reconstruct a portion of the underlying jet p_T. As a result, the residual dependence of the fake factor on the underlying jet p_T is accounted for using a systematic uncertainty. The systematic uncertainty is determined by reweighting the tag jet p_T distribution to a representation of the true underlying jet p_T spectrum determined using MC truth information.

A representation of the underlying true jet p_T spectrum was constructed from the two main sources of non-prompt background in the signal region: $t\bar{t}$ and W+jets. Events from these MCs were required to have a single *tight* lepton, a b-tagged jet that could potentially fake a lepton, and two other jets in the event that pass the nominal signal region selections without the Δy_{jj} and m_{jj} selection (to increase statistics). Figure 8.27 shows the nominal tag jet p_T distribution from the dijet region with the constructed true underlying jet p_T spectrum. The ratio in Figure 8.27 shows the weight that is applied to the tag jet p_T. A more detailed description of this method, along with validation studies, is provided in Appendix A.
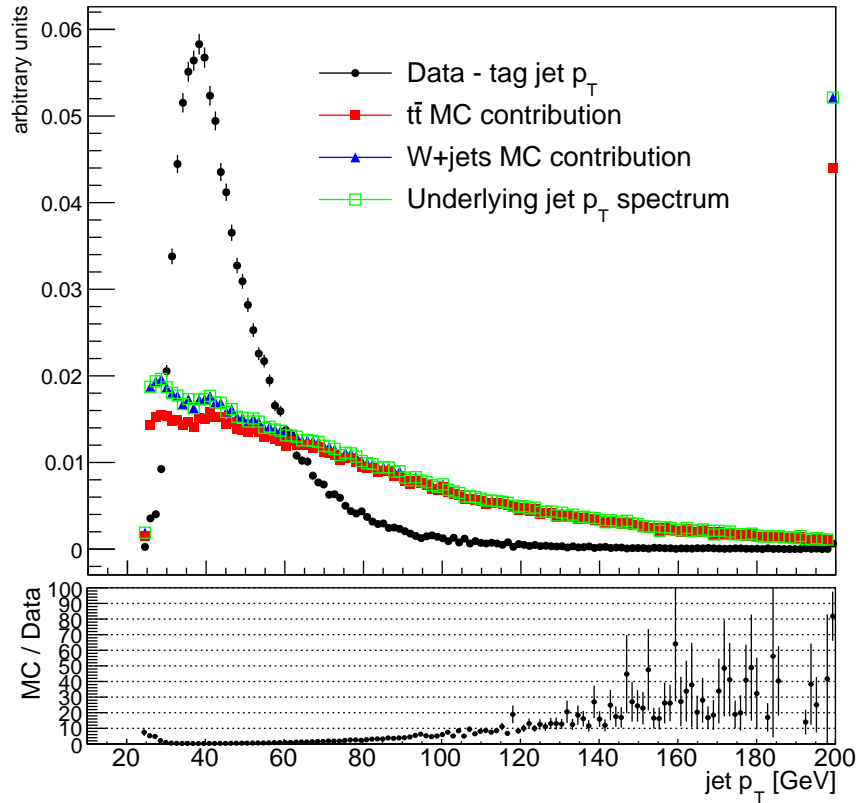
Figure 8.27: Tag jet p_T distribution (black) shown with the derived underlying jet p_T spectrum (green) with relative fractions of $t\bar{t}$ MC (red) and W+jets MC (blue) shown stacked together. The ratio shows the combined MCs compared to the tag jet p_T, which are the resulting weights applied to the dijet region events.

The tag jet p_T distribution is then weighted to this underlying jet p_T spectrum and the fake factor is recalculated. Figure 8.28 shows this recalculated fake factor alongside the nominal fake factor for muons. The electron fake factors are shown in Figure 8.29. The resulting difference between the recalculated fake factor and the nominal fake factor is taken as a systematic uncertainty.

The jet p_T reweighting uncertainty is one of the two largest sources of uncertainty for the fake factor, with statistical limitations causing high fluctuations at high lepton p_T^{loose}. Table 8.8 shows the relative impact of the jet p_T reweighting systematic on the fake factor.
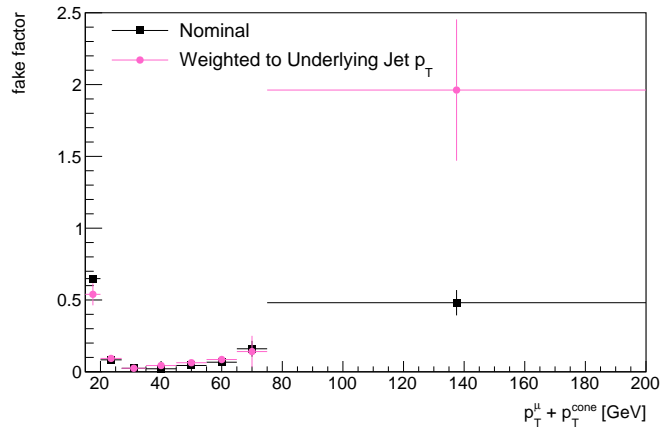
Figure 8.28: Nominal muon fake factor and muon fake factor calculated with the tag jet p_T spectrum weighted to represent the p_T spectrum of the underlying jet.
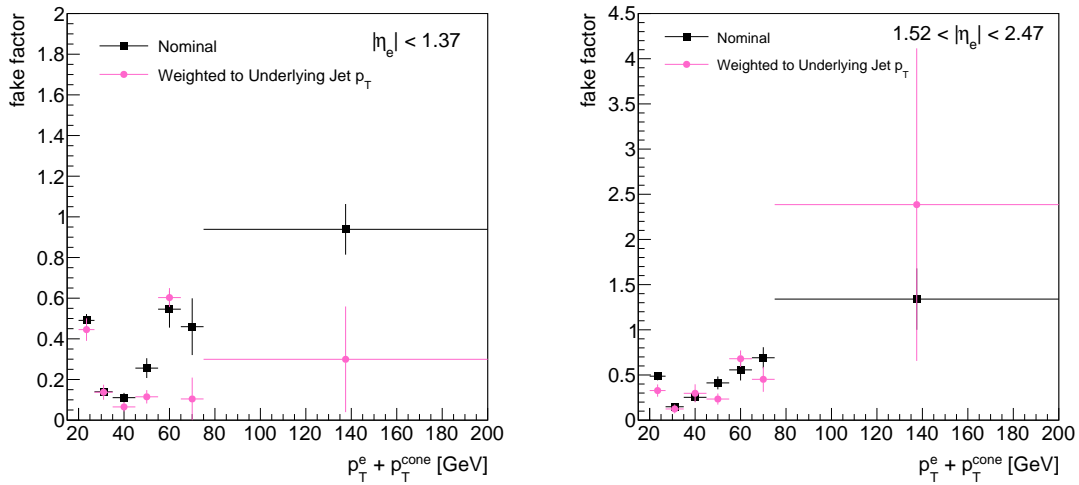
Figure 8.29: Nominal electron fake factors and electron fake factors calculated with the tag jet p_T spectrum weighted to represent the p_T spectrum of the underlying jet. *Left:* central electrons, $|\eta_e| < 1.37$. *Right:* forward electrons, $1.52 < |\eta_e| < 2.47$.

Impact of Jet p_T Reweighting Systematic

p_T^{loose} bin [GeV]	electron ($|\eta| < 1.37$)	electron ($|\eta| > 1.37$)	muon
15-20	-	-	16.9%
20-27	9.2%	32.7%	11.8%
27-35	1.6%	16.3%	1.4%
35-45	41.1%	17.6%	108.4%
45-55	55.1%	43.3%	43.8%
55-65	10.4%	22.2%	28.0%
65-75	77.3%	34.6%	12.1%
75-200	68.1%	78.0%	307.9%

Table 8.8: Impact of jet p_T reweighting systematic uncertainty on electron and muon fake factors in bins of *loose* lepton p_T^{loose}.

8.3.2.5 Summary

The final systematic uncertainties are determined by combining all the collective up and down systematic uncertainties discussed in the previous sections (see Sections 8.3.2.1 - 8.3.2.4) into the envelopes shown in Figure 8.30 for muons and Figure 8.31 for electrons. The uncertainty is propagated to the non-prompt background by executing the analysis with the up/down systematic and statistical envelope fake factors.
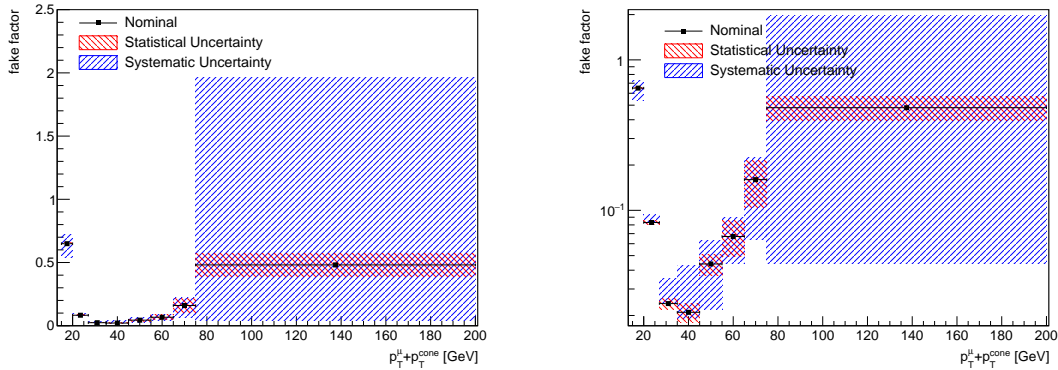
Figure 8.30: *Left:* Nominal muon fake factor shown with statistical uncertainty band and systematic uncertainty band. The systematic uncertainty band is taken as the envelope of all systematic fake factor variations. *Right:* Distributions shown on a log scale.
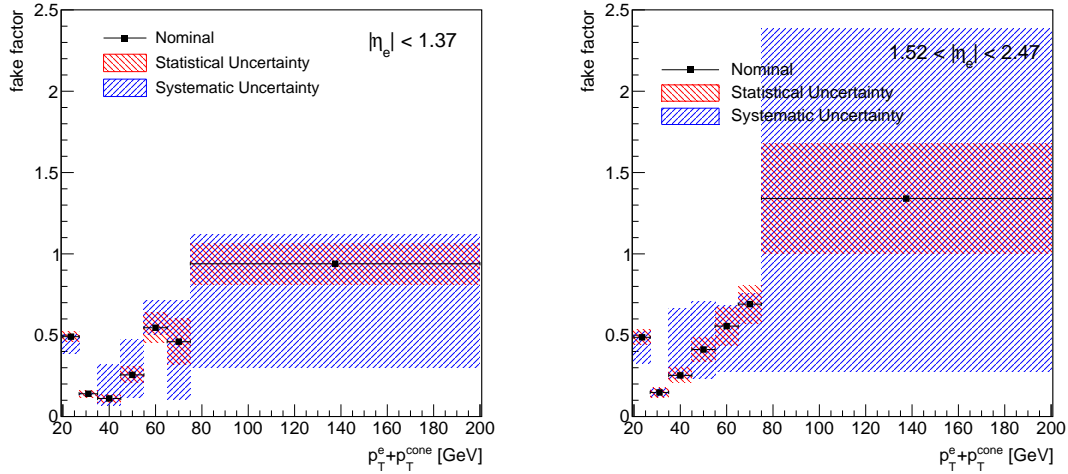
Figure 8.31: Nominal electron fake factors shown with statistical uncertainty bands and systematic uncertainty bands. The systematic uncertainty bands are taken as the envelopes of all systematic fake factor variations. *Left:* central electrons, $|\eta_e| < 1.37$. *Right:* forward electrons, $1.52 < |\eta_e| < 2.47$.

8.3.3 Non-Prompt Background Estimation

The non-prompt background is estimated by applying the fake factors (see Figure 8.20) to a region of collision data called the *signal+loose region*. The signal+loose region lies very close to the signal region with the exception that, instead of having two *signal* leptons, one lepton must be a *loose* lepton. This *loose* lepton is assumed to be a non-prompt lepton. The data from this region is then scaled by the fake factors depending upon the *loose* lepton p_T. The fake factor is a measure of how often a non-prompt lepton passes *tight/signal* lepton selections compared to *loose* lepton selections. Thus, by scaling data in the signal+loose region with the fake factor, the contribution in the signal region from events with a non-prompt lepton is estimated.

To account for contamination in the signal+loose region from events that contain two prompt leptons (such as WZ events), the contribution of these events in the signal+loose region is subtracted using MC simulation[26]. In addition to subtracting events with two prompt same-sign leptons, the contribution in the signal+loose region from charge misID events is also subtracted.

In other words, for a given p_T (/η) bin[27] x, the non-prompt background in the ee and $\mu\mu$

---

[26]Prompt events are subtracted by identifying prompt leptons with MC truth information.

[27]The non-prompt background is estimated in bins of p_T for events with non-prompt muons and bins of p_T and η for events with non-prompt electrons.

channels is estimated as:

$$N_{non-prompt}^{bkg}(x) = f_{lep}(x) \times \left[N_{signal+loose}^{data}(x) - N_{prompt}^{MC}(x) - N_{ch\text{-}misID}^{data}(x) \right], \qquad (8.19)$$

where for a given bin x in the signal+loose region: $N_{signal+loose}^{data}(x)$ is the number of data events, $N_{prompt}^{MC}(x)$ is the number of prompt MC events, and $N_{ch\text{-}misID}^{data}(x)$ is the number of charge misID events with two prompt leptons.

In the $e\mu$ channel, the non-prompt background receives contributions from two sources: (1) events with a prompt muon and a non-prompt electron, and (2) events with a non-prompt muon and a prompt electron. The non-prompt background in this channel is thus estimated using:

$$\begin{aligned} N_{non-prompt}^{bkg}(x) = {} & f_e(x) \times \left[N_{signal\ \mu+loose\ e}^{data}(x) - N_{prompt,loose\ e}^{MC}(x) - N_{ch\text{-}misID,loose\ e}^{data}(x) \right] \\ & + f_\mu(x) \times \left[N_{signal\ e+loose\ \mu}^{data}(x) - N_{prompt,loose\ \mu}^{MC}(x) - N_{ch\text{-}misID,signal\ e}^{data}(x) \right], \end{aligned}$$

$$(8.20)$$

where for a given bin x in the signal+loose region: $N_{signal\ \mu+loose\ e}^{data}(x)$ is the number of data events with a *signal* muon and a *loose* electron; $N_{prompt,loose\ e}^{MC}(x)$ is the number of MC estimated events with a prompt *signal* muon and a prompt *loose* electron; and $N_{ch\text{-}misID,loose\ e}^{data}(x)$ is the number of data-driven charge misID events with a *signal* muon and a *loose* electron. $N_{signal\ e+loose\ \mu}^{data}(x)$, $N_{prompt,loose\ \mu}^{MC}(x)$, and $N_{ch\text{-}misID,signal\ e}(x)$ are defined similarly for events with a *signal* electron and a *loose* muon.

8.3.3.1   Prompt Charge MisID Contamination

The method for estimating the prompt charge misID leptons inside the signal+loose region, which are subsequently subtracted from the non-prompt background, is very similar to the procedure for estimating the charge misID background (see Section 8.2.2): data events in an opposite-sign signal+loose region[28] are weighted with the probability to be misidentified as a same-sign event. The weights are constructed using Equation 8.7, except in the opposite-sign signal+loose region, one of the charge misID rates is the *loose* electron charge misID rate. The *loose* electron charge misID rates are shown in Figure 8.32 as a function of *loose* electron p_T and η.

The validity of estimating the prompt charge misID contamination to the non-prompt background using this data-driven method was studied in a signal+loose validation region. In this signal+loose validation region, the data and estimated background agree within 10%.

---

[28]The composition and purity of the opposite-sign signal+loose region was checked using truth information and found to consist almost entirely of prompt opposite-sign events.
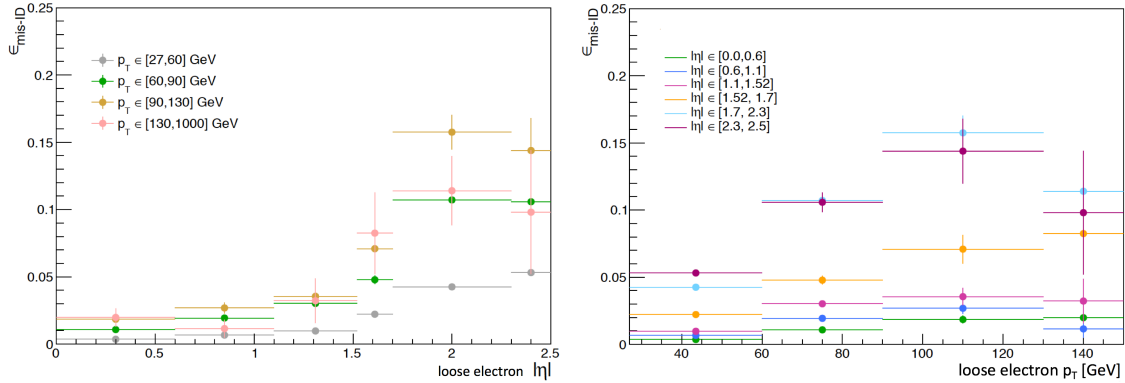
Figure 8.32: Charge misID rates for *loose* electrons retrieved using $Z \to e^+e^-$ events as a function of loose electron η (left) and p_T (right). These rates are used for estimating the charge misID background that is subtracted from the non-prompt background.

8.3.3.2   Non-Prompt Background Modeling

The non-prompt background is validated in the non-prompt validation region (see Table 7.7) where a b-tagged jet is required to enhance the contribution from $t\bar{t}$ events. The signal region m_{jj} and Δy_{jj} cuts are also removed in the non-prompt validation region to increase statistics. The event yield in the non-prompt validation region for data and the expected background is listed in Table 8.9 for the $e^\pm e^\pm$, $\mu^\pm\mu^\pm$, and $e^\pm\mu^\pm$ channels. Assuming Poisson statistics for the observed data, the data and expected background agree within the statistical uncertainty in the $e^\pm e^\pm$ channel. For the $e^\pm\mu^\pm$ and $\mu^\pm\mu^\pm$ channels, the expected background underestimates the observed data by approximately $5 - 20\%$ when taking into account only statistical uncertainties.

Non-Prompt Validation Region

	$e^\pm e^\pm$	$\mu^\pm\mu^\pm$	$e^\pm\mu^\pm$
Non-prompt	153.65 ± 11.93	95.15 ± 3.58	435.40 ± 18.89
e/γ conversion	125.31 ± 2.77	0.01 ± 0.01	465.30 ± 5.37
WZ	39.66 ± 1.03	92.61 ± 1.09	221.31 ± 2.07
$W^\pm W^\pm jj$–QCD	6.49 ± 0.08	22.78 ± 0.16	39.34 ± 0.21
Other prompt	31.59 ± 0.54	74.93 ± 0.80	148.26 ± 1.26
$W^\pm W^\pm jj$–EW	13.50 ± 18.30	33.99 ± 0.26	61.33 ± 0.34
Total Expected	353.37 ± 12.02	285.48 ± 3.83	1309.62 ± 19.79
Data	335	376	1408

Table 8.9: Event yield in the non-prompt validation region. Only statistical uncertainties are shown.

Figure 8.33 shows the p_T distribution for events with subleading electrons $(ee + \mu e)$ and subleading muons $(\mu\mu + e\mu)$ in the non-prompt validation region[29]. The uncertainty bands in Figure 8.33 represent the statistical and systematic uncertainties added in quadrature. With the addition of the systematic uncertainties, the data and expected background now agree within these large uncertainty bands.
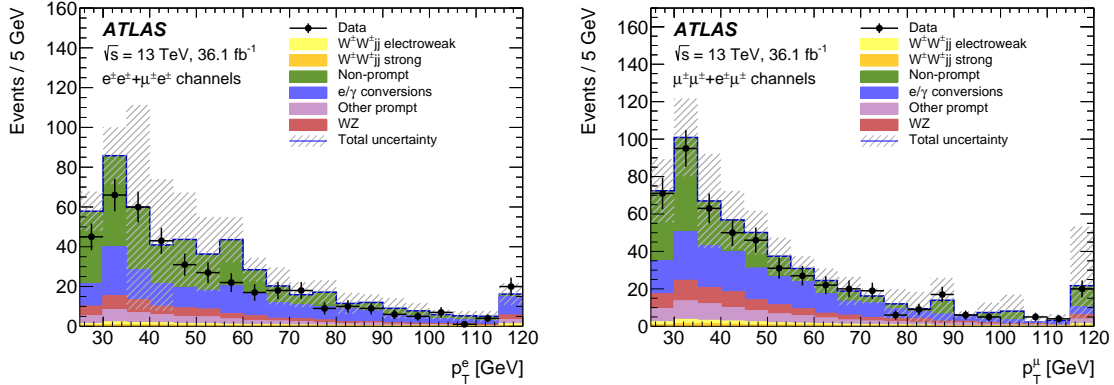
Figure 8.33: Subleading lepton p_T distributions in the non-prompt validation region. Distributions shown for events where the subleading lepton is an electron (left) and a muon (right). Hatched band represents the statistical and systematic uncertainties added in quadrature.

8.3.3.3   Impact of Systematic Uncertainties

The systematic uncertainties impacting the non-prompt background arise from the fake factor systematic and statistical uncertainties (see Section 8.3.2). The four uncertainties assessed on the non-prompt background are summarized in Table 8.10. The impact of each variation is determined by calculating the expected non-prompt background using the uncertainty envelope fake factors and taking the difference between the resulting non-prompt yield and the nominal non-prompt yield. Table 8.11 shows the impact of each systematic uncertainty on the expected non-prompt background in the signal region.

---

[29]Studies have shown that the subleading lepton in the event is more likely than the leading lepton in the event to be the non-prompt lepton.

Category	Uncertainty	Description
Electron Fake Factor	FakeElSta	Statistical uncertainty
	FakeElSys	Systematic uncertainty
Muon Fake Factor	FakeMuSta	Statistical uncertainty
	FakeMuSys	Systematic uncertainty

Table 8.10: List of non-prompt systematic uncertainties.

Impact on Non-Prompt Background Estimation

	Electron Fake Factor			Muon Fake Factor		
	stat.	syst. up	syst. down	stat.	syst. up	syst. down
$e^{\pm}e^{\pm}$	$\pm15\%$	$+15\%$	-49%	–	–	–
$e^{\pm}\mu^{\pm}$	$\pm13\%$	$+15\%$	-39%	$\pm4\%$	$+43\%$	-5%
$\mu^{\pm}\mu^{\pm}$	–	–	–	$\pm13\%$	$+76\%$	-13%

Table 8.11: Impact of fake factor uncertainties (statistical and systematic) on non-prompt background estimated yield in the combined signal+low m_{jj} region ($m_{jj} > 200$ GeV).

8.4   Total Expected Background

In addition to examining each major background in a tailored validation region, the overall modeling of the expected background is investigated in two regions: the low N_{jet} validation region and the low m_{jj} control region (which is also used during the fitting process to constrain the backgrounds).

Both the low N_{jet} and the low m_{jj} regions (see Table 7.6 and 7.8, respectively) represent a phase space orthogonal to the signal region where all major background processes contribute. The low N_{jet} validation region reverses the selection on the jets in the events, while the low m_{jj} control region selects events with 200 GeV $< m_{jj} <$ 500 GeV. The event yields for all lepton channels combined in both the low N_{jet} validation region and the low m_{jj} control region are listed in Table 8.12 with the statistical uncertainties.

Assuming Poisson statistics on the observed data, the expected background and data agree within the statistical uncertainty in the low m_{jj} control region and disagree by less than 1% in the low N_{jet} validation region. The subleading lepton p_T in the low N_{jet} validation region is shown in Figure 8.34 for events with a subleading electron (left) and a subleading muon (right). In Figure 8.34, the uncertainty shown represents the statistical and systematic uncertainties on the measurement added in quadrature. With the addition of the systematic uncertainty, the observed data and expected events agree within the total uncertainty.

	Low m_{jj} CR	Low N_{jet} VR
Non-prompt	30.08 ± 4.37	571.12 ± 19.16
e/γ conversion	13.96 ± 0.68	354.47 ± 25.13
WZ	33.92 ± 0.90	759.43 ± 8.93
$W^{\pm}W^{\pm}jj$–QCD	5.32 ± 0.08	13.45 ± 0.12
Other prompt	3.40 ± 0.16	51.42 ± 0.82
$W^{\pm}W^{\pm}jj$–EW	9.01 ± 0.0	38.18 ± 0.27
Total Expected	95.68 ± 4.52	1788.08 ± 32.85
Data	101	1871

Table 8.12: Event yield in the low m_{jj} control region (low m_{jj} CR) and low N_{jet} validation region (low N_{jet} VR) for all lepton channels combined. Only statistical uncertainties are shown.
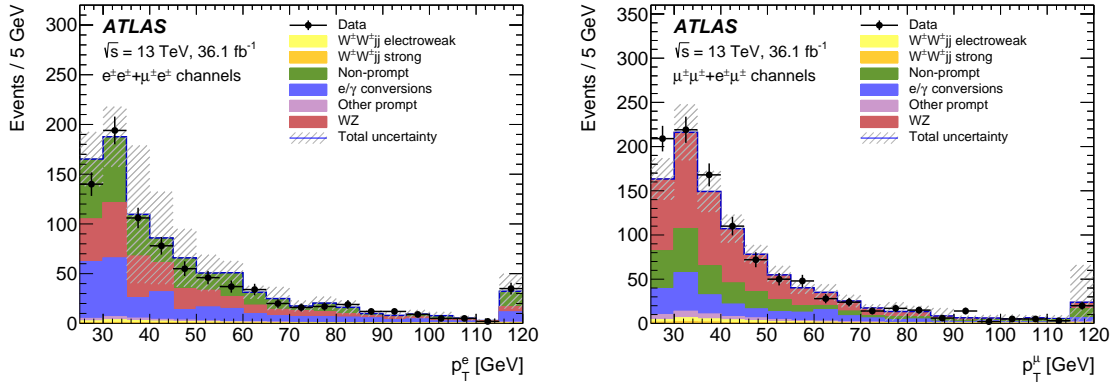
Figure 8.34: Subleading lepton p_T distributions in the low N_{jet} validation region. Distributions shown are for events where the subleading lepton is an electron (left) and a muon (right). Hatched band represents the statistical and systematic uncertainties added in quadrature.

8.4.1 Signal Region Expected Yield

The expected yield of each background process in the signal region is listed in Table 8.13 with the expected $W^{\pm}W^{\pm}jj$–EW yield and observed data. The expected yield is shown for each lepton channel and all lepton channels combined. Figure 8.35 shows the m_{jj} distributions in the signal region for all expected events and the observed data (all lepton channels combined). These expected event distributions are utilized in the likelihood fit method (see Chapter 12). The expected $W^{\pm}W^{\pm}jj$–EW signal is discussed in more detail in Chapter 9.

	e^+e^+	e^-e^-	$e^+\mu^+$	$e^-\mu^-$	$\mu^+\mu^+$	$\mu^-\mu^-$	Combined
WZ	1.9 ± 0.6	1.3 ± 0.4	14.0 ± 4.0	8.9 ± 2.5	5.5 ± 1.6	3.6 ± 1.1	35 ± 10
Non-prompt	4.0 ± 2.3	2.3 ± 1.7	9.0 ± 5.0	6.0 ± 4.0	0.55 ± 0.15	0.67 ± 0.25	23 ± 10
e/γ conversions	1.74 ± 0.29	1.8 ± 0.4	6.1 ± 1.6	3.7 ± 0.8	—	—	13.4 ± 2.5
Other prompt	0.17 ± 0.05	0.14 ± 0.04	0.90 ± 0.19	0.60 ± 0.14	0.36 ± 0.10	0.19 ± 0.05	2.4 ± 0.5
$W^\pm W^\pm jj$–QCD	0.38 ± 0.13	0.16 ± 0.05	3.0 ± 1.0	1.2 ± 0.4	1.8 ± 0.6	0.76 ± 0.25	7.3 ± 2.4
Expected background	8.2 ± 2.4	5.7 ± 1.8	33.0 ± 7.0	21.0 ± 5.0	8.2 ± 1.7	5.3 ± 1.1	81 ± 14
Expected $W^\pm W^\pm jj$–EW	3.8 ± 0.6	1.49 ± 0.22	16.5 ± 2.4	6.5 ± 1.0	9.1 ± 1.4	3.5 ± 0.5	41 ± 6
Data	10	4	44	28	25	11	122

Table 8.13: Expected background, signal, and data event yields in the signal region (before the fit). Yields are shown in each of the six channels and for all channels combined. Statistical, systematic, and theoretical uncertainties are shown added in quadrature.
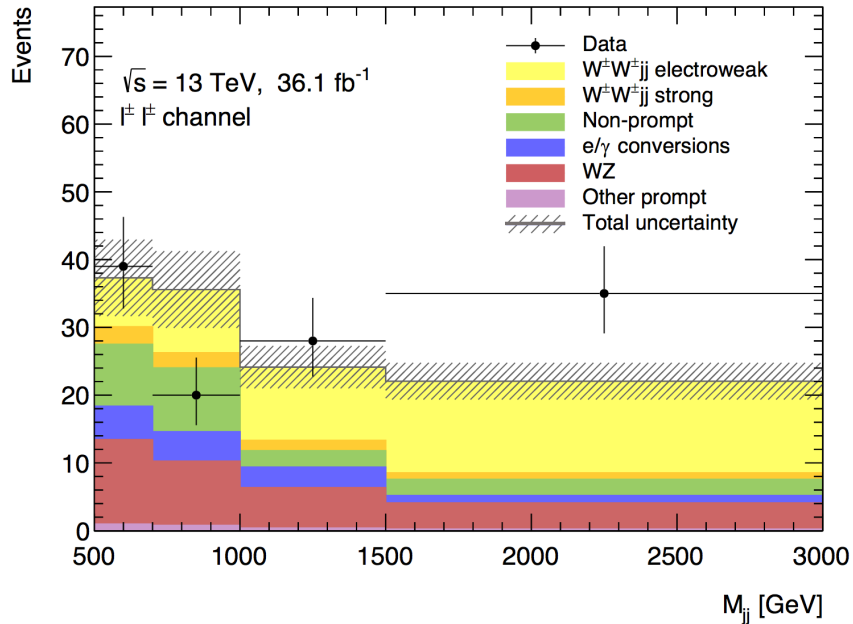
Figure 8.35: Expected event yield in the signal region for all lepton channels combined (before the fit). Hatched band represents the statistical and systematic uncertainties added in quadrature.

Chapter 9

Signal Estimation

The modeling of the expected signal contribution is needed to extract a cross section measurement from observed data, provided the contribution is corrected for detector effects. The modeling of the expected signal contribution also provides the reference theory cross section against which the measured cross section can be compared. Both cross sections (theory and measured) are usually calculated in a fiducial region[1] to prove an experiment-independent result. In this chapter the details of the signal simulation relevant for this measurement are reported.

9.1 Prediction at Generator-Level

The Standard Model $W^{\pm}W^{\pm}jj-$EW predicted cross section calculation is detailed in the following section. The generator-level MC samples and fiducial region used to predict the cross section are defined, and the associated theoretical uncertainties are discussed.

9.1.1 Definition of Fiducial Region

The fiducial region is defined in a phase space that is very similar to the signal region (see Section 7.5). Jets are obtained by clustering all particles except neutrinos, prompt leptons, and prompt photons. Events with leptons originating from τ decays are not included.

The fiducial region is defined as:

- Two same-sign prompt leptons with $p_T > 27$ GeV and $|\eta| < 2.5$ dressed with prompt photons within a $\Delta R < 0.1$

- $m_{ll'} > 20$ GeV

- $\Delta R(ll') > 0.3$

---

[1] A fiducial region is a phase space at generator-level that is designed to be reasonably close to what is accessible at detector-level.

- Transverse momenta of two neutrinos $p_T^{\nu\nu'} > 30$ GeV

- At least two jets with leading (subleading) jet $p_T > 65(35)$ GeV and $|\eta| < 4.5$ reconstructed with the anti-k_t algorithm with radius parameter $R = 0.4$

- Minimum ΔR between selected leptons and jets must be $min(\Delta R(l, jet)) > 0.3$

- $m_{jj} > 500$ GeV

- $\Delta y_{jj} > 2$

Events are required to pass these cuts at truth level.

9.1.2 $W^{\pm}W^{\pm}jj -$ EW Modeling in Fiducial Region

$W^{\pm}W^{\pm}jj-$EW production in the fiducial region is estimated using two generator-level MC samples: Sherpa and PowhegBox+Py8 (see Table 5.1). Figure 9.1 shows the m_{jj} (left) and Δy_{jj} (right) distributions in the fiducial region for SHERPA and POWHEG-BOX, in addition to a third sample generated using MADGRAPH5_aMC@NLO (see Table 5.1, MG5_aMC +H7,Γ_{resc}). Ratios shown are with respect to MG5_aMC _NLO+H7,Γ_{resc}. The impact of the suboptimal color flow in the SHERPA samples (see Section 5.2) is clear at low m_{jj} and low Δy_{jj}.
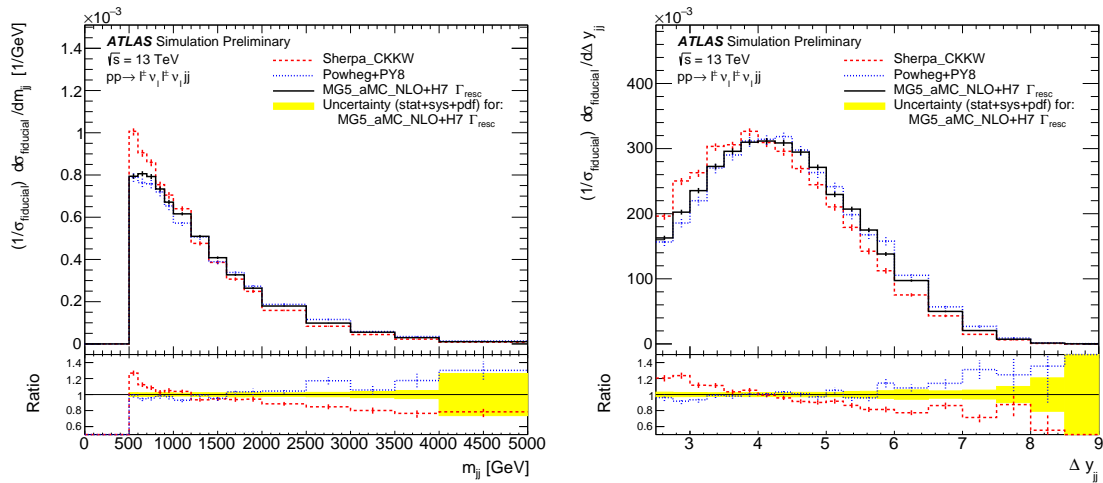
Figure 9.1: Normalized m_{jj} (left) and Δy_{jj} (right) distributions comparing three different event generators: SHERPA, POWHEG-BOX, and MADGRAPH5_aMC@NLO, in the fiducial region [94]. Ratios are calculated with respect to MG5_aMC_NLO+H7,Γ_{resc}. The yellow band corresponds to the quadratic sum of the statistical, PDF, and scale uncertainties.

Due to the modeling difference between SHERPA and POWHEG-BOX, discussions pertaining to predicted cross section values include both generators. Unless stated otherwise,

all analysis figures in this dissertation are shown with the $W^\pm W^\pm jj{-}\mathrm{EW}$ signal predicted using the SHERPA event generator.

9.1.3 Theoretical Uncertainties

The choices made when generating MC samples can have a noticeable impact on the resulting cross section measurements. Therefore, theoretical uncertainties associated with these choices are assessed on the cross section. The uncertainties considered include: the choice of parton shower, the choice of PDF set and α_S value, and the choice of μ_R/μ_F-scale.

Parton Shower

Uncertainties stemming from the choice of parton shower are assessed by varying the parton shower parameters. For the POWHEG-BOX generated sample, this uncertainty is determined by comparing the results of the nominal POWHEG-BOX+PYTHIA 8 sample with a POWHEG-BOX+HERWIG sample. For the SHERPA generated sample, the parton shower is varied using the internal parton shower variations provided by the SHERPA authors. The resulting estimated uncertainty on the predicted fiducial cross section due to the choice of parton shower is $^{+8\%}_{-1\%}$ for SHERPA and $\pm 15\%$ for POWHEG-BOX.

PDF and α_S

Uncertainties associated with the PDF sets originate from the experimental uncertainties of the datasets used to calculate the PDFs, as well as from the functional form chosen in the PDF fits. To determine the uncertainty due to the choice of PDF, two different variation techniques are used: (1) compare the internal variations of the nominal PDF set, and (2) compute the difference between the nominal set and different, additional PDF sets.

The nominal PDF set used in both the SHERPA and POWHEG-BOX samples is the NNPDF3.0nlo set implemented at NNLO order in QCD. This set was determined using 4,078 data points from 30 different experimental datasets [44]. Two additional PDF sets are used to calculate the difference from the nominal PDF set: the CT14 and the MMHT2014 PDF sets, both implemented at NNLO order in QCD. The CT14 PDF set was calculated using 2,947 data points from 33 experimental datasets [154], and the MMHT2014 PDF set used 2,663 data points from 40 different experimental datasets [43]. The results obtained using CT14 and MMHT2014 are both larger than the nominal calculation, resulting in a one-sided uncertainty. The final PDF uncertainty is taken as the envelope of this uncertainty and the uncertainty obtained through internal PDF variations.

When quoting the fiducial cross section, the final PDF uncertainty is shown combined with the uncertainty due to α_S. The nominal value of α_S is evaluated at scale m_Z to be 0.118, which has been determined using experimental data. As a result, α_S has associated uncertainties originating from the experimental uncertainties. In addition, α_S also has uncertainties related to the calculations for α_S, which are carried out at a truncated fixed order.

To assess the impact of these uncertainties on the calculation, the value of α_S is set to 0.117 and 0.119 within the nominal PDF set. The difference in the resulting cross section is taken as the uncertainty. For both SHERPA and POWHEG-BOX, varying α_S results in a relative variation of less than $\pm 0.01\%$.

The final PDF+α_S uncertainty is calculated by adding the final PDF uncertainty and the α_S uncertainty in quadrature. The resulting estimated uncertainty on the predicted fiducial cross section due to the choice of PDF set and α_S value is $^{+2.5\%}_{-1.5\%}$ for SHERPA and $\pm 1.6\%$ for POWHEG-BOX.

Factorization and Renormalization Scale

The μ_R-scale and μ_F-scale are varied to estimate the uncertainty due to missing higher-order corrections of the perturbative expansion of the partonic cross section. This uncertainty is determined using the *7-point scale variation method*. In this approach, μ_R and μ_F are scaled by factors of two in the following combinations:

- $0.5 \times \mu_F$ and $1.0 \times \mu_R$
- $1.0 \times \mu_F$ and $0.5 \times \mu_R$
- $0.5 \times \mu_F$ and $0.5 \times \mu_R$

- $2.0 \times \mu_F$ and $1.0 \times \mu_R$
- $1.0 \times \mu_F$ and $2.0 \times \mu_R$
- $2.0 \times \mu_F$ and $2.0 \times \mu_R$

These combinations, together with the nominal setting ($1.0 \times \mu_F$ and $1.0 \times \mu_R$), result in seven variations. The relative impact of each variation on an observable β is defined as:

$$\delta\beta_i = \beta(\mu_{R,i}, \mu_{F,i}) - \beta(\mu_{R,0}, \mu_{F,0}), \tag{9.1}$$

where $\beta(\mu_{R,i}, \mu_{F,i})$ is the observable measured with the i-th scale variation, and $\beta(\mu_{R,0}, \mu_{F,0})$ is the observable measured with the nominal scale values. The final scale uncertainty is then determined by taking the envelope of all positive $\delta\beta_i$ results and the envelope of all negative $\delta\beta_i$ values.

Using this method, the resulting estimated uncertainty on the predicted fiducial cross section due to the μ_R/μ_F-scale setting is $^{+14.4\%}_{-11.4\%}$ for SHERPA and $^{+0.7\%}_{-2.0\%}$ for POWHEG-BOX.

9.1.4   Predicted Fiducial Cross Section

The predicted fiducial cross section is calculated by multiplying the generator-level inclusive cross section for the process by an acceptance factor, $\mathcal{A}$. The acceptance factor $\mathcal{A}$ represents the efficiency of events generated to fall within the fiducial region:

$$\mathcal{A} = \frac{N_{gen}^{fid}}{N_{gen}^{tot}}, \tag{9.2}$$

where N_{gen}^{fid} is the number of events at generator-level which fall within the fiducial region, and N_{gen}^{tot} is the total number of events simulated at generator-level.

The predicted fiducial cross sections calculated in the fiducial region for the SHERPA and POWHEG-BOX generator-level samples are:

$$\sigma_{\mathrm{Sherpa}}^{\mathrm{fid}} = 2.01 \pm 0.02(\mathrm{stat})\ {}^{+0.29}_{-0.23}(\mathrm{scale})\ {}^{+0.16}_{-0.02}(\mathrm{parton\ shower})\ {}^{+0.05}_{-0.03}(\mathrm{PDF}+\alpha_S)\ \mathrm{fb} \qquad (9.3)$$

$$\sigma_{\mathrm{Powheg}}^{\mathrm{fid}} = 3.08 \pm 0.01(\mathrm{stat})\ {}^{+0.02}_{-0.06}(\mathrm{scale})\ {}^{+0.45}_{-0.45}(\mathrm{parton\ shower})\ {}^{+0.05}_{-0.05}(\mathrm{PDF}+\alpha_S)\ \mathrm{fb} \qquad (9.4)$$

The significant difference between the two values is largely the result of the suboptimal color flow setting in the SHERPA $W^{\pm}W^{\pm}jj-$EW sample (see Section 5.2). The SHERPA and POWHEG-BOX predicted fiducial cross sections are compared with the measured fiducial cross section in Section 13.2.

9.2   Estimation at Detector-Level

While predicted cross sections can be calculated using generator-level samples, detector-level samples are required when comparing signal expectations against observed data. A detector-level sample has undergone additional simulation and digitization to emulate the impact of the detector and reconstruction algorithms (see Section 5.1). Since the detector and reconstruction algorithms have less than perfect efficiencies, the yield of a detector-level sample will be reduced compared to the yield of a generator-level sample.

Figure 9.2 shows the generator-level $W^{\pm}W^{\pm}jj-$EW m_{jj} distribution in the fiducial region (FR) with the detector-level $W^{\pm}W^{\pm}jj-$EW m_{jj} distribution in the signal region (SR) for SHERPA (left) and POWHEG-BOX (right). For both SHERPA and POWHEG-BOX, the yield in the signal region from the detector-level sample is roughly 50% of the yield of the same sample at generator-level in the fiducial region.
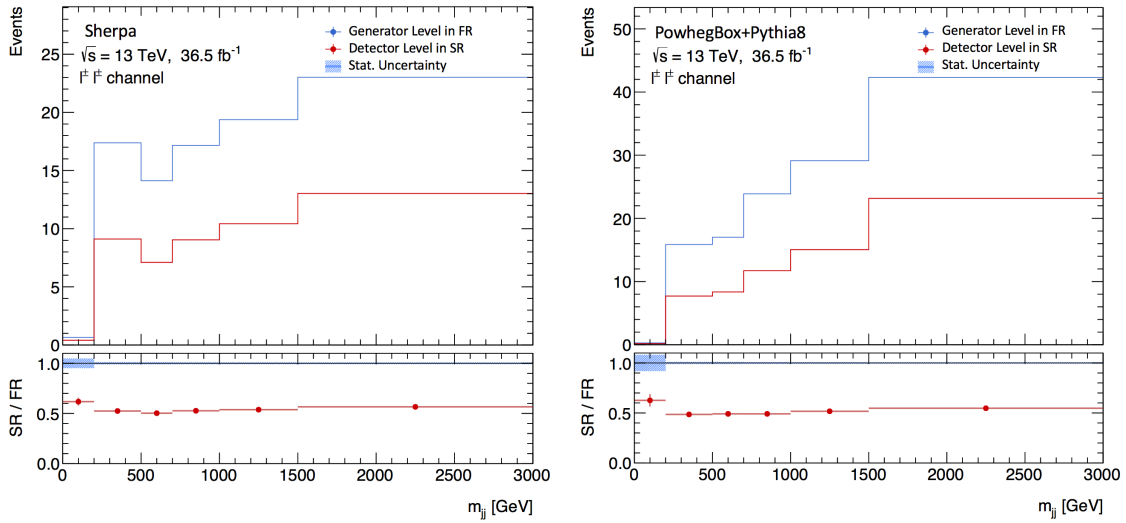
Figure 9.2: $W^{\pm}W^{\pm}jj$−EW m_{jj} distribution in the fiducial region (FR) at generator-level and in the signal region (SR) at detector-level for SHERPA (left) and POWHEG-BOX (right). Statistical uncertainties are shown in the ratio plot. Yield shown for all lepton channels combined.

While the impact of the detector/reconstruction efficiency is accounted for in a detector-level sample, when determining the measured cross section in the signal region, the same theoretical uncertainties estimated for the predicted cross section must be considered. Ideally, the theoretical uncertainties would be assessed using the same methods described in the previous section (see Section 9.1.3), but using detector-level samples instead of generator-level samples. For this analysis, however, all the necessary detector-level samples were not requested for production in a timely manner. Therefore, when necessary, a *folding* procedure is used to transfer the uncertainties calculated at generator-level to the detector-level sample. This alternative method is suboptimal, but it was the best option available at the time. In addition, the difference between the ideal method and the procedure utilized in this analysis is expected to be marginal compared to other uncertainties on the measurement.

9.2.1 Generator-Level to Detector-Level Folding Procedure

When calculating the predicted fiducial cross section, the transition from the total phase space to the fiducial region is carried out using an acceptance factor, $\mathcal{A}$ (see Section 9.1.4). Figure 9.3 depicts a simplified visual representation of this procedure with the additional transition from the fiducial region to the signal region at detector-level. A multiplicative term ($\mathcal{C}_{ij}$) is used to translate the fiducial region at generator-level to the signal region at detector-level.
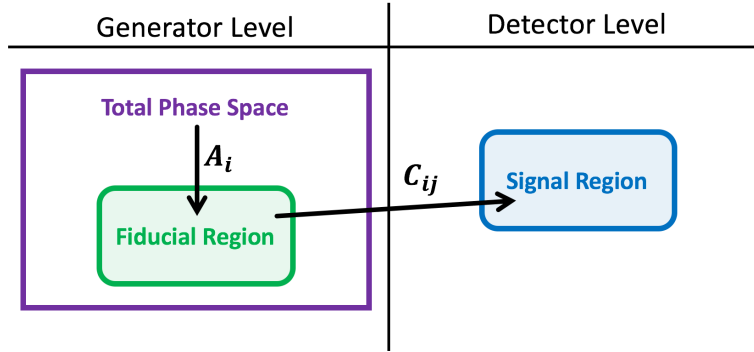
Figure 9.3: Visual representation of the folding procedure to transition from generator-level to detector-level.

In the fiducial region, cross section calculations are carried out in a single m_{jj} bin for all lepton channels combined. In the signal region, results are interpreted using a four bin m_{jj} distribution. Therefore, the process of transferring from the fiducial region at generator-level to the signal region at detector-level must also be considered in bins of the m_{jj} distribution. In the following, the m_{jj} bins in the fiducial region are denoted with the subscript i, while bins in the signal region are denoted with the subscript j. The number of events reconstructed in the signal region at detector-level in m_{jj} bin j (N_j^{det}) can be written as:

$$N_j^{det} = \sum_i \mathcal{C}_{ij} \cdot N_i^{gen}, \tag{9.5}$$

where N_i^{gen} is the number of generator-level events in m_{jj} bin i in the fiducial region.

The term $\mathcal{C}_{ij}$ represents the conditional probability, p(det|gen), that a $W^{\pm}W^{\pm}jj{-}$EW event is reconstructed at detector-level in m_{jj} bin j, given that it was simulated at generator-level with a value in m_{jj} bin i. To determine the conditional probability, three values are required:

- $\mathcal{P}_{ij}{-}$ The probability that an event is reconstructed at detector-level in m_{jj} bin j given its existence in m_{jj} bin i at generator-level.

- $\mathcal{E}_j^{fid}{-}$ The efficiency of an event in signal region m_{jj} bin j at detector-level also passing the fiducial region selections at generator-level.

- $\mathcal{C}_i^{eff}{-}$ The efficiency correction for the normalization difference between events reconstructed at detector-level and events simulated at generator-level (see Figure 9.2).

These variables combine to produce $\mathcal{C}_{ij}$ in the following way:

$$\mathcal{C}_{ij} = \frac{1}{\mathcal{E}_j^{fid}} \cdot \mathcal{P}_{ij} \cdot \mathcal{C}_i^{eff}. \tag{9.6}$$

By summing $\mathcal{C}_{ij}$ over all generator-level m_{jj} bins i (see Equation 9.5), two probabilities are accounted for: (1) the probability for an event simulated in the fiducial region at generator-level to be reconstructed in the signal region at detector-level, and (2) the probability for the simulated event to migrate to a different m_{jj} bin at detector-level. Figure 9.4 depicts the values of $\mathcal{C}_{ij}$ computed using the SHERPA $W^{\pm}W^{\pm}jj$−EW sample. In Figure 9.4, m_{jj}(true) denotes the m_{jj} distribution at generator-level, and m_{jj}(reco) denotes the m_{jj} distribution at detector-level[2].
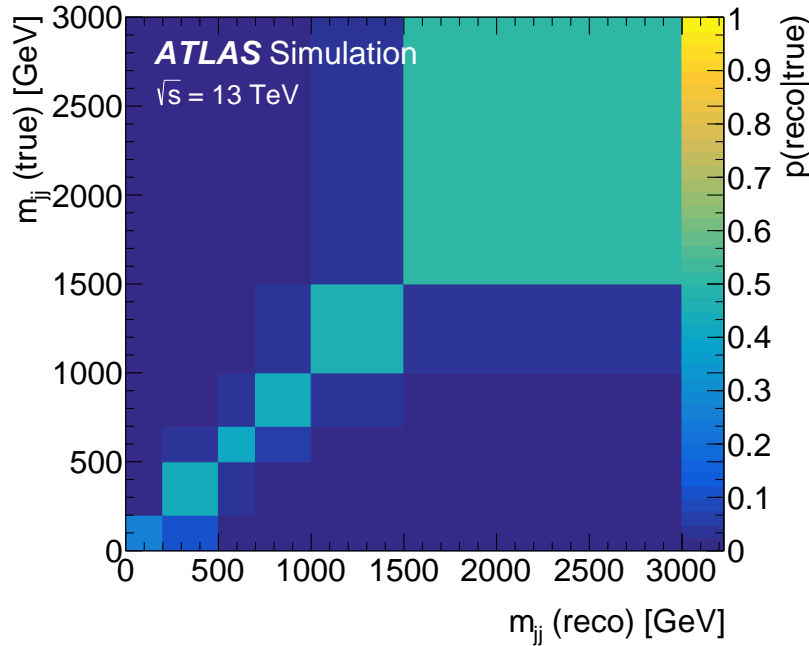
Figure 9.4: Response matrix for the $W^{\pm}W^{\pm}jj$−EW m_{jj} distribution. A matrix element is the conditional probability that a $W^{\pm}W^{\pm}jj$−EW event is reconstructed in a bin of m_{jj}(reco), given that it was generated with a value in bin m_{jj}(true). This response matrix is used for folding from generator-level to detector-level. Values in the response matrix are calculated with SHERPA.

The conditional probability $\mathcal{C}_{ij}$ is a largely diagonalized matrix with the diagonal elements equal to roughly 50% probability. This behavior indicates that, without any bin migrations, an event simulated in m_{jj} bin x in the fiducial region at generator-level has a roughly 50% chance of being reconstructed in m_{jj} bin x in the signal region at detector-level. This 50% probability aligns with the fractional yield difference between the generator-level and the detector-level $W^{\pm}W^{\pm}jj$−EW samples (see Figure 9.2). Using Equation 9.5 and Figure 9.4, the $W^{\pm}W^{\pm}jj$−EW yield in any m_{jj} bin in the signal region at detector-level can be estimated from the generator-level $W^{\pm}W^{\pm}jj$−EW m_{jj} distribution in the fiducial region.

---

[2]Generator-level is also often referred to as truth-level or particle-level. Similarly, detector-level is also referred to as reco-level.

Chapter 10

Theory Uncertainties Propagated to the Fit

In Chapter 9, the theoretical uncertainties impacting the $W^{\pm}W^{\pm}jj-$EW predicted fiducial cross section were introduced and calculated for $W^{\pm}W^{\pm}jj-$EW at generator-level. The impact of each of these theoretical uncertainties on the expected signal region m_{jj} distribution is considered in the fit used to measure the $W^{\pm}W^{\pm}jj-$EW fiducial cross section with observed data. As a result, all the theoretical uncertainties introduced in Chapter 9 must be calculated at detector-level for inclusion into the fit. In addition, the theoretical uncertainties must be assessed for more processes beyond $W^{\pm}W^{\pm}jj-$EW, such as $W^{\pm}W^{\pm}jj-$QCD and WZ. Furthermore, additional theoretical uncertainties not considered during the predicted cross section calculation must be treated.

This chapter outlines all the theoretical uncertainties propagated to the fit used to measure the fiducial $W^{\pm}W^{\pm}jj-$EW cross section with observed data. These theoretical uncertainties can be grouped into three categories: modeling uncertainties, corrective uncertainties, and MC cross section uncertainties. Each of these categories, and their related uncertainties, is described in detail below.

10.1 Modeling Uncertainties

Since $W^{\pm}W^{\pm}jj$ (EW & QCD) and $WZjj$ account for 80% of the total predicted events in the signal region, it is important to understand the detector-level uncertainties on their cross sections in order to obtain an accurate measurement. The sources of uncertainty common to these processes are the same as the theoretical uncertainties discussed for the predicted fiducial $W^{\pm}W^{\pm}jj-$EW cross section (see Section 9.1.3). These sources of uncertainty include: choice of parton shower, PDF set, α_S coupling, and μ_F/μ_R-scale.

When measuring the fiducial cross section with the fit, three regions are used: the signal region, the low m_{jj} region (to constrain backgrounds), and the $WZjj$ control region (where the $WZjj$ background is normalized). As a result, the theoretical uncertainties are calculated

in all three regions, when applicable. Because the $W^{\pm}W^{\pm}jj$ (EW & QCD) contribution in the $WZjj$ control region is not statistically significant, only the theoretical uncertainties for $WZjj$ are calculated in the $WZjj$ control region. Unless stated otherwise, all theoretical uncertainties are calculated in the combined lepton channel and then applied to the individual channels.

10.1.1   Parton Shower

Due to missing detector-level samples, the theoretical uncertainties resulting from parton shower variation cannot be estimated directly in the signal region at detector-level (see Section 9.1.3). Therefore, the theoretical uncertainty is evaluated in the fiducial region at generator-level and folded to the signal region using the procedure described in Section 9.2.1. The procedure applied to $W^{\pm}W^{\pm}jj$ (EW and QCD) and WZ is as follows:

- **$W^{\pm}W^{\pm}jj$**: At generator-level, parton shower uncertainties are determined for the $W^{\pm}W^{\pm}jj-$EW signal and the $W^{\pm}W^{\pm}jj-$QCD background by using the internal shower variation parameters provided by the SHERPA event generator (see Section 9.1.3). The resulting generator-level distributions are then folded to detector-level using the combined response matrix (see Figure 9.4). For $W^{\pm}W^{\pm}jj-$EW, all but one of the variations provided upward fluctuations, resulting in a single "up"-variation envelope.

- **WZ**: As is the case for the $W^{\pm}W^{\pm}$ samples, the uncertainty is calculated using generator-level samples and folded to detector-level. For WZ, the parton shower uncertainty is determined by taking the relative difference between samples generated with two different parton shower algorithms: PYTHIA and HERWIG. This relative difference is then applied to the nominal WZ sample generated with the SHERPA event generator.

Figure 10.1 shows the nominal m_{jj} distribution and shower variation envelopes folded to detector-level for $W^{\pm}W^{\pm}jj-$EW, $W^{\pm}W^{\pm}jj-$QCD, and WZ in the signal region for all lepton channels combined. The relative uncertainty for each sample in the signal region, the low m_{jj} control region, and the WZ control region is listed in Table 10.1. When compared at generator-level in the fiducial region and detector-level in the signal region, the $W^{\pm}W^{\pm}jj-$EW parton shower uncertainties exhibit similar behavior: a single digit *up*-variation uncertainty and almost no uncertainty from the *down*-variation envelope.
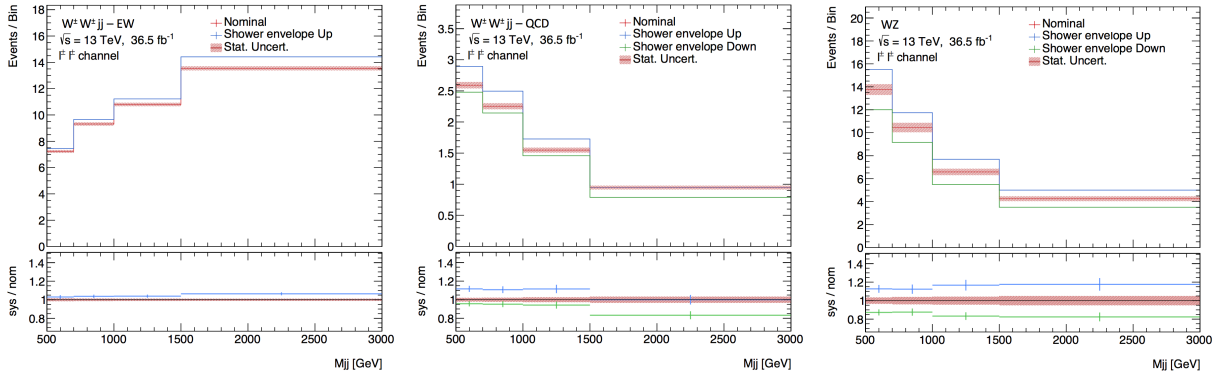
Figure 10.1: Nominal and up/down envelope of parton shower variations in m_{jj} folded to detector-level for $W^\pm W^\pm jj$−EW (left), $W^\pm W^\pm jj$−QCD (center), and WZ (right) in the signal region. Ratios show the variation uncertainty relative to the nominal distribution. Statistical uncertainties of the nominal distribution are shown in red.

Parton Shower Variation Uncertainty

	Signal Region		Low m_{jj} CR		WZ CR	
	up	down	up	down	up	down
$W^\pm W^\pm jj$−EW	$+(4-7)\%$	−	-11%	−	−	−
$W^\pm W^\pm jj$−QCD	$+(0-12)\%$	$-(4-6)\%$	0%	-7%	−	−
WZ	$+(13-16)\%$	$-(13-16)\%$	$+15\%$	-15%	$+25\%$	-25%

Table 10.1: Summary of parton shower variation uncertainty relative to the nominal m_{jj} distribution for $W^\pm W^\pm jj$−EW, $W^\pm W^\pm jj$−QCD, and WZ. Relative uncertainty resulting from the *up*-variation envelope and *down*-variation envelope in the signal region, low m_{jj} control region (low m_{jj} CR), and WZ control region (WZ CR) is shown.

10.1.2   PDF Set

The theoretical uncertainty resulting from varying the PDF set is calculated for the $W^\pm W^\pm$ (EW and QCD) and WZ samples at detector-level using the same method used at generator-level. The uncertainty is determined by taking the envelope of two variation methods: the internal variation of the nominal PDF, and the relative difference between the nominal and additional PDF sets[1] (see Section 9.1.3). The nominal and PDF set variation envelopes for $W^\pm W^\pm jj$−EW, $W^\pm W^\pm jj$−QCD, and WZ at detector-level in the signal region are shown in Figure 10.2.

The relative uncertainty due to the PDF variations for $W^\pm W^\pm jj$−EW, $W^\pm W^\pm jj$−QCD, and WZ are listed in Table 10.2 for the signal region, low m_{jj} control region, and WZ

---

[1]The CT14 and MMHT2014 PDF sets are used as alternative PDFs for both $W^\pm W^\pm$ and WZ.
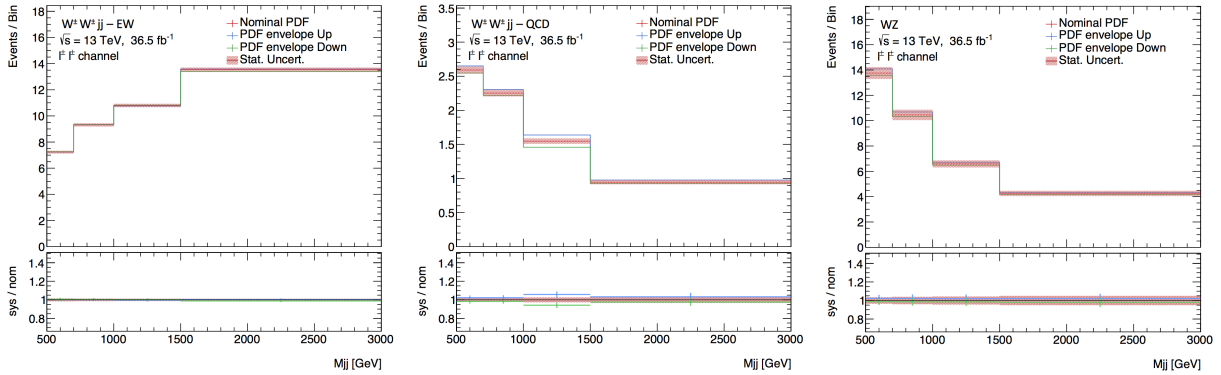
Figure 10.2: Nominal and up/down envelope of PDF set variations in m_{jj} calculated at detector-level for $W^{\pm}W^{\pm}jj-$EW (left), $W^{\pm}W^{\pm}jj-$QCD (center), and WZ (right) in the signal region. Ratios show the variation uncertainty relative to the nominal distribution. Statistical uncertainties of the nominal distribution are shown in red.

control region. For $W^{\pm}W^{\pm}jj-$EW, the envelope PDF variations in all regions differ from the nominal distribution by $\pm < 1\%$ for both the upward and downward envelopes. The relative uncertainty due to PDF variations for the $W^{\pm}W^{\pm}jj-$QCD sample are slightly larger, with all bins of m_{jj} differing from the nominal distribution by $\pm(1-6)\%$. Similarly, the relative uncertainty on the WZ sample in all regions is between $\pm(1-3)\%$, which is less than the statistical uncertainty on the nominal m_{jj} distribution.

PDF Set Variation Uncertainty

	Signal Region		Low m_{jj} CR		WZ CR	
	up	down	up	down	up	down
$W^{\pm}W^{\pm}jj-$EW	$+ < 1\%$	$- < 1\%$	$+ < 1\%$	$- < 1\%$	$-$	$-$
$W^{\pm}W^{\pm}jj-$QCD	$+(2-6)\%$	$-(2-6)\%$	$+3\%$	-1%	$-$	$-$
WZ	$+(2-3)\%$	$-(2-3)\%$	$+2\%$	-1%	$+2\%$	-1%

Table 10.2: Summary of PDF set variation uncertainty relative to the nominal m_{jj} distribution for $W^{\pm}W^{\pm}jj-$EW, $W^{\pm}W^{\pm}jj-$QCD, and WZ. Relative uncertainty resulting from the *up*-variation envelope and the *down*-variation envelope in the signal region, low m_{jj} control region (low m_{jj} CR), and WZ control region (WZ CR) is shown.

10.1.3 QCD Coupling - α_S

The theoretical uncertainty due to the choice of QCD α_S coupling is determined at detector-level by varying α_S and taking the resulting relative difference with the nominal as an

uncertainty. The nominal value of α_S (evaluated at the m_Z scale) is 0.118. This value is varied to 0.117 and 0.119 in the baseline PDF to assess the uncertainties.

Figure 10.3 shows the m_{jj} distributions of $W^{\pm}W^{\pm}jj-$EW, $W^{\pm}W^{\pm}jj-$QCD, and WZ in the signal region for the nominal α_S and the up/down α_S variations. The relative uncertainties in this region, as well as in the low m_{jj} control region and the WZ control region, are listed in Table 10.3. In all regions, the uncertainty is of order $\pm 2\%$ or less, which is within the range of the statistical uncertainty.
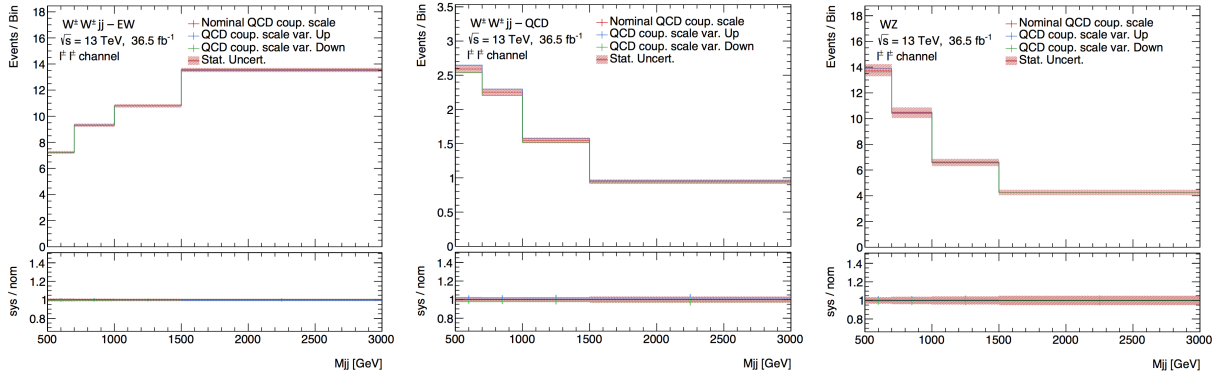
Figure 10.3: m_{jj} distributions for nominal and up/down-variation envelopes of QCD strong coupling, α_S, calculated at detector-level for $W^{\pm}W^{\pm}jj-$EW (left), $W^{\pm}W^{\pm}jj-$QCD (center), and WZ (right) in the signal region. Ratios show the variation uncertainty relative to the nominal distribution. Statistical uncertainties of the nominal distribution are shown in red.

<div align="center">

QCD α_S Variation Uncertainty

	Signal Region	Low m_{jj} CR	WZ CR
$W^{\pm}W^{\pm}jj-$EW	$\pm < 1\%$	$\pm < 1\%$	$-$
$W^{\pm}W^{\pm}jj-$QCD	$\pm 2\%$	$\pm 2\%$	$-$
WZ	$\pm < 1\%$	$\pm 1\%$	$\pm < 1\%$

</div>

Table 10.3: Summary of QCD coupling α_S variation uncertainty relative to the nominal m_{jj} distribution for $W^{\pm}W^{\pm}jj-$EW, $W^{\pm}W^{\pm}jj-$QCD, and WZ in the signal region, low m_{jj} control region (low m_{jj} CR), and WZ control region (WZ CR). Relative uncertainties from up/down-variations are symmetric and shown simply as a $\pm$ value.

10.1.4 μ_R/μ_F-scale Variations

The uncertainty due to the μ_R-scale and μ_F-scale is estimated at detector-level using the same method applied at generator-level: the 7-point scale variation method. The resulting

up/down-variation envelopes for $W^\pm W^\pm jj$−EW, $W^\pm W^\pm jj$−QCD, and WZ in the signal region are shown in Figure 10.4.

The $W^\pm W^\pm jj$−EW scale variation uncertainty is much smaller than the uncertainty for $W^\pm W^\pm jj$−QCD and WZ. For $W^\pm W^\pm jj$−EW, the relative uncertainty in all regions is $\leq 4\%$, whereas the relative uncertainty for $W^\pm W^\pm jj$−QCD and WZ is between $\pm(22-44)\%$ and $\pm(17-29)\%$, respectively. In addition to being smaller in magnitude, at lower m_{jj} ($m_{jj} < 1000$ GeV) the up/down-variation envelope for $W^\pm W^\pm jj$−EW results in opposite m_{jj} fluctuations relative to the nominal value (i.e., the up-variation results in negative fluctuations, and the down-variation results in positive fluctuations). The complete list of relative μ_F/μ_R-scale uncertainties for $W^\pm W^\pm jj$−EW, $W^\pm W^\pm jj$−QCD, and WZ at detector-level in the signal region, low m_{jj} control region, and WZ control region is shown in Table 10.4.
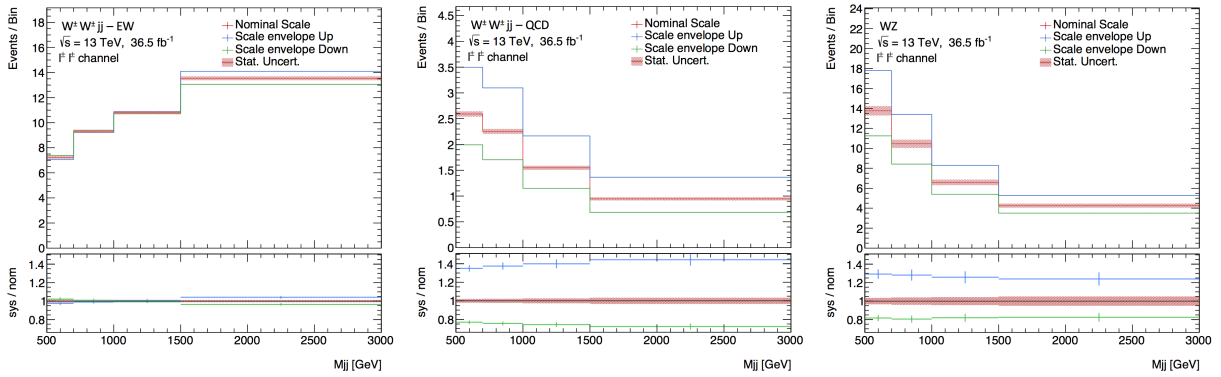
Figure 10.4: m_{jj} distributions for nominal and up/down envelope of μ_R/μ_F-scale variations calculated at detector-level for $W^\pm W^\pm jj$−EW (left), $W^\pm W^\pm jj$−QCD (center), and WZ (right) in the signal region. Ratios show the variation uncertainty relative to the nominal distribution. Statistical uncertainties of the nominal distribution are shown in red.

$\boldsymbol{\mu_F/\mu_R}$-scale Variation Uncertainty

	Signal Region		Low m_{jj} CR		WZ CR	
	up	down	up	down	up	down
$W^\pm W^\pm jj$−EW	$(-2\%)-(+4\%)$	$(+2\%)-(-4\%)$	-4%	$+4\%$	–	–
$W^\pm W^\pm jj$−QCD	$+(35-44)\%$	$-(23-28)\%$	$+32\%$	-22%	–	–
WZ	$+(24-29)\%$	$-(17-20)\%$	$+28\%$	-19%	$+27\%$	-19%

Table 10.4: Summary of μ_F/μ_R-scale variation uncertainty relative to the nominal m_{jj} distribution for $W^\pm W^\pm jj$−EW, $W^\pm W^\pm jj$−QCD, and WZ. Relative uncertainty resulting from the *up*-variation envelope and *down*-variation envelope in the signal region, low m_{jj} control region (low m_{jj} CR), and WZ control region (WZ CR) is shown.

10.2   Corrective Uncertainties

In addition to the theoretical modeling uncertainties, two additional theoretical uncertainties are assessed on the $W^{\pm}W^{\pm}jj-$EW signal sample when measuring the $W^{\pm}W^{\pm}jj-$EW fiducial cross section with observed data. These additional uncertainties are not considered when calculating the predicted fiducial cross section in order to remove any double counting when comparing the predicted and measured fiducial cross section values. These uncertainties include: a correction for the difference between $W^{\pm}W^{\pm}jj-$EW predictions calculated with a LO electroweak matrix element and an NLO electroweak matrix element, and an uncertainty for the interference between EW and QCD diagrams during $W^{\pm}W^{\pm}jj$ production.

10.2.1   NLO Electroweak Correction

The $W^{\pm}W^{\pm}jj-$EW signal samples simulated at detector-level only include LO electroweak matrix element calculations (see Section 5.3.1). Adding in higher-order corrections to the matrix element calculation can have a significant impact on the resulting cross section. During the course of the analysis, complete NLO corrections for $W^{\pm}W^{\pm}$ electroweak and strong production were computed by theorists [155]. Using these calculations, an uncertainty on the nominal $W^{\pm}W^{\pm}jj-$EW signal sample is assessed to account for the potential impact of the higher-order NLO electroweak corrections.

The NLO corrections to $W^{\pm}W^{\pm}jj-$EW of the order $\mathcal{O}(\alpha_{EW}^{7})$ are calculated in Ref. [155] at generator-level. Figure 10.5 shows the LO $W^{\pm}W^{\pm}jj-$EW m_{jj} distribution and the NLO-corrected $W^{\pm}W^{\pm}jj-$EW m_{jj} distribution at generator-level as determined in Ref. [155][2].

---

[2]The LO and NLO $W^{\pm}W^{\pm}jj-$EW m_{jj} distributions were provided by the authors of Ref. [155] and were rebinned to match the m_{jj} binning scheme of this analysis.
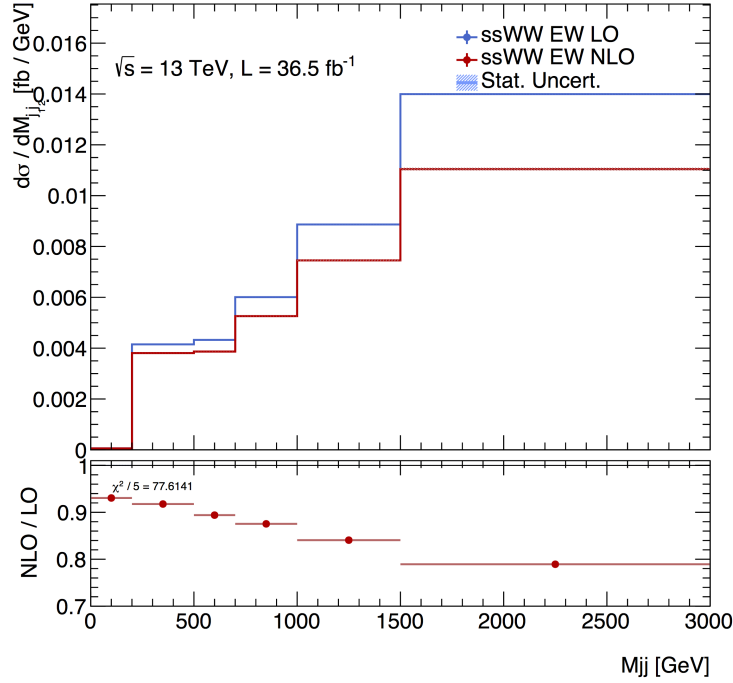
Figure 10.5: Generator-level NLO and LO differential cross sections for $W^{\pm}W^{\pm}jj-$EW production used to determine NLO EW correction. Distributions created using data provided by Ref. [155].

The distributions shown in Figure 10.5 are folded to detector-level using the procedure described in Section 9.2.1. The difference between the resulting folded LO and NLO $W^{\pm}W^{\pm}jj-$EW m_{jj} distributions is taken as a relative NLO EW correction factor which is applied as a theoretical uncertainty to the nominal $W^{\pm}W^{\pm}jj-$EW signal sample. To provide a conservative estimate, the uncertainty is mirrored on the nominal value to give a symmetrized uncertainty band. Figure 10.6 shows the nominal and relative uncertainty distributions from the mirrored NLO EW correction in the low m_{jj} control region and the signal region. The NLO EW correction results in an uncertainty between $\pm(1-6)\%$ in the signal region and $\pm 7\%$ in the low m_{jj} control region.
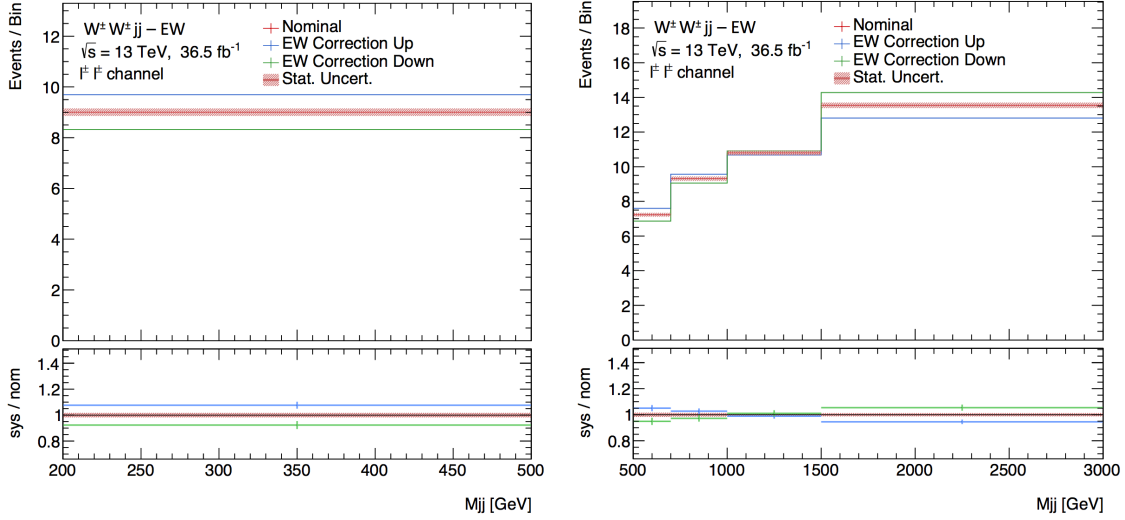
Figure 10.6: Nominal $W^{\pm}W^{\pm}jj-$EW distribution and relative systematic uncertainty distributions due to the NLO EW correction at detector-level in the low m_{jj} control region (left) and the signal region (right). Ratios show the relative uncertainties. Statistical uncertainties of the nominal distributions are shown in red.

10.2.2 EW-QCD Interference

In addition to the NLO EW correction, another theoretical uncertainty is assigned to the detector-level $W^{\pm}W^{\pm}jj-$EW sample that is not taken into account at generator-level: the interference between EW and QCD $W^{\pm}W^{\pm}$ production.

In Section 2.4, the various production diagrams for $W^{\pm}W^{\pm}$ are categorized into $W^{\pm}W^{\pm}jj-$EW and $W^{\pm}W^{\pm}jj-$QCD. This simple categorization does not hold, however, once $W^{\pm}W^{\pm}$ production is discussed in terms of cross section calculations. In reality, the $W^{\pm}W^{\pm}$ cross section is proportional to the square of the sum of all contributing diagrams:

$$
\begin{aligned}
\sigma_{W^{\pm}W^{\pm}} &\propto |\mathcal{M}_{EW} + \mathcal{M}_{QCD}|^2 \\
&\propto |\mathcal{M}_{EW}|^2 + |\mathcal{M}_{QCD}|^2 + 2\text{Re}(\mathcal{M}_{EW}\overline{\mathcal{M}}_{QCD}) \\
&\equiv \sigma_{EW} + \sigma_{QCD} + \sigma_{INT}.
\end{aligned}
\tag{10.1}
$$

Therefore, the total $W^{\pm}W^{\pm}$ cross section is the sum of the EW production cross section, the QCD production cross section, and the interference contribution. The EW and QCD production cross sections are both positive, while the interference can be positive or negative. Since the $W^{\pm}W^{\pm}jj-$EW and $W^{\pm}W^{\pm}jj-$QCD samples are generated independently, the effect of the interference is not included. Thus, the theoretical impact of the interference is assessed separately and treated as an additional uncertainty on $W^{\pm}W^{\pm}jj-$EW during the fiducial cross section measurement with observed data.

To calculate the EW/QCD interference uncertainty, four different $W^{\pm}W^{\pm}$ signals are generated (at generator-level) for the process $pp \to \mu^+\nu_\mu\mu^+\nu_\mu jj$ using MADGRAPH5_aMC@NLO:

- $W^{\pm}W^{\pm}jj-$Incl: An inclusive $W^{\pm}W^{\pm}$ sample generated including EW production, QCD production, and the interference between EW/QCD production.

- $W^{\pm}W^{\pm}jj-$EW: Sample produced including only EW production $W^{\pm}W^{\pm}$ diagrams.

- $W^{\pm}W^{\pm}jj-$QCD: Sample produced including only QCD-induced $W^{\pm}W^{\pm}$ diagrams.

- $W^{\pm}W^{\pm}jj-$INT: Sample generated including only the EW/QCD interference term at LO.

Each sample is generated in a very inclusive phase space which only requires $|\eta_{jj}| < 10$, $p_T^{jet} > 20$ GeV, and $m_{jj} > 0$ GeV. The generator cross sections of these four processes in this inclusive phase space are shown in Table 10.5.

σ_{Inc}	σ_{EW}	σ_{QCD}	σ_{INT}
3.646fb^{-1}	2.132fb^{-1}	1.371fb^{-1}	0.227fb^{-1}

Table 10.5: Generator cross sections for inclusive $W^{\pm}W^{\pm}$ sample, purely EW $W^{\pm}W^{\pm}$ production, QCD production of $W^{\pm}W^{\pm}jj$ final state, and the interference between the EW and QCD production. Cross sections are calculated in the inclusive generation phase space which only requires $|\eta_{jj}| < 10$, $p_T^{jet} > 20$ GeV, and $m_{jj} > 0$ GeV. Statistical uncertainties on generated cross sections are below the quoted significant digits.

The relative contribution of each sample, normalized to 36 fb^{-1} and required to pass the selections defining the analysis signal region, are shown in Figure 10.7. The resulting interference is observed to be positive and accounts for roughly $6 - 7\%$ of the inclusive $W^{\pm}W^{\pm}$ sample.

To calculate an uncertainty on $W^{\pm}W^{\pm}jj-$EW due to the EW/QCD interference, the generator-level $W^{\pm}W^{\pm}jj-$INT contribution is normalized to the MADGRAPH purely $W^{\pm}W^{\pm}jj-$EW contribution. Both distributions are then folded to detector-level, and the relative difference between the two detector-level samples is taken as the relative uncertainty on the nominal SHERPA $W^{\pm}W^{\pm}jj-$EW sample. In order to assign a more conservative uncertainty, the calculated uncertainty is mirrored to give a symmetrized uncertainty band. The resulting uncertainty envelopes for $W^{\pm}W^{\pm}jj-$EW in the low m_{jj} control region and in the signal region are shown as a function of m_{jj} in Figure 10.8.

In the low m_{jj} control region, the EW/QCD interference results in a relative uncertainty of $\pm 8\%$. In the signal region, the relative uncertainty ranges between $\pm 4\%$ for the EW/QCD interference envelopes, depending upon the m_{jj} bin.
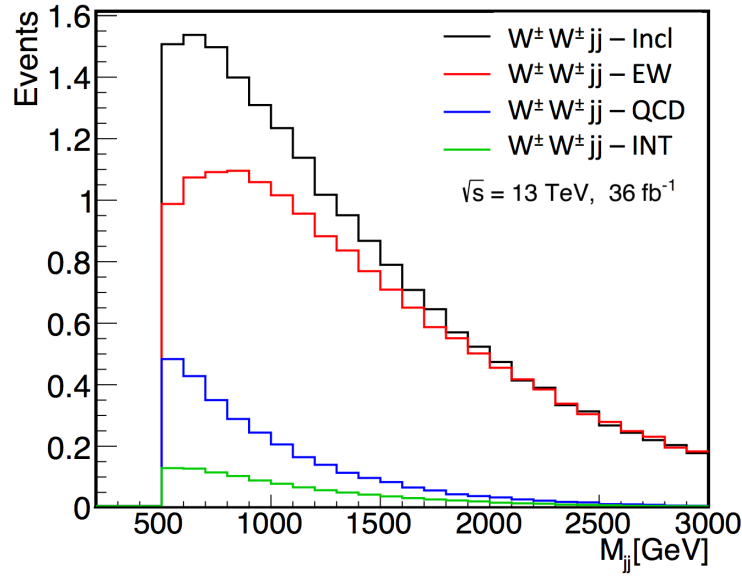
Figure 10.7: m_{jj} distribution for MADGRAPH generated $W^\pm W^\pm jj-$Incl, $W^\pm W^\pm jj-$EW, $W^\pm W^\pm jj-$QCD, and $W^\pm W^\pm jj-$INT samples normalized to 36 fb^{-1} in the signal region. The $W^\pm W^\pm jj-$Incl sample contains all EW and QCD diagrams in addition to the interference between them. The $W^\pm W^\pm jj-$INT sample contains only the EW/QCD interference term. The $W^\pm W^\pm jj-$EW and $W^\pm W^\pm jj-$QCD samples contain purely electroweak and strong production diagrams, respectively.
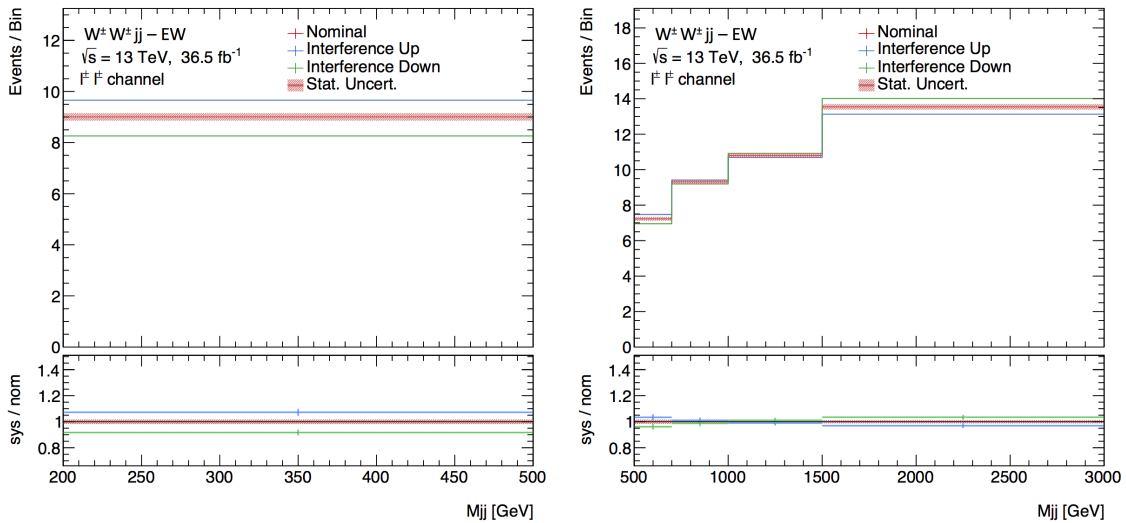
Figure 10.8: Nominal $W^\pm W^\pm jj-$EW detector-level m_{jj} distribution and relative uncertainty distributions due to EW-QCD interference in the low m_{jj} control region (left) and in the signal region (right). Ratios show the relative uncertainties. Statistical uncertainties of the nominal distribution are shown in red.

10.3 Additional MC Cross Section Uncertainty

In addition to the theoretical uncertainties applied to the $W^\pm W^\pm jj$ and WZ samples, uncertainties are applied to the other processes estimated with MC samples to account for their theoretical uncertainties. These additional processes include ZZ, VVV, and $V\gamma$. Ideally, all the theoretical uncertainties determined for the $W^\pm W^\pm jj$ and WZ samples in the previous sections would be calculated for these MC samples, as well. However, due to the limited statistics of these MC samples, this is not possible. Since a significant amount of time and CPU is required to produce detector-level samples, producing MC samples with higher statistics for these processes was not feasible. Instead, a single uncertainty is applied to each MC sample to account for the potential theoretical uncertainty on the process cross section.

The uncertainties applied to account for any theoretical uncertainty on the ZZ, VVV, and $V\gamma$ MC cross sections are listed in Table 10.6. These values are often conservative and are based on the values that were used for the Run-1 $W^\pm W^\pm jj$ analysis [13].

Background Process	Relative Uncertainty
ZZ	20%
VVV	30%
top processes	30%
$W\gamma$	20%
$Z\gamma$	20%

Table 10.6: Uncertainty assigned to the cross section of MC samples with limited statistics.

10.4 Summary

Table 10.7 summarizes all the theoretical uncertainties discussed in this chapter. The largest source of theoretical uncertainty for the detector-level $W^\pm W^\pm jj-$EW event yield in the signal region is the parton shower uncertainty (see Section 10.1.1). For $W^\pm W^\pm jj-$QCD and WZ, the largest source of theoretical uncertainty is the μ_R/μ_F-scale uncertainty (see Section 10.1.4). However, the parton shower uncertainty also has a significant impact on WZ prediction in the signal region. The impact of these theoretical uncertainties on the measured $W^\pm W^\pm jj-$EW cross section is discussed in Chapter 13.

Category	Uncertainty	Description
$W^{\pm}W^{\pm}jj$−EW	signal_EW6_TheoPDF	PDF shape uncertainty
	signal_EW6_TheoScale	μ_R/μ_F-scale shape uncertainty
	signal_EW6_TheoShower	Parton shower shape uncertainty
	signal_EW6_TheoAlphas	QCD coupling scale shape uncertainty
	TheoInterference	Interference between EW and QCD $W^{\pm}W^{\pm}jj$
	TheoEWCorr	Uncertainty on LO $W^{\pm}W^{\pm}jj$−EW cross section
$W^{\pm}W^{\pm}jj$−QCD	signal_EW4_TheoPDF	PDF shape uncertainty
	signal_EW4_TheoScale	μ_R/μ_F-scale shape uncertainty
	signal_EW4_TheoShower	Parton shower shape uncertainty
	signal_EW4_TheoAlphas	QCD coupling scale shape uncertainty
$WZjj$	WZ_TheoPDF	PDF shape uncertainty
	WZ_TheoScale	μ_R/μ_F-scale shape uncertainty
	WZ_TheoShower	Parton shower shape uncertainty
	WZ_TheoAlphas	QCD coupling scale shape uncertainty
MC Cross Sections	Wgamma_XS	$W\gamma$ cross section uncertainty
	Zgamma_XS	$Z\gamma$ cross section uncertainty
	ZZ_XS	ZZ cross section uncertainty
	top_XS	Top processes cross section uncertainty
	triboson_XS	VVV cross section uncertainty

Table 10.7: Summary of the theoretical uncertainty components. Many of these uncertainties have a shape dependency (e.g., see Figure 10.4). Each of these uncertainties is included in the fit as a nuisance parameter (see Section 12.3).

Chapter 11

Standard ATLAS Object Uncertainties

Due to the nature of simulating the interaction between particles produced in a pp collision, there are inherent uncertainties associated with MC-based predictions. Every reconstructed object has some uncertainty on its energy scale and resolution. In addition, if an object has been required to pass some particle/jet identification, there is an uncertainty associated with the efficiency of these selections. The uncertainties affecting this measurement can be organized into three categories depending on whether they relate to leptons, jets, or E_T^{miss}. In this chapter, tables show the relative impact of each systematic uncertainty on the expected signal and background yields in the signal region.

11.1   Lepton

The reconstruction process for leptons (see Sections 6.3 and 6.4) leads to a number of uncertainties. These uncertainties can be broken down into the following categories:

Muons:

- Muon trigger efficiency

- Muon reconstruction and identification efficiency

- Muon isolation efficiency

- Muon track-to-vertex efficiency

- Muon momentum scale/resolution

Electrons:

- Electron trigger efficiency

- Electron reconstruction efficiency

- Electron identification efficiency

- Electron isolation efficiency

- Electron energy scale/resolution

The modeling of lepton trigger, identification, and isolation efficiencies, as well as energy scales/resolutions, were studied using $J/\psi{\rightarrow}ee/\mu\mu$ and $Z{\rightarrow}ee/\mu\mu$ events in data and

simulation. Each measurement can have a number of intrinsic uncertainties which must be propagated to the analysis. Tables 11.1 and 11.2 list the specific systematic uncertainties considered for each of the above categories for electrons and muons, respectively.

Electron Category	Uncertainty	Notes
Trigger Efficiency	EL_EFF_Trigger_Total_1NPCOR_PLUS_UNCOR	
Reconstruction Efficiency	EL_EFF_Reco_Total_1NPCOR_PLUS_UNCOR	
Identification Efficiency	EL_EFF_ID_CorrUncertaintyNP EL_EFF_ID_SIMPLIFIED_UncorrUncertaintyNP	15 components 16 components
Isolation Efficiency	EL_EFF_Iso_Total_1NPCOR_PLUS_UNCOR	
Energy Resolution	EG_RESOLUTION_ALL	
Energy Scale	EG_SCALE_ALLCORR EG_SCALE_E4SCINTILLATOR EG_SCALE_LARCALIB_EXTRA2015PRE EG_SCALE_LARTEMPERATURE_EXTRA2015PRE EG_SCALE_LARTEMPERATURE_EXTRA2016PRE	 Only for 2015 data and $|\eta| > 2.5$ Only for 2016 data

Table 11.1: List of the electron systematic uncertainty components. The effect of these uncertainties on the expected yield in the signal region is shown in Table 11.3.

The intrinsic uncertainties on these measurements for leptons considered in this analysis ($p_T > 15$ GeV) are quite small, usually less than 1%. The propagated systematic uncertainty in the signal region due to lepton reconstruction/identification and trigger efficiency is shown in Table 11.3. In this table, "lepton reconstruction" refers to the collection of uncertainties listed in Tables 11.1 and 11.2, with the exception of trigger efficiency, which is listed separately.

For all channels, the uncertainty due to trigger efficiency is less than 0.5%. The uncertainty due to lepton reconstruction for the signal and background estimations in the signal region is between $1 - 6\%$ with the exception of the $Z\gamma$ background, which has a large uncertainty resulting from the very low statistics in the signal region.

Muon Category	Uncertainty	Notes
Trigger Efficiency	MUON_EFF_TrigStatUncertainty MUON_EFF_TrigSystUncertainty	
Reconstruction and Identification Efficiency	MUON_EFF_STAT MUON_EFF_SYS MUON_EFF_STAT_LOWPT MUON_EFF_SYST_LOWPT	For muons with $p_T > 15$ GeV For muons with $p_T < 15$ GeV
Isolation Efficiency	MUON_ISO_STAT MUON_ISO_SYS	
Track-to-Vertex Association Efficiency	MUON_TTVA_STAT MUON_TTVA_SYS	
Momentum Resolution	MUON_ID MUON_MS	From Inner Detector From Muon System
Momentum Scale	MUON_SCALE	

Table 11.2: List of the muon systematic uncertainty components. The effect of these uncertainties on the expected yield in the signal region is shown in Table 11.3. The muon systematic uncertainty with the largest impact on the measured fiducial cross section is the muon reconstruction and identification efficiency systematic uncertainty, MUON_EFF_SYS (see Figure 13.6). Overall, the impact of the muon systematic uncertainties on the measured fiducial cross section is much smaller than other analysis systematic uncertainties considered (see Section 13.1.3).

Process	Lepton Reconstruction (%)			Trigger Efficiency (%)		
	$e^{\pm}e^{\pm}$	$e^{\pm}\mu^{\pm}$	$\mu^{\pm}\mu^{\pm}$	$e^{\pm}e^{\pm}$	$e^{\pm}\mu^{\pm}$	$\mu^{\pm}\mu^{\pm}$
$W^{\pm}W^{\pm}jj-$EW	1.45	1.14	1.83	0.02	0.08	0.47
$W^{\pm}W^{\pm}jj-$QCD	1.62	1.19	1.89	0.02	0.08	0.41
WZ	1.52	1.24	3.07	0.03	0.09	0.43
VVV	1.66	1.27	2.48	0.02	0.07	0.47
$t\bar{t}V$	2.57	3.27	2.66	0.03	0.08	0.39
ZZ	3.59	3.10	5.70	0.03	0.10	0.36
$W\gamma$	1.40	1.13	-	0.01	0.14	-
$Z\gamma$	1.26	22.01	-	0.02	0.07	-

Table 11.3: Systematic uncertainties of lepton reconstruction and trigger efficiency for the expected signal and background in the signal region in three channels.

11.2   Jet

As is the case for leptons, jet reconstruction and identification has a number of associated uncertainties. These uncertainties can be categorized as:

- Jet energy scale (JES) uncertainty

- Jet energy resolution (JER) uncertainty

- JVT cut efficiency

- Jet b-tagging inefficiency

Table 11.5 lists the specific uncertainties considered for each of the above categories. The intrinsic uncertainty of each category is summarize briefly below.

Jet Category	Uncertainty	Notes
Energy Scale (JES)	JET_EffectiveNP	8 components from in-situ analysis
	JET_EtaIntercalibration_Modeling	η intercalibration modeling uncertainty
	JET_EtaIntercalibration_TotalStat	η intercalibration statistics/method uncertainty
	JET_EtaIntercalibration_NonClosure	η intercalibration non-closure
	JET_Pileup_OffsetMu	Pile-up μ dependency
	JET_Pileup_OffsetNPV	Pile-up number PV dependency
	JET_Pileup_PtTerm	Pile-up p_T term uncertainty
	JET_Pileup_RhoTopology	Pile-up density ρ uncertainty
	JET_Flavor_Composition	Flavor composition uncertainty
	JET_Flavor_Response	Flavor response uncertainty
	JET_BJES_Response	b-jet uncertainty
	JET_PunchThrough_MC15	Punch-through jet uncertainty
	JET_RelativeNonClosure_MC15	MC non-closure
	JET_SingleParticle_HighPt	High p_T jet behavior uncertainty
Energy Resolution (JER)	JET_JER_SINGLE_NP	
JVT Efficiency	JET_JvtEfficiency	
b-tagging Inefficiency	FT_EFF_Eigen_B	b-jet SF uncertainties $-$ 3 components
	FT_EFF_Eigen_C	c-jet SF uncertainties $-$ 3 components
	FT_EFF_Eigen_L	Light-jet SF uncertainties $-$ 5 components
	FT_EFF_extrapolation	Extrapolation to high p_T jets uncertainty
	FT_EFF_extrapolation_from_charm	τ-jet uncertainty

Table 11.4: List of the jet systematic uncertainty components. The effect of these uncertainties on the expected yield in the signal region is shown in Table 11.5. The impact of these uncertainties on the measured fiducial cross section is discussed in Section 13.1.3.

JES Uncertainty: The JES calibration process (see Section 6.5) results in over a dozen systematic uncertainties including the uncertainties related to the removal of pile-up contributions, the modeling of back-to-back jets (η intercalibration), and the flavor composition/response. Figure 11.1 illustrates the various JES uncertainties for jets at $\eta = 0.0$ as a function of jet p_T for data collected in 2015 (left) and 2016 (right). The total uncertainty is shown as a lilac band with the various components represented. For jets with $p_T > 30$ GeV, the total JES uncertainty is less than 4% and is dependent upon the p_T and η of the jet.
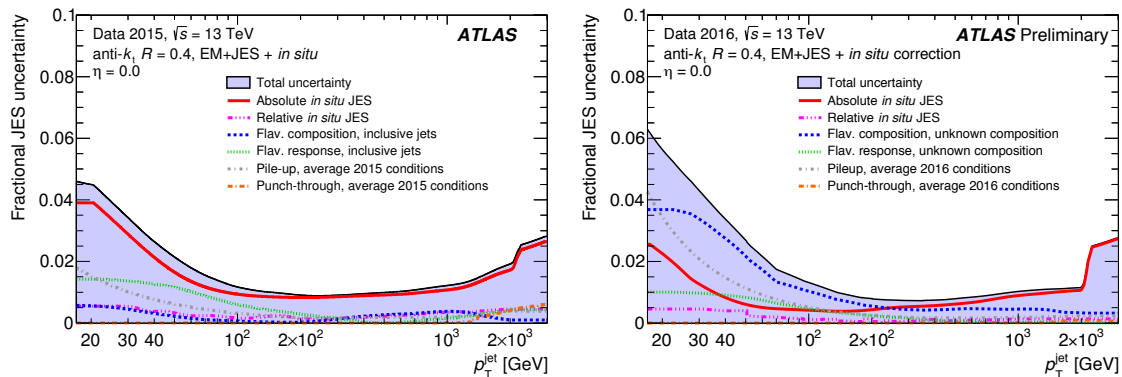
Figure 11.1: The relative Jet Energy Scale (JES) uncertainty for jets at $\eta = 0.0$ as a function of jet p_T for data collected in 2015 (left) and 2016 (right) [133, 139].

JER Uncertainty: For the JER uncertainty, the intrinsic uncertainty is derived from measurements of jet response in data (see Figure 6.13). The total JER uncertainty (systematic and statistical added in quadrature) is approximately 3% for central jets with p_T around 20 GeV and decreases for higher p_T jets.

JVT Uncertainty: The systematic uncertainties on the JVT selection result from the uncertainty in the MC simulation used to determine the JVT cut efficiency, e.g., the impact of the MC generator's choice of fragmentation model. The resulting systematic uncertainty decreases from 2% to 1% as the jet p_T increases from 20 GeV to 60 GeV.

***b*-tagging Inefficiency:** The *b*-tagging efficiency uncertainty is composed of several different uncertainties, including the uncertainty on the data-to-simulation scale factors used to correct the rate of mistagging both light-flavor jets and *c*-jets as *b*-jets in MC to agree with the rate in data.

11.2.1 Impact in Signal Region

The resulting impact of the JES, JER, and JVT uncertainties is combined and referred to as "jet-related uncertainties". The jet *b*-tagging inefficiency is considered separately. The

relative uncertainties in the signal region for each of these categories (see Table 11.5) are determined by propagating the uncertainty on the jet reconstruction/identification procedures through the analysis chain.

The propagated systematic uncertainty in the signal region due to jet-related uncertainties and b-tagging uncertainties are summarized in Table 11.5. Some backgrounds have extra large uncertainties due to low statistics and fluctuations. However, these background processes only contribute a small number of events to the signal region. Therefore, the large uncertainties do not have a serious impact on the final cross section uncertainty.

Process	Jet-Related (%)			b-tagging Inefficiency (%)		
	$e^\pm e^\pm$	$e^\pm \mu^\pm$	$\mu^\pm \mu^\pm$	$e^\pm e^\pm$	$e^\pm \mu^\pm$	$\mu^\pm \mu^\pm$
$W^\pm W^\pm jj$−EW	2.28	2.22	2.28	1.81	1.76	1.74
$W^\pm W^\pm jj$−QCD	3.41	3.04	2.85	2.56	2.48	2.48
WZ	9.58	5.03	8.45	2.49	2.23	2.40
VVV	13.09	13.39	16.85	2.96	3.77	4.95
$t\bar{t}V$	17.65	11.97	14.27	15.02	9.04	13.83
ZZ	15.71	15.76	35.18	2.23	2.35	2.89
$W\gamma$	7.05	33.36	-	1.97	2.94	-
$Z\gamma$	16.22	370.44	-	1.08	3.10	-

Table 11.5: Jet-related and b-tagging systematic uncertainties for signal and background in the signal region in three channels.

11.3 E_T^{miss}

The systematic uncertainties associated with E_T^{miss} reconstruction (see Section 6.6) are listed in Table 11.6. All three uncertainties relate to the *soft event*, i.e., the E_T^{miss} calculation from tracks not associated with any hard-scatter tracks (the unused tracks). The systematic uncertainty due to the *soft* tracks is evaluated by comparing the observables measured in data and MC simulation.

In Table 11.7, the E_T^{miss} systematic uncertainties are grouped together in a singular E_T^{miss} reconstruction uncertainty. Table 11.7 shows the impact of the E_T^{miss} systematic uncertainty in the signal region for signal and background processes.

With the exception of the ZZ and $t\bar{t} + V$ backgrounds, the uncertainty in the signal region due to E_T^{miss} reconstruction is less than 2% for all lepton channels. However, the uncertainty on the ZZ and $t\bar{t} + V$ background, which has low statistics in the signal region, is still less than 5% in all lepton channels.

E_T^{miss} **Category**	**Uncertainty**	**Notes**
Track-based soft-term	MET_SoftTrk_ResoPara	Longitudinal resolution uncertainty
	MET_SoftTrk_ResoPerp	Transverse resolution uncertainty
	MET_SoftTrk_Scale	Longitudinal scale uncertainty

Table 11.6: List of the E_T^{miss} systematic uncertainty components. The effect of these systematic uncertainties on the expected yield in the signal region is shown in Table 11.7.

Process	E_T^{miss} **Reconstruction (%)**		
	$e^\pm e^\pm$	$e^\pm \mu^\pm$	$\mu^\pm \mu^\pm$
$W^\pm W^\pm jj-$EW	0.26	0.17	0.21
$W^\pm W^\pm jj-$QCD	0.41	0.22	0.34
WZ	0.93	0.79	1.63
VVV	0.00	0.46	0.00
$t\bar{t}V$	1.75	4.16	1.62
ZZ	4.84	3.26	3.24
$W\gamma$	0.00	0.00	-
$Z\gamma$	0.00	0.00	-

Table 11.7: Systematic uncertainty due to E_T^{miss} reconstruction for signal and background in the signal region in three channels.

11.4 Pile-up Reweighting

Another source of systematic uncertainty common to all ATLAS analyses is the pile-up reweighting uncertainty. In order to correct the underlying event distribution in data and MC, the MC events are reweighted to match the distribution observed in data [156]. A variation in the pile-up reweighting of MC is included to cover the uncertainty on the ratio between the predicted and measured inelastic cross-section in the fiducial volume defined by $M_X > 13$ GeV, where M_X is the mass of the hadronic system [156]. This variation results in a single systematic uncertainty: PRW_DATASF.

The impact of the pile-up reweighting uncertainty on expected signal and background yields in the signal region can be seen in Table 11.8. Once again, for processes with significant contributions in the signal region (such as $W^\pm W^\pm jj-$EW, $W^\pm W^\pm jj-$QCD, and WZ), the relative uncertainty is below 5%. The uncertainty on the smaller background contributions is much larger.

Process	Pile-up Reweighting (%)		
	$e^{\pm}e^{\pm}$	$e^{\pm}\mu^{\pm}$	$\mu^{\pm}\mu^{\pm}$
$W^{\pm}W^{\pm}jj$−EW	0.48	0.97	2.42
$W^{\pm}W^{\pm}jj$−QCD	4.99	0.45	0.33
WZ	2.99	3.49	3.33
VVV	19.37	24.66	6.87
$t\bar{t}V$	8.73	10.69	4.18
ZZ	1.22	3.20	4.58
$W\gamma$	4.11	14.17	-
$Z\gamma$	12.57	11.51	-

Table 11.8: Systematic uncertainty due to pile-up reweighting for signal and background in the signal region in three channels.

11.5   Summary

The largest source of uncertainty in the signal region for all background processes in all lepton channels is almost exclusively jet-related uncertainties (see Section 11.2). For $W^{\pm}W^{\pm}jj$−EW, $W^{\pm}W^{\pm}jj$−QCD, and WZ the largest jet-related uncertainties (see Table 11.5) in the signal region are the JES jet flavor composition uncertainty and the JER uncertainty. The only background/channel combinations where the jet-related uncertainties are not the dominant source of uncertainty are: $W^{\pm}W^{\pm}jj$−QCD in the ee channel, and VVV in the ee and $e\mu$ channels (VVV is statistically limited). In these cases, the pile-up reweighting uncertainty is the largest source of uncertainty.

All ATLAS object uncertainties discussed in this chapter are considered when determining the measured $W^{\pm}W^{\pm}jj$−EW fiducial cross section. The treatment of the uncertainties in the fit is discussed in Section 12.3. The impact of the uncertainties on the measured $W^{\pm}W^{\pm}jj$−EW cross section is summarized in Chapter 13.

Chapter 12

Fitting Method and Cross Section Extraction

To extract the $W^{\pm}W^{\pm}jj-$EW cross section, a maximum likelihood fit is performed using the expected m_{jj} distributions for each background process and the $W^{\pm}W^{\pm}jj-$EW signal. The fit is a "vertical" fit, where the "stacked" expected signal and background m_{jj} distributions are manipulated within the systematic uncertainties to obtain the best representation of the observed data. Systematic uncertainties enter the fit as nuisance parameters (NPs) that can impact the signal and background m_{jj} distributions' yields and/or shapes. A total of 149 NPs are considered: 31 NPs for MC statistical uncertainties, 7 NPs for specific background-process modeling uncertainties, 19 NPs for theoretical uncertainties, and 92 NPs for standard ATLAS object uncertainties. The fit is performed in the signal region, the low m_{jj} control region, and the WZ control region simultaneously. The low m_{jj} and WZ control regions are included in the fit to constrain the expected background in the signal region.

This chapter describes the maximum likelihood method utilized in the fit, details how the fit was implemented, delineates the uncertainty treatment method, and presents the results of the fit performed with an Asimov dataset. The process of extracting the $W^{\pm}W^{\pm}jj-$EW cross section from the fit is also discussed.

12.1 Maximum Likelihood Method

The number of predicted signal events per channel c and m_{jj} bin b can be written as the product of the $W^{\pm}W^{\pm}jj-$EW fiducial cross section σ_{fid} (see Section 9.1.4), the signal efficiency $\epsilon_{c,b}(\theta)$, and the integrated luminosity L_0:

$$N_{c,b}^{sig}(\theta) = \sigma_{fid} \cdot \epsilon_{c,b}(\theta) \cdot L_0. \tag{12.1}$$

Here, θ represents the set of NPs that parameterize the effect of each systematic uncertainty on the the signal and background expectations in each region. Equation 12.1 is equivalent to the number of events in the channel c and m_{jj} bin b of the detector-level

$W^{\pm}W^{\pm}jj$−EW MC sample. With Equation 12.1, the total expected number of events in a given channel and bin can be expressed as:

$$
\begin{aligned}
N_{c,b}^{exp}(\mu, \theta) &= \mu \cdot N_{c,b}^{sig}(\theta) + N_{c,b}^{bkg}(\theta) \\
&= \mu \cdot \sigma_{fid} \cdot \epsilon_{c,b}(\theta) \cdot L_0 + N_{c,b}^{bkg}(\theta),
\end{aligned}
\tag{12.2}
$$

where $N_{c,b}^{bkg}(\theta)$ is the sum of all expected background events in channel c and bin b, and μ is the signal strength parameter defined as the the ratio of the measured cross section to the SM predicted cross section. In other words, μ is the measure of how well the number of observed signal events agrees with the number of signal events predicted by the Standard Model.

The binned likelihood function is given by[1]:

$$
\mathcal{L}(\mu|\theta) = \prod_{c \in \text{channels}} \prod_{b \in \text{bins}} \text{Poisson}(N_{c,b}^{meas}|N_{c,b}^{exp}(\mu, \theta)) \cdot \text{Gaussian}(L_0|\theta_L, \Delta_L) \cdot \prod_{s \in \text{syst}} F(a_s|\theta_s),
\tag{12.3}
$$

where:

- $N_{c,b}^{meas}$ is the number of measured events in bin b for channel c.

- Gaussian$(L_0|\theta_L, \Delta_L)$ is the luminosity term taking into account the luminosity uncertainty (Δ_L) and NP (θ_L).

- $F(a_s|\theta_s)$ is the PDF which constrains the NP θ_s. Auxiliary measurements used to constrain the NP are represented by a_s. For all NPs except the MC statistics, a Gaussian PDF is used. For the MC statistic NPs, a Poisson PDF is used. Log-normal PDFs are used for normalization uncertainties to ensure that they are always positive.

The expected signal and background yields ($N_{c,b}^{exp}(\mu, \theta)$) are adjusted by the set of NPs within the constraints of the systematic uncertainties. The yields after the fit correspond to the values that best represents the observed data yield, and are often referred to as the *post-fit* values[2].

The test statistic q_μ is defined as the profile likelihood ratio:

$$
q_\mu = -2 \ln \frac{\mathcal{L}(\mu|\hat{\hat{\theta}}_\mu)}{\mathcal{L}(\hat{\mu}|\hat{\theta})},
\tag{12.4}
$$

where $\hat{\mu}$ (the fitted signal strength) and $\hat{\theta}$ are the unconditional parameter values that maximize the overall likelihood function, and $\hat{\hat{\theta}}_\mu$ represents the conditional parameter values

---

[1]More information about the fit method can be found in Ref. [157].

[2]*Post-fit* refers to a value after the fit method has been applied. Similarly, *pre-fit* refers to the value before the fit method is applied.

that maximize the likelihood function for a given μ value. Using this test statistic, the compatibility of the observed data to a background-only hypothesis ($\mu = 0$) is determined. If the observed data is found to be inconsistent with the background-only prediction by more than five standard deviations (5σ), the observation of the $W^{\pm}W^{\pm}jj-$EW process is claimed.

12.2   Fit Implementation

The binned likelihood fit described in the previous section is performed on the signal and background m_{jj} distributions in the signal region, the low m_{jj} control region, and the $WZjj$ control region simultaneously to extract the $W^{\pm}W^{\pm}jj-$EW cross section. Each region is considered in the fit in the following way:

- **Signal Region:**   The signal region is included in the fit with four m_{jj} bins in the range 500 GeV $< m_{jj} <$ 3000 GeV with lower bin limits: 500 GeV, 700 GeV, 1 TeV, and 1.5 TeV. The fit is performed on all six lepton channels: e^+e^+, e^-e^-, $e^+\mu^+$, $e^-\mu^-$, $\mu^+\mu^+$, and $\mu^-\mu^-$.

- **WZ Control Region:**   The WZ control region is included in the fit as a single m_{jj} bin: 200 GeV $< m_{jj} <$ 3000 GeV. All channels are combined into a single ll channel.

- **Low m_{jj} Control Region:**   The low m_{jj} control region is included in the fit with a single m_{jj} bin: 200 GeV $< m_{jj} <$ 500 GeV. All six lepton channels are considered individually: e^+e^+, e^-e^-, $e^+\mu^+$, $e^-\mu^-$, $\mu^+\mu^+$, and $\mu^-\mu^-$.

The low m_{jj} control region and the WZ control region are included in the fit to constrain the background processes. A normalization factor for the WZ background is determined in these two regions and is included in the fit of the signal region as a free parameter.

12.3   Treatment of Uncertainties

Every source of systematic uncertainty (see Chapters 8, 10, and 11) is included in the fit as an NP that can impact the overall normalization and/or shape of the expected signal and background m_{jj} distributions. For convenience, the systematic uncertainties have been grouped into seven categories: theory-modeling, theory-corrective, theory-MC cross section, charge misID, non-prompt, $V\gamma$, and ATLAS objects. In addition to the systematic uncertainties, the MC statistical uncertainties are included as NPs in the fit. The treatment of the MC statistical uncertainty and each group of systematic uncertainties in the fit is discussed below.

MC Statistics: In order to reduce the number of NPs needed for the fit, the uncertainty resulting from limited MC statistics is included in the fit as a single NP per m_{jj} bin, region, and channel, resulting in 31 NPs for MC statistics. In each m_{jj} bin, the total statistical uncertainty is calculated from the statistical uncertainty of all contributing MC samples except the $W^\pm W^\pm jj-$EW signal sample[3]. The corresponding NP is then taken as the relative statistical uncertainty on the total expected MC event yield. In the fit, the MC statistics NPs are constrained using Poisson PDFs and are treated as a normalization effect.

Theory - Modeling: For $W^\pm W^\pm$ (EW and QCD) and WZ, the systematic uncertainties regarding the PDF, μ_R/μ_F-scale, parton shower, and QCD coupling scale (α_S) are included in the fit as individual NPs (see Table 10.7). They are included as shape variations. These variations also have a normalization effect by construction; however, this effect is not considered in the fit since the effect is included in the uncertainties on the predicted fiducial cross section (see Section 9.1.4).

Theory - Corrective: The uncertainties due to the $W^\pm W^\pm jj-$EW cross section NLO correction and the $W^\pm W^\pm jj$ EW-QCD interference are calculated only in the combined channel since it is assumed that they do not depend on lepton flavor and charge. Thus, the same relative corrections are used in all channels with one NP for the NLO correction and one NP for the EW-QCD interference (see Table 10.7). These NPs are included as shape variations only, meaning that the systematic variations are normalized to the nominal distribution.

Theory - MC Cross Section: The theoretical uncertainty on the cross section of MC-estimated background processes with limited statistics is included as a single NP for each MC sample (see Table 10.7). For each NP, the same value is used for every m_{jj} bin, region, and channel (see Table 10.6). The NPs are treated as a normalization uncertainty.

Charge MisID: The two sources of uncertainty on the charge misID background (see Section 8.2.2.3) are considered in the fit with NPs: one NP for the charge misID scale factor uncertainty (CF_SFunc), and one NP for the charge misID background without the energy correction (CF_NoCorr). These NPs are treated as shape uncertainties in the fit while also taking into account the difference in the normalization.

Non-Prompt: Four NPs (see Table 8.10) are introduced to parameterize the systematic and statistical uncertainty on the non-prompt background. In the fit, these uncertainties are included as shape uncertainties while also taking into account the difference in normalization.

---

[3]The statistical uncertainty of the $W^\pm W^\pm jj-$EW signal sample is quite low due to the high number of events generated. Since the sample has low uncertainties, the total relative uncertainty in each m_{jj} bin is reduced. To provide a more conservative estimate, the $W^\pm W^\pm jj-$EW MC statistical uncertainty is not included in the fit.

$V\gamma$: A NP is included for the Vγ background scale factor (Conv_Model_Vgamma). This NP is only considered as a normalization effect.

ATLAS Objects: All ATLAS object uncertainties (see Tables 11.1−11.7) are included in the fit as NPs: one for pile-up reweighting (PRW_DATASF), 39 for electrons, 13 for muons, 36 for jets, and three for E_T^{miss}. All sources of uncertainty are considered as shape uncertainties with the normalization effects also considered in the variations.

Summary

In total, 149 NPs are taken into account during the fit. Table 12.1 shows the number of NPs associated with the different types of systematic uncertainties.

Category	Number of NPs	NP Treatment
MC Statistics	31	normalization
Non-Prompt	4	shape and normalization
Charge misID	2	shape and normalization
Vγ	1	normalization
Theory	14	shape
MC Cross Section	5	normalization
Electron	39	
Jet	36	
Muon	13	shape and normalization
E_T^{miss}	3	
Pile-up Reweighting	1	

Table 12.1: Number of nuisance parameters input into the fit to account for each type of systematic uncertainty. The treatment of the NPs in the fit (shape/normalization) is also listed.

The total uncertainty on the $W^{\pm}W^{\pm}jj-$EW cross section measurement is obtained by varying the test statistic q_μ by one unit with respect to the minimum. The total systematic uncertainty on the $W^{\pm}W^{\pm}jj-$EW cross section measurement is obtained by subtracting the statistical uncertainty in quadrature from the total uncertainty with all NPs fixed to their best-fit values.

12.4 Fit Method with Asimov Data

To test the validity of the method, the fit is performed with an Asimov dataset. Asimov data is a representative dataset constructed using the expected yield from all contributing processes. When an Asimov dataset is used in a fit, the values obtained for all estimators (μ, θ, etc.) should reflect their true values, i.e., μ should equal one.

In the nominal fit, the WZ and low m_{jj} control regions are used to determine the WZ normalization factor, μ_{WZ}, that is applied to the WZ background in the signal region. To include this procedure in the Asimov fit, the Asimov fit procedure consists of three steps:

1. Measure μ_{WZ} in a separate fit to the WZ and low m_{jj} control regions using observed data $\Rightarrow \mu_{WZ}^{\mathrm{CR}}$.

2. Generate the Asimov data using WZ background scaled by μ_{WZ}^{CR}.

3. Perform fit with Asimov data applying μ_{WZ}^{CR} as an unconstrained normalization factor in the fit of the WZ control region, low m_{jj} control region, and signal region.

Using the observed data and expected signal/background events in the WZ control region and the low m_{jj} control region, the WZ normalization factor is determined to be:

$$\mu_{WZ}^{\mathrm{CR}} = 0.907 \pm 0.070(\mathrm{stat}) \pm 0.319(\mathrm{syst}), \tag{12.5}$$

where the statistical and systematic uncertainties have been symmetrized, and "syst" includes the theoretical systematic uncertainties and the experimental systematic uncertainties. Using μ_{WZ}^{CR}, Asimov datasets are generated for all six lepton channels in the signal region, the low m_{jj} control region, and the WZ control region. Table 12.2 lists the expected event yield and the resulting Asimov data yield in the signal region for all channels combined. The uncertainty on the "Total Expected" background consists of the statistical, theoretical, and systematic uncertainties added in quadrature. The uncertainty on the Asimov data is simply the Poisson statistical uncertainty.

The nominal fit procedure is conducted using the Asimov data in all six lepton channels in the signal region and low m_{jj} control region and the combined ll channel in the WZ control region. The resulting WZ normalization factor and signal strength (μ) after the fit are:

$$\mu_{WZ}^{\mathrm{Asimov}} = 0.907 \, ^{+0.071}_{-0.068}(\mathrm{stat}) \, ^{+0.124}_{-0.062}(\mathrm{exp.\ syst}) \, ^{+0.355}_{-0.247}(\mathrm{theo.\ syst}) \tag{12.6}$$

$$\mu_{\mathrm{Asimov}} = 1.000 \, ^{+0.245}_{-0.227}(\mathrm{stat}) \, ^{+0.118}_{-0.098}(\mathrm{exp.\ syst}) \, ^{+0.087}_{-0.092}(\mathrm{theo.\ syst}), \tag{12.7}$$

where "theo. syst" includes all theoretical systematic uncertainties, and "exp. syst" includes all experimental systematic uncertainties. The post-fit m_{jj} distribution of the Asimov data fit is shown in Figure 12.1.

Process	All Channels Combined
WZ	31.8 ± 9.3
Non-prompt	23.3 ± 11.6
e/γ conversions	13.4 ± 3.5
Other prompt	2.4 ± 0.5
$W^{\pm}W^{\pm}jj$–QCD	7.3 ± 2.5
$W^{\pm}W^{\pm}jj$–EW	40.9 ± 2.9
Total Expected	119.1 ± 16.9
Asimov Data	119.1 ± 10.9

Table 12.2: Expected signal region yield for signal, background, and Asimov data before the final Asimov fit. Values shown are for all ll channels combined. The WZ background has been scaled with μ_{WZ}^{CR}. Statistical, theoretical, and systematic uncertainties are shown added in quadrature. The uncertainty on the Asimov data is the Poisson statistical uncertainty.

The post-fit value of the WZ normalization factor ($\mu_{WZ}^{\mathrm{Asimov}}$) remains the same as the input value (μ_{WZ}^{CR}), indicating that the fit determined the best-fit value of μ_{WZ} is the expected value. Similarly, the best-fit signal strength parameter, μ_{Asimov}, is determined to be equal to one. In other words, the fit determined that the best representation of the Asimov dataset is the expected signal/background distributions as fed to the fit. Since the Asimov dataset is constructed using the expected signal and background distributions, this indicates the fit performs as expected in this scenario.
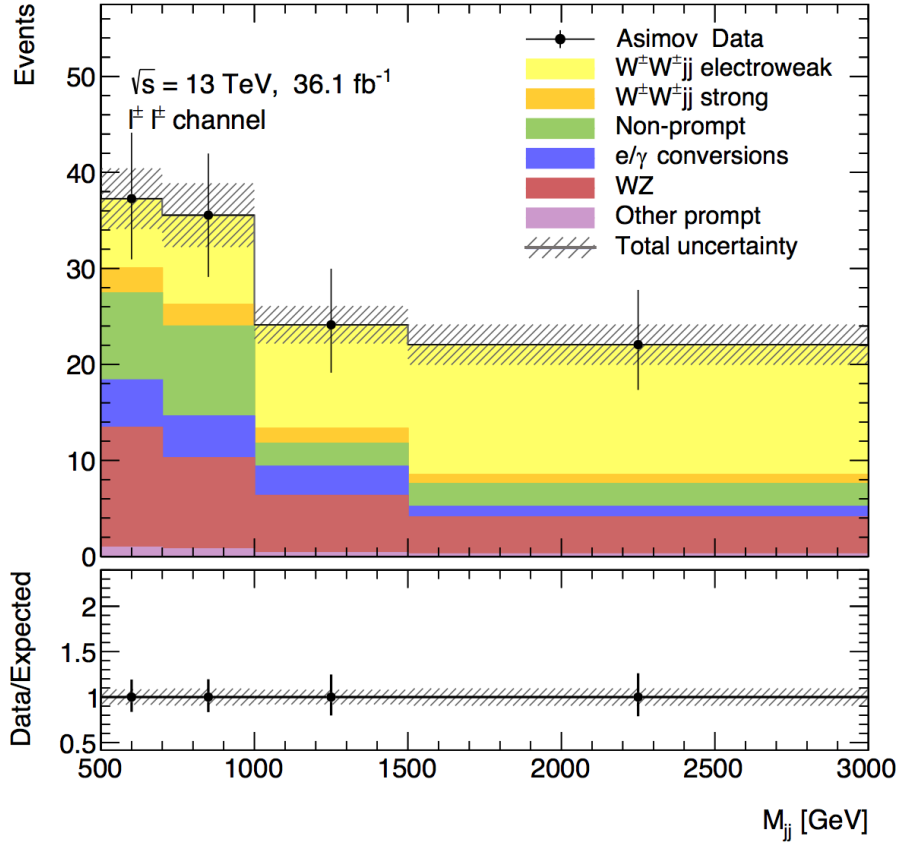
Figure 12.1: Event yield in the signal region with all lepton channels combined with Asimov data. Signal and background distributions are shown as predicted after the fit. The hatched band represents the statistical and systematic uncertainties of the background predictions added in quadrature.

12.5   Cross Section Extraction Method

After the fit is performed, the number of observed $W^{\pm}W^{\pm}jj-$EW events in the signal region can be written in simplified terms as:

$$N_{sig}^{obs} = \mu_{obs} \cdot N_{sig}^{exp},\qquad(12.8)$$

where N_{sig}^{exp} is the number of expected signal events. The number of expected events in the signal region can be written in terms of the expected fiducial cross section using the simplified form of Equation 12.1:

$$N_{sig}^{exp} = \sigma_{fid}^{exp} \cdot \epsilon \cdot L_0.\qquad(12.9)$$

In this simplified form, σ_{fid}^{exp} is the expected fiducial cross section predicted by MC simulation, and ϵ is the efficiency of transitioning from the fiducial region to the signal region. With this definition, the number of observed signal events can be written as:

$$N_{sig}^{obs} = \mu_{obs} \cdot \sigma_{fid}^{exp} \cdot \epsilon \cdot L_0. \tag{12.10}$$

If $\mu_{obs} \neq 1$, Equation 12.10 suggests σ_{fid}^{exp} incorrectly predicts the data by a factor μ_{obs}. This is equivalent to saying the measured fiducial cross section does not agree with the expected fiducial cross section by a factor of μ_{obs}, or:

$$\sigma_{fid}^{meas} = \mu_{obs} \cdot \sigma_{fid}^{exp}. \tag{12.11}$$

This argument, while presented in simplified terms, remains accurate when evaluated more precisely. Hence, the measured fiducial cross section is extracted from the likelihood fit by taking the product of the expected fiducial cross section (see Equation 9.3) and the fitted signal strength (μ_{obs}).

Chapter 13

Results

The previous chapters described all the components necessary to observe $W^{\pm}W^{\pm}jj-$EW production with the ATLAS detector. This chapter presents the final results of the $W^{\pm}W^{\pm}jj-$EW production observation. First, the fit results in the WZ and low m_{jj} control regions and the signal region are discussed. Next, the impact of the systematic uncertainties is described. Finally, the measured fiducial cross section is presented.

13.1 Fit Results

A binned maximum likelihood fit (see Chapter 12) is performed on $W^{\pm}W^{\pm}jj-$EW signal and background processes[1] in the low m_{jj} control region, the WZ control region, and the signal region[2]. The WZ control region and low m_{jj} control region are included in the fit to constrain the background processes and normalize the WZ background.

The WZ background normalization free parameter determined by the fit is:

$$\mu_{WZ} = 0.86 \; ^{+0.07}_{-0.07}(\text{stat}) \; ^{+0.18}_{-0.08}(\text{exp. syst}) \; ^{+0.31}_{-0.23}(\text{theo. syst}), \tag{13.1}$$

where *exp. syst* refers to the experimental systematics and *theo. syst* refers to the theoretical systematics (modeling and corrective). This normalization factor is largely constrained by the observed number of data events in the WZ control region.

The observed signal strength in the signal region determined by the fit is:

$$\mu_{obs} = 1.44 \; ^{+0.26}_{-0.24}(\text{stat}) \; ^{+0.13}_{-0.11}(\text{exp. syst}) \; ^{+0.07}_{-0.08}(\text{theo. syst}). \tag{13.2}$$

The observed signal strength[3] is measured with respect to the SHERPA predicted fiducial cross section.

---

[1]The expected signal and background event yield in each lepton channel are shown in Table 8.13.

[2]The signal region is defined in Section 7.5.

[3]The published observed signal strength quotes the uncertainties in two categories: statistical and systematic, where systematic includes the experimental, the theoretical, and the absolute normalization uncertainty of the prediction. Quoted this way, the observed signal strength is: $\mu_{obs} = 1.44 \; ^{+0.26}_{-0.24}(\text{stat}) \; ^{+0.28}_{-0.22}(\text{syst})$.

Figure 13.1 shows the results of the test statistic likelihood (LLH) scan (see Equation 12.4) for the Asimov dataset and the observed data. The vertical line at $\mu = 0$ is representative[4] of the background-only hypothesis. The background-only hypothesis is rejected with an observed 6.5σ significance[5].
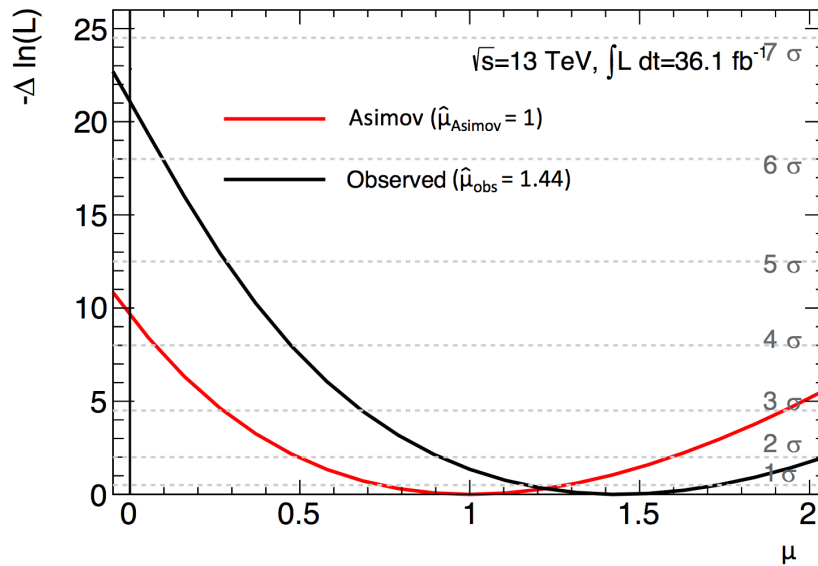
Figure 13.1: Likelihood scan for all six channels combined using all nuisance parameters. Results for the Asimov dataset (red) and the observed data (black) are shown. The vertical line at $\mu = 0$ is representative of the background-only hypothesis, but is not the true likelihood scan result.

13.1.1   Control Region Yields

Figure 13.2 and Table 13.1 show the post-fit event yields in the WZ control region and the low m_{jj} control regions. The observed data and fitted events agree within the total uncertainty in all regions.

---

[4]The true LLH scan for the background-only hypothesis would vary away from zero due to the uncertainties on the measurement.

[5]The expected significance for the Asimov dataset ($\mu_{Asimov} = 1$) is 4.4σ.
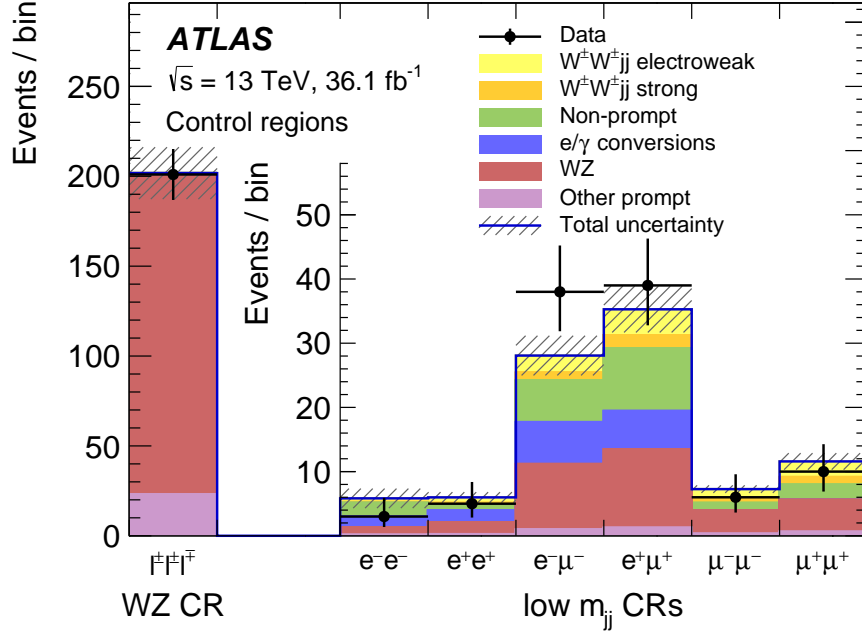
Figure 13.2: Event yield in the WZ control region with all lepton channels combined and the low m_{jj} control region for each channel. Signal and background distributions are shown as predicted after the fit. The hatched band represents the statistical and systematic uncertainties of the background predictions added in quadrature.

	WZ **Control Region**	Low m_{jj} **Control Region**						
	Combined	e^+e^+	e^-e^-	$e^+\mu^+$	$e^-\mu^-$	$\mu^+\mu^+$	$\mu^-\mu^-$	Combined
WZ	177.07 ± 53.29	1.85 ± 0.45	1.13 ± 0.34	12.24 ± 2.21	10.19 ± 1.95	4.98 ± 0.91	3.61 ± 0.66	34.01 ± 5.77
Non-prompt	0.00 ± 0.00	0.95 ± 0.27	2.12 ± 1.34	9.78 ± 3.03	6.47 ± 2.50	2.37 ± 0.89	1.19 ± 0.17	22.88 ± 6.64
e/γ conversions	1.58 ± 0.01	1.83 ± 0.30	1.71 ± 0.44	5.96 ± 1.96	6.53 ± 1.45	0.00 ± 0.00	0.00 ± 0.00	16.03 ± 3.20
Other prompt	23.08 ± 0.17	0.25 ± 0.08	0.15 ± 0.06	1.24 ± 0.26	0.98 ± 0.24	0.62 ± 0.14	0.31 ± 0.09	3.53 ± 0.67
$W^{\pm}W^{\pm}jj$–QCD	0.00 ± 0.00	0.23 ± 0.07	0.13 ± 0.05	2.02 ± 0.56	1.24 ± 0.35	1.18 ± 0.33	0.65 ± 0.18	5.45 ± 1.47
$W^{\pm}W^{\pm}jj$–EW	0.00 ± 0.00	0.88 ± 0.12	0.59 ± 0.11	4.04 ± 0.56	2.67 ± 0.39	2.45 ± 0.35	1.52 ± 0.21	12.14 ± 1.70
Total Fitted	201.74 ± 62.54	5.99 ± 0.88	5.83 ± 1.77	35.28 ± 4.65	28.07 ± 3.81	11.59 ± 1.47	7.27 ± 0.76	94.03 ± 9.89
Observed Data	201	5	3	39	38	10	6	101

Table 13.1: Data, signal, and background event yields in the WZ and low m_{jj} control regions after the fit. Yields are shown in each of the six channels and for all channels combined. Statistical, theoretical, and systematic uncertainties are shown added in quadrature. The statistic, theoretical, and systematic uncertainties are computed by varying each source of uncertainty (NP) by one standard deviation up and down, symmetrizing them, and combining resulting differences according to their correlation. The statistical uncertainty is the uncertainty on the mean fitted background yield and does not include Poisson fluctuations.

13.1.2   Signal Region Yield

The signal region contains 122 data events with a best-fit yield of 69 ± 7 background events. The post-fit m_{jj} distribution in the signal region for all channels combined is shown in Figure 13.3(top) and for each individual channel in Figure 13.4. Table 13.2 lists the fitted event yields in the signal region for each channel and all channels combined. Additional post-fit signal region kinematic distributions are shown in Appendix B.

The observed data and fitted events in the signal region agree within the total uncertainty in all bins of the m_{jj} distribution except 700 GeV $< m_{jj} <$ 1000 GeV. In this bin (see Figure 13.3), the background exceeds the observed data by roughly two standard deviations. In Figure 13.4, the background over-estimation is only statistically significant in the $e^+\mu^+$ channel where the data is approximately 1σ below the fitted yield. Given the low statistics, the observed behavior is likely a statistical fluctuation. Even with the background over-estimation in the 700 GeV $< m_{jj} <$ 1000 GeV, the agreement between the fitted yield and observed data results in $\chi^2/\text{DOF} \approx 1.1$, as shown in Figure 13.3(bottom).

	e^+e^+	e^-e^-	$e^+\mu^+$	$e^-\mu^-$	$\mu^+\mu^+$	$\mu^-\mu^-$	Combined
WZ	1.48 ± 0.32	1.09 ± 0.27	11.6 ± 1.9	7.9 ± 1.4	5.0 ± 0.7	3.4 ± 0.6	31 ± 4
Non-prompt	2.2 ± 1.1	1.2 ± 0.6	5.9 ± 2.5	4.7 ± 1.6	0.56 ± 0.05	0.68 ± 0.13	15 ± 5
e/γ conversions	1.6 ± 0.4	1.6 ± 0.4	6.3 ± 1.6	4.3 ± 1.1	—	—	13.9 ± 2.9
Other prompt	0.16 ± 0.04	0.14 ± 0.04	0.90 ± 0.20	0.63 ± 0.14	0.39 ± 0.09	0.22 ± 0.05	2.4 ± 0.5
$W^\pm W^\pm jj$–QCD	0.35 ± 0.13	0.15 ± 0.05	2.9 ± 1.0	1.2 ± 0.4	1.8 ± 0.6	0.76 ± 0.25	7.2 ± 2.3
Fitted background	5.8 ± 1.4	4.1 ± 1.1	27.6 ± 3.5	18.8 ± 2.6	7.7 ± 0.9	5.1 ± 0.6	69 ± 7
Fitted $W^\pm W^\pm jj$–EW	5.6 ± 1.0	2.2 ± 0.4	24 ± 5	9.4 ± 1.8	13.4 ± 2.5	5.1 ± 1.0	60 ± 11
Data	10	4	44	28	25	11	122

Table 13.2: Data, signal, and background event yields in the signal region after the fit. Yields are shown in each of the six channels and for all channels combined. The total uncertainty is computed by varying each source of uncertainty by one standard deviation up and down, symmetrizing them, and combining resulting differences according to their correlation. The statistical uncertainty included in the total uncertainty is the uncertainty on the mean fitted background yield and does not include Poisson fluctuations.
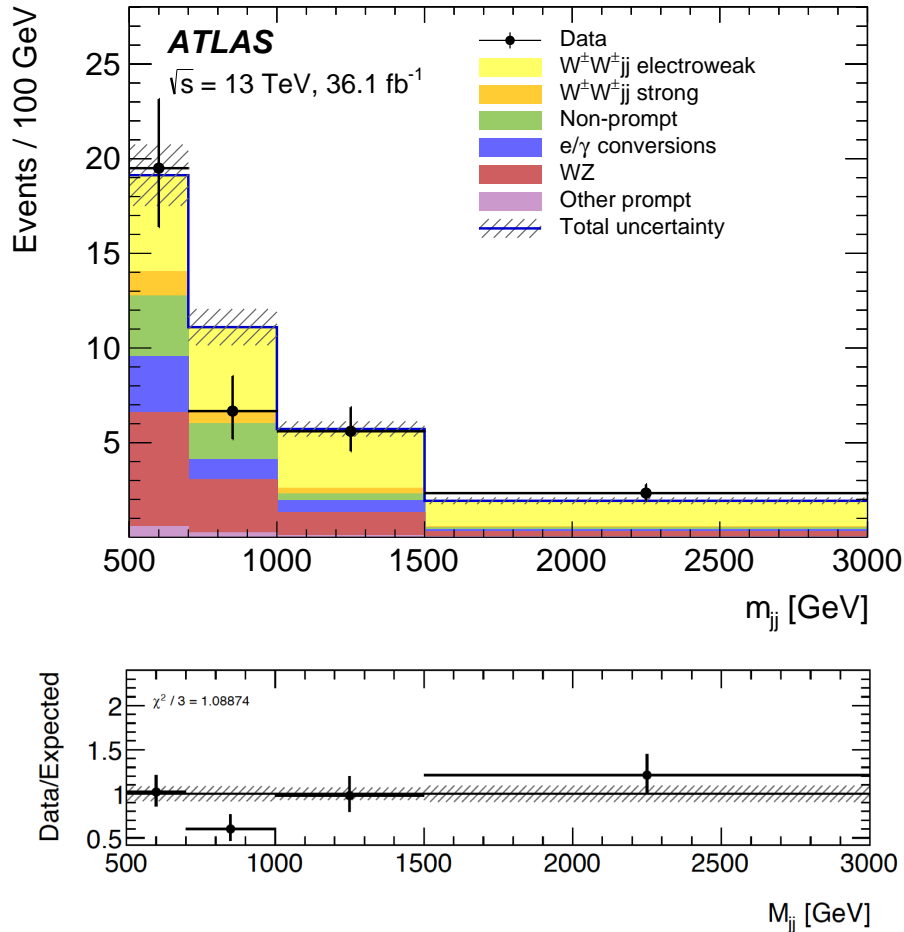
Figure 13.3: *Top:* The m_{jj} distribution for events passing all selections defining the signal region. Results of all lepton channels are shown together. Signal and background distributions are shown as predicted after the fit. *Bottom:* The ratio of the observed data and fitted yield m_{jj} distributions in the signal region. The hatched band represents the statistical and systematic uncertainties of the background predictions added in quadrature.
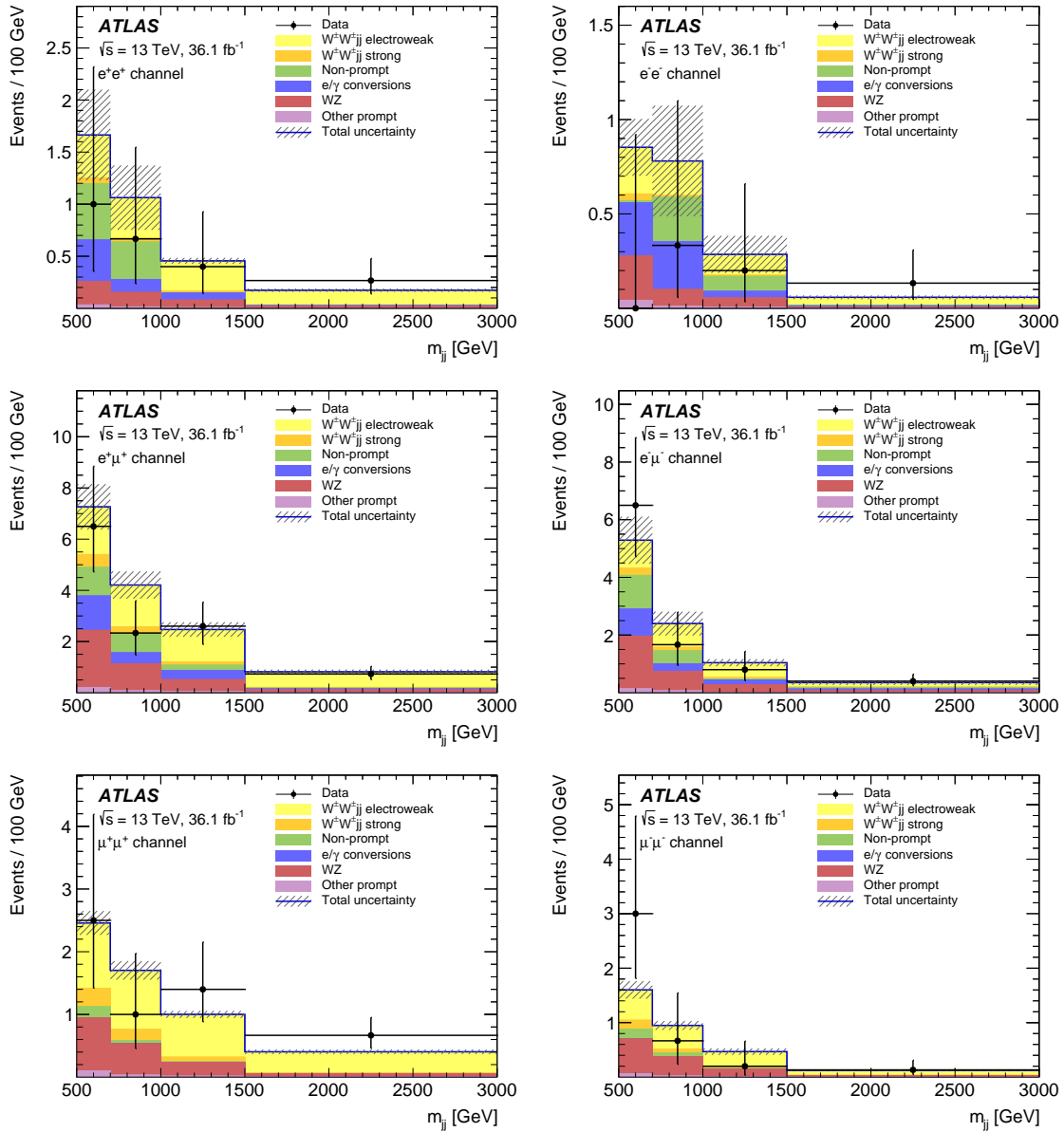
Figure 13.4: The m_{jj} distributions for events passing all selections defining the signal region. Distributions are shown for each lepton channel. Signal and background distributions are shown as predicted after the fit. The hatched band represents the statistical and systematic uncertainties of the background predictions added in quadrature.

13.1.3 Nuisance Parameters

Each analysis systematic uncertainty is included in the fit as an NP. This section details the impact of the NPs on the fit results. While discussing the NPs in the context of the fit results, the following definitions are used:

- θ_0: expected/pre-fit θ value

- $\hat{\theta}$: best-fit θ (unconditional fit) that maximizes the LLH function (see Equation 12.3)

- $\Delta\theta$: expected/pre-fit θ uncertainty

- $\Delta\hat{\theta}$: post-fit $\hat{\theta}$ uncertainty

- $\hat{\mu}$: best-fit signal strength

- $\hat{\hat{\mu}}$: conditionally-fitted signal strength, i.e., signal strength determined from fit with a NP set to a specific value

13.1.3.1 Pull

During the fit, each NP is allowed to float within its systematic uncertainties ($\Delta\theta$) to determine the $\hat{\theta}$ value that corresponds to the best-fit signal strength ($\hat{\mu}$). The *pull* of an NP, which quantifies how far the NP had to be "pulled" from the expected value, is defined as:

$$pull(\theta) = \frac{\hat{\theta} - \theta_0}{\Delta\theta}. \tag{13.3}$$

NPs are often pulled from their expected values due to the signal/background yield needing to be increased or decreased to better agree with the observed data. While the term "pulled" may seem to imply the NPs are manipulated manually to force agreement with the data, this is not the case. The pull is simply a measure of the difference between the most probable NP value as determined by the fit ($\hat{\theta}$) and the expected NP value (θ_0). After the fit, all $\hat{\theta}$ values are within 1σ of the corresponding θ_0 values. The 15 NPs with the largest pulls are shown in Figure 13.5.

The three NPs with the largest pulls are: (1) the JER uncertainty (JET_JER_SINGLE_NP), (2) the electron fake factor systematic uncertainty (FakeElSys), and (3) the JES jet flavor composition uncertainty (JET_Flavor_Composition).

- The JER uncertainty NP is pulled down by roughly 0.5σ (with respect to post-fit NP uncertainty) to decrease the event yield in the signal region $700\,\text{GeV} < m_{jj} < 1000\,\text{GeV}$ bin to better agree with the observed data.

- The electron fake factor systematic uncertainty NP is pulled down by approximately 1σ (with respect to post-fit NP uncertainty) to decrease the non-prompt background yield in the low m_{jj} control region channels containing electrons.
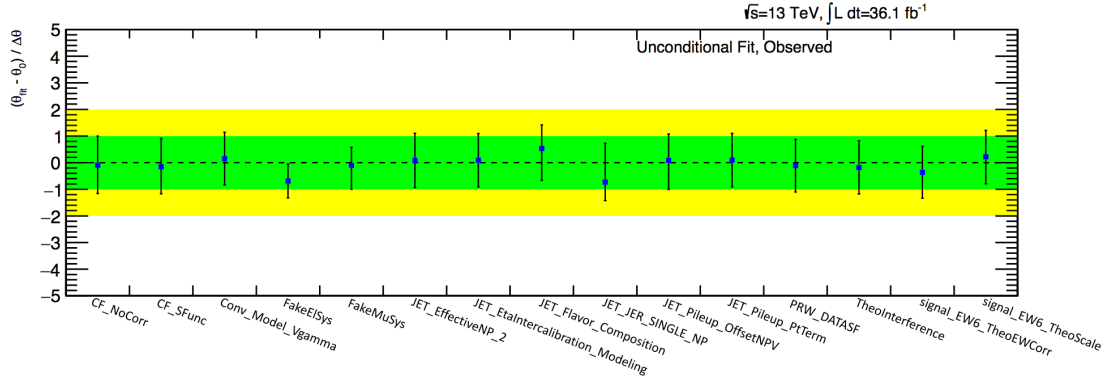
Figure 13.5: NP pulls from unconditional fit (where μ is allowed to float to best fit the data) for the 15 NPs with the largest pulls. The error bars indicate the difference between the pre-fit NP systematic uncertainties and the post-fit NP systematic uncertainties ($\frac{\Delta\hat{\theta}}{\Delta\theta}$). The yellow (green) band represents a 1σ (2σ) pull.

- The JES jet flavor composition NP is pulled up by roughly 0.5σ (with respect to post-fit NP uncertainty) to increase the background yield in the signal region high m_{jj} bins.

13.1.3.2   Impact

The impact of each NP on the fitted signal strength $\hat{\mu}$ is determined by:

$$impact(\theta) = \Delta\mu^{\pm} = \hat{\hat{\mu}}_{\hat{\theta}\pm\Delta\theta} - \hat{\mu}, \tag{13.4}$$

where $\hat{\hat{\mu}}_{\hat{\theta}\pm\Delta\theta}$ is the fitted signal strength measured with the condition $\theta = \hat{\theta} \pm \Delta\theta$.

Figure 13.6 shows the pre-fit and post-fit impact of the 20 NPs with the largest impact on the signal strength $\hat{\mu}$. The pre-fit/post-fit impact is determined by comparing $\hat{\mu}$ with $\hat{\mu}$ resulting from a fit where the considered NP is shifted from $\hat{\theta}$ by its pre-fit/post-fit uncertainties $\Delta\theta/\Delta\hat{\theta}$ (see Equation 13.4).

The five NPs with the largest impact on the signal strength $\hat{\mu}$ are: (1) the $W^{\pm}W^{\pm}jj-$EW parton shower uncertainty, (2) the WZ parton shower uncertainty, (3) the $W^{\pm}W^{\pm}jj-$QCD μ_R/μ_F-scale uncertainty, (4) the electron fake factor systematic uncertainty, and (5) the JES jet flavor composition uncertainty. The $W^{\pm}W^{\pm}jj-$EW parton shower uncertainty NP impact is largely one-sided due to the fact that the $W^{\pm}W^{\pm}jj-$EW parton shower uncertainty has a very small down-variation (see Section 10.1.1).

Figure 13.6 also illustrates that the following NPs are constrained[6] by the fit: (1) electron fake factor systematic uncertainty, (2) muon fake factor systematic uncertainty, (3) JES jet flavor composition uncertainty, (4) JER uncertainty, and (5) $W^{\pm}W^{\pm}jj-$QCD μ_R/μ_F-scale

---

[6]An NP is constrained by the fit if $\frac{\Delta\hat{\theta}}{\Delta\theta} < 1$. A fraction less than one indicates the post-fit systematic uncertainty of the NP is less than the pre-fit, or, in other words, that the observed data constrains the allowed range for the NP to a smaller range than originally assigned.

uncertainty. NPs constrained by the fit are visible in Figure 13.6 in two ways: (1) the pre-fit NP impact (open rectangles) is larger than the post-fit NP impact (filled rectangles), and (2) the NP pull error bars (measure of $\frac{\Delta\hat{\theta}}{\Delta\theta}$) are smaller than one.
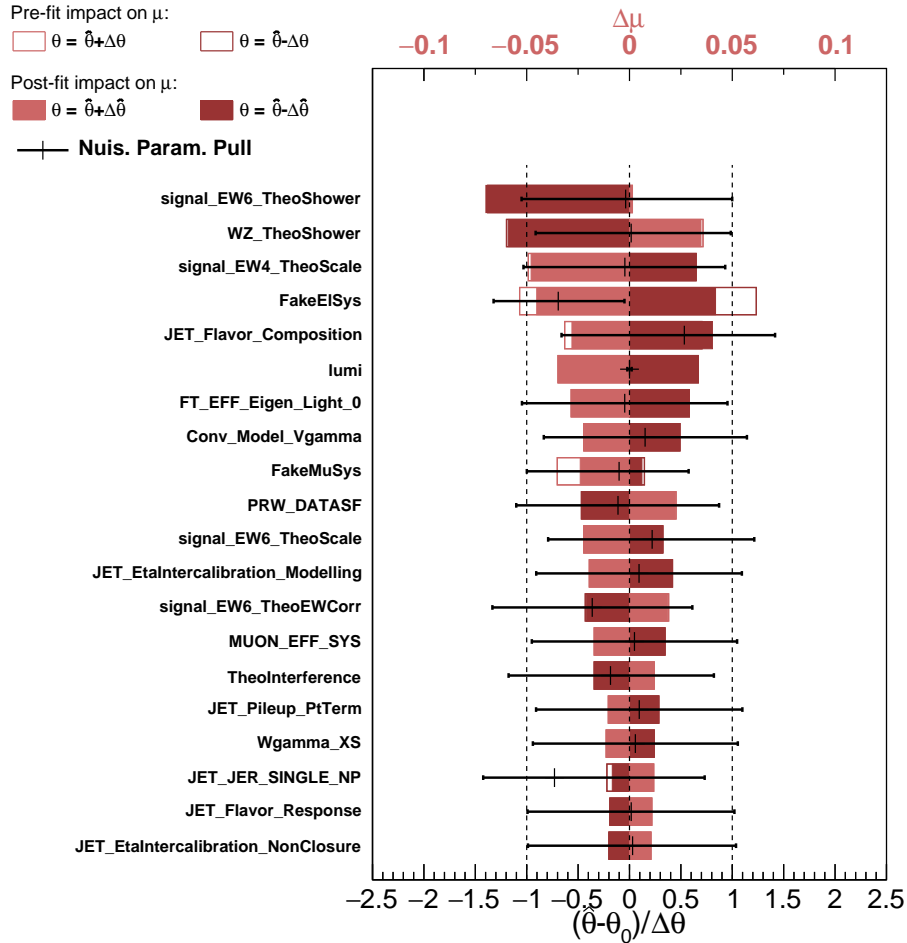
Figure 13.6: Ranking of the 20 NPs with the largest impact on μ ordered according to their impact on the measured signal strength μ using observed data. The empty rectangles correspond to the pre-fit impact on μ, and the filled rectangles correspond to the post-fit impact on μ (shown on the upper scale at top of figure). The impact of each NP, $\Delta\mu$, is computed by comparing the nominal best-fit $\hat{\mu}$ with the result of the fit when the considered NP is fixed to its best-fit value, $\hat{\theta}$, shifted by its pre-fit (post-fit) uncertainties $\pm\Delta\theta$ ($\pm\Delta\hat{\theta}$). The black points show the NP pulls with respect to their nominal values, θ_0, and their relative post-fit errors, $\Delta\hat{\theta}/\Delta\theta$ (shown on the lower scale at bottom of figure). NPs for the MC statistical uncertainty are not included.

13.2   Measured Fiducial Cross Section

Using the fitted signal strength μ_{obs} (see Equation 13.2), the measured fiducial cross section is extracted (see Equation 12.11). With the SHERPA predicted fiducial cross section, the measured fiducial cross section is:

$$\sigma^{\text{fid}}_{meas} = 2.89 \; {}^{+0.51}_{-0.48}(\text{stat}) \; {}^{+0.24}_{-0.22}(\text{exp. syst}) \; {}^{+0.14}_{-0.16}(\text{theo. syst}) \; {}^{+0.08}_{-0.06}(\text{lumi}) \text{ fb}, \qquad (13.5)$$

where *exp. syst* refers to the experimental systematics, *theo. syst* refers to the theoretical systematics (modeling and corrective), and *lumi* refers to the uncertainty due to the luminosity uncertainty.

Figure 13.7 shows the measured fiducial cross section with the expected fiducial cross sections predicted by SHERPA and POWHEG-BOX. For the predicted fiducial cross section measurements, the total uncertainty is shown with a solid blue band. Since it is the largest source of uncertainty for the SHERPA predicted fiducial cross section, the μ_R/μ_F-scale uncertainties are shown separately for the predicted fiducial cross sections. The statistical uncertainty on the measured fiducial cross section is shown with a hatched uncertainty band. The combined total of the statistical and experimental systematic uncertainties for the measured fiducial cross section is shown with the solid orange uncertainty band.

A measure of the impact of the systematic uncertainties on the measured fiducial cross section is shown in Table 13.3. In Table 13.3, the impact of each group of systematic uncertainties is determined without taking into account correlations. The categories (Experimental, Theoretical, Luminosity) correspond to the uncertainty categories quoted for the measured fiducial cross section (see Equation 13.5). The main sources of experimental systematic uncertainty on the measured fiducial cross section are the result of the non-prompt background systematic uncertainty, the statistical uncertainty on the backgrounds, and the jet+E_T^{miss} related uncertainties. The largest sources of theoretical uncertainty are the theory-modeling uncertainties for the WZ, $W^\pm W^\pm jj-$QCD, and $W^\pm W^\pm jj-$EW.
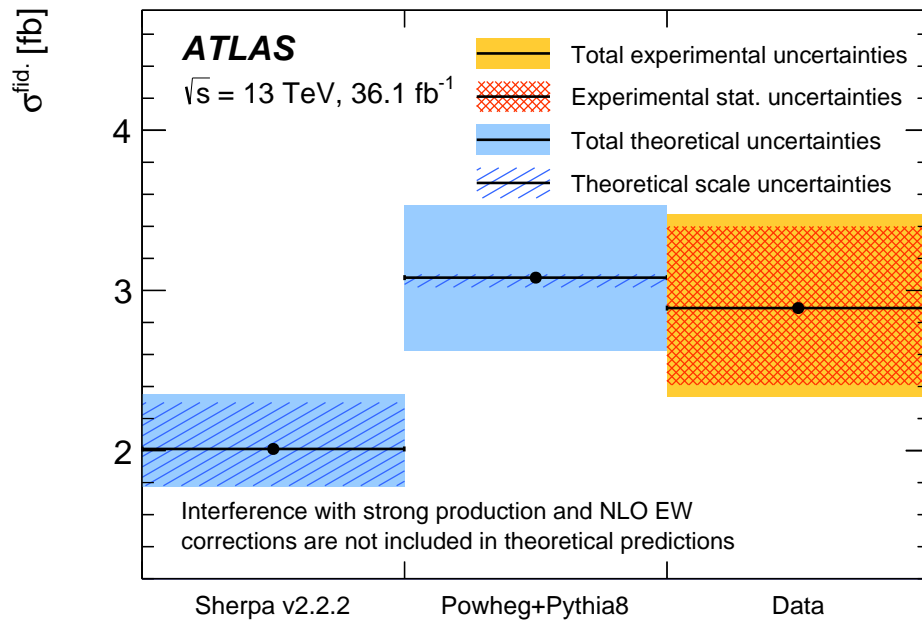
Figure 13.7: Comparison of the measured fiducial cross section and the theoretical calculations from SHERPA and POWHEGBOX+PYTHIA8. Statistical uncertainties of the measured value are depicted as a hatched orange band, while the combined statistical and experimental uncertainty is shown as a light orange band. For the predicted fiducial cross sections, the theoretical uncertainties from the scale dependence are depicted as a dashed blue band. The total theoretical uncertainties, which includes uncertainties in the PDF and parton shower model, are depicted by a light blue band. The theoretical predictions include neither the $W^\pm W^\pm jj$ EW-QCD interference nor the NLO electroweak corrections.

Source	Impact [%]
Experimental	
Electrons	0.6
Muons	1.3
Jets and E_T^{miss}	3.2
b-tagging	2.1
Pile-up	1.6
Background, statistical	3.2
Background, non-prompt	3.3
Background, charge misID	0.3
Background, other	1.8
Theoretical	
$W^{\pm}W^{\pm}jj$ EW-QCD interference	1.0
$W^{\pm}W^{\pm}jj$−EW, NLO correction	1.4
$W^{\pm}W^{\pm}jj$−EW, shower, scale, PDF & α_s	2.8
$W^{\pm}W^{\pm}jj$−QCD, shower, scale, PDF & α_s	2.9
WZ, shower, scale, PDF & α_s	3.3
Luminosity	2.4

Table 13.3: Impact of different components of systematic uncertainty on the measured fiducial cross section, without taking into account correlations. The impact of one source of systematic uncertainty is computed by first performing the fit with the corresponding nuisance parameter fixed to one standard deviation (up or down) from the value obtained in the nominal fit, and then symmetrizing these up- and down-variations. The impacts of several sources of systematic uncertainty are added in quadrature for each component. The categorization of sources of systematic uncertainties into experimental and theoretical corresponds to the categorization used for the measured fiducial cross section. "Background, other" combines the impact of the $V\gamma$ and MC cross-section uncertainties.

Chapter 14

Conclusion and Outlooks

A measurement of the fiducial cross section for $W^{\pm}W^{\pm}$ electroweak production has been performed using pp collisions with $\sqrt{s} = 13$ TeV at the LHC. The collision data used for the measurement was collected in 2015 and 2016 using the ATLAS detector and corresponds to an integrated luminosity of 36.1 fb^{-1}. The measured fiducial cross section is $2.89^{+0.51}_{-0.48}$(stat) $^{+0.29}_{-0.28}$(syst) fb and is compatible with the Standard Model predictions of $2.01^{+0.23}_{-0.23}$ fb (SHERPA) and $3.08^{+0.45}_{-0.46}$ fb (POWHEG-BOX). This measurement provides the first observation of $W^{\pm}W^{\pm}$ electroweak production using the ATLAS detector with a significance of 6.5 standard deviations.

Currently, the fiducial cross section measurement is limited by the statistical uncertainty. In the not too distant future, however, this will no longer be the case. An additional 100 fb^{-1} of data has already been recorded by the ATLAS detector in 2017-2018, and a total integrated luminosity of approximately 3000 fb^{-1} is expected over the next 15 years. MC simulation studies indicate that with 3000 fb^{-1} a measurement of the $W^{\pm}W^{\pm}jj-$EW cross section will no longer be limited by statistics. Instead, the $W^{\pm}W^{\pm}jj-$EW cross section measurement will have a total uncertainty of 6% and will be limited by experimental systematic uncertainties [158]. Without statistical limitations, $W^{\pm}W^{\pm}$ electroweak production can be utilized to further probe the nature of EWSB and physics beyond the Standard Model. For example, studies with 3000 fb^{-1} of simulated data show the purely longitudinal scattering component of $W^{\pm}W^{\pm}$ can be extracted with a significance of 3σ when taking into account only statistical uncertainty [158]. $W^{\pm}W^{\pm}$ electroweak production can also be used as an avenue to search for anomalous quartic gauge couplings [159] or a doubly charged Higgs boson [160, 161]. In short, observing $W^{\pm}W^{\pm}$ electroweak production is just the beginning – there is still a wealth of interesting physics yet to come.

Appendix A

Jet p_T Reweighting Method and Validation

The non-prompt background estimation is dependent upon the underlying jet p_T spectrum (see Section 8.3.1.1). Parameterizing the fake factor as a function of $p_T + p_T^{cone}$ reduces the non-prompt background sensitivity to the underlying jet p_T but does not completely remove the dependency. As a result, if the underlying jet p_T spectrum in the region where the fake factors are determined (dijet region) differs from the spectrum in the region where the fake factors are applied (signal+loose region[1]), the non-prompt background estimate can be skewed. Therefore, the residual dependence on the underlying jet p_T spectrum is accounted for with a systematic uncertainty.

The underlying jet p_T systematic uncertainty is evaluated by calculating fake factors with events where the tag jet p_T has been reweighted to a representative distribution of the true underlying jet p_T in the signal+loose region. This appendix details the method and validation of how the underlying jet p_T spectrum is determined. The impact of reweighting the tag jets to the modeled underlying jet p_T is also discussed.

A.1 Modeling the Underlying Jet p_T

Due to the nature of the object reconstruction, the true underlying jet p_T spectrum in the signal+loose region cannot be recovered. As a result, a model of the underlying jet p_T is created using MC simulation. Studies show that the majority of the non-prompt background is the result of W+jets and $t\bar{t}$ events. Therefore, the underlying jet p_T spectrum is modeled using W+jets and $t\bar{t}$ MC events containing a jet that could potentially produce a non-prompt lepton in a region designed to be similar to the signal+loose region. In this region, events that could potentially produce a non-prompt lepton are selected by requiring:

---

[1]Recall, the signal+loose region differs from the signal region only by requiring one *loose* lepton and one *signal* lepton instead of two *signal* leptons.

- Exactly one prompt *signal* lepton.

- At least two jets passing the requirements of tag jets in the signal region: jet $p_T >$ 65(35) GeV for leading (subleading).

- An additional jet determined to be a *b*-jet at truth-level with $|\eta| < 2.5$[2]. This jet is referred to as the potential non-prompt lepton (PNPL) jet, since it could result in a non-prompt lepton with the same electric charge as the prompt lepton.

In addition to these requirements, the events are required to pass preselection (see Section 7.1), pass single lepton triggers (see Section 7.3), have one other *b*-tagged jet in the event[3], and have $E_T^{miss} > 30$ GeV. The selections defining potential non-prompt lepton (PNPL) events are summarized in Table A.1. Studies show that requiring the additional signal region selections, such as m_{jj} and Δy_{jj}, does not impact the modeled underlying jet p_T spectrum shape and only reduces the statistics of events passing the selections. Hence, no requirements on m_{jj} and Δy_{jj} are applied.

Potential Non-Prompt Lepton Event Selections	
General	Preselection (see Section 7.1) Single lepton triggers (see Section 7.3) $E_T^{miss} > 30$ GeV
Prompt Lepton	$N_{lep} = 1$ *Signal* lepton (see Section 7.4)
PNPL Jet	*b*-jet identified with MC truth information $|\eta| < 2.5$
Other Jets	At least two additional jets ($N_{jet}^{other} > 2$) One additional *b*-tagged jet ($N_{b-tagged}^{other} = 1$) $p_T > 65(35)$ GeV for leading (subleading) jet

Table A.1: Summary of selections used to define events which could result in a non-prompt background event.

Figure A.1 provides an illustration of how a PNPL event could be formed from a $t\bar{t}$ event. In Figure A.1, the quarks/gluons that, once hadronized, could potentially be considered as

---

[2]The η selection is to ensure any resulting non-prompt lepton would be within the detector acceptance for leptons.

[3]The requirement of one additional *b*-jet in the event is added to further select $t\bar{t}$ and W+jets, specifically when applying selections to collision data.

tag jets are highlighted in pink. The prompt lepton is highlighted in yellow, and the $\bar{b}$-quark[4] which, once hadronized, becomes the PNPL jet is highlighted in green.
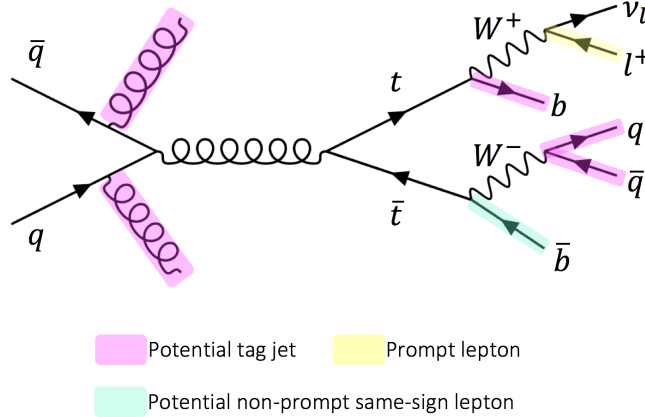
Figure A.1: Illustration of how a $t\bar{t}$ event could potentially result in a non-prompt lepton. The quarks/gluons highlighted in pink illustrate potential final state tag jets. The lepton highlighted in yellow represents the prompt *signal* lepton. The $\bar{b}$-quark highlighted in green represents the PNPL jet that could produce a non-prompt lepton with the same electric charge as the prompt lepton.

The PNPL jet p_T distributions for $t\bar{t}$ and W+jets MC events that pass the PNPL event selections (see Table A.1) are shown in Figure A.2 with the tag jet[5] p_T distribution observed in the dijet region using collision data (see Section 8.3.1). The PNPL jet p_T distributions in Figure A.2 are shown with respect to the scale on the right side of the plot. The difference between the tag jet p_T distribution and the PNPL jet p_T distributions in Figure A.2 highlights the difference between the underlying jet p_T spectrum in the dijet region (represented by the tag jet[6] p_T distribution) and the underlying jet p_T spectrum in the signal+loose region (modeled by the PNPL jet p_T distributions).

Using the PNPL jet p_T distributions from the $t\bar{t}$ and W+jets MC events, a model of the underlying jet p_T spectrum in the signal+loose region is created. The model is created by scaling the contributions of the $t\bar{t}$ events and W+jets events to an accurate representation of the data.

---

[4]Only the $\bar{b}$ quark in Figure A.1 can form the PNPL jet since the other heavy-flavor jets resulting directly from the $t\bar{t}$ decay would produce a lepton with the opposite electric charge compared to the prompt lepton.

[5]Tag jet events in Figure A.2 are required to pass the selections outlined in Table 8.5.

[6]The tag jet is balanced against the non-prompt lepton in the dijet region, and is, thus, a measure of the p_T of the jet reconstructed as the non-prompt lepton.
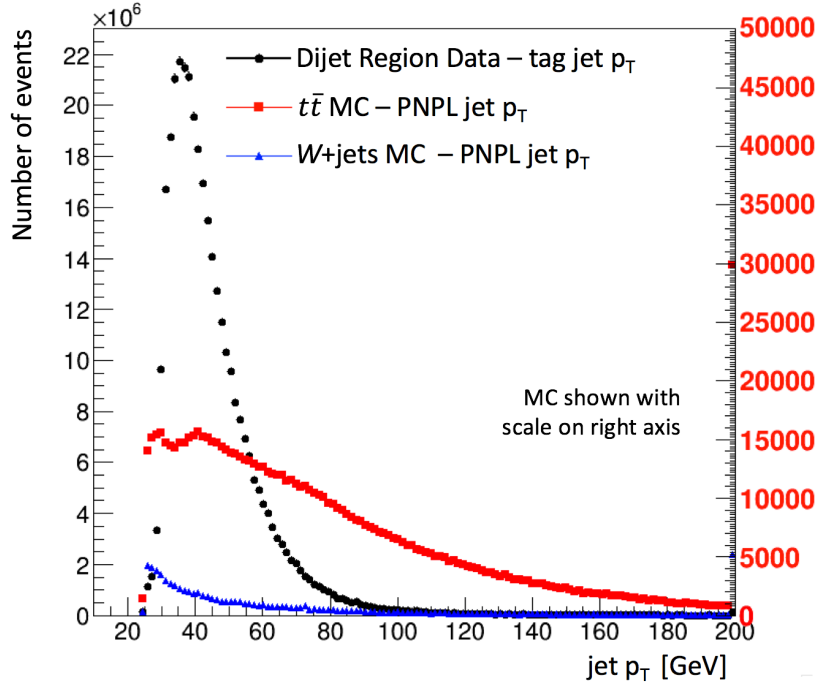
Figure A.2: Jet p_T distribution of the tag jet in collision dijet data shown with the PNPL jet p_T distributions for $t\bar{t}$ MC events and W+jets MC events. The MC PNPL jet p_T distributions are shown using the right-hand scale (written in red).

A.1.1 Validating the Underlying Jet p_T Spectrum Contributions

In order to determine what fraction of the underlying jet p_T spectrum should result from $t\bar{t}$ events and what fraction should result from W+jets events, the PNPL jet p_T spectra in collision data and the $t\bar{t}/W$+jets MCs are compared in a validation region. The validation region, outlined in Table A.2, differs from the nominal PNPL Event Region (see Table A.1) by requiring the PNPL jet is b-tagged instead of identified as a b-jet by MC truth information. Comparing the collision data and MC events in this validation region also validates that the MC events provide a good approximation of the collision data.

In the nominal version of this method (the version implemented in the analysis), the fractions of the $t\bar{t}$ and W+jets contributions to the underlying jet p_T spectrum are determined through manual manipulation of the overall normalization of the MC PNPL jet p_T distributions to improve agreement with the data distribution. An alternative/updated method of determining the fractions (involving fitting the collision data with the PNPL jet p_T distributions) was developed but not utilized in the analysis (see Section A.3). The final underlying jet p_T spectrum is achieved by scaling the $t\bar{t}$ distribution by a factor of 1.05 and the W+jets distribution by a factor of 3.1[7]. In an attempt to account for differences in the underlying

---

[7]The scaling factor applied to the W+jets distribution is higher than anticipated, however this just

Potential Non-Prompt Lepton Event Validation Region	
General	Preselection (see Section 7.1) Single lepton triggers (see Section 7.3) $E_T^{miss} > 30$ GeV
Prompt Lepton	$N_{lep} = 1$ *Signal* lepton (see Section 7.4)
PNPL Jet	*b*-tagged jet $|\eta| < 2.5$
Other Jets	At least two additional jets ($N_{jet}^{other} > 2$) One additional *b*-tagged jet ($N_{b-tagged}^{other} = 1$) $p_T > 65(35)$ GeV for leading (subleading) jet

Table A.2: Summary of selections used to construct the validation region which is used to validate the modeling of events that could result in a non-prompt background event. This region differs from the nominal PNPL event region by requiring the PNPL jet is *b*-tagged instead of identified as a *b*-jet using truth information. Changing this requirement allows for the MC distributions to be compared with collision data, where no truth information exists.

jet p_T spectra of non-prompt electrons and non-prompt muons, PNPL events containing a prompt electron are analyzed independently from PNPL events containing a prompt muon[8].

    Figure A.3 shows the PNPL jet p_T distributions for data and MC events in the PNPL Event Validation Region (see Table A.2). The W+jets and $t\bar{t}$ MC distributions are stacked and scaled by a factor of 3.1 and 1.05, respectively. The distributions for PNPL events containing a prompt muon are shown on the left, while the PNPL jet p_T distributions for PNPL events containing a prompt electron are shown on the right. In each plot, the lower window shows the ratio of the data over the total of the two MC distributions with the scale factors applied.

---

reveals that the W+jets cross section is not well modeled in MC.

    [8]There is no way to determine the flavor of the non-prompt lepton that would be produced by the PNPL jet (although statistically, it would be a muon). Dividing the PNPL jets in this manner provides two independent distributions with which to weight the non-prompt electron/muon events in the dijet region.
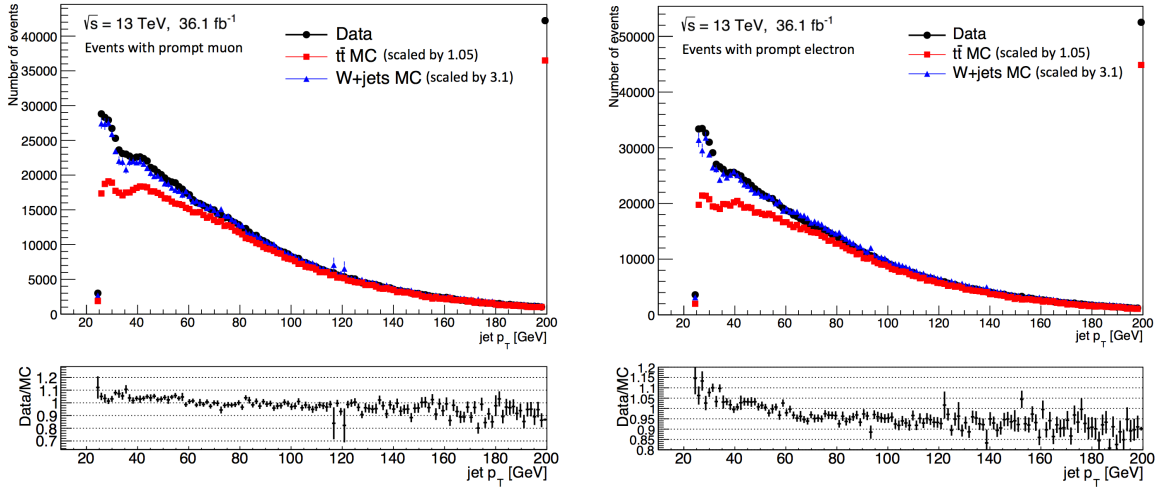
Figure A.3: Jet p_T distributions for PNPL jets in data and $t\bar{t}/W$+jets MC events in the PNPL Event Validation Region (PNPL jet is b-tagged). The $t\bar{t}$ and W+jets MC distributions have been scaled by a factor of 1.05 and 3.1, respectively. Ratio plots show the ratio of data to the combination of both scaled MC distributions. *Left:* Distributions for events with a prompt muon. *Right:* Distributions for events with a prompt electron.

As mentioned previously, the MC scale factors (3.1 for W+jets and 1.05 for $t\bar{t}$) are determined through manual manipulation of the overall normalization of the MC jet p_T distributions shown in Figure A.3. To further validate the scale factors, other kinematic variables are compared in the PNPL Event Validation Region with the scale factors applied. Figure A.4 shows the agreement between the data and scaled MCs in PNPL jet η, and Figure A.5 shows the agreement in E_T^{miss}. The agreement between the data and the combined scaled MCs is within approximately 10% in all plots. Given this, the underlying jet p_T spectrum in the signal+loose region is modeled by the PNPL jet p_T distributions for $t\bar{t}$ and W+jets MC events in the PNPL Event Region (truth b-jet required) scaled by 1.05 and 3.1, respectively.
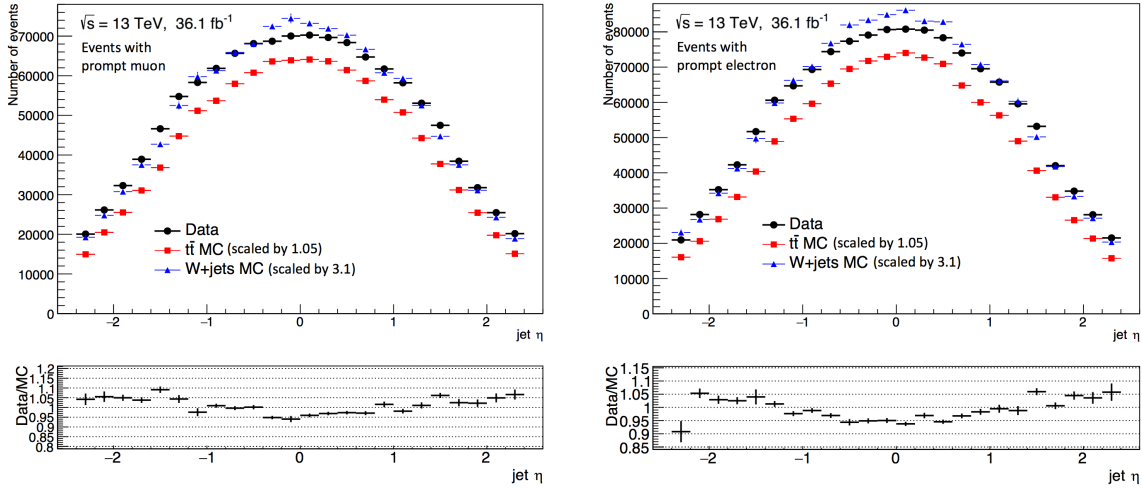
Figure A.4: Jet η distributions for PNPL jets in data and $t\bar{t}/W$+jets MC events in the PNPL Event Validation Region (PNPL jet is b-tagged). The $t\bar{t}$ and W+jets MC distributions have been scaled by a factor of 1.05 and 3.1, respectively. Ratio plots show the ratio of data to the combination of both scaled MC distributions. *Left:* Distributions for events with a prompt muon. *Right:* Distributions for events with a prompt electron.
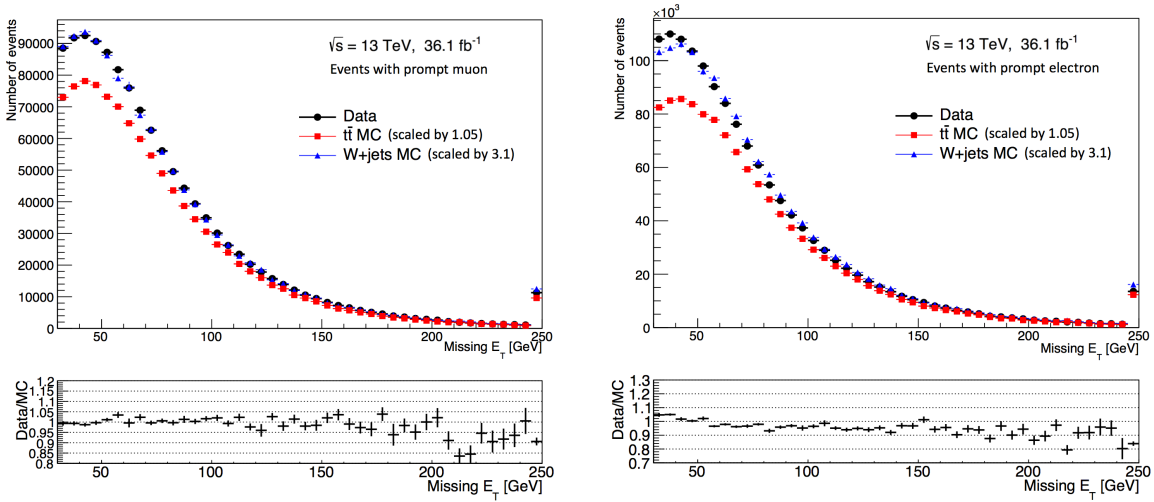
Figure A.5: E_T^{miss} distributions for data and $t\bar{t}/W$+jets MC events in the PNPL Event Validation Region (PNPL jet is b-tagged). The $t\bar{t}$ and W+jets MC distributions have been scaled by a factor of 1.05 and 3.1, respectively. Ratio plots show the ratio of data to the combination of both scaled MC distributions. *Left:* Distributions for events with a prompt muon. *Right:* Distributions for events with a prompt electron.

A.1.2 Resulting Underlying Jet p_T Spectrum

The model of the underlying jet p_T spectrum constructed from the $t\bar{t}$ and W+jets PNPL jet p_T distributions is shown in Figure A.6. The tag jet p_T distributions in the dijet region are also shown for comparison. Figure A.6(left) displays the distributions in the electron channel, meaning: the tag jet p_T distribution is of jets balanced against a non-prompt electron, and the PNPL jet p_T distributions are from PNPL events which contain prompt electrons. Figure A.6(right) displays the distributions in the muon channel, which is defined the same way as the electron channel, but for muon events. The lower panels in Figure A.6 show the ratio of the underlying jet p_T spectra to the tag jet p_T distributions. These ratios are used to weight events in the dijet region.
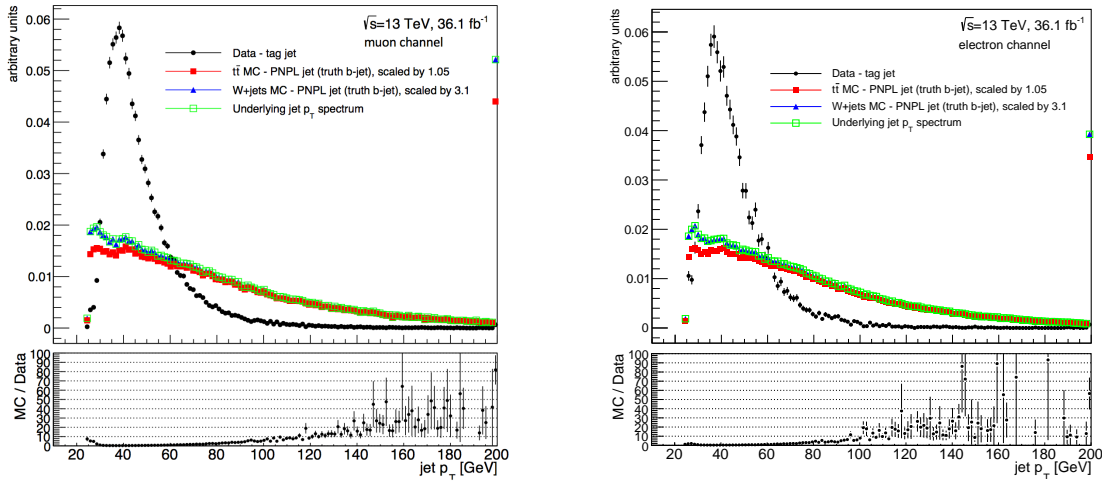
Figure A.6: Jet p_T distributions of the tag jet in collision dijet data shown with the PNPL jet p_T distributions for $t\bar{t}$ MC events and W+jets MC events, stacked and scaled by 1.05 and 3.1, respectively. Together, the $t\bar{t}$ and W+jets distributions combine to form the underlying jet p_T distribution, shown in green. Distributions are normalized to the same unit area. The ratio of the underlying jet p_T spectrum to the data represents the weight applied to the events in the dijet region. *Left:* Tag jet distribution for events with a non-prompt muon and PNPL jet p_T distributions for events with a prompt muon. *Right:* Tag jet distribution for events with a non-prompt electron and PNPL jet p_T distributions for events with a prompt electron.

A.2 Reweighting the Dijet Region Events

Figure A.7 displays the weights applied to events in the dijet region to correct the tag jet p_T spectrum (and thus the underlying jet p_T spectrum) to better agree with the underlying

jet p_T spectrum in the signal+loose region. Ideally, the electron channel weights would be applied to events in the dijet region which contain a non-prompt electron, and the muon channel weights would be applied to events in the dijet region which contain a non-prompt muon.
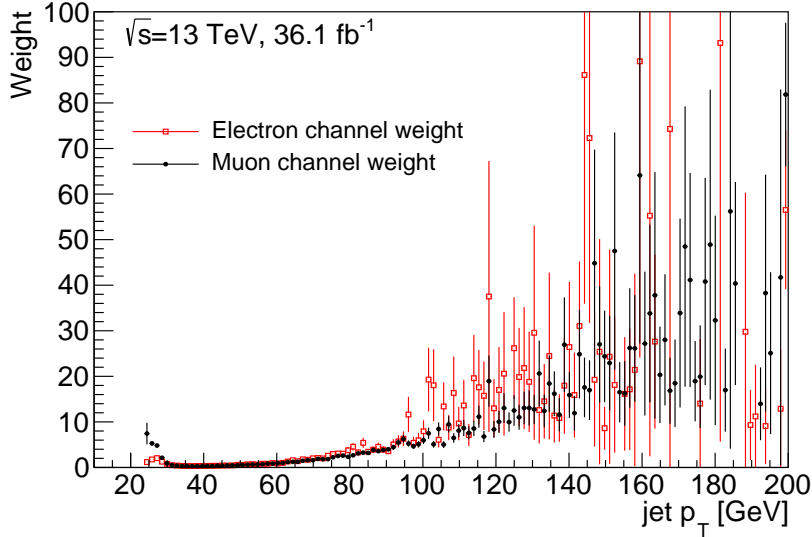
Figure A.7: Weights applied to events in the dijet region, depending upon the tag jet p_T, to correct the tag jet p_T distribution to the modeled underlying jet p_T spectrum in the signal+loose region. The electron channel weights are determined using events in the dijet region with non-prompt electrons and events in the PNPL event region with prompt electrons. The muon channel weights are determined using events in the dijet region with non-prompt muons and events in the PNPL event region with prompt muons.

Unfortunately, at the point in time when the analysis was frozen for ATLAS approval, the electron channel weights were not fully produced and understood[9]. As a result, in the nominal analysis, the muon channel weights are applied to all events in the dijet region (non-prompt muon and non-prompt electron). Since the shape of the tag jet p_T distributions in the electron and muon channels are similar and the modeled underlying jet p_T spectra in the two channels are roughly the same, it was assumed the electron weights would be similar to the muon weights. Once the electron channel weights were finalized and compared with the muon channel weights (see Figure A.7), it was decided not to unfreeze the analysis and propagate the electron channel weights through the full analysis because doing so would have delayed the ATLAS approval of this analysis[10]. This decision was made because the

---

[9]There was a bug in the weight code at the time when determining the electron weights. The electron channel results shown in Figures A.6 and A.7 were finalized the day after the analysis was frozen.

[10]This logic was also the reason the optimized method was not implemented in the analysis.

electron channel weights and the muon channel weights roughly agree within the statistical uncertainty of the electron channel weights.

A.2.1 Impact on Fake Factors

All events in the dijet region, both collision data and MC, are weighted with the muon channel weights depending upon each event's tag jet p_T. The impact of the weights on the p_T distributions used to calculate the muon fake factor is shown in Figure A.8. Figure A.8(left) depicts the nominal *tight* muon p_T distribution (top left) and *loose* muon $p_T + p_T^{cone}$ distribution (bottom left). Figure A.8(right) shows the same distributions after the events are weighted with the muon channel weights according to each event's tag jet p_T.

Just as weighting the dijet region events results in a tag jet p_T spectrum with more high p_T jets, the weighting also results in a lepton p_T spectrum with more high p_T leptons. For example, the *tight* muon p_T distribution has approximately an order of magnitude more events in the highest p_T bin.
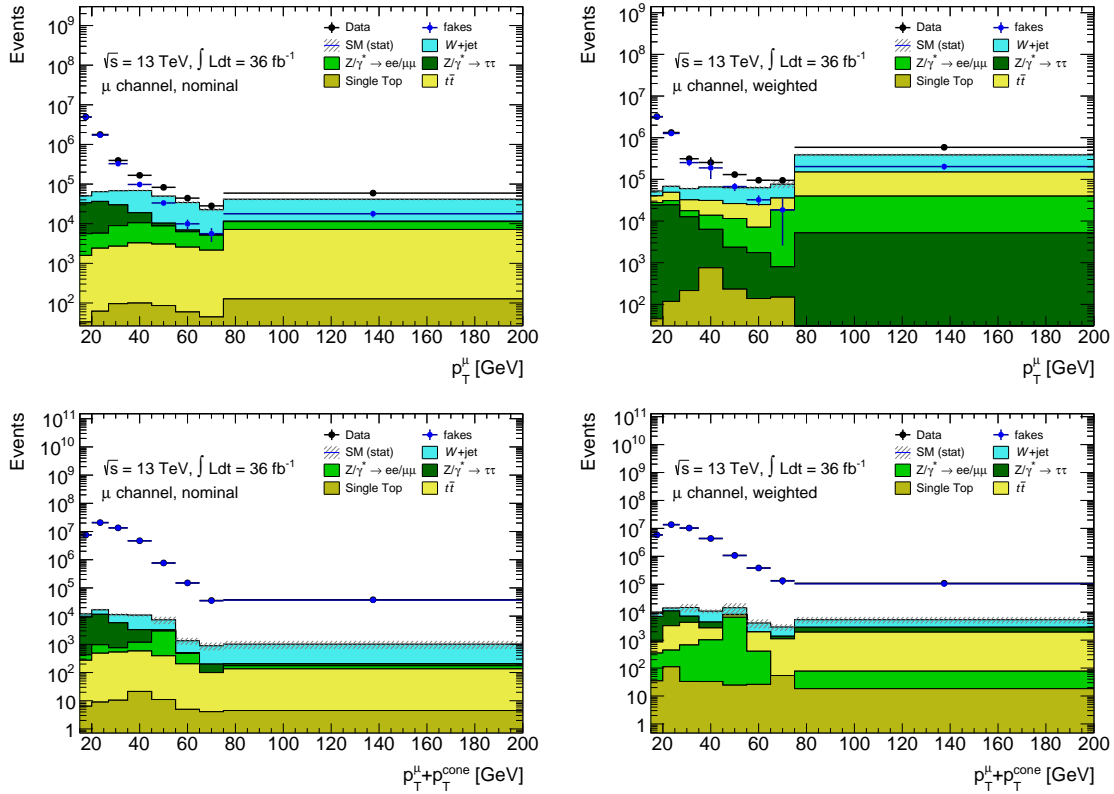
Figure A.8: *Left:* Nominal *tight* muon p_T distributions (top left) and *loose* muon $p_T + p_T^{cone}$ distributions (bottom left) for dijet data and MC prompt contamination in the dijet region. *Right:* *Tight* muon p_T distributions (top right) and *loose* muon $p_T + p_T^{cone}$ distributions (bottom right) for dijet data and MC prompt contamination in the dijet region for events weighted to the underlying jet p_T spectrum in the signal+loose region. The "fakes" distributions represent the dijet data with the MC prompt contamination subtracted.

The fake factors calculated from the weighted events are shown in Figure A.9 for muons and Figure A.10 for electrons (central and forward). The nominal fake factors with the total systematic and statistical uncertainty bands are also shown in Figures A.9 and A.10 for reference. For both the electron and muon fake factors, the underlying jet p_T systematic uncertainty provides, in a number of bins, one of the total systematic uncertainty band boundaries; thus confirming the dependency of the fake factor on the underlying jet p_T spectrum.
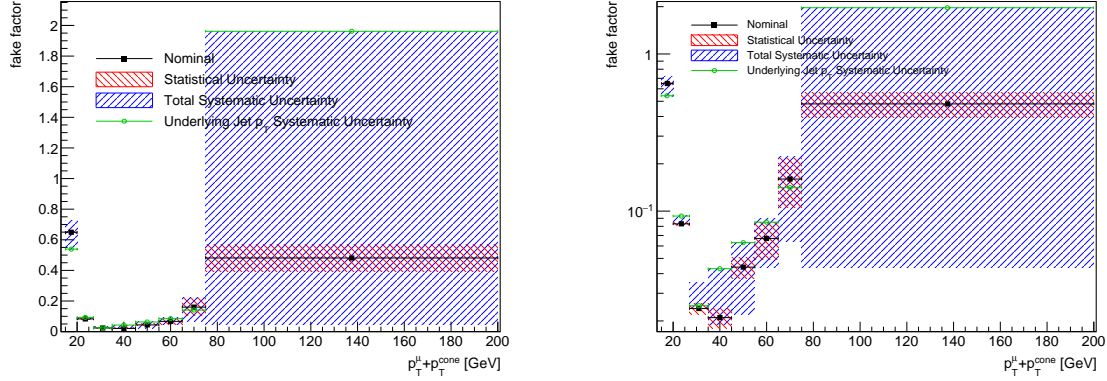
Figure A.9: *Left:* Muon fake factor calculated using events weighted to correct the tag jet p_T spectrum to match the underlying jet p_T spectrum modeled in the signal+loose region (green open circles) shown with the nominal muon fake factor (black filled squares) and the total systematic and statistical uncertainty bands. *Right:* Distributions shown on a log scale.
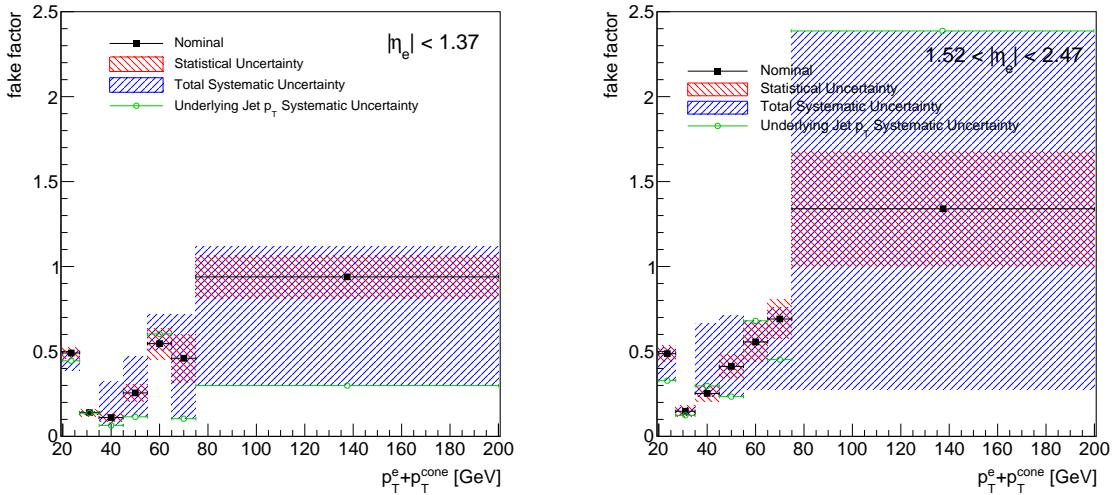
Figure A.10: Electron fake factor calculated using events weighted to correct the tag jet p_T spectrum to match the underlying jet p_T spectrum modeled in the signal+loose region (green open circles) shown with the nominal electron fake factor (black filled squares) and the total systematic and statistical uncertainty bands. *Left:* Central electron fake factor, $|\eta| < 1.37$. *Right:* Forward electron fake factor, $1.52 < |\eta| < 2.47$.

A.3   Updated Underlying Jet p_T Modeling Method

Immediately following the completion of the measurement documented in Sections A.1 and A.2, a more robust, updated method was developed. This version contains a number of updates compared to the nominal method, including:

- The PNPL Event Region selection $N^{other}_{b-tagged} = 1$ is adjusted to be $N^{other}_{b-tagged} > 0$.

- The $t\bar{t}$ and W+jets fractional contributions to the underlying jet p_T spectrum are determined using a fitting algorithm instead of manual manipulation.

- The electron underlying jet p_T systematic uncertainty is determined using the updated electron channel weights instead of the muon channel weights.

Each of these updates are discussed in more detail in Sections A.3.1 - A.3.3. The impact of the updates on the underlying jet p_T systematic uncertainty fake factors is detailed in Section A.3.4.

A.3.1   Updated PNPL Event Regions

In the nominal method of modeling the underlying jet p_T spectrum in the signal+loose region, an additional b-tagged jet (in addition to the PNPL jet) is required to be present in the event. This selection enriches the region with the processes that often produce the non-prompt background, $t\bar{t}$ and W+jets, when selecting in collision data. In the updated method of modeling the underlying jet p_T spectrum, this b-tagged selection is modified. Instead of requiring exactly one additional b-tagged jet, *at least* one additional b-tagged jet is required. This modified selection still preferentially selects $t\bar{t}$ and W+jets events, but with higher statistics since it also includes $t\bar{t}$ and W+jets events that, for example, radiate a gluon that results in a $b\bar{b}$ pair. The updated PNPL Event Region selections and updated PNPL Event Validation Region selections are outlined in Tables A.3 and A.4, respectively.

Updated Potential Non-Prompt Lepton Event Selections	
General	Preselection (see Section 7.1) Single lepton triggers (see Section 7.3) $E_T^{miss} > 30$ GeV
Prompt Lepton	$N_{lep} = 1$ *Signal* lepton (see Section 7.4)
PNPL Jet	b-jet identified with MC truth information $|\eta| < 2.5$
Other Jets	At least two additional jets ($N_{jet}^{other} > 2$) **At least** one additional b-tagged jet ($N_{b-tagged}^{other} > 0$) $p_T > 65(35)$ GeV for leading (subleading) jet

Table A.3: Summary of the updated selections used to define events which could result in a non-prompt background event.

Updated Potential Non-Prompt Lepton Event Validation Region	
General	Preselection (see Section 7.1) Single lepton triggers (see Section 7.3) $E_T^{miss} > 30$ GeV
Prompt Lepton	$N_{lep} = 1$ *Signal* lepton (see Section 7.4)
PNPL Jet	b-tagged jet $|\eta| < 2.5$
Other Jets	At least two additional jets ($N_{jet}^{other} > 2$) **At least** one additional b-tagged jet ($N_{b-tagged}^{other} > 0$) $p_T > 65(35)$ GeV for leading (subleading) jet

Table A.4: Summary of the updated selections used to construct the validation region where the modeling of events that could result in a non-prompt lepton event is validated. This region differs from the nominal PNPL Event Region by requiring the PNPL jet is b-tagged instead of identified as a b-jet using truth information. Changing this requirement allows for the MC distributions to be compared with collision data, where no truth information exists.

A.3.2 $t\bar{t}$ and W+jets Fitted Fractional Contributions

In the nominal method, the fraction of $t\bar{t}$ and W+jets in the PNPL Event Validation Region is determined by manipulating the $t\bar{t}$ and W+jets normalization scales manually and comparing the resulting combined distribution against the collision data. To acquire a more accurate fractional combination of $t\bar{t}$ and W+jets in the PNPL Event Validation Region (and better represent the data), a fitting algorithm, TFractionFitter [162], is implemented in the updated method.

TFractionFitter is a ROOT [163] based fitting program that fits MC distributions as fractions to a data distribution. TFractionFitter uses a standard likelihood fit and Poisson statistics. The program takes the original MC distributions, generates two new MC distributions by randomly selecting values from the original distributions, and then performs a fit to the data distribution with the new MC distributions. Using TFractionFitter, the $t\bar{t}$ and W+jets distributions are fit to the collision data jet p_T distribution in the updated PNPL Event Validation Region (see Table A.4). Figure A.11 shows the TFractionFitter results in the muon channel (left) and the electron channel (right). The MC distributions are shown with their relative fitted fractions, in addition to the combined MC result.
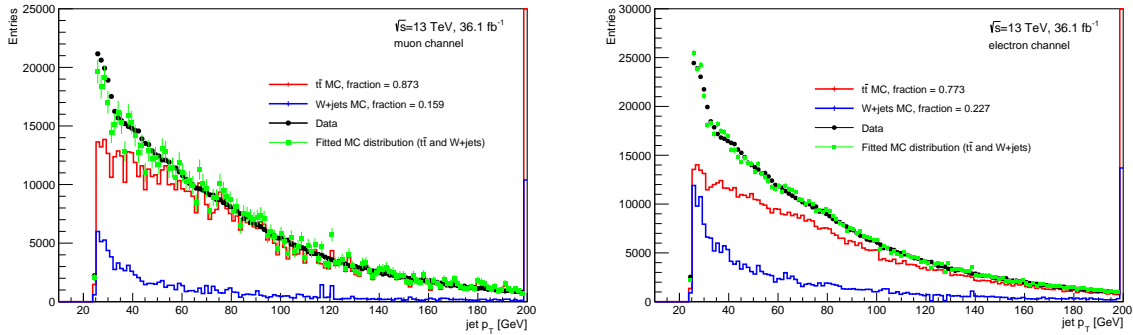
Figure A.11: *Left:* Jet p_T distribution for PNPL jets in the updated PNPL Event Validation Region for events containing a prompt muon. The data (black) is shown with the combined fitted MC distribution (green) along with the contributing fitted fraction of $t\bar{t}$ (red) and W+jets (blue) MC PNPL jets (b-tagged). *Right:* Jet p_T distribution for PNPL jets in the updated PNPL event validation region for events containing a prompt electron. The data (black) is shown with the combined fitted MC distribution (green) along with the contributing fitted fraction of $t\bar{t}$ (red) and W+jets (blue) MC PNPL jets (b-tagged). The fitted fraction of each MC is written in the legend.

In the muon channel, the $t\bar{t}$ fraction in the PNPL Event Validation Region is 0.873 and the W+jets fraction is 0.159, as determined by TFractionFitter. These fractions correspond to a χ^2/DOF= 1.07, indicating a good fit to the data. In the electron channel, the $t\bar{t}$ fraction is 0.773 and the W+jets fraction is 0.227. These fractions correspond to a χ^2/DOF= 1.978,

which indicates a poorer fit. The higher χ^2 value for the fit in the electron channel suggests that the description of the underlying jet p_T spectrum for electrons is not quite accurate.

A.3.3 Updated Weights

The updated underlying jet p_T distribution is modeled using the $t\bar{t}$ and W+jets MC distributions in the PNPL Event Region (PNPL jets are identified as b-jets using MC truth information) scaled by the TFractionFitter fractions[11]. Figure A.12 illustrates the resulting underlying jet p_T distributions. The lower panels in Figure A.12 display the ratios of the underlying jet p_T spectra to the tag jet p_T distributions[12] in the muon channel (left) and the electron channel (right).
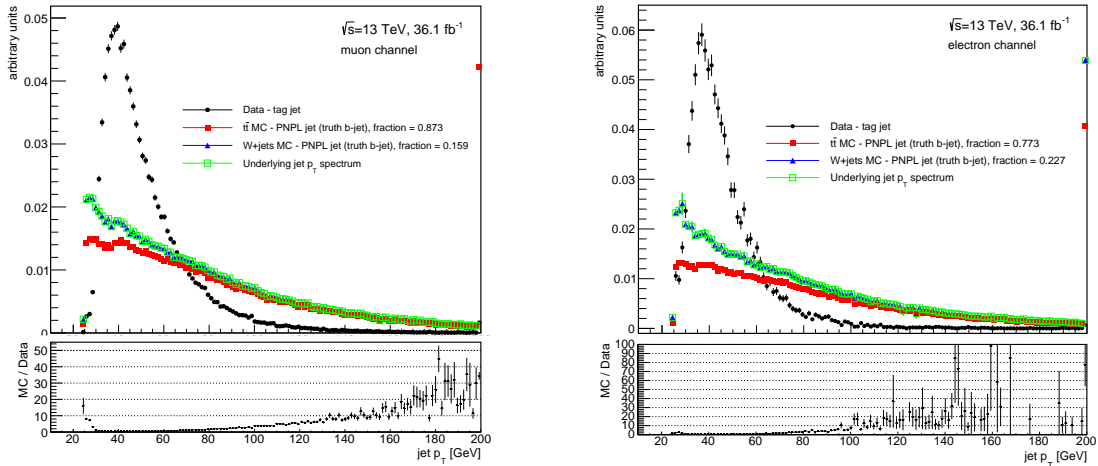
Figure A.12: Jet p_T distributions of the tag jet in collision dijet data shown with the PNPL jet p_T distributions for $t\bar{t}$ and W+jets MC events scaled by the TFractionFitter results. Together, the $t\bar{t}$ and W+jets distributions combine to form the underlying jet p_T distribution, shown in green. Distributions are normalized to the same unit area. The ratio of the underlying jet p_T spectrum to the data represents the weight applied to the events in the dijet region. *Left:* Tag jet distribution for events with a non-prompt muon and PNPL jet p_T distributions for events with a prompt muon. *Right:* Tag jet distribution for events with non-prompt electron and PNPL jet p_T distributions for events with a prompt electron.

---

[11]Each distribution is normalized such that the integral of each individual MC distribution is the correct fitted fraction of the sum integral of the two MC contributions.

[12]The tag jet p_T distributions are slightly different compared to the nominal tag jet p_T distributions. This is due to the fact that the updated method is conducted using reprocessed samples which have slight corrections compared to the nominal selections, e.g., the electron p_T threshold was correctly lowered to 15 GeV instead of 20 GeV.

Figure A.13 displays the updated muon channel weights shown with the nominal muon channel weights (originally shown in Figure A.7). The updated muon channel weights are, on average, lower than the nominal muon channel weights, with a smaller statistical uncertainty.

Figure A.14 shows the updated electron channel weights displayed with the nominal muon channel weights (left) and the nominal electron channel weights (right). More specifically, Figure A.14(left) compares the weights applied to events with a non-prompt electron in the dijet region in the nominal analysis (nominal muon channel weights) and in the updated analysis (updated electron channel weights). Similarly, Figure A.14(right) compares the weights applied to events with a non-prompt electron in the dijet region in the updated analysis (updated electron channel weights) to what was measured, but not applied due to time limitations, in the nominal analysis (nominal electron channel weights). Unlike the comparison of the updated and nominal muon channel weights, the electron channel weights have not changed significantly with the updated method compared to the nominal method. The electron channel weights are also significantly limited statistically at high p_T.
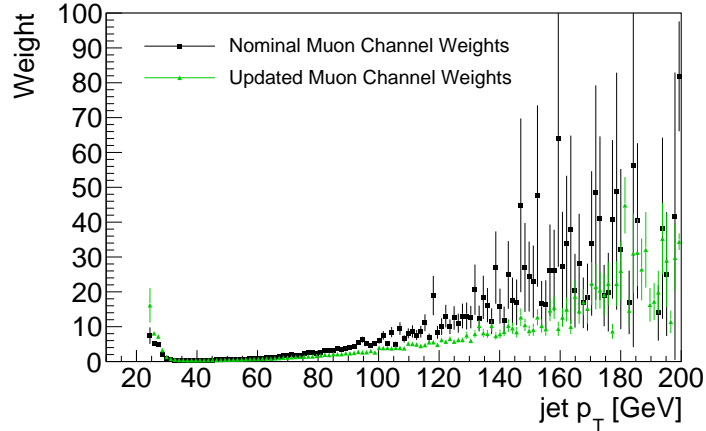
Figure A.13: Nominal (black squares) and updated (green triangles) muon channel weights. These weights are determined by taking the ratio of the modeled underlying jet p_T spectrum in the PNPL Event Region (nominal or updated) for events with a prompt muon to the tag jet p_T distribution in the dijet region for events with a non-prompt muon.
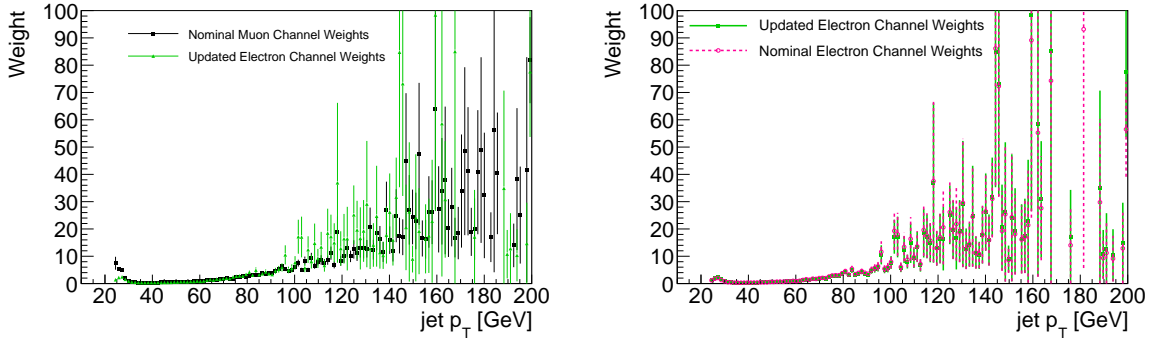
Figure A.14: *Left:* Updated electron channel weights (green triangles) shown with the nominal muon channel weights (black squares). In the nominal method, due to time limitations, the nominal muon weights are used to weight events with a non-prompt electron in the dijet region. *Right:* Updated electron channel weights (green triangles) shown with the nominal electron channel weights (pink circles) which were not finalized until after the analysis was frozen for ATLAS approval.

A.3.4 Impact on Fake Factor

In this section, the underlying jet p_T systematic uncertainty fake factors are referred to simply as *underlying fake factors*, for brevity.

When applying the updated weights to events in the dijet region and calculating the underlying fake factors, four changes are made with respect to the nominal method:

1. The weight applied to each event is interpolated from the weight distributions for a given tag jet p_T in order to reduce the impact of large bin-to-bin fluctuations in the weight distributions.

2. Events with non-prompt electrons are weighted with the updated electron channel weights (instead of the muon channel weights, as was done in the nominal method).

3. A weight of 50 is applied in the electron channel to any non-prompt electron event with tag jet $p_T > 150$ GeV to correct for unphysical weights resulting from low statistics[13].

4. The electron fake factor is calculated in 8 p_T bins instead of 7 p_T bins, adding in the previously inaccessible 15-20 GeV bin.

The updated underlying fake factors, calculated taking into account these changes, are shown in Figure A.15 for muons and Figure A.16 for electrons (central and forward). In

---

[13]A more robust method of dealing with the unphysical weights was considered for development, but was ultimately deemed unnecessary since the nominal method was determined to be sufficient.

both figures, in addition to the updated underlying fake factor, the nominal fake factor and the nominal underlying fake factor[14] are also shown.

For the muon fake factor, the updated underlying fake factor differs only slightly from the nominal underlying fake factor. The updated underlying fake factor also has a lower statistical uncertainty compared to the nominal underlying fake factor. The reduced statistical uncertainty and minimal shift in central value further validates the significant difference between the underlying fake factors and the nominal fake factor in the highest p_T bin.
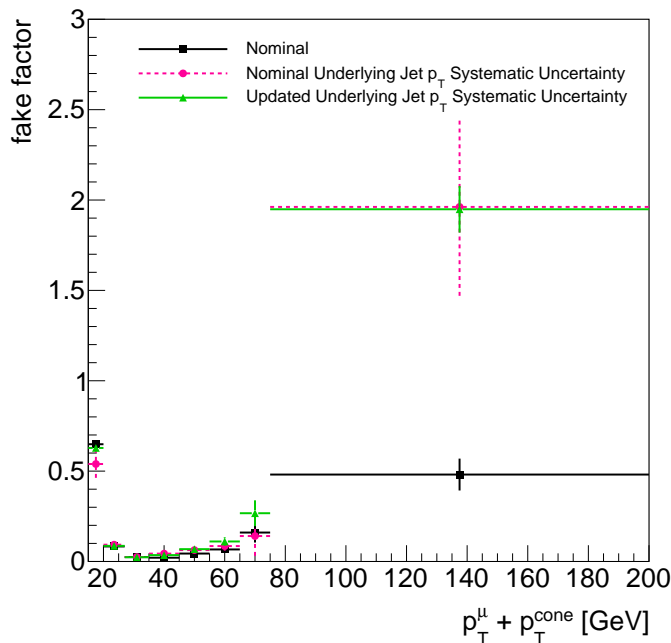
Figure A.15: Updated muon underlying jet p_T systematic uncertainty fake factor (green triangles) shown with the nominal fake factor (black squares) and the nominal underlying jet p_T systematic uncertainty fake factor (pink circles).

For the electron fake factors, larger discrepancies between the updated and nominal underlying fake factors' central values are observed. However, the nominal and updated underlying fake factors do largely agree within their statistical uncertainties, with the exception of the low p_T bins where the impact of the additional 15-20 GeV bin is visible. During the nominal analysis, the statistical uncertainty of the systematic fake factors is not considered when determining the total systematic uncertainty band; only the central values are considered. Therefore, while the updated and nominal underlying electron fake factors are not (for the most part) statistically different, they could still result in a statistically significant

---

[14]The *nominal underlying fake factor* refers to the fake factor calculated using the method described in Sections A.1 and A.2.

difference in the final electron fake factor systematic uncertainty band, specifically at high lepton p_T.
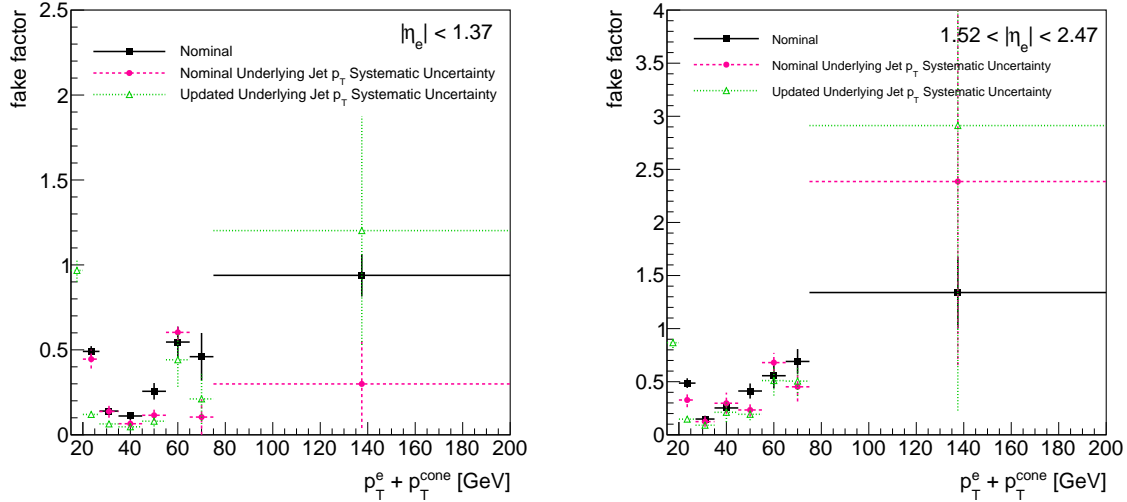
Figure A.16: Updated electron underlying jet p_T systematic uncertainty fake factors (green triangles) shown with the nominal fake factors (black squares) and the nominal underlying jet p_T systematic uncertainty fake factors (pink circles). *Left:* Fake factors for central electrons, $|\eta| < 1.37$. *Right:* Fake factors for forward electrons, $1.52 < |\eta| < 2.47$.

When propagated through the full analysis chain, the updated underlying fake factors do reduce the systematic uncertainty on the non-prompt background compared to the nominal estimation, but only slightly. As a result, the decision was made to proceed with the nominal method rather than begin the ATLAS approval procedure again[15]. Therefore, the results outlined in this section serve simply as a cross check for the nominal method of modeling the underlying jet p_T spectrum and as a reference for potential future studies.

---

[15]If the ATLAS approval process had been started again from the beginning, the analysis may not have been approved in time for the upcoming spring physics conferences.

Appendix B

Additional Post-Fit Plots

Figure B.1: The Δy_{jj} distribution for events passing all selections defining the signal region. Results of all lepton channels are shown together. Signal and background distributions are shown as predicted after the fit. The fitted signal strength and nuisance parameters have been propagated, with the exception of those for interference and electroweak corrections for which a constant uncertainty is assigned. The hatched band represents the statistical and systematic uncertainties of the background predictions added in quadrature. The background from $V\gamma$ and electron charge misID are combined in the "e/γ conversions" category. The "other prompt" category combines ZZ, VVV, and $t\bar{t}V$ background contributions. The last bin includes the overflow.

Figure B.2: The m_{ll} distribution for events passing all selections defining the signal region. Results of all lepton channels are shown together. Signal and background distributions are shown as predicted after the fit. The fitted signal strength and nuisance parameters have been propagated, with the exception of those for interference and electroweak corrections for which a constant uncertainty is assigned. The hatched band represents the statistical and systematic uncertainties of the background predictions added in quadrature. The background from $V\gamma$ and electron charge misID are combined in the "e/γ conversions" category. The "other prompt" category combines ZZ, VVV, and $t\bar{t}V$ background contributions. The last bin includes the overflow.

Figure B.3: The transverse mass m_{1T} distribution for events passing all selections defining the signal region. Results of all lepton channels are shown together. Signal and background distributions are shown as predicted after the fit. The fitted signal strength and nuisance parameters have been propagated, with the exception of those for interference and electroweak corrections for which a constant uncertainty is assigned. The hatched band represents the statistical and systematic uncertainties of the background predictions added in quadrature. The background from $V\gamma$ and electron charge misID are combined in the "e/γ conversions" category. The "other prompt" category combines ZZ, VVV, and $t\bar{t}V$ background contributions. The transverse mass is defined as $m_{1T} = \sqrt{\left(\sqrt{m_{ll}^2 + p_{T,ll}^2} + E_T^{miss}\right)^2 - \left(p_{T,ll} + E_T^{miss}\right)^2}$. The last bin includes the overflow.
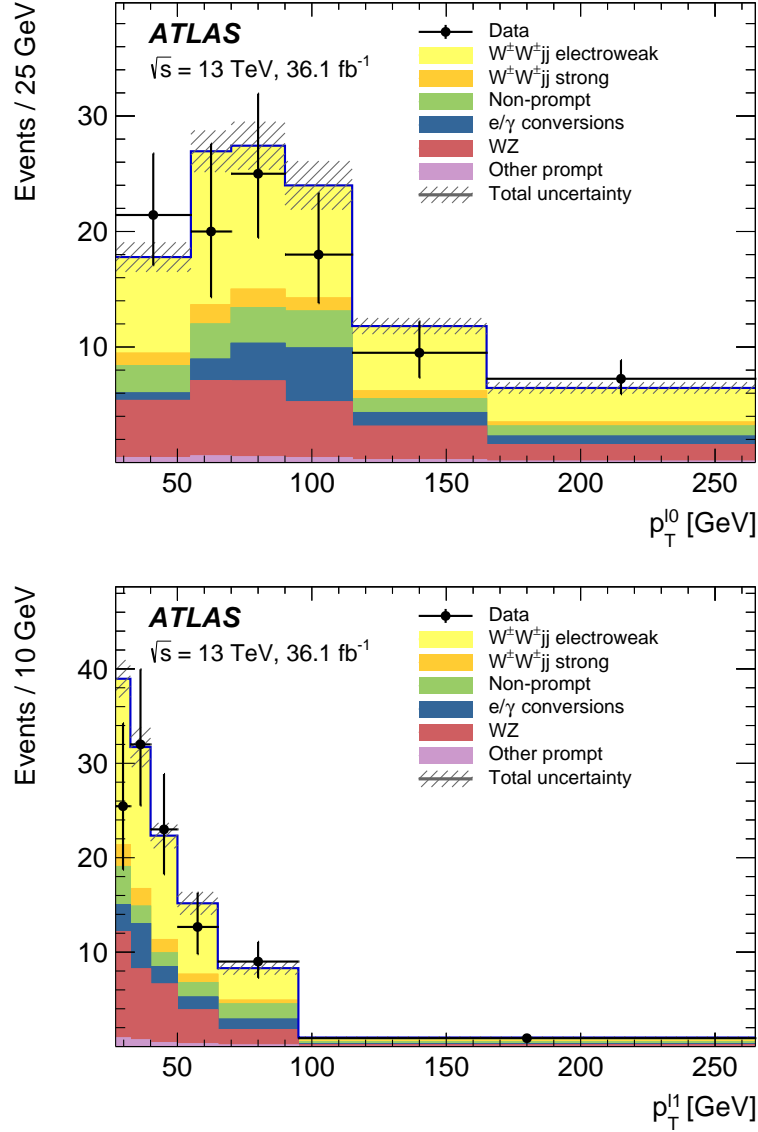
Figure B.4: The leading (top) and subleading (bottom) lepton p_T distributions for events passing all selections defining the signal region. Results of all lepton channels are shown together. Signal and background distributions are shown as predicted after the fit. The fitted signal strength and nuisance parameters have been propagated, with the exception of those for interference and electroweak corrections for which a constant uncertainty is assigned. The hatched band represents the statistical and systematic uncertainties of the background predictions added in quadrature. The background from $V\gamma$ and electron charge misID are combined in the "e/γ conversions" category. The "other prompt" category combines ZZ, VVV, and $t\bar{t}V$ background contributions. The last bin includes the overflow.

Figure B.5: The leading (top) and subleading (bottom) jet p_T distributions for events passing all selections defining the signal region. Results of all lepton channels are shown together. Signal and background distributions are shown as predicted after the fit. The fitted signal strength and nuisance parameters have been propagated, with the exception of those for interference and electroweak corrections for which a constant uncertainty is assigned. The hatched band represents the statistical and systematic uncertainties of the background predictions added in quadrature. The background from $V\gamma$ and electron charge misID are combined in the "e/γ conversions" category. The "other prompt" category combines ZZ, VVV, and $t\bar{t}V$ background contributions. The last bin includes the overflow.

Appendix C

Measurement of ATLAS Track Reconstruction Inefficiency in Dense Jet Environments Using dE/dx

To become an ATLAS author, each member is required to complete a task that benefits the entire ATLAS community. These tasks can involve code maintenance, detector maintenance, etc. As my authorship qualification task, I assisted in examining the ATLAS track reconstruction algorithms in dense jet environments. The following is a revised edition of the note I wrote regarding my qualification task [164]. The results of my ATLAS author qualification task were also included in a physics journal publication [165].

C.1 Introduction

The characterization of the ATLAS track reconstruction algorithms' performance in dense environments (like the core of high p_T jets) is important for a number of ongoing performance studies and physics analyses, including: the calibration of the jet energy scale using charged particle quantities [166], the calibration of the jet mass in large radius jets [167], and topologies with boosted τ leptons [168]. In many cases, the leading sources of systematic uncertainty in analyses such as those listed above are due to track reconstruction uncertainties.

Tracks in the core of high p_T jets are more likely to be lost than tracks which are more isolated. In these dense environments, it is not uncommon for multiple particles to deposit energy in the same/nearby pixels in the pixel detector, which results in a single merged cluster[1] during track reconstruction. Methods to identify and resolve such merged measurements are implemented in the ATLAS software [169, 170]. However, a residual inefficiency in reconstructing tracks remains due to the high density and collimation of charged particles in high p_T jets. In the study summarized in this appendix, the ionization energy loss

---

[1]A cluster is a group of pixel sensors associated together by a clustering algorithm [169].

$(\mathrm{d}E/\mathrm{d}x)$ of charged particles is used to: (1) deduce the probability of losing a track in the core of a jet, (2) measure the residual inefficiency in track reconstruction, and (3) estimate the systematic uncertainty on the track reconstruction efficiency as measured in simulation due to lost tracks.

The ATLAS ID is designed to reconstruct the trajectories of charged particles, measure their momenta, and perform vertex reconstruction in the pseudorapidity range of $|\eta| < 2.5$. In addition, a measure of the collected charge is available from the pixel detector via the time-over-threshold (ToT) technique [171]. The ToT is a measure of the time the pulse spends above a given threshold and is approximately proportional to the charge. The $\mathrm{d}E/\mathrm{d}x$ of a charged particle traversing the pixel sensor is measured from the charge collected in the clusters associated with the reconstructed track. With single particles and thin layers, the $\mathrm{d}E/\mathrm{d}x$ measurements are expected to follow a Landau distribution [26]. A single particle of LHC energy is expected to be a minimum ionizing particle (MIP). Therefore, two particles contributing to the same cluster are expected to deposit twice the energy of a single MIP.

Due to the magnetic field, the spatial separation of charged particles increases in the transverse direction as they traverse the detector. Thus, the probability of merging clusters is greater in the inner pixel layers. The IBL only has 4 bits available to encode the ToT information, while the second barrel layer, the B-layer, has 8 bits available to encode ToT information. As a result, the B-layer provides an enhanced ToT resolution. Therefore, the cluster $\mathrm{d}E/\mathrm{d}x$ values corresponding to the B-layer of the pixel detector are used to examine the track reconstruction efficiency in dense jet environments.

In this appendix: Section C.2 describes the data and simulation samples used; Section C.3 describes the method used to measure the inefficiency; and Section C.4 presents the measurement of the fraction of lost tracks and the track reconstruction inefficiency in data and simulation.

C.2   Data and Simulation Samples

This study uses a sample of pp collisions at $\sqrt{s} = 13$ TeV recorded during 2015 corresponding to an integrated luminosity of 2.8 fb^{-1}. Events are selected from data using single jet triggers with a minimum jet trigger p_T threshold of 100 GeV. Each trigger is prescaled by a reduction factor depending upon the instantaneous luminosity and the jet energy on which it triggered. This prescaling suppresses the number of low p_T jets while keeping all high p_T jet events with at least one jet with $p_T > 1$ TeV, thereby resulting in a more uniform jet p_T spectrum. Appropriate data quality requirements are applied to all data sets. Events are also required to have at least one reconstructed PV with at least three tracks.

Data is compared to an inclusive dijet MC sample generated with PYTHIA 8.186. Generator parameters are set according to the A14 tune for the parton shower and hadronization, and are taken from the NNPDF2.3LO PDF set. MC samples generated with HERWIG++ 2.7.1 and SHERPA 2.1 are also studied. For HERWIG++, parameters corresponding to the UEEE5 tune are used with the CTEQ6L1 PDF set. For SHERPA, parameters correspond-

ing to the CT10 PDF set are used. The ATLAS detector response is simulated using the GEANT4 framework. Events from MC simulation are reweighted to match the number of events which were triggered on in data.

C.3 Track Reconstruction Inefficiency Measurement

A single charged particle at the LHC has the dE/dx distribution of an MIP. When multiple particles traveling closely through the detector contribute to the same cluster, the measured cluster dE/dx is compatible with multiple MIPs. The resulting dE/dx distribution is distinctive compared to the dE/dx distribution of a single MIP. By fitting the cluster dE/dx for reconstructed tracks near the core of the jet, tracks reconstructed from single particles can be statistically separated from tracks reconstructed from multiple particle contributions.

Near the jet core the charged particle density is high, and particles can be heavily collimated. The tracks of these particles are, therefore, more likely to have been reconstructed from merged clusters. The fraction of lost tracks can be inferred from the number of reconstructed tracks associated with a cluster dE/dx compatible with multiple MIPs. By measuring the fraction of lost tracks in data and simulation, the residual track reconstruction inefficiency can be estimated.

C.3.1 Jet and Track Selection

Jets are reconstructed from topological clusters using the anti-k_t algorithm with a distance parameter $R = 0.4$. Jets are selected requiring $p_T^{jet} > 200$ GeV and $|\eta^{\mathrm{jet}}| < 2.5$. It was previously demonstrated that the properties of jets in simulation agree well with data [136].

Reconstructed tracks are selected using the following requirements:

- exactly one pixel hit per layer

- $p_T^{\mathrm{trk}} > 10$ GeV

- $|\eta^{\mathrm{trk}}| < 1.2$

- $|d_0^{\mathrm{BL}}| < 1.5$ mm

- $|z_0^{\mathrm{BL}} \sin\theta| < 1.5$ mm

- number of SCT hits ≥ 6

- number of pixel holes[2] ≤ 1

---

[2]Holes are defined as intersections of the reconstructed track trajectory with a sensitive detector element that do not result in a hit. These are estimated by closely following the track trajectory and comparing the hits-on-track with the intersected modules. Inactive modules, or regions such as edge areas on the silicon sensors, are excluded from the hole definition.

where d_0^{BL} is the transverse impact parameter calculated with respect to the measured beam-line position, and z_0^{BL} is the difference between the longitudinal position of the track along the beamline at the point where d_0^{BL} is measured and the longitudinal position of the PV.

C.3.2 Fit Method

A cluster $\mathrm{d}E/\mathrm{d}x$ distribution of tracks inside the jet core is fit using two $\mathrm{d}E/\mathrm{d}x$ template distributions:

1. A **single-track template** $\mathrm{d}E/\mathrm{d}x$ distribution constructed using tracks reconstructed from a cluster where only a single particle contributed.

2. A **multiple-track template** $\mathrm{d}E/\mathrm{d}x$ distribution constructed using tracks reconstructed from a merged cluster to which multiple particles contributed.

These templates are created in a purely data-driven way by applying the selections illustrated in Figure C.1. A *Not-Multiply-Used* cluster is defined as a cluster associated with exactly one track candidate. A *Multiply-Used* cluster is defined as a cluster associated with two or more track candidates.
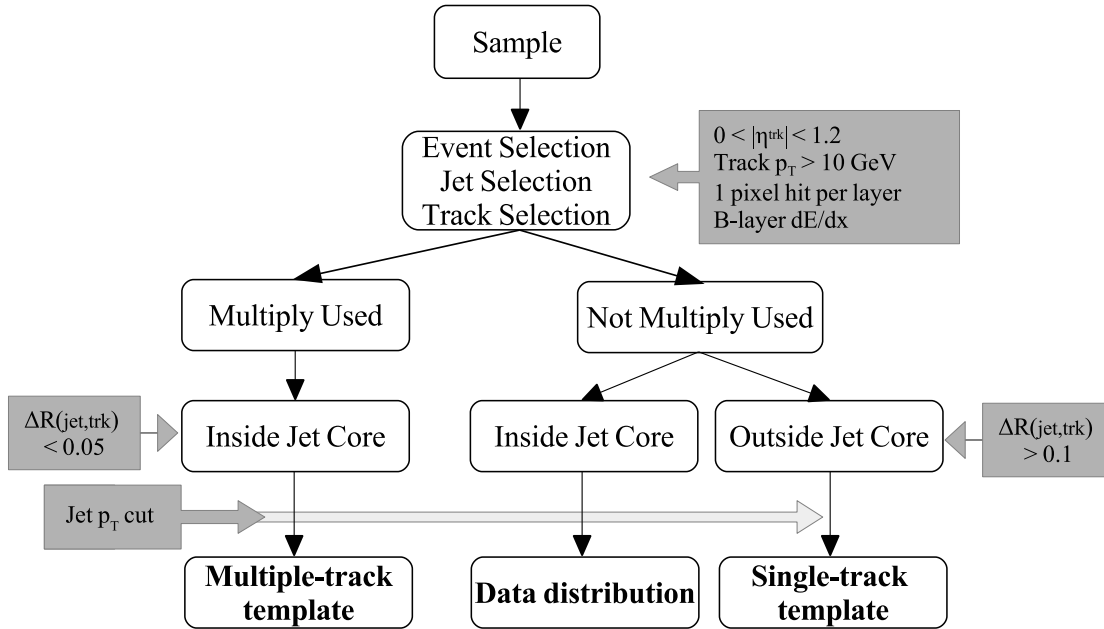
Figure C.1: Definition of the templates and $\mathrm{d}E/\mathrm{d}x$ distributions for data and simulation.

The *data distribution* is created from tracks inside the jet core (ΔR(jet,trk)< 0.05) that are reconstructed from a Not-Multiply-Used cluster. The *single-track template* is taken from tracks reconstructed from Not-Multiply-Used clusters that are outside the jet core

(ΔR(jet,trk)> 0.1)[3]. The *multiple-track template* is taken from tracks reconstructed from Multiply-Used clusters that are inside the jet core.

Examples of the resulting distributions are shown in Figure C.2. The single-track template contains a single peak at the dE/dx value expected for a MIP traversing the B-layer of the pixel detector. The multiple-track template exhibits a peak in the dE/dx range corresponding to two particles. A third, smaller peak also occurs in the multiple-track template at $dE/dx > 3.2$ MeVg^{-1}cm^2 resulting from clusters created by three particles.

The fraction of tracks containing a B-layer hit consistent with multiple particles traversing the area that is not used by other reconstructed tracks is determined by fitting the data distribution (see Figure C.2(right)) with both templates. Collimated particle pair simulation studies conducted using pseudo-tracking[4] show that the multiple-track template is correlated with the dE/dx distribution of reconstructed tracks overlapping with lost tracks. The studies also reveal that selecting tracks reconstructed from Multiply-Used clusters matching this multiple-track template is consistent with selecting lost tracks. Hence, the fit fraction of the multiple-track template is interpreted as the fraction of lost tracks, F^{lost}.
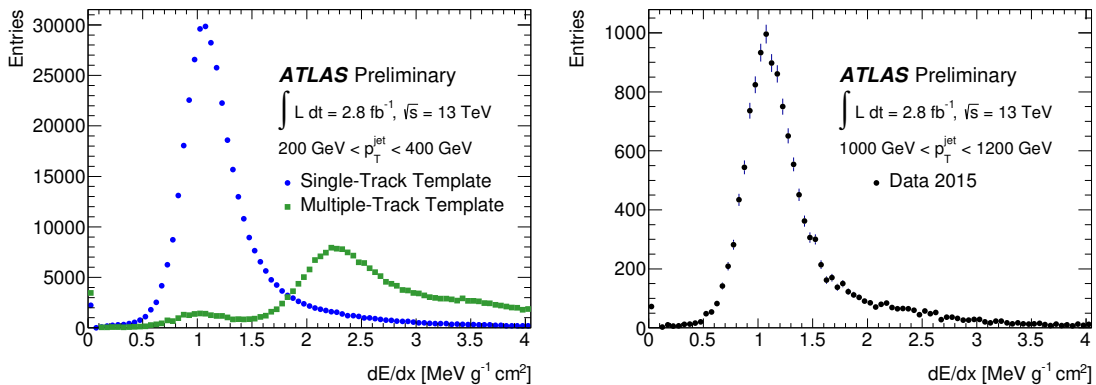
Figure C.2: Single-track and multiple-track templates for data (left) and the dE/dx distribution for Not-Multiply-Used clusters near the jet core (ΔR(jet,trk)< 0.05) for data with a jet p_T in the range 1000 GeV $< p_T^{\text{jet}} < 1200$ GeV (right).

To minimize the effect of clusters created by three particles, the fit is performed over the range $0.67 - 3.07(0.8 - 3.2)$ MeVg^{-1}cm^2 for data (simulation). The ranges are chosen to have the same fraction of clusters inside the fit range with respect to all clusters in the distribution.

To study the dependence of lost tracks on jet p_T, the fit is performed in seven different bins of jet p_T ranging from 200 GeV to 1600 GeV. For simulation, separate templates are constructed for each jet p_T bin. For data, the single-track and multiple-track templates are derived from the lowest jet p_T bin, shown in Figure C.2(left), due to low statistics at higher

---

[3]It is expected that outside the jet core the contribution of lost tracks is negligible.

[4]Pseudo-tracking is a tool that reconstructs tracks with ideal performance by directly fitting the hits from the truth particle.

jet p_T. Within the statistical uncertainty of the high p_T bins, the templates derived from the lowest jet p_T bin have the same shape within the fit range. An additional check using a high-statistics simulation is discussed in Section C.3.3.

C.3.3   Systematic Uncertainty

The dominant source of uncertainty for the simulated results is generator dependency. A systematic uncertainty is estimated by comparing the fit results of PYTHIA 8, SHERPA, and HERWIG++ generated samples, as shown in Figure C.3. For each jet p_T bin, the largest difference between the fit fractions of the three generators is taken to be the systematic uncertainty for that jet p_T bin. The systematic uncertainty is then symmetrized and applied to all simulation results. The relative systematic uncertainties due to generator dependency on the fraction of lost tracks, F^{lost}, are listed in Table C.1.
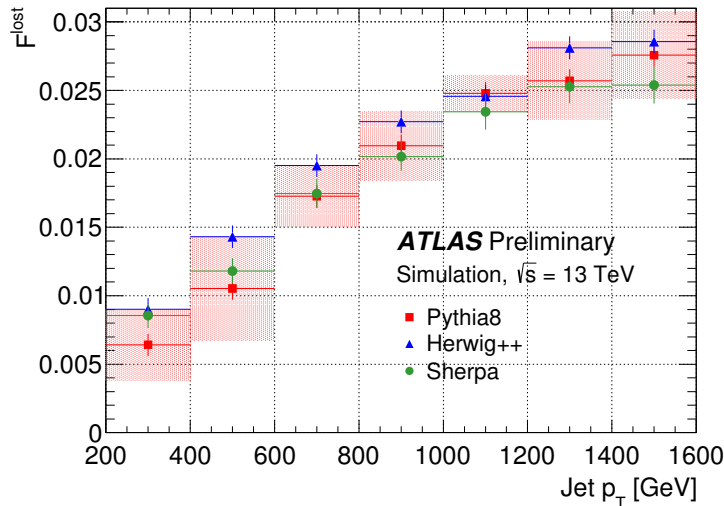
Figure C.3: The fraction of lost tracks, F^{lost} , as a function of jet p_T for simulation with PYTHIA 8 (red squares), HERWIG++ (blue triangles), and SHERPA (green circles). Error bars indicate statistical uncertainty, while the red error band indicates the jet p_T dependent systematic uncertainty applied to the PYTHIA 8 simulation as a result of F^{lost} generator dependency.

The measured fraction of lost tracks, F^{lost}, varies as a function of the dE/dx fit range. The effect of the fit range is estimated by increasing the range beyond the baseline selection. The lower edge of the fit range is chosen to include all statistically significant bins. Hence, the fit results are stable under variation of the fit range lower bound. The effect of the upper fit range limit is studied by increasing the upper limit six times in 0.2 MeVg^{-1}cm^2 increments. For both data and simulation, F^{lost} increases on order 5% over its previous value with each increment. The impact is greater in data, and a symmetric uncertainty equal to

| Jet p_T bin [GeV] | Data | | Simulation |
	Fit Range	Low p_T Templates	Generator Dependency
200–400	0.17	0.00	0.41
400–600	0.18	0.14	0.36
600–800	0.16	0.13	0.13
800–1000	0.23	0.10	0.12
1000–1200	0.12	0.11	0.05
1200–1400	0.13	0.17	0.11
1400–1600	0.25	0.11	0.12

Table C.1: Relative values of leading systematic uncertainties on the fraction of lost tracks for data and simulation (PYTHIA 8) in bins of jet p_T.

the maximum change in F^{lost} is applied as a systematic uncertainty to each jet p_T bin in data. The relative values for this systematic uncertainty are listed in Table C.1.

The second leading systematic uncertainty for data is the result of fitting all data jet p_T bins with the templates from the lowest jet p_T bin (see Section C.3.2). An additional check is performed with a high-statistics simulation to assess the impact of this decision. This check reveals a small bias in F^{lost} due to the fraction of tracks in the multiple-track template reconstructed from clusters with more than three contributing particles relative to the number of tracks reconstructed from clusters with two contributing particles. This effect varies with jet p_T. To account for this bias, a p_T-dependent multiplicative correction is determined and applied to the data. The correction term is determined by comparing the F^{lost} values for simulation fit using templates derived from each jet p_T bin with the F^{lost} values of simulation fit using templates derived in the lowest jet p_T bin. The correction term is applied to data F^{lost} values after all fitting procedure is complete. The difference between the two simulation F^{lost} values compared to determine the correction term is also included as a systematic uncertainty. The corresponding relative values of are listed in Table C.1.

C.4   Results

Figures C.4 and C.5 show the fit results for simulation (Figure C.4) and data (Figure C.5) in two bins of jet p_T: 200 GeV $< p_T^{jet} <$ 400 GeV (left) and 1000 GeV $< p_T^{jet} <$ 1200 GeV (right). For both data and simulation, the single-track and multiple-track dE/dx templates provide a good description of the dE/dx distribution.

The fraction of lost tracks is shown in Figure C.6 as a function of jet p_T for data and simulation. As the jet p_T increases from 200 GeV to 1600 GeV, F^{lost} ranges from 1% to 5% for both data and simulation. The relative discrepancy between track reconstruction inefficiency in data and simulation is determined by taking the ratio of F^{lost} as determined
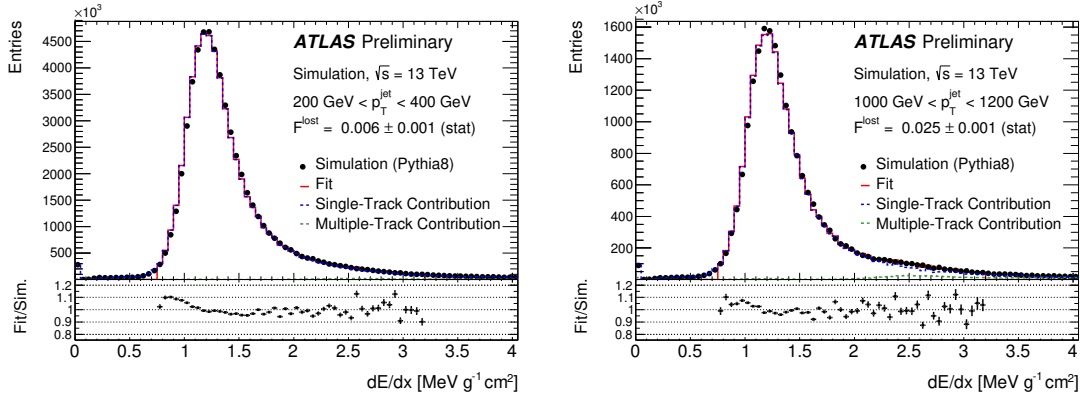
Figure C.4: Simulation (PYTHIA 8) dE/dx distributions (black circles) with fit results (red solid line) in two bins of jet p_T. The Single-Track template scaled by $1\text{-}F^{\text{lost}}$ is shown as the Single-Track Contribution (blue dashed line), and the Multiple-Track template scaled by F^{lost} is shown as the Multiple-Track Contribution (green dashed line). The bottom panel in each plot shows the ratio of fit/simulation within the fit range (0.8–3.2 MeVg^{-1}cm^2).
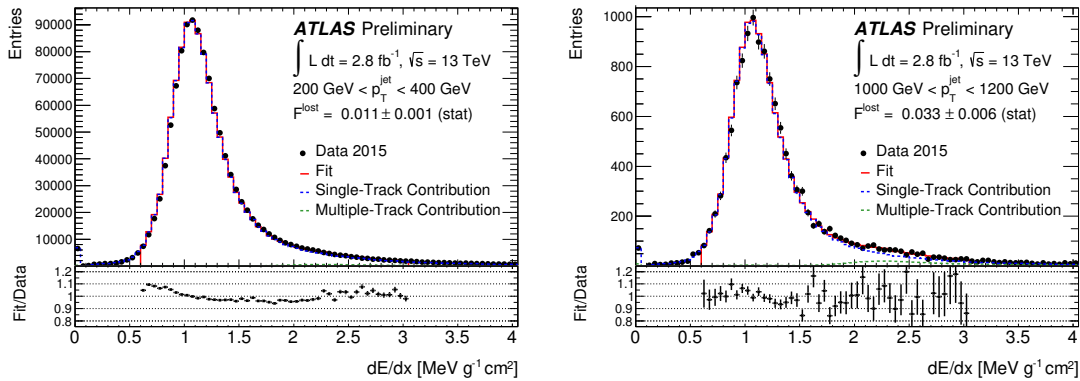
Figure C.5: Data dE/dx distributions (black circles) with fit results (red solid line) in two bins of jet p_T. The Single-Track template scaled by $1\text{-}F^{\text{lost}}$ is shown as the Single-Track Contribution (blue dashed line), and the Multiple-Track template scaled by F^{lost} is shown as the Multiple-Track Contribution (green dashed line). The bottom panel in each plot shows the ratio of fit/data within the fit range (0.67–3.07 MeVg^{-1}cm^2).

in data and simulation. Figure C.7 shows this ratio taking into account both statistical and systematic uncertainties. The relative discrepancy is found to be independent of jet p_T. When fit to a constant value, Figure C.7 reveals the discrepancy is approximately 25% $\pm7\%$(stat) $\pm(15-75)\%$(syst), where the systematic uncertainty varies depending upon jet p_T bin.
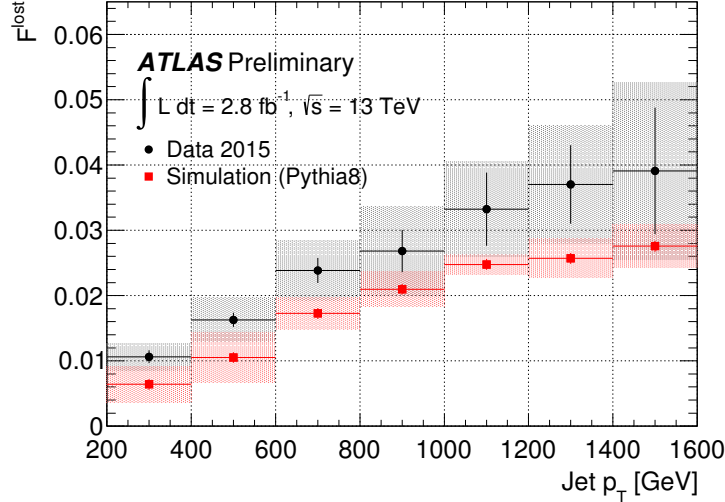
Figure C.6: The measured fraction of lost tracks, F^{lost}, in the jet core ($\Delta R(\text{jet,trk}) < 0.05$) as a function of jet p_T for data (black circles) and simulation (red squares). Black error bars indicate statistical uncertainty, while the grey and red error bands indicate the total uncertainty for data and simulation, respectively.
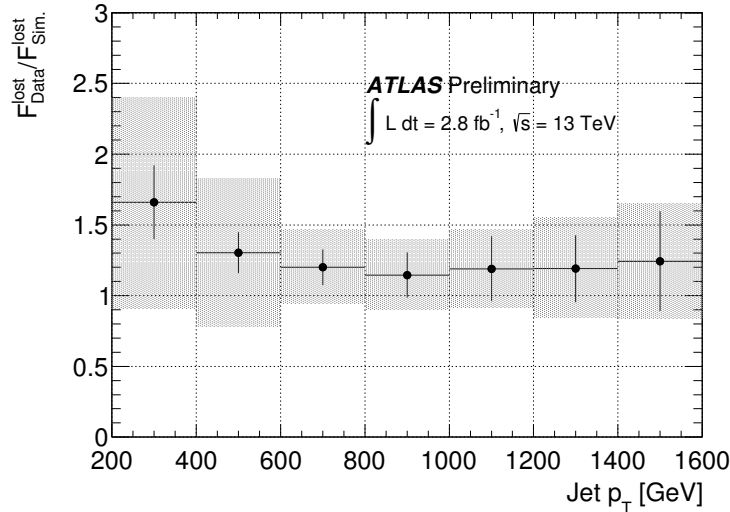
Figure C.7: The ratio of the fraction of lost tracks, F^{lost}, in data with respect to simulation (PYTHIA 8) as a function of jet p_T. Black error bars indicate the combined statistical uncertainty of data and simulation, while the grey error band indicates the total uncertainty, taking into account the statistical and systematic uncertainties of both data and simulation.

Bibliography

[1] S.L. Glashow, *Partial symmetries of weak interactions*, Nucl. Phys. **22** (1961) 579.

[2] A. Salam and J.C. Ward, *Electromagnetic and weak interactions*, Phys. Lett. **11** (1964) 168.

[3] S. Weinberg, *A model of leptons*, Phys. Rev. Lett. **19** (1967) 1264.

[4] G. Aad et al. [ATLAS Collaboration], *Observation of a new particle in the search for the Standard Model Higgs boson with the ATLAS detector at the LHC*, Phys. Lett. B **716** (2012) 1, arXiv: `1207.7214` `[hep-ex]`.

[5] S. Chatrchyan et al. [CMS Collaboration], *Observation of a new boson at a mass of 125 GeV with the CMS experiment at the LHC*, Phys. Lett. B **716** (2012) 30, arXiv: `1207.7235` `[hep-ex]`.

[6] B. W. Lee, C. Quigg, and H. B. Thacker, Phys. Rev. D **16** (1977) 1519.

[7] B. W. Lee, C. Quigg, and H. B. Thacker, Phys. Rev. Lett. **38** (1977) 883.

[8] M. J. G. Veltman, Acta Phys. Polon. **B8** (1977) 475.

[9] LEP Collaborations, *A Combination of preliminary electroweak measurements and constraints on the standard model*, (2004), arXiv: `0412015` `[hep-ex]`.

[10] F. Abe et al. [CDF Collaboration], *Limits on WWZ and $WW\gamma$ couplings from WW and WZ production in $p\bar{p}$ collisions at $\sqrt{s} = 1.8$ TeV*, Phys. Rev. Lett. **75** (1995) 1017, arXiv: `9503009` `[hep-ex]`.

[11] S. Abachi et al. [D0 Collaboration], *Measurement of the $WW\gamma$ gauge boson couplings in $p\bar{p}$ collisions at $\sqrt{s} = 1.8$ TeV*, Phys. Rev. Lett. **75** (1995) 1034, arXiv: `9505007` `[hep-ex]`.

[12] M. Aaboud et al. [ATLAS Collaboration], *Observation of electroweak production of a same-sign W boson pair in association with two jets in pp collisions at $\sqrt{s} = 13$ TeV with the ATLAS detector*, Submitted to: Phys. Rev. Lett. (2019), For auxillary material see https://atlas.web.cern.ch/Atlas/GROUPS/PHYSICS/PAPERS/STDM-2017-06, arXiv: `1906.03203` `[hep-ex]`.

[13] G. Aad et al. [ATLAS Collaboration], *Evidence for Electroweak Production of $W^{\pm}W^{\pm}jj$ in pp Collisions at $\sqrt{s} = 8$ TeV with the ATLAS Detector*, Phys. Rev. Lett. **113** (2014) 141803, arXiv: `1405.6241` `[hep-ex]`.

[14] V. Khachatryan et al. [CMS Collaboration], *Study of vector boson scattering and search for new physics in events with two same-sign leptons and two jets*, Phys. Rev. Lett. **114** (2015) 051801, arXiv: `1410.6315` `[hep-ex]`.

[15] A. M. Sirunyan et al. [CMS Collaboration], *Observation of electroweak production of same-sign W boson pairs in the two jet and two same-sign lepton final state in proton-proton collisions at $\sqrt{s} = 13$ TeV*, Phys. Rev. Lett. **120** (2017) 081801.

[16] UA 1 Collaboration, *Experimental Observation of Isolated Large Transverse Energy Eletrons with Associated Missing Energy at $\sqrt{s} = 540$ GeV*, Phys. Lett. B **122** (1983) 103.

[17] UA 2 Collaboration, *Observation of Single Isolated Electrons of High Transverse Momentum in Events with Missing Transverse Energy at the CERN $\overline{p}p$ Collider*, Phys. Lett. B **122** (1983) 476.

[18] F. Abe et al. [CDF Collaboration], *Observation of Top Quark Production in $\overline{p}p$ Collisions with the Collider Detector at Fermilab*, Phys. Rev. Lett. **74** (14 1995) 2626, arXiv: `9503002` `[hep-ex]`.

[19] S. Abachi et al. [D0 Collaboration], *Search for High Mass Top Quark Production in $p\overline{p}$ Collisions at $\sqrt{s} = 1.8$ TeV*, Phys. Rev. Lett. **74** (13 1995) 2422, arXiv: `9411001` `[hep-ex]`.

[20] G. Goldhaber et al., *Observation in e^+e^- Annihilation of a Narrow State at 1865 Mev/c^2 Decaying to $K\pi$ and $K\pi\pi\pi$*, Phys. Rev. Lett. **37** (1976) 255.

[21] I. Peruzi et al., *Observation of a Narrow Charged State at 1876 MeV/c^2 Decaying to an Exotic Combination of $K\pi\pi$*, Phys. Rev. Lett. **37** (1976) 569.

[22] G. J. Feldman et al., *Observation of the Decay $D^{*+} \to D^0\pi^+$*, Phys. Rev. Lett. **38** (1977) 1313.

[23] S. W. Herb et al., *Observation of a Dimuon Resonance at 9.5 GeV in 400-GeV Proton-Nucleus Collisions*, Phys. Rev. Lett. **39** (5 1977) 252.

[24] Michael E. Peskin and Daniel V. Schroeder, *An Introduction to Quantum Field Theory*, Westview Press, 1995.

[25] Matthew D. Schwartz, *Quantum Field Theory and the Standard Model*, Cambridge University Press, 2014.

[26] M. Tanabashi et al. [Particle Data Group], *Review of Particle Physics*, Phys. Rev. D **98** (2018) 030001.

[27] F. Englert and R. Brout, *Broken Symmetry and the Mass of Gauge Vector Mesons*, Phys. Rev. Lett. **13** (9 1964) 321.

[28] Peter W. Higgs, *Broken Symmetries and the Masses of Gauge Bosons*, Phys. Rev. Lett. **13** (16 1964) 508.

[29] P. A. R. Ade et al., *Planck 2015 results. XIII. Cosmological parameters*, Astron. Astrophys. **594** (2016) A13, arXiv: `1502.01589 [astro-ph.CO]`.

[30] Gianfranco Bertone, Dan Hooper, and Joseph Silk, *Particle dark matter: evidence, candidates and constraints*, Physics Reports **405** (2005) 279.

[31] Y. Fukuda et al. [Super-Kamiokande Collaboration], *Evidence for Oscillation of Atmospheric Neutrinos*, Phys. Rev. Lett. **81** (8 1998) 1562.

[32] A. D. Sakharov, *Violation of CP invariance, C asymmetry, and baryon asymmetry of the universe*, JETP Lett. **5** (1967) 24.

[33] Nima Arkaniâ Hamed, Savas Dimopoulos, and Gia Dvali, *The hierarchy problem and new dimensions at a millimeter*, Phys. Lett. B **429** (1998) 263.

[34] F. Mandl and G. Shaw, *Quantum Field Theory*, John Wiley and Sons, 2007.

[35] Gavin P. Salam, "Elements of QCD for hadron colliders", *High-energy physics. Proceedings, 17th European School, ESHEP 2009, Bautzen, Germany, June 14-27, 2009*, 2010, arXiv: `1011.5131 [hep-ph]`.

[36] J. D. Bjorken and E. A. Paschos, *Inelastic Electron-Proton and γ-Proton Scattering and the Structure of the Nucleon*, Phys. Rev. **185** (5 1969) 1975.

[37] R. P. Feynman, *The behavior of hadron collisions at extreme energies*, Conf. Proc. **C690905** (1969) 237.

[38] Sidney D. Drell and Tung-Mow Yan, *Partons and their applications at high energies*, Annals of Physics **66** (1971) 578.

[39] V. N. Gribov and L. N. Lipatov, *Deep inelastic e p scattering in perturbation theory*, Sov. J. Nucl. Phys. **15** (1972) 438.

[40] Yuri L. Dokshitzer, *Calculation of the Structure Functions for Deep Inelastic Scattering and e+ e- Annihilation by Perturbation Theory in Quantum Chromodynamics.*, Sov. Phys. JETP **46** (1977) 641.

[41] Guido Altarelli and G. Parisi, *Asymptotic Freedom in Parton Language*, Nucl. Phys. B **126** (1977) 298.

[42] Hung-Liang Lai et al., *New parton distributions for collider physics*, Phys. Rev. D **82** (2010) 074024, arXiv: `1007.2241 [hep-ph]`.

[43] L. A. Harland-Lang et al., *Parton distributions in the LHC era: MMHT 2014 PDFs*, Eur. Phys. J. C **75** (2015) 204, arXiv: `1412.3989 [hep-ph]`.

[44] Richard D. Ball et al., *Parton distributions for the LHC Run II*, JHEP **04** (2015) 040, arXiv: `1410.8849 [hep-ph]`.

[45] John M. Campbell, J. W. Huston, and W. J. Stirling, *Hard Interactions of Quarks and Gluons: A Primer for LHC Physics*, Rept. Prog. Phys. **70** (2007) 89, arXiv: `0611148 [hep-ph]`.

[46] ATLAS Collaboration, *Standard Model Summary Plots Summer 2019*, ATL-PHYS-PUB-2019-024, 2019, URL: http://cds.cern.ch/record/2682186.

[47] Christian Gumpert, "Measurement of Electroweak Gauge Boson Scattering in the Channel $pp \rightarrow W^{\pm}W^{\pm}jj$ with the ATLAS Detector at the Large Hadron Collider", 2014, URL: https://cds.cern.ch/record/2003240.

[48] Lyndon Evans and Philip Bryant, *LHC Machine*, JINST **3** (2008) S08001.

[49] R W Assmann, M Lamont, and S Myers, *A Brief History of the LEP Collider*, Nucl. Phys. B, Proc. Suppl. **109** (2002) 17, URL: https://cds.cern.ch/record/549223.

[50] K. Aamodt et al. [ALICE Collaboration], *The ALICE Experiment at the CERN LHC*, JINST **3** (2008) S08002.

[51] G. Aad et al. [ATLAS Collaboration], *The ATLAS Experiment at the CERN Large Hadron Collider*, JINST **3** (2008) S08003.

[52] S. Chatrchyan et al. [CMS Collaboration], *The CMS experiment at the CERN LHC*, JINST **3** (2008) S08004.

[53] A. Augusto Alves Jr. et al. [LHCb Collaboration], *The LHCb Detector at the LHC*, JINST **3** (2008) S08005.

[54] Philippe Mouche, *Overall view of the LHC*, (2014), photo, URL: https://cds.cern.ch/record/1708847.

[55] Apollinari G. et al., *High-Luminosity Large Hadron Collider (HL-LHC): Technical Design Report V. 0.1*, CERN Yellow Reports: Monographs, CERN, 2017, URL: https://cds.cern.ch/record/2284929.

[56] Communications Education and Outreach Group [CERN], *LHC the guide*, 2017.

[57] Esma Mobs, *The CERN accelerator complex*, (2018), photo, URL: https://cds.cern.ch/record/2636343.

[58] *Radiofrequency cavities*, (2012), URL: https://cds.cern.ch/record/1997424.

[59] ATLAS Collaboration, *Luminosity determination in pp collisions at $\sqrt{s} = 13$ TeV using the ATLAS detector at the LHC*, ATLAS-CONF-2019-021, 2019, URL: http://cds.cern.ch/record/2677054.

[60] "Luminosity Public Results Run2", 2017, URL: https://twiki.cern.ch/twiki/bin/view/AtlasPublic/LuminosityPublicResultsRun2.

[61] David J Griffiths, *Introduction to electrodynamics; 4th ed.* Re-published by Cambridge University Press in 2017, Pearson, 2013, URL: https://cds.cern.ch/record/1492149.

[62] Joao Pequenao, "Computer generated image of the whole ATLAS detector", 2008, URL: https://cds.cern.ch/record/1095924.

[63] Matthias Schott and Monica Dunford, *Review of single vector boson production in pp collisions at $\sqrt{s} = 7$ TeV*, Eur. Phys. J. C **74** (2014) 60, arXiv: `1405.1160`, URL: `http://cds.cern.ch/record/1699952`.

[64] ATLAS Collaboration, *Track Reconstruction Performance of the ATLAS Inner Detector at $\sqrt{s} = 13$ TeV*, ATL-PHYS-PUB-2015-018, 2015, URL: `http://cds.cern.ch/record/2037683`.

[65] ATLAS Collaboration, *ATLAS Insertable B-Layer Technical Design Report*, CERN-LHCC-2010-013. ATLAS-TDR-19, 2010, URL: `https://cds.cern.ch/record/1291633`.

[66] G. Darbo, *Experience on 3D Silicon Sensors for ATLAS IBL*, JINST **10** (2015) C05001, arXiv: `1411.6937 [physics.ins-det]`.

[67] Joao Pequenao, "Computer Generated image of the ATLAS calorimeter", 2008, URL: `https://cds.cern.ch/record/1095927`.

[68] M. Aaboud et al. [ATLAS Collaboration], *Performance of the ATLAS Trigger System in 2015*, Eur. Phys. J. C **77** (2017) 317, arXiv: `1611.09661 [hep-ex]`.

[69] "Trigger Operation Public Results", 2016, URL: `https://twiki.cern.ch/twiki/bin/view/AtlasPublic/TriggerOperationPublicResults`.

[70] G. Aad et al. [ATLAS Collaboration], *Measurement of $W^{\pm}$ and Z-boson production cross sections in pp collisions at $\sqrt{s} = 13$ TeV with the ATLAS detector*, Phys. Lett. B **759** (2016) 601, arXiv: `1603.09222 [hep-ex]`.

[71] T. Gleisberg et al., *Event generation with SHERPA 1.1*, JHEP **0902** (2009) 007, arXiv: `0811.4622 [hep-ph]`.

[72] Andy Buckley et al., *General-purpose event generators for LHC physics*, Phys. Rept. **504** (2011) 145, arXiv: `1101.2599 [hep-ph]`.

[73] D. R. Yennie, Steven C. Frautschi, and H. Suura, *The infrared divergence phenomena and high-energy processes*, Annals Phys. **13** (1961) 379.

[74] S. Agostinelli et al., GEANT4—*a simulation toolkit*, Nucl. Instrum. Meth. A **506** (2003) 250.

[75] J. Allison et al., *Geant4 developments and applications*, IEEE Trans. on Nucl. Sci. **53** (2006) 270.

[76] J. Allison et al., *Recent developments in Geant4*, Nucl. Instrum. Meth. A **835** (2016) 186.

[77] Michael Leyton, "Minimum Bias and Underlying Event Measurements with ATLAS", *Proceedings, MPI@LHC 2011*, ATL-PHYS-PROC-2012-033, 2012 11, arXiv: `1202.2090 [hep-ex]`.

[78] Z. Marshall, *Simulation of Pile-up in the ATLAS Experiment*, (2013), URL: `https://cds.cern.ch/record/1605834`.

[79] G Aielli, "Cavern background measurement with the ATLAS RPC system", tech. rep. ATL-MUON-PROC-2012-005, CERN, 2012, URL: https://cds.cern.ch/record/1457509.

[80] G. Corcella et al., *HERWIG 6: An Event generator for hadron emission reactions with interfering gluons (including supersymmetric processes)*, JHEP **01** (2001) 010, arXiv: hep-ph/0011363.

[81] M. Bahr et al., *Herwig++ Physics and Manual*, Eur. Phys. J. C **58** (2008) 639, arXiv: 0803.0883 [hep-ph].

[82] Johannes Bellm et al., *Herwig 7.0/Herwig++ 3.0 release note*, Eur. Phys. J. C **76** (2016) 196, arXiv: 1512.01178 [hep-ph].

[83] Torbjörn Sjöstrand et al., *An Introduction to PYTHIA 8.2*, Comput. Phys. Commun. **191** (2015) 159.

[84] Johan Alwall et al., *MadGraph 5 : Going Beyond*, JHEP **06** (2011) 128, arXiv: 1106.0522 [hep-ph].

[85] Johan Alwall et al., *The automated computation of tree-level and next-to-leading order differential cross sections, and their matching to parton shower simulations*, JHEP **07** (2014) 158, arXiv: 1405.0301 [hep-ph].

[86] Stefano Frixione, Paolo Nason, and Carlo Oleari, *Matching NLO QCD computations with Parton Shower simulations: the POWHEG method*, JHEP **11** (2007) 070, arXiv: 0709.2092 [hep-ph].

[87] Wolfgang Kilian, Thorsten Ohl, and Jurgen Reuter, *WHIZARD: Simulating Multi-Particle Processes at LHC and ILC*, Eur. Phys. J. C **71** (2011) 1742, arXiv: 0708.4233 [hep-ph].

[88] J. Baglio et al., *VBFNLO: A Parton Level Monte Carlo for Processes with Electroweak Bosons – Manual for Version 2.7.0*, (2011), arXiv: 1107.4038 [hep-ph].

[89] K. Arnold et al., *Release Note – Vbfnlo-2.6.0*, (2012), arXiv: 1207.4975 [hep-ph].

[90] N. Davidson, T. Przedzinski, and Z. Was, *PHOTOS Interface in C++: Technical and Physics Documentation*, (2010), arXiv: 1011.0937 [hep-ph].

[91] Pierre Artoisenet et al., *Automatic spin-entangled decays of heavy resonances in Monte Carlo simulations*, JHEP **03** (2013) 015, arXiv: 1212.3460 [hep-ph].

[92] D. J. Lange, *The EvtGen particle decay simulation package*, Nucl. Instrum. Meth. A **462** (2001) 152.

[93] Alessandro Ballestrero et al., *Precise predictions for same-sign W-boson scattering at the LHC*, Eur. Phys. J. C **78** (2018) 671, arXiv: 1803.07943 [hep-ph].

[94] ATLAS Collaboration, *Modelling of the vector boson scattering process $pp \to W^{\pm}W^{\pm}jj$ in Monte Carlo generators in ATLAS*, ATL-PHYS-PUB-2019-004, 2019, URL: https://cds.cern.ch/record/2655303.

[95] Stefano Frixione and Bryan R Webber, *Matching NLO QCD computations and parton shower simulations*, JHEP **2002** (2002) 029.

[96] Simone Alioli et al., *A general framework for implementing NLO calculations in shower Monte Carlo programs: the POWHEG BOX*, JHEP **06** (2010) 043.

[97] Tom Melia et al., *W+W+ plus dijet production in the POWHEG BOX*, The European Physical Journal C **71** (2011) 1670.

[98] Alessandro Ballestrero et al., *PHANTOM: A Monte Carlo event generator for six parton final states at high energy colliders*, Comput. Phys. Commun. **180** (2009) 401, arXiv: 0801.3359 [hep-ph].

[99] Mauro Moretti, Thorsten Ohl, and Jurgen Reuter, *O'Mega: An Optimizing matrix element generator*, (2001) 1981, arXiv: 0102195 [hep-ph].

[100] S. Hoche for the Sherpa collaboration, "Status of Sherpa event generator", Multi-Boson Interactions Workshop at the University of Michigan, 2018.

[101] Sally Dawson, *The effective W approximation*, Nucl. Phys. B **249** (1985) 42.

[102] Baptiste Cabouat and Torbjörn Sjöstrand, *Some Dipole Shower Studies*, Eur. Phys. J. C **78** (2018) 226, arXiv: 1710.00391 [hep-ph].

[103] P. Skands, S. Carrazza, and J. Rojo, *Tuning PYTHIA 8.1: the Monash 2013 tune*, EEur. Phys. J. C **74** (2014) 3024.

[104] ATLAS Collaboration, *ATLAS Run 1 Pythia8 tunes*, ATL-PHYS-PUB-2014-021, 2014, URL: http://cds.cern.ch/record/1966419.

[105] ATLAS Collaboration, *Example ATLAS tunes of Pythia8, Pythia6 and Powheg to an observable sensitive to Z boson transverse momentum*, ATL-PHYS-PUB-2013-017, 2013, URL: https://cds.cern.ch/record/1629317.

[106] Herwig Collaboration, *Herwig 7.1 Tunes*, 2018, URL: https://herwig.hepforge.org/tutorials/mpi/tunes.html (visited on 07/02/2019).

[107] Sherpa Team, *Sherpa 2.2.2 Manual - Tunes*, 2017, URL: https://sherpa.hepforge.org/doc/SHERPA-MC-2.2.2.html#TUNE (visited on 07/02/2019).

[108] John C. Collins, *Sudakov form-factors*, Adv. Ser. Direct. High Energy Phys. **5** (1989) 573, arXiv: 0312336 [hep-ph].

[109] ATLAS Collaboration, *ATLAS simulation of boson plus jets processes in Run 2*, ATL-PHYS-PUB-2017-006, 2017, URL: http://cds.cern.ch/record/2261937.

[110] ATLAS Collaboration, *Multi-Boson Simulation for 13 TeV ATLAS Analyses*, ATL-PHYS-PUB-2017-005, 2017, URL: http://cds.cern.ch/record/2261933.

[111] ATLAS Collaboration, *Studies on top-quark Monte Carlo modelling with Sherpa and MG5_aMC@NLO*, ATL-PHYS-PUB-2017-007, 2017, URL: https://cds.cern.ch/record/2261938.

[112] ATLAS Collaboration, *Improvements in $t\bar{t}$ modelling using NLO+PS Monte Carlo generators for Run2*, ATL-PHYS-PUB-2018-009, 2018, URL: http://cds.cern.ch/record/2630327.

[113] Tanju Gleisberg and Stefan Höche, *Comix, a new matrix element generator*, JHEP **12** (2008) 039, arXiv: 0808.3674 [hep-ph].

[114] Steffen Schumann and Frank Krauss, *A Parton shower algorithm based on Catani-Seymour dipole factorisation*, JHEP **03** (2008) 038, arXiv: 0709.1027 [hep-ph].

[115] Stefan Höche et al., *QCD matrix elements and truncated showers*, JHEP **0905** (2009) 053.

[116] G. Aad et al. [ATLAS Collaboration], *Measurement of the Z/γ^* boson transverse momentum distribution in pp collisions at $\sqrt{s} = 7$ TeV with the ATLAS detector*, JHEP **09** (2014) 145, arXiv: 1406.3660 [hep-ex].

[117] J. Pumplin et al., *New generation of parton distributions with uncertainties from global QCD analysis*, JHEP **07** (2002) 012, arXiv: hep-ph/0201195 [hep-ph].

[118] Fabio Cascioli, Philipp Maierhofer, and Stefano Pozzorini, *Scattering Amplitudes with Open Loops*, Phys. Rev. Lett. **108** (2012) 111601, arXiv: 1111.5206 [hep-ph].

[119] Stefan Höche et al., *QCD matrix elements + parton showers: The NLO case*, JHEP **04** (2013) 027, arXiv: 1207.5030 [hep-ph].

[120] Torbjörn Sjöstrand, Stephen Mrenna, and Peter Z. Skands, *PYTHIA 6.4 Physics and Manual*, JHEP **05** (2006) 026, arXiv: hep-ph/0603175.

[121] Peter Zeiler Skands, *Tuning Monte Carlo Generators: The Perugia Tunes*, Phys. Rev. D **82** (2010) 074018, arXiv: 1005.3457 [hep-ph].

[122] T Cornelissen et al., "Concepts, Design and Implementation of the ATLAS New Tracking (NEWT)", tech. rep. ATL-SOFT-PUB-2007-007, CERN, 2007, URL: http://cds.cern.ch/record/1020106.

[123] Andreas Salzburger, *Optimisation of the ATLAS Track Reconstruction Software for Run-2*, J. Phys. Conf. Ser. **664** (2015) 072042.

[124] R. Fruhwirth, *Application of Kalman filtering to track and vertex fitting*, Nucl. Instrum. Meth. A **262** (1987) 444.

[125] ATLAS Collaboration, *Early Inner Detector Tracking Performance in the 2015 data at $\sqrt{s} = 13$ TeV*, ATL-PHYS-PUB-2015-051, 2015, URL: http://cds.cern.ch/record/2110140.

[126] A. Salzburger, "The ATLAS Track Extrapolation Package", tech. rep. ATL-SOFT-PUB-2007-005, 2007, URL: https://cds.cern.ch/record/1038100.

[127] M. Aaboud et al. [ATLAS Collaboration], *Reconstruction of primary vertices at the ATLAS experiment in Run 1 proton-proton collisions at the LHC*, Eur. Phys. J. C **77** (2017) 332.

[128] "Number of tracks vs. mu with full 2016 data", 2016, URL: https://atlas.web.cern.ch/Atlas/GROUPS/PHYSICS/PLOTS/IDTR-2016-015/.

[129] M. Aaboud et al. [ATLAS Collaboration], *Muon reconstruction performance of the ATLAS detector in proton-proton collision data at $\sqrt{s} = 13$ TeV*, Eur. Phys. J. C **76** (2016) 292.

[130] "ATLAS Muon Combined Performance with the full 2016 dataset", 2017, URL: https://atlas.web.cern.ch/Atlas/GROUPS/PHYSICS/PLOTS/MUON-2017-001/.

[131] W. Lampl et al., "Calorimeter Clustering Algorithms: Description and Performance", tech. rep. ATL-LARG-PUB-2008-002, 2008, URL: https://cds.cern.ch/record/1099735.

[132] M. Aaboud et al. [ATLAS Collaboration], *Electron reconstruction and identification in the ATLAS experiment using the 2015 and 2016 LHC proton-proton collision data at $\sqrt{s} = 13$ TeV*, Submitted to: Eur. Phys. J. (2019), arXiv: 1902.04655 [physics.ins-det].

[133] M. Aaboud et al. [ATLAS Collaboration], *Jet energy scale measurements and their systematic uncertainties in proton-proton collisions at $\sqrt{s} = 13$ TeV with the ATLAS detector*, Phys. Rev. D **96** (2017) 072002.

[134] G. Aad et al. [ATLAS Collaboration], *Topological cell clustering in the ATLAS calorimeters and its performance in LHC Run 1*, Eur. Phys. J. C **77** (2017) 490, arXiv: 1603.02934 [hep-ex].

[135] G. P. Salam M. Cacciari and G. Soyez, *The anti-ktjet clustering algorithm*, JHEP **04** (2008) 063, arXiv: 0802.1189 [hep-ph].

[136] ATLAS Collaboration, *Properties of Jets and Inputs to Jet Reconstruction and Calibration with the ATLAS Detector Using Proton-Proton Collisions at $\sqrt{s} = 13$ TeV*, ATL-PHYS-PUB-2015-036, 2015, URL: http://cds.cern.ch/record/2044564.

[137] Zachary Marshall and the ATLAS Collaboration, *Simulation of Pile-up in the ATLAS Experiment*, J. Phys.: Conf. Ser. **513** (2014) 022024.

[138] G. Aad et al. [ATLAS Collaboration], *Jet energy measurement with the ATLAS detector in proton-proton collisions at $\sqrt{s} = 7$ TeV*, Eur. Phys. J. C **73** (2013) 2304.

[139] "JES Public Plots for Moriond 2017", 2017, URL: https://atlas.web.cern.ch/Atlas/GROUPS/PHYSICS/PLOTS/JETM-2017-003/.

[140] ATLAS Collaboration, *Optimisation of the ATLAS b-tagging performance for the 2016 LHC Run*, ATL-PHYS-PUB-2016-012, 2016, URL: http://cds.cern.ch/record/2160731.

[141] M. Aaboud et al. [ATLAS Collaboration], *Performance of b-jet identification in the ATLAS experiment*, JINST **11** (2016) P04008.

[142] M. Aaboud et al. [ATLAS Collaboration], *Measurements of b-jet tagging efficiency with the ATLAS detector using $t\bar{t}$ events at $\sqrt{s} = 13$ TeV*, JHEP **08** (2018) 089, arXiv: 1805.01845 [hep-ex].

[143] M. Aaboud et al. [ATLAS Collaboration], *Performance of missing transverse momentum reconstruction with the ATLAS detector using proton-proton collisions at $\sqrt{s} = 13$ TeV*, Eur. Phys. J. C **78** (2018) 903.

[144] "Missing transverse energy performance and systematic uncertainties using the full 2015 dataset", 2016, URL: http://atlas.web.cern.ch/Atlas/GROUPS/PHYSICS/PLOTS/JETM-2016-003/.

[145] M. Aaboud et al. [ATLAS Collaboration], *Luminosity determination in pp collisions at $\sqrt{s} = 8$ TeV using the ATLAS detector at the LHC*, Eur. Phys. J. C **76** (2016) 653.

[146] Matteo Cacciari, Gavin P. Salam, and Gregory Soyez, *The Catchment Area of Jets*, JHEP **04** (2008) 005, arXiv: 0802.1188 [hep-ph].

[147] "Public Egamma Trigger Plots for Collision Data", 2016, URL: https://twiki.cern.ch/twiki/bin/view/AtlasPublic/EgammaTriggerPublicResults.

[148] Lidia Dell'Asta and Savanna Marie Shaw, "Muon trigger public plots with full 2016 dataset", tech. rep. ATL-COM-DAQ-2017-005, CERN, 2017, URL: https://cds.cern.ch/record/2242824.

[149] ATLAS Collaboration, *Tagging and suppression of pileup jets with the ATLAS detector*, ATLAS-CONF-2014-018, 2014, URL: https://cds.cern.ch/record/1700870.

[150] "JVT Public Plots for ICHEP 2016", 2016, URL: https://atlas.web.cern.ch/Atlas/GROUPS/PHYSICS/PLOTS/JETM-2016-011/.

[151] S. Schael et al., *Precision electroweak measurements on the Z resonance*, Phys. Rept. **427** (2006) 257, arXiv: 0509008 [hep-ex].

[152] M. Aaboud et al. [ATLAS Collaboration], *Measurements of top-quark pair to Z-boson cross-section ratios at $\sqrt{s} = 13, 8, 7$ TeV with the ATLAS detector*, JHEP **02** (2017) 117, arXiv: 1612.03636 [hep-ex].

[153] Will Di Clemente, "Measurement of electroweak production of same-sign W boson pairs with ATLAS", 2019, URL: http://cds.cern.ch/record/2674035.

[154] Sayipjamal Dulat et al., *New parton distribution functions from a global analysis of quantum chromodynamics*, Phys. Rev. D **93** (2016) 033006, arXiv: 1506.07443 [hep-ph].

[155] Benedikt Biedermann, Ansgar Denner, and Mathieu Pellen, *Complete NLO corrections to W^+W^+ scattering and its irreducible background at the LHC*, JHEP **10** (2017) 124, arXiv: 1708.00268 [hep-ph].

[156] M. Aaboud et al. [ATLAS Collaboration], *Measurement of the Inelastic Proton-Proton Cross Section at $\sqrt{s} = 13$ TeV with the ATLAS Detector at the LHC*, Phys. Rev. Lett. **117** (2016) 182002, arXiv: 1606.02625 [hep-ex].

[157] "HistFactory: A tool for creating statistical models for use with RooFit and RooStats", tech. rep. CERN-OPEN-2012-016, CERN, 2012, URL: `https://cds.cern.ch/record/1456844/files/CERN-OPEN-2012-016.pdf`.

[158] ATLAS Collaboration, *Prospects for the measurement of the $W^{\pm}W^{\pm}$ scattering cross section and extraction of the longitudinal scattering component in pp collisions at the High-Luminosity LHC with the ATLAS experiment*, ATL-PHYS-PUB-2018-052, 2018, URL: `https://cds.cern.ch/record/2652447`.

[159] Genessis Perez, Marco Sekulla, and Dieter Zeppenfeld, *Anomalous quartic gauge couplings and unitarization for the vector boson scattering process $pp \to W^+W^+jjX \to \ell^+\nu_\ell\ell^+\nu_\ell jjX$*, Eur. Phys. J. C **78** (2018) 759, arXiv: `1807.02707` [hep-ph].

[160] M. Aaboud et al. [ATLAS Collaboration], *Search for doubly charged Higgs boson production in multi-lepton final states with the ATLAS detector using proton-proton collisions at $\sqrt{s} = 13\,TeV$*, Eur. Phys. J. C **78** (2018) 199, arXiv: `1710.09748` [hep-ex].

[161] M. Aaboud et al. [ATLAS Collaboration], *Search for doubly charged scalar bosons decaying into same-sign W boson pairs with the ATLAS detector*, Eur. Phys. J. C **79** (2018) 58, arXiv: `1808.01899`.

[162] Rene Brun and Fons Rademakers, *TFractionFitter Class Reference*, 2015, URL: `https://root.cern.ch/root/html532/TFractionFitter.html` (visited on 08/05/2019).

[163] Rene Brun and Fons Rademakers, *ROOT - An object oriented data analysis framework*, Nucl. Inst. and Meth. in Phys. Res. A **389** (1997) 81, see also http://root.cern.ch/.

[164] ATLAS Collaboration, *Measurement of track reconstruction inefficiencies in the core of jets via pixel dE/dx with the ATLAS experiment using $\sqrt{s} = 13$ TeV pp collision data*, ATL-PHYS-PUB-2016-007, 2016, URL: `https://cds.cern.ch/record/2140460`.

[165] M. Aaboud et al. [ATLAS Collaboration], *Performance of the ATLAS Track Reconstruction Algorithms in Dense Environments in LHC Run 2*, Eur. Phys. J. C **77** (2017) 673.

[166] G. Aad et al. [ATLAS Collaboration], *Jet energy resolution in proton-proton collisions at $\sqrt{s} = 7$ TeV recorded in 2010 with the ATLAS detector*, Eur. Phys. J. C **73** (2013) 2306, arXiv: `1210.6210` [hep-ex].

[167] G. Aad et al. [ATLAS Collaboration], *Jet mass and substructure of inclusive jets in $\sqrt{s} = 7$ TeV pp collisions with the ATLAS experiment*, JHEP **05** (2012) 128, arXiv: `1203.4606` [hep-ex].

[168] G. Aad et al. [ATLAS Collaboration], *A search for high-mass resonances decaying to $\tau^+\tau^-$ in pp collisions at $\sqrt{s} = 8$ TeV with the ATLAS detector*, JHEP **07** (2015) 157, arXiv: `1502.07177` [hep-ex].

[169] G. Aad et al. [ATLAS Collaboration], *A neural network clustering algorithm for the ATLAS silicon pixel detector*, JINST **9** (2014) P09009, arXiv: `1406.7690` [hep-ex].

[170] ATLAS Collaboration, *The Optimization of ATLAS Track Reconstruction in Dense Environments*, ATL-PHYS-PUB-2015-006, 2015, URL: `https://cds.cern.ch/record/2002609`.

[171] G. Aad et al. [ATLAS Collaboration], *ATLAS pixel detector electronics and sensors*, JINST **3** (2008) P07007.